Model guided capacitance tomography
a Bayesian approach to flow regime independent multiphase flow measurement

Drury, Ross

Award date:
2019

Awarding institution:
Coventry University

MODEL GUIDED CAPACITANCE TOMOGRAPHY:

A Bayesian approach to flow regime independent multiphase flow measurement

ROSS JAMES DRURY

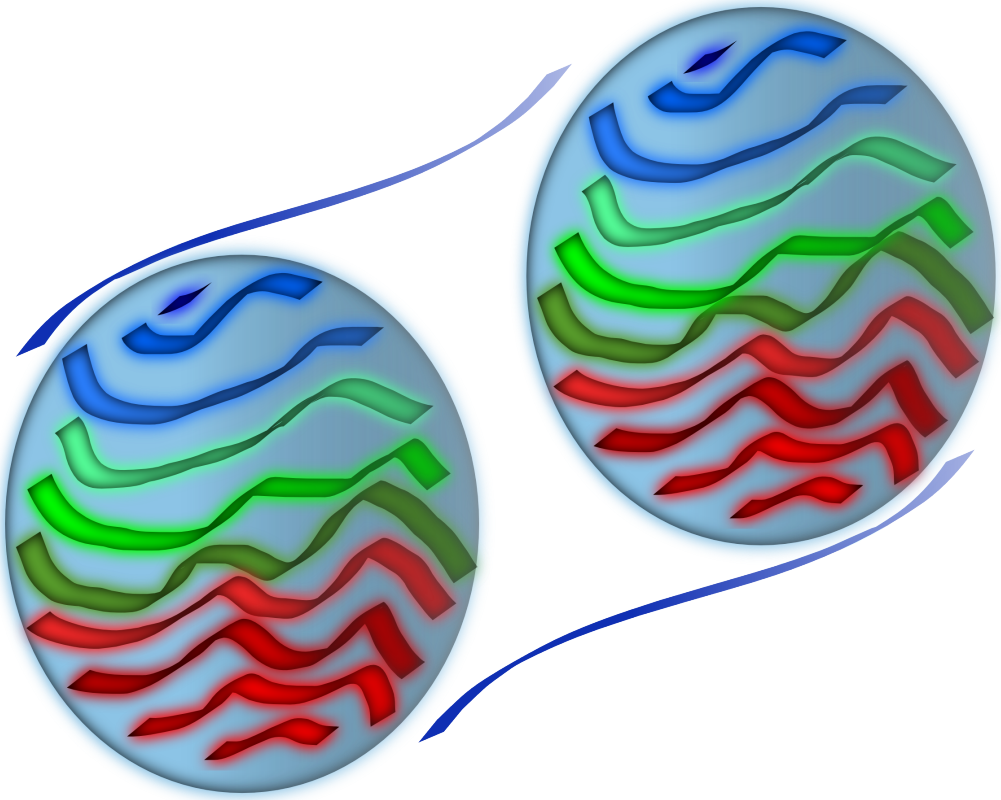

A thesis submitted in partial fulfilment of the University's requirements for the Degree of Doctor of Philosophy

Complex Fluids and Systems
Engineering, Environment and Computing
Coventry University

January 2019

SUPERVISORS:
Prof. Andrew Hunt
Prof. James Brusey
Prof. Elena Gaura

LOCATION:
Coventry, UK

TIME FRAME:
January 2016 - January 2019

To friends and family, for remaining such.

ABSTRACT

Multiphase metering can provide substantial benefits to the oil and gas industry, including reduction in processing equipment and floor space at oil wells as well as improving profitability, and hence production lifetime of mature oil wells. This can be achieved by removing the need for phase separation at each oil well, which is required to perform single-phase flow measurement. If a multiphase flow measurement system can be developed, with an acceptable uncertainty, and with the capability of metering all flow regimes which occur in oil and gas pipelines, the overall extraction and distribution process can be simplified greatly. This would in turn provide significant financial benefits to the industry.

Providing a single multiphase measurement system which can achieve these goals has proven difficult, considering the complexity of the flows that occur. The three main criteria to achieve a suitable system are: a) suitability for sub-sea implementation, b) the ability to operate on all flow regimes, and c) to not be reliant on empirical correlations due to their limitations. Electrical Capacitance Tomography (ECT) is an example of an instrument suited to oil and gas applications due to its non-intrusive and non-invasive nature. For slug flows, ECT is a capable cross-correlation based multiphase flow meter, but for segregated flows, such as annular, its capability is compromised, due to a heavy reliance on correlations, and by its principal of measuring fluid interfaces only, which restricts its ability to recover individual phase velocities.

Three studies are conducted with the aim of developing ECT as a multiphase flow measurement system, focusing on providing a solution which can be applied to all flow regimes and does not rely on empirical correlations. The first study includes experiments on vertical slug and annular industrial scale flows, whereby a method is proposed that uses the similarities between wave properties measured for both flow regimes, allowing self derivation of correlation parameters using slug flow data. The results show that a power law approximation can describe similarities in wave properties, and by using the method outlined annular flow properties can be estimated within plus or minus 50% without any empirically derived parameters.

The second study is on improving cross-correlation metering of slug flows. Experiments are conducted on horizontal oil and gas industrial scale flows. Velocity discontinuities are identified by their structure at the slug front through observation of tomographic images. Three distinct slug front structures are categorised and tested to analyse their affect on the cross-correlation measurement. Individual measurement

methods are prescribed depending on slug front structure and a method of selective based cross-correlation is described. Results show that by using this method the superficial mixture velocity can be obtained within an error margin of $+/-5\%$, an improvement on previous studies where $+/-10\%$ is a typical benchmark.

The final study is an implementation of a particle filtering system, incorporating tomography and a computational fluid model. Experiments are conducted on a vertical lab scale flow loop where gas is applied through a column of oil. A simulation database is created using an Euler-Euler model which is referenced through a particle filtering algorithm. Data from ECT and pressure transducers are used to update the recursion and allow an estimation of gas flowrate over time, without the use of empirical correlations, and with the potential to be applied to all flow regimes. The results showed that the mean gas superficial velocity of a range of tests can be estimated within an error margin of $+/-5\%$.

"For in prosperity a man is often puffed up with pride,
whereas tribulations chasten and humble him through suffering and sorrow.
In the midst of prosperity the mind is elated, and in prosperity a man forgets himself;
in hardship he is forced to reflect on himself, even though he be unwilling.
In prosperity a man often destroys the good he has done;
amidst difficulties he often repairs what he long since did in the way of wickedness."

— King Alfred the Great

ACKNOWLEDGEMENTS

I would like to thank my supervisory team for their support during this process. For providing the funding for this work, and facilitating the experiments conducted in it, thank you to the National Engineering Laboratory (NEL), in particular David Millington. For providing the measurement instrument that this work is founded on, thank you to Atout Process. To my colleagues, thank you for sharing this experience with me and making it so enjoyable, I wish you all the luck in the world.

CONTENTS

LIST OF FIGURES

LIST OF TABLES

ACRONYMS

CAD Computer Aided Design

CFD Computational Fluid Dynamics

CSF Continuum Surface Force

DDAG Decision Directed Acyclic Graph

ECT Electrical Capacitance Tomography

EIT Electrical Impedance Tomography

ERT Electrical Resistance Tomography

FEM Finite Element Method

FRIMM Flow Regime Independent Multiphase Measurement

HMM Hidden Markov Model

HPC High Performance Computer

LBP Linear Back Projection

LS Level Set

MAC Marker And Cell

MCMC Markov Chain Monte Carlo

MIT Magnetic Induction tomography

MPI Message Passing Interface

MRI Magnetic Resonance Imaging

NEL National Engineering Laboratory

NTP Normal Temperature and Pressure

QCV Quick Closing Valves

RCD Relative Capacitance Difference

RCR Relative Capacitance Ratio

SIR Sequential Importance Re-sampling

SVM Support Vector Machines

VOF Volume Of Fluid

Part I

INTRODUCTION AND LITERATURE SURVEY

1

INTRODUCTION

We are as reliant on oil and gas as ever, to heat our homes, to fuel our cars, to power our industries. Despite the growth of renewable energy it is apparent that in the absence of a greater source of cheap energy, oil and gas production will dominate for the foreseeable future. However, improvements can be made to both reduce the emissions and environmental impact of oil and gas processing, as well as reduce the cost to the consumer. This can be achieved by improving the efficiency of the overall oil and gas production process, for which many options are available. The work in this thesis has focussed specifically on creating an alternative measurement strategy to the current practices at the oil wells themselves, where the oil is extracted, metered and distributed.

Current upstream practices see the extracted multiphase mixture of oil, gas, water, and solids from the oil well begin processing immediately, at the well itself. In this process, the mixture is separated into its individual components at the oil well, typically using large gravity separator tanks, where the fluids separate by means of gravity, due to differences in density. Despite this method being applied at most oil wells sufficiently, the incurred requirement for large and heavy equipment, well test lines, and high platform space and load requirements at every oil well is expensive and inefficient, compared to such a process being pushed further down the production line [52]. Ideally, the process at the oil well would require minimal equipment and maintenance, and would simply act to transport the extracted mixture to a single processing location. This would allow for the processing to be conducted for multiple wells at a single location, allowing a significant reduction in equipment requirement, and improving the overall processing efficiency. Furthermore, this would also increase the financial viability of extraction at mature oil wells, where the amount of oil and gas gained is reduced, with the increase in water. For such oil wells, justifying their operation becomes difficult, as the amount of useful fluids are reduced, therefore the cost of maintaining processing at these locations soon outweighs the benefits and thus become unsustainable. If, as suggested, the processing can be pushed further down the production line, mature oil wells will become a feasible source of oil, effectively replacing, in part, energy that would require an entirely new oil well to be established.

The main reason that separation is needed, is to measure the amount of oil and gas recovered from the oil well. This is required to ensure the correct quantities of oil and gas, conforming to international stand-

ards on measurement uncertainty, are distributed to their designated location. Considering that oil and gas pipelines can transport fluids around the world, through varying tax domains, it is clear to see that a high accuracy of metering is paramount, for both the distributor and the customer. By separating the phases, single phase flowmeters can be used to meter individual phases separately, then distribute accordingly. Single phase meters capable of determining the flowrates to uncertainties of less than 1%, and are thus an obvious choice in cases of custody transfer [37], due to significant developments over many years. In order to replace the need to separate phases and meter them individually, an alternative strategy is to use multiphase metering, where all phases of the extracted mixture are measured simultaneously. Although this removes the need for early processing, it does, however have its own problems. Due to the added complexity of multiphase flow, conducting flow measurement within an accuracy which is acceptable for this application is difficult. One of the most prevalent issues is with regard to flow regimes, where different flow patterns occur, dependent on the relative velocity of the phases.. Providing a single measurement unit which can adapt to all the flow regimes encountered is yet to be solved. Despite some progress in multiphase metering, with commercial meters achieving $+/-10\%$ for a reasonable flow range [51], solutions so far are limited in terms of achieving a suitable accuracy, their applicability to flow regimes and fluid properties, and have particular issues concerning flows which are undergoing transitions between flow regimes. Furthermore, some such devices rely on empirically derived correlations and calibration to meter the flows successfully, again limiting their applicability.

The solution to greatly improving the oil and gas measurement and distribution process relies on the development of a Flow Regime Independent Multiphase Measurement (FRIMM) system, which does not rely on empirical correlations, and thus can act independently in providing a high degree of accuracy in measuring individual phase flowrates. Although the achieved accuracy must be suitable, with uncertainty less than 5% as a reasonable figure, it is conceivable that such systems could be successfully applied without reaching the uncertainty levels achievable with single phase flowmeters. This is due to the significant reduction in costs, with respects to less equipment and floorspace needed at each oil well, which such meters would bring to the overall oil and gas process, justifying small reductions in the meter accuracies. It may also be the case that multiphase metering systems could act as a mechanism for fiscal metering, where these systems become cash registers for oil and gas distribution. In this thesis, an attempt has been made to provide a foundation for the described FRIMM systems, based on the use of Electrical Capacitance Tomography (ECT) as the main sensor, while incorporating other methods.

1.1 RESEARCH CHALLENGES

With the aim of providing a foundation for a new solution to multiphase flow metering, the following research challenges can be defined. Firstly, a sufficient knowledge and understanding of the current potential and limitations of ECT as a multiphase meter is required in order to determine a suitable route to further development in the oil and gas industry. Furthermore, by identifying any independent developments to ECT for metering the specific flows encountered in industry could not only provide an improvement in potential, but may also be utilised to determine how the proposed advanced developments can be implemented or improved.

The main challenge presented in this work is to determine the validity in the integration of ECT with a CFD model in a statistical framework such as particle filtering, which has been shown to be a useful tool in other applications. Alongside this, there is a clear advantage in ensuring that the proposed development does not rely heavily on empirical data, which has become a significant limiting factor in alternative solutions. Finally, with the acceptance that this work can only provide the foundation for the desired solution, an important goal in this work is to clearly outline what will be required in the future to build on this work, with the goal of producing a practical multiphase flow meter to be utilised in the oil and gas industry.

1.2 KNOWLEDGE CONTRIBUTIONS

Two contributions to knowledge are made in this work. The first, a prerequisite of the second, is the analysis of the current potential of Electrical Capacitance Tomography (ECT) to the flow measurement of multiphase liquid-gas flows, inclusive of multiple flow regimes. That is, through obtaining phase fraction and cross-correlation velocities, highlight which flow types, and to what degree of accuracy, ECT is able to measure the critical flow parameters (focussed on phase superficial velocities in this work) as a standalone meter, . This includes: the incorporation of the imaging ability of ECT to analyse the structures present to develop the current method of slug flow cross-correlation measurement, as well as the combination of information from multiple flow regime measurements, to assist in the flow measurement of flow regimes which are not particularly susceptible to tomography based measurement.

The second contribution of this work is to create a recursive based system which incorporates CFD modelling and the known measurement and model inaccuracies, and can therefore extend the current reach of tomographic measurement into a more complex system with greater potential. With the restrictions that, the system does not rely on both trained data sets due to the untenable flow situations that

could be encountered, but also empirically derived correlations, which again, cannot model a large enough variation in flow and system properties.

1.3 PUBLICATIONS

Ross Drury, Andrew Hunt, James Brusey, *Identification of horizontal slug flow structures for application in selective cross-correlation metering*, Flow Measurement and Instrumentation, 2019 [Accepted manuscript, in publication process]
Accepted journal paper submitted to Flow Measurement and Instrumentation due for publication in 2019. This paper is based on the work in Section 5.2 and is provided in Appendix A.

1.4 ACKNOWLEDGEMENT OF CONTRIBUTED WORK

This section includes acknowledgements to other researchers / organisations which contributed to the studies conducted.

- National Engineering Laboratory (NEL) for both providing the funding for this work, along with access to facilities for the experiments conducted.
- David Millington for organising and running experiments included in this thesis, as well as the joint work on ECT for multiphase flow metering and conductive phases included in Appendix B.
- Atout Process Ltd. for providing the ECT sensor along with the associated software tools used in all experiments in this work.
- Coventry University for providing a flowloop used in one of the experiments in this work.

1.5 ACKNOWLEDGEMENT OF SOFTWARE TOOLS

This section acknowledges the software tools used throughout this work.

PYTHON The object oriented Python programming language is utilised in this work for developing and running the scripts for the algorithms of the particle filtering system and the interfacial wave method. Additionally, a Python script using the OpenGL graphics package is used to develop the ECT software which generates the tomographic images of slug flow structures.

R The statistical based programming language R is used for data analysis and the generation of graphs in this document, in particular with the use of the ggplot2 graphical package.

SENSOR TOOLKIT ECT software provided by Atout Process Ltd. used to obtain the raw capacitance data used within this work, as well as providing the calibration tool for the sensor.

ECT32 V3 This software package, which is bespoke for the ECT instrument provided by Atout Process Ltd. used in this work, provided a tool to easily view and analyse tomographic images, and was particularly used in the analysis of slug flow structures as well as the general analysis of all ECT data.

FLOWAN 2 The third ECT software package provided by Atout Process Ltd. was used in this work to conduct the full analysis of ECT data, particularly the application of cross-correlation.

OPENFOAM The open source CFD package OpenFOAM is utilised in this work for all CFD simulations including both validation and the application of the particle filtering system.

LYX LyX is the document processing package used to create this document.

CLASSICTHESIS A Lyx template used to format this document.

1.6 THESIS STRUCTURE

This thesis is structured as follows:

CHAPTER 2 Capacitance tomography and its place in multiphase flow measurement.

A literature survey focussing on developments in the use of ECT to measure multiphase flows. This includes its development as an early instrument, its application to different flow regimes, and its ability in flow regime identification.

CHAPTER 3 Particle filtering methods and multiphase CFD.

A literature survey on the particle filtering method, its general formulation, and the different method variations that have been applied, followed by a section on CFD models for application in multiphase flows.

CHAPTER 4 Research outline, experimental setup and data collection

Chapter presenting the three experiments used to obtain data presented in this work, including the general description, schematics, flow ranges and associated equipment used.

CHAPTER 5 Flow regime independent tomographic flow measurement.

An outline of the the three main studies undertaken, including justification/motivation with respect to FRIMM, as well as method, results and discussion.

CHAPTER 6 Future system proposal.

Chapter showcases a *future system* based on the work conducted previously, highlighting what would be required in the future in order to use this work as a foundation to produce an effective solution to multiphase flow metering.

CHAPTER 7 Conclusion

A chapter providing the conclusions and future work for each study, a summary of the thesis output, and finally the answers to the proposed research questions.

2

CAPACITANCE TOMOGRAPHY AND ITS PLACE IN MULTIPHASE FLOW MEASUREMENT

In this chapter the aim is to provide a background knowledge of the use of capacitance based tomography in multiphase flow measurement, in order to build a foundation in understanding current developments, and in particular, the areas which require improvement. This then will provide a basis for some of the work in this thesis and justify both its requirement and possible impact. The topics broadly include: the use of ECT in multiple flow regimes, where it has been successfully applied, and its limitations.

This chapter is structured in the following way:

2.1 Provides background knowledge of ECT including its early development, operating principle and design.

2.2 Describes the application of ECT in the online identification of flow regimes, including methods and development.

2.3 Outlines the significant limitation of ECT when applied to conductive fluids, as well as some proposed solutions.

2.4 Describes the successful application of ECT to flow measurement of slug flows, along with variants in method and correlations.

2.5 Outlines the the use of inter-facial wave properties in annular and stratified flow, including for heavy oil flows.

2.1 ECT FUNDAMENTALS AND DEVELOPMENT

The term 'tomography' can be described by its Greek origins, with 'tomos', (a slice) and 'graphia' (representation). In the context of process tomography, this slice representation takes the form of cross-sectional images of a non-visible space, obtained via a multitude of sensors and used to provide both spatial and temporal information of process parameters. In applications of multiphase / multicomponent systems, the process parameters of interest are the phases or components (oil,gas and water) themselves, which in turn provide information of phase distribution and overall content within the cross-section. In order to provide such information, the sensors used must measure a property that significantly changes between the phases[1], and hence can be used to identify the interfaces between them. Many different

1 The term phases is used here in reference to both 'phases' and 'components' as used previously, which has now become a general notation to refer to these separate cases.

properties have been used to distinguish between phases with tomographic based sensors in this way, including: resistance, inductance, and impedance. In this work, capacitance based tomography is used, which distinguishes different phases according to their dielectric property (insulating capability) by the measuring the capacitance between a pair of electrodes.

2.1.1 *Background and operating principle*

The development of ECT began in the 1980's at the University of Manchester with the work of Beck and colleagues [10][61]. Their prototype ECT system provided images of static distribution models representing typical two-phase flow regimes. By the early to mid 1990's this system had already developed significantly due to the rapid increase in computational resources, allowing the design of the transputer system and imaging software [127] that produced real-time images. This led to early applications in, for example, oil pipeline measurements [128] and engine flame imaging [54], where the system was capable of 315 frames per second for a six electrode system. Further developments increased the imaging rate significantly to around 5000 frames per second [63] by improving the sensor circuit design.

While a single set of electrodes can identify the cross-sectional structure of a flow, much attention has been focussed on systems with dual measurement planes, positioned a short distance apart, allowing the cross-correlation of the two separate signals (in turn, providing a velocity measurement), and in turn, including ECT in the cross-correlation flowmeter family [11]. These developments have increased the systems potential to include applications in the aerospace industry for example, with measuring mass and velocity to estimate sloshing forces caused by propellent within a fuel tank [62].

The operating principle of ECT systems is broadly described as follows.

1. The capacitance is measured between a pairs of electrodes mounted around the area of interest (the pipe wall in the context of this work), where this capacitance is defined as the ratio of increase in stored charge relative to an increase in voltage difference between the electrode pair [120].

2. This is repeated at high frequency for each independent electrode pairing ($N(N-1)/2$ where N is the number of electrodes) using a multiplexing method to iterate through each pairing. This provides a vector of measurements, with the vector size dependent on the number of independent electrode pairs present.

3. The vector of measurements is then interpreted through a set of sensitivity maps for each electrode pair. The sensitivity map describes the sensor sensitivity at all locations within the sensing

area (cross-section). They consist of a set of 2D matrices, one for each independent electrode pair. The size of this matrix is the length of the measurement matrix by the number of pixels desired in the resulting image.

4. The values are normalised by use of the calibration measurements taken at conditions of the sensing area filled with low permittivity, as well as high permittivity, providing a relative permittivity value. These measurements are finally constructed into images through a specific reconstruction algorithm. The interpretation of the measurements can vary depending on the image reconstruction algorithm used, the most typical and simplest being Linear Back Projection (LBP). A mathematical description of this process is provided in Section 2.1.5.

ECT provides many benefits as a flowmeter technology, especially for the oil and gas industry. These include its non-intrusive and non-invasive nature, which is particularly important if such devices are deployed in oil and gas processes, where the pipes harsh internal environment would cause severe and costly maintenance issues. If sensors that physically interrupt the flow, such as turbine or orifice meters, are used, significant pressure drops are incurred that can compromise both the sensor and the pipeline. On the other hand, sensors that line the pipe walls, such as some Electrical Resistance Tomography (ERT) devices, or ones that require cavities in the pipe wall, such as Ultrasonic Doppler, can be vulnerable to build-up of deposits at sensor locations, that can significantly affect the sensors operation [85]. A further advantage of ECT, compared to other electrical tomographic methods, is its advanced stage of development, providing high measurement stability and sampling rate, allowing quantitative information to be gained at high speeds, which is a necessity for multiphase flow measurement. Finally, ECT, along with other electrical based tomographic methods, are relatively inexpensive compared to their 'hard field' counterparts used in the medical industry, such as Magnetic Resonance Imaging (MRI).

2.1.2 *Design principles*

The most vital outcomes from the system design of capacitance based tomography devices is outlined by Plaskowski et al. [1] as:

- A good signal-to-noise ratio, giving high sensitivity to changes in concentration
- Minimising baseline drift due to temperature changes, especially in industrial flows where the instrument is not calibrated for long intervals

Figure 2.1: Photo of ECT sensor provided by Atout Process Ltd., mounted on a flowloop test section.

- A homogeneous measurement sensitivity distribution. However with applications such as gas-solids flow, this is not always possible.
- High immunity to electrostatic interference, reducing the effect on measurement from reasons other than changes in concentration.

2.1.2.1 *Guard electrodes*

Guard electrodes are additional electrodes positioned between and around the measurement electrodes. The main purpose of a guard electrode is to avoid the electric field lines between two electrodes spreading axially, thus ensuring a parallel electric field pattern across the sensor. The use of guard electrodes in ECT systems is a necessity to fulfil the desired outcomes outlined previously. For sensors where the electrodes are short compared with the sensor diameter, extra axial guard electrodes are positioned at both ends of the measurement electrodes, along with one positioned between the two measurement electrodes. The result of introducing guard electrodes is the improvement in axial resolution of the sensor, along with an improvement in sensitivity [82]. Figure 2.2 shows an image of inside the ECT device used in this work, where the separate measurement and guard electrodes can be seen.

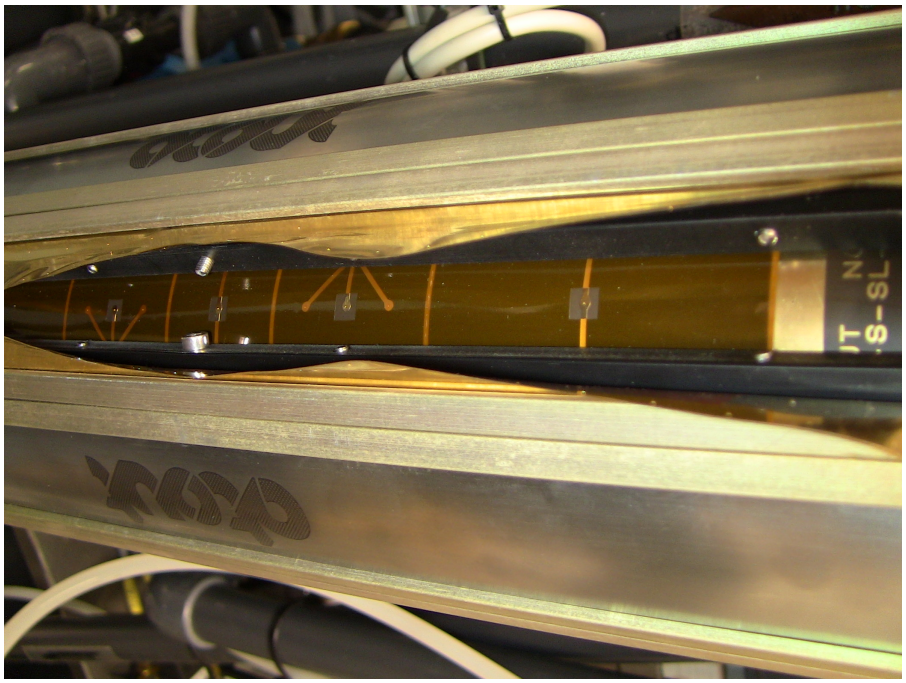

Figure 2.2: Image of ECT sensor showing electrodes exposed, with the order of electrode type from either edge as: Guard, Measurement, Guard, Measurement, Guard.

2.1.2.2 *Number of electrodes*

A significant design consideration in ECT is with regard to the number of electrodes positioned surrounding the sensing area. In selecting the number of electrodes, a choice is made by its effect on image resolution (both axial and radial), the sensor sensitivity, and the achievable image capture rate. With an increasing number of electrodes, the achievable resolution will increase, however, due to the reduction in electrode size, the sensitivity will decrease. Furthermore, a greater number of electrodes, and thus measurements taken, increases computation time, and hence decreases the image capture rate [1]. Typical ECT devices have either 6, 8 or 12 electrodes, which is generally accepted as suitable numbers for most applications.

2.1.2.3 *Electrode fabrication*

Despite varying between sensor manufacturers, a typical electrode fabrication method, as outlined by Atout Process Ltd. [81], is as follows. The fabrication process consists of using photolithography on a flexible copper-coated plastic laminate. This laminate is etched with the desired electrode design pattern, and then attached on the outside to a copper foil, ready to be applied to the pipe exterior. The measurement electrodes must then be surrounded by an earthed, metal screen, which the guard and measuring electrodes are connected to by screened coaxial connecting leads. The screen works to remove

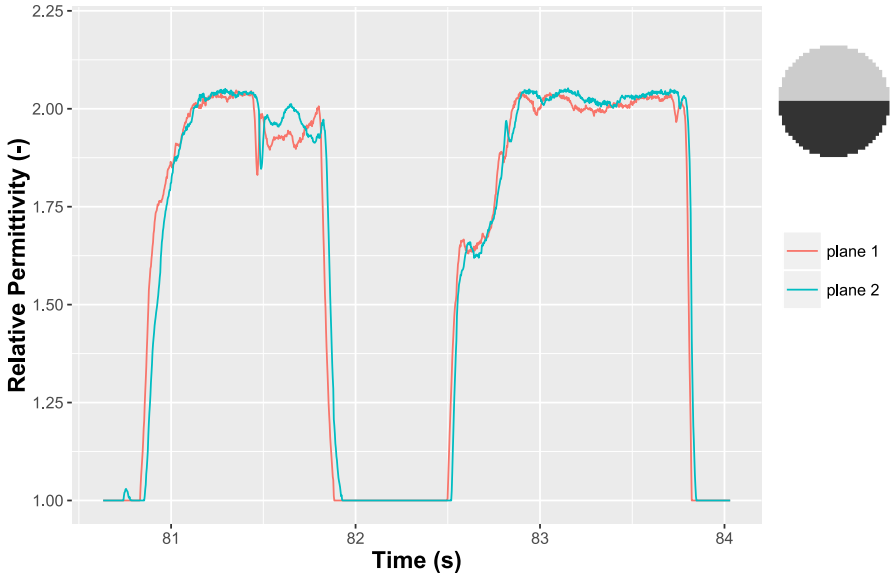

Figure 2.3: Example permittivity data from two measurement planes for slug flow. Cross-section image in top right displays the area (dark) in which the permittivity data is related to.

the effects of extraneous variations and signals during earthing, but must also provide the ECT sensor with strong mechanical stability considering the environment encountered when deployed [82]. Finally, the multiple electrodes, with earthed screens, are connected together with an equal spacing, by either a simple screw or a more complex spring clamp system, allowing the sensor to be easily clamped to a pipe section or integrated as part of a spool piece.

2.1.3 *Multi-plane operation*

As mentioned in Section 2.1.1, a common configuration of ECT systems is to employ dual measurement planes, allowing the two signals to be cross-correlated. In this way, a velocity based measurement can be obtained from the time difference between comparable signal fluctuations from the two measurement planes, given the known distance between the two planes. This principle is demonstrated in Figure 2.3, showing the two plane signals for slug flow. The most important design consideration when employing dual plane systems, is that the separation distance is short enough to ensure that there is minimal change in the flow structure [30], whilst conforming to the restriction posed by the sampling frequency and image reconstruction time, as pointed out by Elmy et al. [38]. Assuming that this criteria has

been satisfied, the cross-correlation function can be employed using the following.

$$R_{xy}(\tau) = \lim_{T\to\infty} \frac{1}{T} \int_0^T x(t)y(t+\tau)\mathrm{d}t \tag{2.1}$$

Where: $x(t)$ and $y(t)$ are the measured functions of permittivity (or relative density) in time, T is the length of time within the process and the integration limits (0 to T) is the integration window[2] for the selected data segment. At the maximum of this function ($R_{xy}(\tau)$), the corresponding value of τ represents the time difference at the highest point of correlation between the two signals. Through knowledge of the distance between measurement planes L, the cross-correlation velocity is calculated as:

$$U_{cc} = L/\tau \tag{2.2}$$

The cross-correlation process for imaging devices has two main variables affecting how it can be used: integration window size and signal location. Firstly, the duration of the integration window can be either extended, to cover a large range of signals, and hence provide an average transit time, or shortened, to provide a measurement of velocity over a more specific point in time. The selection of the integration window depends on the application and is discussed in greater detail in Section 2.4.1. Secondly, the signals used to cross-correlate can be obtained from specific points in the imaged cross-section, as opposed to the entire cross-section. This gives the ability to conduct cross-correlation on signals relating to particular areas in the measurement region, and can be applied to alleviate negative effects of signal fluctuations in said regions that are not of interest.

2.1.4 *Calibration and pre-processing*

The calibration process of ECT is relatively simple, requiring only the knowledge of the relative permittivity of the materials for which to measure. Therefore, a typical calibration process requires stable measurements of the inter-electrode capacitances to be taken when the measurement zone is completely filled with both the low and high permittivity dielectric materials. The pipe is first emptied (low permittivity) and the measurement is normalised to a value of 0, then the pipe is subsequently filled with the other (high permittivity) material, and the measurement is normalised to 1. Additionally, prior to operation, any system parameters are configured, with examples such as: image reconstruction method and iteration rate, normalising procedure, and data acquisition rate. Finally, the set of sensitivity maps

2 The term 'integration window' is used in Section 2.4 and 5.2 in the context of an input to the cross-correlation process, as defined in the ECT software package.

for each electrode pairing are obtained, which can be produced via simple analytical solution directly from capacitance values and sensor design parameters [81], or by the more complex method of using an internal electrode, as proposed by Dong et al. [31]. Or finally, by the use of the Finite Element Method (FEM) [1], which is more suitable for complex geometries.

2.1.5 *Image reconstruction*

The image reconstruction procedure for ECT systems has always been considered critical, due to its significant effect on obtainable accuracy. The requirement of image reconstruction is best described by the two most prevalent issues concerned with this method. The first is caused by the 'soft field' nature of ECT, referring to the fact that the electric field at all points in the cross-section is itself a function of changes of permittivity at any discrete point (pixel). This has a detrimental effect on the achievable spacial resolution, as opposed to 'hard field' sensors such as MRI used in the medical industry . The second main issue is regarding the solution to the inverse problem, an integral part of the imaging process (explained in greater detail at a later stage), which is ill-posed, due to the number of desired image pixels (spatial resolution) outnumbering the amount of independent measurements in all cases. An ill-posed problem can be defined as one which does not adhere to the conditions that:

- a solution exists, is unique, and depends continuously on the data of the problem [7].

The problem of ill-posedness in particular, creates the need for image reconstruction algorithms rather than more common inversion methods.

2.1.5.1 *Reconstruction types*

As pointed out by Cui et al. [26], image reconstruction techniques can be broadly categorised into indirect (with linearisation) and direct (without linearisation) methods. Indirect methods produce the low spatial resolution problem mentioned previously but require significantly less computation time [20], as opposed to direct methods, such as that used by Mueller et al. [90] and Bruhl and Hanke [16], which take longer to compute, but do not require iterative procedures and produce better images. For this reason, it is generally accepted that the application of either direct or indirect methods should depend on whether the process to be imaged is static or dynamic. As the focus of this work is centred on the dynamic process of fluid flow, direct methods of image reconstruction are deemed outside the scope of this work because of their effect on computation time being an important factor, and will therefore not be discussed further.

The main linearisation methods available are summarised by Cohen-Bacrie et al. [21] as the following:

- **The integral method** – sensitivity matrix is calculated analytically and uses assumptions of a circular medium and dipolar input current patterns
- **The sensitivity method** – sensitivity matrix is computed using Geselowitz theorem, with resulting high computational burden
- **First order approximation of the FEM** – computational modelling through FEM with sensitivity matrix obtained as the Jacobian of the model
- **Linearisation through Fourier coefficients** – expansion of Green function in Fourier series to analytically derive the potentials around the object

2.1.5.2 *The forward and inverse problem*

The necessity for derivation of sensitivity matrices can be explained through firstly defining the forward problem as:

$$\mathbf{c} = S\mathbf{g} \tag{2.3}$$

where $\mathbf{c}$ is a vector containing m normalised capacitance measurements with the size of m determined by the number of independent inter-electrode measurements, $\mathbf{g}$ is a vector containing n normalised pixel permittivity, with the size of n dependent on the number of desired image pixels (spacial resolution) and S is the sensitivity matrix of size m by n.

In this problem, the vector $\mathbf{g}$ is what is required to produce the image, the vector $\mathbf{c}$ is obtained from the sensor and the sensitivity matrix S has been obtained via the methods outlined previously. Therefore, to obtain the permittivity vector, the inverse problem is the requirement to find $\mathbf{g}$, with:

$$\mathbf{g} = S^{-1}\mathbf{c} \tag{2.4}$$

and so the inverse of the sensitivity matrix is required. This, as mentioned previously, is an ill-posed problem, as the sensitivity matrix will almost always be non-square since the number of image pixels desired is typically greater than the number of independent capacitance measurements available.

The simplest and most commonly applied method to solve the inverse problem is to substitute the inverse of the sensitivity matrix with its transpose, giving:

$$\mathbf{g} \backsimeq S^{T}\mathbf{c} \tag{2.5}$$

This method is called Linear Back Projection (LBP) and provides a simple yet effective solution which is still widely used for online image reconstruction [26].

To improve image quality, many iterative methods have been developed. A simple technique is presented here, which is based on LBP, but with the capability to reduce the negative effect of using the transpose of the sensitivity matrix. Firstly, we assume the inverse problem presented in eq. (2.4) is used to calculate an initial permittivity vector $\mathbf{g}$. Using these values, an updated set of capacitance measurements can be obtained, due to the difference incurred if $\mathbf{g_k}$ is re-entered into the forward problem in eq. (2.3). An updated iteration of the permittivity vector can therefore be obtained as:

$$\mathbf{g_{k+1}} = \mathbf{g_k} + d\mathbf{g}$$

$$\mathbf{g_{k+1}} = \mathbf{g_k} + (S^T\mathbf{c} - S^TS\mathbf{g_k}) = \mathbf{g_k} + S^T(\mathbf{c} - S\mathbf{g_k}) \tag{2.6}$$

A fixed relaxation factor β (with typical values between 0.5 and 0.95) can also be introduced as is typical in iterative schemes:

$$\mathbf{g_{k+1}} = \mathbf{g_k} + \beta S^T(\mathbf{c} - S\mathbf{g_k}) \tag{2.7}$$

We are therefore provided with an iterative development of LBP that can be used to improve image quality and overcome some deficiencies of the LBP method.

The previous description of the permittivity is a simple example of iterative methods applied to image reconstruction, though much work, especially for static process applications, has been conducted on improved and complex methods to improve image accuracy. Such methods include the well known Landweber method [76] and Tikhonov regularisation [114], both of which are loosely based around eq. (2.6), as they iteratively update specifically the image vector [73]. Alternatives to this framework have also been proposed, such as that proposed by Liu et al. [80], where the sensitivity matrix itself is iteratively updated prior to online imaging, once generated is used as the fixed sensitivity matrix as with LBP. The main advantage of this method is, that once the prior processing is complete, it will provide image quality similar to that of Landweber but with the online performance of LBP.

2.2 IDENTIFICATION OF FLOW REGIME

In any process involving multiphase or multicomponent flows, certain ranges of flow regimes / patterns occur depending on the relative energy between the phases or components at any given time. These occurrences therefore span a vast multitude of industries, including

process, oil and gas and nuclear. In certain applications, it may be required to sustain a certain flow regime, for example, to gain an increase in heat transfer properties by sustaining dispersed flow. In these cases, monitoring of the flow regime condition allows information to feedback to control processes in order to sustain the preferred flow pattern. Whereas, for upstream oil and gas applications, the flow pattern may vary depending on the state of the oil well. In such cases, knowledge of the flow regime can help in both modelling and measurement of the process. The presented benefits of tracking flow regime provide evidence of not only the need to sufficiently detect the current flow pattern within a process, but also to conduct it in an efficient, effective and reliable way to successfully apply to the industrial applications that require it.

2.2.1 *Instrumentation*

Due to the importance of flow regime detection for many industries, a number of studies have been conducted to provide this with a range of instrumentation. Basic methods which suit, in general, small scale, low pressure systems all the way up to the harsh environments encountered in heavy industry and even sub-sea deployment. One example of a more basic method, is through analysis of images gained from high-speed cameras [134][106], working on the basis that typical flow patterns can be determined simply through visual inspection, giving a simple solution. The main issues encountered with this choice of instrumentation are:

A. A transparent test section is required, which is unworkable in many applications;

B. The lack of visibility of the core of the flow, which can be important when determining the nature of flows near to the transition between slug and annular flow for example;

C. Despite the images providing the information to the user, for online automatic detection, it seems counter-intuitive to conduct further processes considering that the information is already contained in the image.

A more sophisticated measurement than visual inspection can be obtained using intrusive probes, where conductivity based probes are the most common along with internal electrode based devices with electrodes mounted around the tube bore [25], or, alternatively, parallel wires can be installed within the pipe [43][70], providing a simpler construction. Such methods have the advantage of sensing the core of the flow as opposed to the camera based method described previously. However, although their potential is improved, the invasive nature still poses problems for many applications. For example, in

the oil and gas industry, where rough particulates are found within the flow, parallel wire conductance probes are unacceptable, and despite internal electrodes being more appropriate, as they remain non-invasive, they still create an environment prone to degradation and accumulation of deposits as they intrude on the pipe, which could lead to measurement inaccuracies and increased maintenance.

It follows from previously that non-intrusive (and non-invasive) sensors are the most desirable method to detect flow regimes for industrial application, which is reflected by the large majority of research tending towards this. The most common design is to employ a single clamp-on electrode pair as a sensor, thus obtaining a relatively cheap and simple measurement device, with some of the most common measurement types including: ultrasonic [39], conductivity [55], electrostatic [60, 59] and impedance [88, 86, 77]. In order to move from only obtaining information on phase content, to an estimation of flow regime, a greater depth of analysis is required (compared to processing of images), and in most cases leading to methods such as neural networks being adopted. Although the classification and process can vary, such as with regard to the number of hidden layers. Despite fulfilling many needs for application and feasibility, to implement supervised learning methods such as neural networks, there is an additional requirement of training data. Although training data is available, providing sufficient data for the system to fully learn the effects of changing variables, such as system or fluid properties, becomes very difficult (if not impossible), and hence their effectiveness for all flow types is likely to be greatly limited.

For the identification of a flow regime through tomography, a vast range of methods have been presented. These can broadly be classified into two categories, being:

- How the tomographic data is interpreted
- How the interpreted data is analysed

In answer to the first category, there are in general, two approaches, to either work with the raw capacitance data, or to perform some type of image reconstruction. As for the second category, there are many variations and additional methods that can be used to analyse the data, depending on how the data is interpreted.

2.2.2 *Raw capacitance data*

One option for how tomographic data is interpreted is to simply use the raw capacitance signals. The main benefit from this is to remove the need for image processing; this reduces the computational resources required as well as reducing the errors, due to both the soft-field nature of the sensor and the reconstruction process itself. It can be argued that the reduction in computation is not substantially

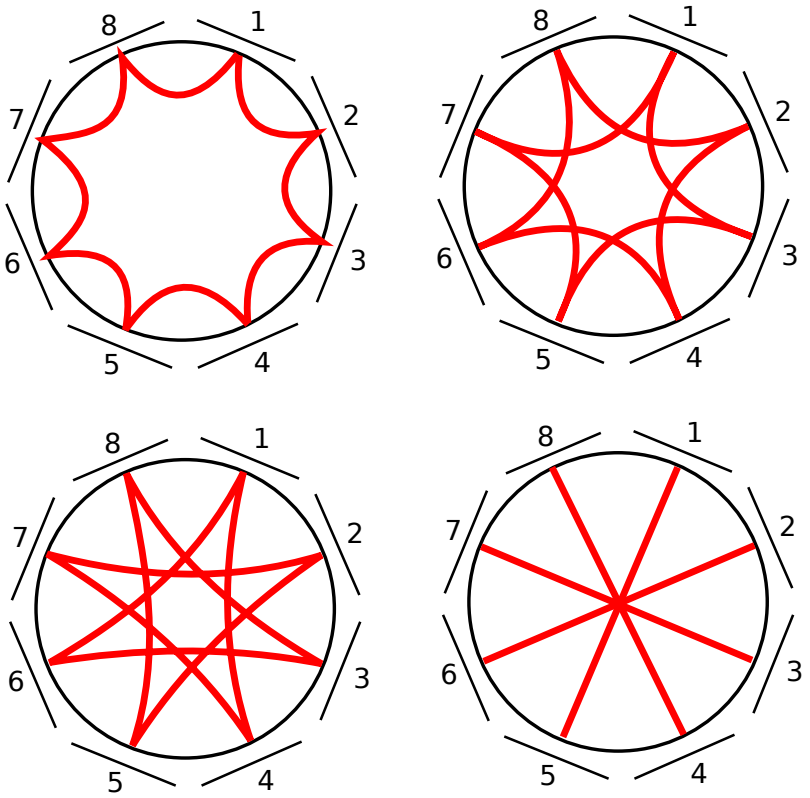

Figure 2.4: Electrode pairing configuration.

beneficial if, for instance, a LBP algorithm is used, which is capable for processing images in real-time. However, this makes the assumption that the tomographic sensor is used solely to determine flow regime, whereas it may be, that such identification is a secondary function of a multi-phase tomographic based meter. In such a case, computational efficiency may become a bigger factor.

Considering that no image is constructed in this method, some researchers have concluded that when using a multi-electrode sensor, it is necessary to differentiate between the electrodes depending on their position [71, 130]. The categories proposed are: adjacent electrodes, opposite facing electrodes and electrodes of the same spacing, with the number of these categories determined by the number of electrodes in the sensor. The main advantage of using these categories is to analyse different regions within the cross-section without image reconstruction. The most prominent pairs are the adjacent electrodes, sensing the outer region of the cross-section close to the pipe wall, and the opposite electrodes, representing a slice through the cross-section; the four categories of pairing configuration for an 8 electrode sensor are portrayed in Figure 2.4. Examples of two methods that employ a criterion based algorithm, using the measurements from the separate groups, includes the work of Jeanmeure et al. [71] using a logical flow diagram where each regime is determined systematically, and Zhang et al. [130] using a Decision Directed Acyclic Graph (DDAG), a

more complex way of determination which better suits the advanced method of employing Support Vector Machines (SVM).

Although the previous methods are appropriate, the classification of electrodes depending on their relative position is not always used. Dupre et al.[36] used raw capacitance readings of all electrodes (12 in this case) to provide flow regime identification. This method extracts eigenvalues of statistical parameters used to determine the pattern, and selects important electrode values depending on their position when organised from lowest to highest. By ordering measurements in this way, it can be said that the different electrode groups are still effectively utilised, only automatically as opposed to pre-defined. One advantage of this is that the method will still operate the same, even if the sensor is rotated. This itself is a rather small advantage considering that the computational resources required are increased when assessing certain criteria this way.

2.2.2.1 *Criteria for flow regimes*

The studies highlighted in the previous section that use raw capacitance data, have a criteria based system for defining the current flow regime. It can be seen from these studies that the criteria is effectively the same, with a slight variation in how it is achieved. Considering stratified flow firstly, which is significant, due to it being the only flow regime which is not symmetrical in its ideal condition. All of the studies considered, set the criteria on the basis of the difference between electrodes at the top of the pipe and the bottom. Jeanmeure et al. [71] sum the capacitance readings of both the electrodes covering the top and bottom of the pipe (including electrodes of multiple group classification) and the ratio of top to bottom is given a boundary value of 0.1 according to their data. Dupre et al. [36] use the ratio of the eigenvalue mean of electrodes in position 11 and 1 (representing the second highest and lowest eigenvalue) with a boundary value of 0.75. Finally, Zhang et al. [130] uses a feature parameter based on other work [126], where a single electrode pair from absolute top and bottom positions is used, and the capacitance value itself is again used. All these methods are based on the effect of gravity on the fluid during stratified flow and therefore represent an ideal criteria for this type.

The criteria for defining annular flow differs in the studies more than for stratified flow. Dupre et al. [36] identify annular flow by simply determining if it does not satisfy the criteria for stratified flow, which is possible, as prior to both of these, the flow has already been determined as continuous. Whereas Jeanmuere et al. [71] use the average capacitance of opposite electrode pairs (see Figure 2.4 (bottom right)), with a boundary of less than 0.5. This seems appropriate due to annular flow giving the lowest cross-sectional capacitance of any symmetrical flow regime, though it could be argued that there may be annular flows which overcome this boundary outside of the tested

data, especially when considering high entrainment rates. Zhang et al. [130] use a combination of the similarity of the mean value between adjacent electrodes (giving an indication of symmetry), along with the difference between this result and the individual capacitance values (indicating the similarity between the outer and central region of the pipe). This seems more in depth of a solution compared to the previous, but would be expected, due to the DDAG method which subjects each data set to all defined criteria. It is clear that all methods operate on principle of symmetry, with some also focussing on radial disparity as well. It is also noted that the boundary becomes more subjective for annular flows, which also applies to the use of SVM [130], where the boundaries are developed directly from training data.

The final flow regime to be discussed is that of intermittent flows (i.e. slug and plug). Considering firstly the work of Dupre et al. [36], a method found numerously in studies, including those outside of raw capacitance based methods is used, which includes considering multiple data points in time, and calculating the sum of the eigenvalues for the standard deviation within the measurements. This focuses on the large changes in structure which is apparent for slug and plug flows. Furthermore, criteria for differentiating between slug and plug flows are included, where the ratio of the data, from a close to middle range electrode pair is passed through both a high pass and a low pass filter (with 10Hz cut-off), is utilised. Jeanmuere et al. [71], define all intermittent flows as 'other', therefore if the flow does not fit the criteria for annular or stratified flow, it is categorised as 'other". Though much simpler, this method does not differentiate between slug and plug flow and is therefore limited. Overall, it would seem that the more complex method is advantageous, however, this operation must be conducted over a certain time interval which would cause issues in a real-time application, as procedures must be put in place to ensure a reasonable response time was achieved when the flow changes. This highlights the great advantage of single point analysis [71], when considering that a horizontal slug flow, for example, would fluctuate between stratified and 'other' flow type, which could then be interpreted as slug flow via a simple algorithm.

2.2.3 *Outline of ideal system*

The previous section has outlined the range of methods and measurement devices which have been used in other studies to achieve flow regime detection. Although these techniques have been proven effective in the corresponding tests made, typically on single regime offline data files, many studies neglect certain issues that occur when considering real-time applications for a wide variety of applications, consisting of highly varying systems and fluid properties. This problem is particularly common in both instrumentation and modelling of

multiphase processes, and therefore is a main focus of this paper. With this in mind, four criteria are outlined specifically for the application of tomography to flow regime identification, which are generally not or only partially fulfilled. The criteria for which a suitable method (as part of a greater flow measurement system) would desirably adhere to, is as follows:

- To not require full image reconstruction for each data point, allowing a more efficient approach with the possibility of the saved computational resource being diverted to a parallel process with a greater need for it.
- To allow online estimation of flow regime without referring to previous data points, improving efficiency through less unnecessary data, but more importantly to remove any need for a prediction window (i.e. a value of time range for which the most likely regime is calculated), removing ambiguity of measurement during a transition.
- To remove any reliance of a boundary or threshold value in the decision process, where such values are often determined from a single experimental setup and fluid property, thus the value becomes a function of the system / properties and hence may require further system dependent tests to provide the most suitable value.

2.3 CAPACITANCE TOMOGRAPHY AND CONDUCTIVE FLUIDS

Due to the operating principle of ECT devices measuring material permittivity, they are most suited for non-conductive materials. This obviously presents an issue with flows encountered in the oil and gas industry, where the presence of water is common. The problems encountered when conductive materials are present is, firstly, short-circuiting can occur between two electrodes positioned close to one another, rendering the interpretation of the measurement area invalid, due to a conductive path created between electrodes, as well as other contacted materials such as pipe walls plant equipment. This is sometimes referred to as parasitic coupling [27]. Also, even when this is not the case, there remains a significant high-contrast issue between the fluids present, where the permittivity difference of oil and gas are around 40 times smaller than in comparison with water [131], causing difficulties in distinguishing the lower permittivity phases through their capacitance – permittivity profile. Despite such complications, capacitance based sensors are still considered a feasible solution for conductive fluid measurement, both as an independent device or coupled in a dual-modality setting.

To overcome the stated issues encountered when conductive fluids are present, modifications to the capacitance normalising procedure

are often employed. In cases of two phase oil and gas, the constrained Relative Capacitance Difference (RCD) is used, as first presented by Garaets and Borst [41].

$$RCD = \frac{\Delta C}{\Delta C_{max}} = \frac{C_m - C_l}{C_h - C_l} \; ; \; 0 \leq RCD \leq 1 \tag{2.8}$$

Where C_m is the initial measured capacitance, and C_h and C_l are the capacitance values measured when the pipe is filled with high (water) and low permittivity fluids respectively. This is effectively a standard normalising procedure for ECT, except where water becomes the high permittivity, as well as the restraint imposed on the RCD value, which is required considering that high conductive fluid content will often produce values outside this range, leading to image distortion. Values of RCD greater than unity have been reported by dos Reis and Goldstein Jr.. [33] for experiments on gas-water horizontal slug flows, and were attributed to electric field distortions due to fast changing liquid levels. Caniere et al. [17] also encountered this for a range of gas-water flows, particularly in annular flow, and suggested the cause as electric polarisation, as moving interfaces can create extra current during charging and recharging; they also noted that signals of values greater than unity were not obtained in de-mineralised water. Demori et al. [27] explain this issue as primarily a consequence of parasitic coupling, and propose a modelisation of the phenomena along the pipe to account for this, by comparing results of oil fraction obtained through capacitance readings of oil-water flows to those obtained through Quick Closing Valves (QCV), a difference of 3% was obtained.

An alternative to RCD was presented by Liao and Zhou [79], specifically for cases with a high permittivity background, presented for probing anomalous low permittivity objects in water, known as the Relative Capacitance Ratio (RCR):

$$RCR = \frac{C_m - C_h}{C_l - C_h} \approx \frac{C_h - C_m}{C_h} \tag{2.9}$$

The simplification made here is on the basis that $C_l \ll C_h$ and thus represents the relative change ratio of C_h. By using RCR, there is no requirement to calibrate to the lower permittivity material, and the result is that the capacitances become much larger, attributed to the "ions effect" [118], compared to the stray capacitance values, and therefore are mitigated. Due to the formulation of RCR, it is noted that the resulting image will contain low values for high permittivity domains, and high values for low permittivity domains, thus a simple formulation is presented to invert the result.

2.3.1 *Dual-modality*

Despite the possibility of ECT functioning independently to measure flows with low conductive fluids present, it is generally accepted that

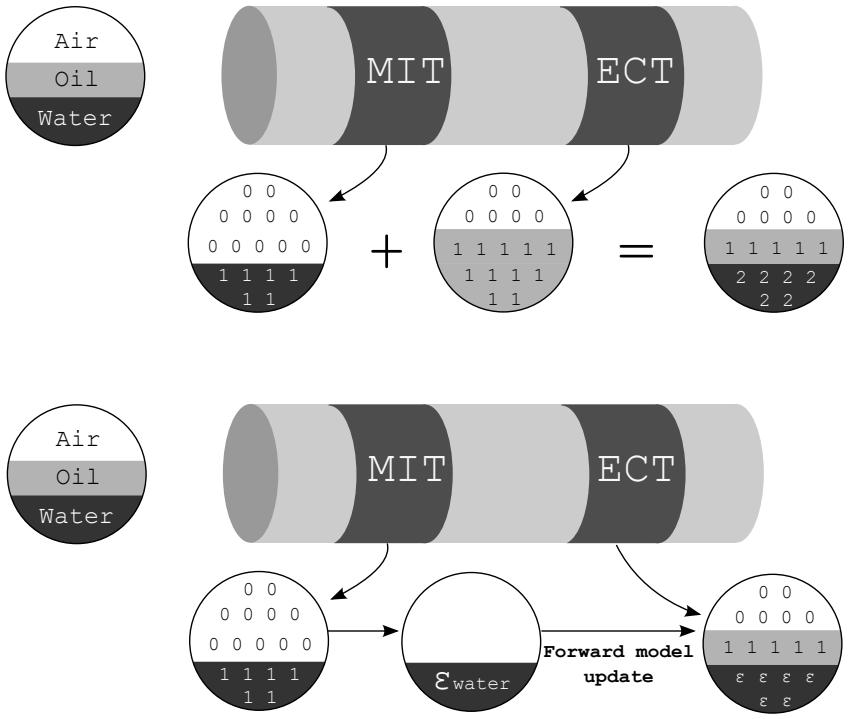

Figure 2.5: Outline of the dual modality / data fusion methods proposed by Sun and Yang [108] (top), and Zhang et al. [131] (bottom)

in order to handle higher conductive fluid content effectively, the combination of multiple tomographic devices working in sync is a desirable solution. The device to work alongside ECT must measure conductivity in principle, with examples such as Magnetic Induction tomography (MIT) deemed a suitable choice. This choice is particularly useful, as it retains all the main benefits of non-intrusive and non-invasiveness, which is not necessarily the case for all electrical based tomography such as ERT, or more generally Electrical Impedance Tomography (EIT), where the electrodes are fitted on the interior of the pipe [120].

Applying dual-modality tomography systems to fluid flows has been considered for some time now [58], due to the increase in applications it provides. As stated by Qiu et al. [97], one of the most important challenges of designing multi-modal systems is to ensure that all modalities work co-operatively in terms of data acquisition and communication of the hardware, along with the data fusion process. This, of course is not a fixed definition of a solution, and thus many variations have been attempted. Despite the hardware aspect of this problem being an integral part of the solution, for the scope of this work, the data fusion procedure is of much greater relevance as it specifies the requirements for ECT to operate in a dual-modality setting, without the need to utilise other hardware at this stage. For this reason, data fusion will be discussed in further detail.

Sun and Yang [108] presented an interesting data fusion algorithm, due mainly to its simplicity, for operating ECT and ERT devices together. They suggested that by calibrating ECT to oil and gas, as in normal operation, all that was required to overcome the high contrast issue was to set any pixel of value more than unity (those of which are affected by the conductive fluid) to 1. What this achieves is to combine oil and water, in this case, to appear the same in the image data produced by ECT. Therefore, ECT is used to define the interface between gas and oil as well as gas and water, then ERT provides the interface between oil and water. However, their results showed that interfaces between fluids were not straight in stratified tests and sometimes unclear, and with increasing water content, the achievable accuracy reduced.

A more complex solution to dual modality is proposed by Zhang et al. [131] for the combination of ECT and MIT systems to measure three phase flows, where an air background condition is successfully imaged. The proposed solution allows ECT and MIT to work as a sequential process where, firstly, MIT is used to obtain the location of the conductive water present. This information is fed into the ECT system where it is used to modify the sensitivity map (assign a relative permittivity equal to that of the water used in the region where it is detected) used in the forward model of the ECT system. Therefore, MIT images the location of water, and ECT images the boundary of oil and gas in the remaining regions without the negative effect of the high contrast issue; this procedure is effective as it directly tackles the contrasting effect of conductive fluids on ECT. However, attempts to apply this to a water background condition were less successful, though it is suggested that higher frequency operation of ECT could improve this. Finally, it is important to note that these tests consisted of imaging only cylindrical probes, thus the update of the ECT forward model is simplified. To operate in real flows, the model update would be more complex and would require significant computational resource to operate in real time. Furthermore, this method would not solve the issue of conductive paths which may be encountered in real applications. The principle of both methods presented here are illustrated in Figure 2.5.

2.4 SLUG TRANSLATIONAL VELOCITY MEASUREMENT

Slug flow is a common phenomena in industrial multi-phase flows, caused by the effect of the Kelvin-Helmholtz instability on waves at the fluid/gas interface [35]. The effects of oscillating temperature and pressure caused by this flow pattern has promoted much research into the modelling, and in some applications, the prevention of slugging. Despite this, it is accepted that prevention procedures can be unreliable

and lead to loss in production [95], and hence the need for accurate measurement of slug flows will continue.

Due to the intermittent nature of slug flows, the flow measurement of both phases within the process is easier to achieve, in comparison to annular flow, for example. This is due to the assumption that the liquid body acts as a piston, and therefore its mean velocity, measured as the slug translational velocity, can be said to be equal to that of the body of gas downstream. Hence, if the liquid velocity is measured, and the gas fraction downstream is known, the volumetric flowrate of the gas slug can be estimated, leaving only the gas entrained within the liquid slug which is considered small in comparison. This can also be applied to the liquid phase when the liquid body occupies the entire cross-section (apart from entrained gas), though during periods of gas slugs, liquid flow remains as either a stratified pool in horizontal flows, or as an annulus in vertical flows. Nevertheless, correlations are available to relate the measured velocity of the slug to the liquid flowrate as is the case with other flow regimes. It can be seen then, that imaging devices that act as cross-correlation meters, such as ECT, have the potential to fulfil the requirements for measurement of slug flows.

2.4.1 *Cross-correlation application*

As mentioned in Section 2.1.3, one of the possible configurations available when using cross-correlation, is that the window of integration can be extended or shortened, depending on the amount of data being included in the process. Larger correlation windows have been used to obtain average correlation of multiple liquid slug signals [87], which is attractive in unstable cases, for example, when closer to transition zones between different flow regimes, where slugs are non-uniform in length and frequency. Alternatively, a smaller window, but still longer than the slug duration, can provide individual slug velocity measurement [117] whilst maintaining a strong 'pulse like' signal, which is more suitable for cross-correlation. Although the different integration windows described may be most suited to continuous slug velocity measurement, the most informative technique is to consider the slug fronts and tails separately [107, 116]. The measured slug front and tail velocities are then either treated separately, or an average value is used as the measured translational velocity [4]. Finally, care must be taken to ensure that the signal produced by either front or tail, is representative of the actual slug velocity [116].

2.4.2 *Achievable accuracy*

In order to recover the phase flowrates, the mixture superficial velocity is first obtained; the addition of the phase superficial velocities is

equal to that of the mixture, hence if the gas superficial velocity is obtained, as described previously, the liquid superficial velocity can also be recovered. The estimation of mixture superficial velocity therefore becomes the main objective and has been achieved using a range of instrumentation, although the specific correlation techniques tend to be similar. Zhang and Dong [130] used a resistance based tomography device and cross correlated the raw voltage data, as opposed to a reconstructed image, obtaining an error margin of 10% with a noticeably better accuracy for mixture velocities less than $2m/s$. However, their method included using sample data to construct a coefficient matrix to assist the measurement. Reis and Goldstein [33] achieved a greater accuracy for a larger range of mixture velocities for steady points using a capacitance method, though tests conducted near the flow regime transition zone gave large discrepancies, which were attributed to velocity discontinuities along the gas / liquid flow. Ahmed [3], also used a capacitance sensor for investigation of slug flows, obtaining a more reliable linear trend between slug translational velocity and mixture velocity; with a noticeable deviation for higher mixture velocities, as with Zhang and Dong [130], as well as for low tested values of mixture velocity ($< 0.5m/s$). Van Hout et al. [117] went further to analyse the effect of pipe inclination angle on such measurements, and successfully derived a model to account for dispersed bubble within the liquid slug region, achieving overall a prediction within 15% of the measured flowrates. The deviation in these results was relatively low, which can be attributed to the use of fibre optic probes, being intrusive to the flow, and hence not a suitable solution for the environments encountered in oil and gas applications.

2.4.3 *Drift flux model and its relevance*

To relate the slug translational velocity, measurable by cross-correlation, to the actual gas and liquid flowrates, it is possible to simplify the treatment of the fluids by describing them as a mixture. The drift-flux model, proposed by Zuber and Findlay [135] and later developed by Ishii [68] [67], describes multiple phases as a single mixture, with added additional terms to account for phase specific behaviour, with the drift velocity between phases as the prime example. This simplification has, firstly, provided a basis for computational models for certain cases where the assumption of motion holds, with its simplicity allowing reduced complexity and computational time. Secondly, some useful relations have been derived from this model, the most prevalent being the linear relationship between slug translational velocity and the mixture superficial velocity [91] which, as mentioned by Dukler and Faber [35], is by far the most popular relation used for prediction in this field. To arrive at this linear relationship from the drift-flux model,

we begin by deriving the continuity equation for gas in a two-phase system, neglecting inter-phase mass transfer:

$$\frac{\partial \alpha_g \rho_g}{\partial t} + \nabla \bullet (\alpha_g \rho_g u_g) \tag{2.10}$$

where u_g is the gas velocity and $\nabla \bullet ()$ is the divergence operator. This can then be simplified further by firstly assuming incompressibility, then assuming that the time averaged superficial velocity and the homogeneous velocity is constant, and finally only considering changes in the axial plane.

$$\frac{\partial \alpha_g}{\partial t} + \frac{\partial j_g}{\partial z} = 0 \tag{2.11}$$

where: j_g is the superficial gas velocity. From here, we can linearise the spatial derivative term to give:

$$\frac{\partial \alpha_g}{\partial t} + \frac{\partial j_g}{\partial \alpha_g}\frac{\partial \alpha_g}{\partial z} = 0 \tag{2.12}$$

eq. (2.12) has now taken the form of a 1-dimensional wave equation, where the wave speed $\left(\frac{\partial j_g}{\partial \alpha_g}\right)$ represents the kinematic wave speed at the phase interface. As pointed out initially by Zuber and Findlay [135] and investigated thoroughly by Lucas and Walton [83], this term is equivalent to the measured wave speed from cross-correlation.

$$u_{cc} = u_{kw} = \frac{\partial j_g}{\partial \alpha_g} \tag{2.13}$$

In order to derive a relationship for this term, we can introduce area averaging and proper mean values to obtain the area averaged, void fraction weighted gas velocity, as outlined by Ishii [67], giving:

$$\ll u_g \gg = \frac{< j_g >}{< \alpha_g >} = C_o < j > + \ll V_{gj} \gg \tag{2.14}$$

where $<>$ and $\ll\gg$ operators represent area averaged and area averaged void fraction weighted respectively. j is the mixture superficial velocity, C_o is the distribution parameter and V_{gj} is the drift velocity.

To further develop eq. (2.14) to include the kinematic wave speed term, we can re-arrange and differentiate with respects to α_g by using the product rule, as follows (averaging operators have been removed for simplicity):

$$j_g = \alpha_g \left(C_o j + V_{gj}\right) \tag{2.15}$$

$$\frac{\partial j_g}{\partial \alpha_g} = (1)\left(C_o j + V_{gj}\right) + \alpha_g \frac{\partial \left(C_o j + V_{gj}\right)}{\partial \alpha_g} \tag{2.16}$$

The term furthest on the right hand side is not straightforward to solve. However, for slug flows, both the distribution parameter and the drift velocity terms are not functions of α_g and therefore it can be assumed that this term is zero, hence giving, for slug flows:

$$\frac{\partial j_g}{\partial \alpha_g} = C_o j + V_{gj} \tag{2.17}$$

This then matches the linear approximation proposed by Nicholson et al. [91] for the slug translational velocity. From here, it is obvious that what is required to calculate the mixture superficial velocity, other than the cross-correlation measurement, is values for C_o and V_{gj}. For horizontal slug flows, the most popular definition for the distribution coefficient relies solely on the densities of the two fluids, as pointed out by Ishii [68]:

$$C_o = 1.2 - 0.2\sqrt{\frac{\rho_g}{\rho_l}} \tag{2.18}$$

where ρ_g and ρ_l are the densities of gas and liquid respectively. The corresponding relation for drift velocity is given as a function of the system only:

$$V_{gj} = 0.54\sqrt{gD} \tag{2.19}$$

with D being the pipe diameter.
An important development of these correlations was presented by Bendiksen [13] who observed a velocity change due to flow pattern transition with flows that exceeded a threshold of 3.5 for their proposed modified Froude number. The following demonstrates the amended drift flux correlations usage, inclusive of Bendiksen's critical Froude number:

$$\begin{cases} Fr_m \geq 3.5 \Rightarrow & Co = 1.2 - 0.2\sqrt{\frac{\rho_g}{\rho_l}} \\ Fr_m < 3.5 \Rightarrow & Co = 1.05 \end{cases} \begin{cases} Fr_m \geq 3.5 \Rightarrow & V_{gj} = 0 \\ Fr_m < 3.5 \Rightarrow & V_{gj} = 0.54\sqrt{gD} \end{cases} \tag{2.20}$$

where:

$$Fr_m = \frac{U_{sg} + U_{sl}}{\sqrt{\frac{\rho_l - \rho_g}{\rho_l} gD}} \tag{2.21}$$

This method for assigning the drift flux correlations has had particular success in predicting industrial scale slug flows.

2.4.4 *Measurement Limitations of cross-correlation flowmeters*

Considering now the physical measurement process of slug translational velocity, as opposed to the relation between measured velocity and flow parameters, it is clear that limitations still exist. The most prominent of these limitations is the requirement for the velocity measurement to take place at the fluid interface (between liquid front and gas tail or vice versa), and to be equal to the actual slug translational velocity. As cross-correlation meters such as ECT can only measure inter-facial velocity rather than fluid particle motion, if this inter-facial velocity is not representative of the entire slug body, the measured time delays between planes will be inaccurate and the resulting velocity will not conform to the proposed linear relation, hence the accuracy will be negatively affected. This velocity discontinuity was observed by Reis and Goldstein [33] for two-phase liquid-gas flows, who described it as the fundamental cause of measurement inaccuracies in their results, specifically for tests conducted close to flow regime transitions.

2.5 KINEMATIC WAVES IN ANNULAR AND STRATIFIED-WAVY FLOWS

For some time now, it has been agreed that, in annular flows there consists two common types of waves acting at the interface between the two fluids [56], being small-amplitude ripple waves of relatively low velocity, and disturbance waves with a much larger amplitude and occurring over long distances. In addition to these commonly observed waves, a third 'ephemeral wave' was first reported by Sekoguchi et al. [103] and later investigated further by Wolf et al. [122], which are similar in appearance to a disturbance wave except at lower velocities. Of all these wave types, disturbance waves have, by far, received the most attention by researchers due to their significance in inter-facial transfer of energy, mass and momentum [98], and their stability in comparison to ripple waves. Much attention has been focused on the development of such waves through the pipe [133, 123, 6] with findings suggesting that, depending on wave property, 20-50 pipe diameters in length may be required to achieve stability, with some [53] suggesting that stability can never truly be reached. Other work has focused more on the properties of waves, such as average film thickness [94, 98, 105], wave frequency and wave velocity, with relation to fluid velocities and properties such as viscosity. Another example is with the relation between disturbance wave properties and entrainment of liquid within the gas core, essential for dry-out estimation in nuclear reactors, for example. In terms of modelling such behaviour, wave properties have been related to the flow through use of dimensionless parameters, in particular: Reynolds, Weber, Froude and Strouhal numbers. This has been successful overall in relation to the general trends, however,

defining appropriate values for the parameters that are applicable over a large range of systems and fluids has proven more difficult. This is especially true for high viscosity fluids. Despite some work [105] focusing on improving these relations for especially large and varied data, the vast majority of tests conducted in this field use fluids with relatively low viscosity (typically < 500 cP).

2.5.1 *Correlations for wave properties*

As mentioned previously, much work has be undertaken on relating properties of waves encountered at the interface of multiphase flows, with the superficial phase velocities, in order to predict phase flowrates in flows such as annular and stratified-wavy. This section reviews some of the most prevalent relations proposed and analyses their applicability, limitations and accuracy.

2.5.1.1 *Disturbance wave frequency*

Disturbance wave frequency has been analysed for fully developed flow[3], where a consistent frequency is achieved. This frequency increases with increasing gas and liquid flowrate, and decreases with increasing liquid viscosity and decreasing surface tension. However, producing accurate correlations to recover flowrates, which account for the multitude of both system and fluid properties, has proven difficult. Considering first, the work of Schubring and Shedd, who derived correlations for both horizontal [100] and vertical [101] annular flow, relating wave frequency to the superficial gas velocity. For horizontal annular flows, two separate correlations were proposed based on dimensional analysis, with the first constructed from data gathered from pipe diameters of 8.8 and 15.1mm:

$$f_w = 0.005 \frac{j_g}{D\sqrt{x}} \tag{2.22}$$

where: f_w is the wave frequency, j_g is the superficial gas velocity, D is the pipe diameter and x is related to the mass flow ratio between phases as $x = \frac{\dot{m}_g}{\dot{m}_g + \dot{m}_l}$. And for the larger pipe diameter (26.3mm):

$$f_w = 0.035 \frac{j_g \sqrt{Fr_{mod}}}{D} \tag{2.23}$$

with the modified Froude number defined as:

$$Fr_{mod} = \frac{\rho_g j_g}{\rho_l \sqrt{gD}}$$

where ρ_g and ρ_l are the gas and liquid densities respectively.

3 Fully developed flow defined in this case as that which is conducted on a system with a sufficient length value in terms of equivalent diameters

For the data tested, a correlation to within 6% was achieved, though despite the multiple pipe diameters used, the diameters remain small compared to that experienced in industry. The correlation for larger diameters was tested with other data by Setyawan et al. [105] who confirmed its superiority compared to other similar relations, but noted that large errors were incurred when tested against fluids with different viscosities and surface tension. This can be expected, due to the lack of viscosity representation in eq. (2.23). The expressions in eq. (2.22) and (2.23) can be better interpreted as the modified Froude number as a function of the Strouhal number, as proposed by Hall Taylor et al. [111] as:

$$Sr = \frac{f_w D}{j_g} \tag{2.24}$$

As for vertical flows, a similar correlation was proposed [101], again with reference to the Strouhal number as a function of a dimensionless quantity:

$$\frac{f_w D}{j_g} = 0.0056 \quad \frac{\rho_g j_g^2}{\rho_l g D x} \Bigg)^{1/4} \tag{2.25}$$

Ousaka et al. [93] provided an alternative relation, also based on Strouhal number, except with the superficial velocity term exchanged to liquid instead of gas. This liquid Strouhal number is then related to the ratio of Reynolds number for each phase as follows, for horizontal or near horizontal flows:

$$Sr = \frac{f_w D}{j_l} = 0.066 \left(\frac{Re_g}{Re_l} \right)^{1.18} \tag{2.26}$$

where: $Re_g = \frac{\rho_g j_g D}{\mu_g}$ and $Re_l = \frac{\rho_l j_l D}{\mu_l}$

This relation was also amended by Alamu and Azzopardi [5], where the viscosity term is effectively dropped from the Reynolds number ratio term, giving the Lockhart-Martinelli parameter (X) as follows:

$$\frac{f_w D}{j_l} = 0.4292 X^{-0.908} \tag{2.27}$$

where

$$X = \sqrt{\frac{\rho_l U_{sl}^2}{\rho_g U_{sg}^2}}$$

2.5.1.2 *Disturbance wave speed*

It is accepted that wave velocity increases, as with frequency, with increasing gas and liquid flowrates, and decreases with higher liquid viscosities. For the relation of measured wave speed to flow characteristics, correlations consisting of similar variables to that of wave

frequency have been developed. Schubring and Shedd proposed relations for wave velocity for the same datasets used for frequency, as outlined previously. For horizontal flows, the following correlation is proposed [100]:

$$u_{kw} = 0.42 \frac{j_g}{\sqrt{x}} Re_g^{-0.25} \tag{2.28}$$

their results display a prediction of within +/- 20% for the data tested. Setyawan et al. [104] used the same relation with slightly modified parameters in line with their data for similar pipe diameters. As for vertical annular flows, the following was proposed [101]:

$$u_{kw} = 2.55 j_g (Re_g x)^{-1/3} \tag{2.29}$$

again, the results correlate to within around +/- 20%, though the data appears to suggest that for higher superficial liquid velocity values, the correlation becomes less accurate for higher wave velocities.

Ousaka et al. [93] used the same basis of Reynolds ratio, as used for frequency prediction, for wave velocity, with a normalised wave velocity:

$$\frac{u_{kw}}{j_l} = 3 \left(\frac{Re_g}{Re_l} \right)^{0.78} \tag{2.30}$$

Setyawan et al. [105] used a large range of data sets from various researchers to develop a correlation relating the normalised wave velocity to multiple ratios of flow properties, including surface tension. Through a trial and error based approach, the most accurate parameters are given as:

$$\frac{u_{kw}}{j_l} = 7.25 \left(\frac{\rho_g}{\rho_l} \right)^{0.35} \left(\frac{\mu_l}{\mu_g} \right)^{-0.7} \left(\frac{Re_l}{Re_{gm}} \right)^{-0.7} \left(\frac{\sigma_l}{\sigma_w} \right)^{0.2} \tag{2.31}$$

where: Re_{gm} is the modified gas Reynolds number as $Re_{gm} = \frac{\rho_g (U_{sg} - U_{sl}) D}{\mu_g}$, and with σ_l, σ_w being the liquid and water surface tension respectively. This correlation proved the most accurate for all data considered, including data gathered from the other researchers presented in this section, with the correlation prediction within $+/-50\%$ of the measurements. However, it is clear from the data that the variance in the prediction increases substantially for higher normalised wave velocities (> 200), and the prediction tends to under-estimate the measurement for lower normalised wave velocities (<40).

From analysing the proposed correlations and their corresponding accuracy outlined previously, it is clear that reasonable predictions can be made from measurable properties such as wave velocity and frequency, and that a combination of these correlations and measurements could provide an improved result compared to that presented. Despite this, the accuracy potential does not correspond to levels

required in practical flow measurement if used alone. This can be seen by the results from the largest test range example presented here [105] achieving $+/-50\%$, tested for data from only small diameter pipes and low viscosity. Therefore it can be assumed that for industrial scale systems and flows, the achievable accuracy would deteriorate, and hence the measurement capability would not be acceptable. One possible solution, as is common in application, is to calibrate the correlations to a specific system, fluid range and fluid type. Although this would provide an acceptable measurement capability, it does not account for changes of fluid properties during operation, nor the possibility that in-situ type calibration may not be possible, or at least financially viable. This then suggests that: to achieve a general purpose (inter-flow regime) multiphase measurement device, the metering of annular / stratified wavy type flows would not be adequately achieved by correlation of wave properties, and therefore would need further consideration.

2.5.2 *Drift flux model for wave speeds*

For annular and stratified wavy flows, the drift flux model can be utilised to develop a relation between the measured kinematic wave speed and the superficial mixture velocity, as seen previously in Section 2.4.3 for slug flows. Recall eq. (2.14), gained through the development stages pointed out by Ishii [67], relating the gas superficial velocity to the mixture superficial velocity:

$$j_g = \alpha_g \left(C_o j + V_{gj} \right)$$

as before, the product rule is used to produce a definition for the kinematic wave speed term:

$$\frac{\partial j_g}{\partial \alpha_g} = \left(C_o j + V_{gj} \right) + \alpha_g \frac{\partial \left(C_o j + V_{gj} \right)}{\partial \alpha_g} \tag{2.32}$$

unlike slug flows, the distribution co-efficient C_o and the drift velocity V_{gj} are in fact functions of α_g. For example, in annular flows, with the condition that $\frac{\rho_g}{\rho_l} \ll 1$ [68] the distribution co-efficient is evaluated to be:

$$C_o = 1 + \frac{1-\alpha}{\alpha + 4\sqrt{\frac{\rho_g}{\rho_l}}} \tag{2.33}$$

which suggests that for annular flows, C_o should be close to unity. The mean drift velocity is given as:

$$\bar{V}_{gj} = \left(\frac{1-\alpha}{\alpha + 4\sqrt{\frac{\rho_g}{\rho_l}}} \right) \left[j + \sqrt{\frac{\Delta \rho g D (1-\alpha)}{0.015 \rho_l}} \right] \tag{2.34}$$

where the drift velocity is related to the mean drift velocity by:

$$\bar{V}_{gj} = V_{gj} + (C_o - 1)j \tag{2.35}$$

which has been derived from the original definition by Zuber and Findlay [135]:

$$V_{gj} = v_\infty (1 - \alpha)^k \tag{2.36}$$

where v_∞ is the terminal rise velocity of a single bubble in an infinite media, and k is related to the bubble size. Therefore, the term furthest on the right of eq. (2.32) cannot be neglected as is the case for slug flows, and hence must be evaluated. However, the evaluation of the term $\alpha_g \frac{\partial\left(C_o j + V_{gj}\right)}{\partial \alpha_g}$ is not straightforward, and a typical method to avoid this is to determine it experimentally. Following the procedure taken by Xuewei et al. [124], recognising that both this term and the drift velocity itself are functions of α_g and thus can be grouped as such, eq. (2.32) can be re-written as:

$$\frac{\partial j_g}{\partial \alpha_g} = C_o j + f(\alpha_g) \tag{2.37}$$

From here, if the mixture superficial velocity is known, the kinematic wave speed is measured and eq. (2.37) is used for calculation of the distribution co-efficient, then $f(\alpha_g)$ can be calculated experimentally. This was carried out by Xuewei et al. [124] for stratified flows and dispersed oil in water and water in oil flows, where linear relations of $f(\alpha_g)$ were derived, with significant differences between flow types.

2.5.3 *High viscosity flows*

For cross-correlation meters, stratified-wavy and annular flows produce a dilemma. Despite the ability to measure multiple properties, including: volume fraction, wave speed, wave frequency etc., we remain heavily reliant on correlations to relate such properties to the liquid and gas fluxes. Despite said correlations providing reasonable results when parameters are adjusted, differences in system properties, as well as fluid properties, can drastically alter the achievable accuracy in industrial application. One of the most prominent examples of such a change, common in the oil and gas industry, is that of viscosity. Not only does viscosity change depending on temperature and location, the typically high viscosity oil that is encountered in oil wells, does not scale well in its behaviour with respect to the fluids used in laboratories to initially test the correlations.

For high viscosity fluids, the majority of work has focused on slug flows, due mainly to their common appearance in industrial flows. With much of the focus based on liquid holdup, pressure and slug frequency [46, 45], considering their obvious significance in operation

and modelling. An important effect of heavy oil, also well covered in literature, is the significant effects on the transition between flow patterns of stratified to slug, for horizontal flows, and annular to slug in vertical flows. Much less is known about the comparison between slug and annular waves in general, as opposed to transitional properties. Recently, Zhao et al. [132] compared slug and annular flow with heavy oil, in terms of pressure gradient, mean liquid holdup and superficial gas velocity, using a simple threshold method to calculate the liquid holdup of the slug film. The results identified that the two can be compared.

The next chapter continues the literature survey, focussing on the proposed method of particle filtering. Investigating its development, and why it could be useful for tomographic based flow measurement, along with the available methods of implementation and their suitability to this application.

3

PARTICLE FILTERING METHODS AND MULTIPHASE CFD

In this chapter the literature survey is continued with a focus on the particle filtering method that has been proposed to assist tomography in achieving the goal of multiphase flow measurement. In addition, it also includes a focussed review of relevant CFD models that are capable of modelling two phase flows and hence can be applied in the particle filtering system.

The chapter is structured in the following way:

3.1 Provides a short background to particle filtering, describing the method and how operates

3.2 Shows a more detailed mathematical description of particle filtering, in particular the Bootstrap method.

3.3 Gives a detailed description of 4 advanced particle filtering developments, describing benefits and limitations.

3.4 An introduction to the CFD method and both the Volume of Fluid (VOF) model and Euler-Euler (Multi-fluid model)

3.5 Provides a mathematical description of the VOF model.

3.6 Provides a mathematical description of the Euler-Euler multi-fluid model.

3.1 BACKGROUND

Particle filtering is a recursive state estimation method derived through Bayes theorem. The basis for this technique is to combine a measurement of either the state or some variable linked to the state (of which its relationship is known), with some prior knowledge of the state. The prior knowledge in particle filtering is gained recursively, and hence reflects the expected outcome of the next time step (when a new measurement is available) based on the prediction of the previous time step. This is achieved by utilising a system dynamic model which can propagate the previous prediction through time, to gain an expected value at the next time interval. This method is particularly useful for systems in which the noise associated with both measurement and model is known, and thus can be included in the prediction. Furthermore, particle filtering is suited specifically for non-linear systems and non-Gaussian noise, as opposed to its 'sister' method the Kalman filter.

Particle filtering operates by creating large numbers of hypotheses (particles) within the state space, normally multi-dimensional, which in essence should cover the range of possible states. At each time step, the particles are propagated through time using the state dynamic model, and are then compared to the acquired measurement at that time. By comparing the measurement and prior knowledge from the particle positions, along with statistical knowledge relating to the noise of both measurement and model, the particles are weighted by their probability. Once complete, the particles usually undergo some sort of distributing procedure to ensure diversification, before the process is repeated. At each time step, a prediction, or a distribution, relating to the state can be outputted, and hence used as the estimation of the state at that time. At the beginning of the process, the prior information (particle positions within the state space) does not provide any insight as no information has yet been delivered, therefore the particles must be spread sparsely across a large state space. Over time, the particles become more concentrated in regions of high probability and thus the prior information recursion becomes more informative.

3.2 ORIGINS AND DEVELOPMENT

This section begins with providing a brief description of particle filtering theory, followed by a literature survey on advance particle filtering methods.

3.2.1 *The particle filtering method*

Given some state space representation of a time series model, along with corresponding discrete measurements y at a given time interval, we wish to recursively estimate a posterior probability density of the state x. This posterior will represent an informed prediction of state by considering the measurement received, our information about how this measurement relates statistically to the state, along with our prior information from the previous time step. We start by defining the system dynamic and measurement model as:

$$x_t = f(x_{t-1}, w_t) \tag{3.1}$$

$$y_{t+1} = h(x_t, v_t) \tag{3.2}$$

where w_t and v_t represent system and measurement noise respectively. In order to implement particle filtering, we therefore require the following models relating to the system:
Initial Prior

$$P(x_0)$$

Dynamic model (for $t \geq 1$)

$$P(x_t|x_{t-1})$$

Measurement model (for $t \geq 1$):

$$P(y_t|x_t)$$

Where the initial prior is required for the first iteration, as initially we have no prior information from previous time steps, and is generally a simple distribution. The dynamic model describes how the state will change in time, and finally the measurement model indicates, for a given state, the probability of receiving a measurement value, which can be any distribution that we are able to fully evaluate (requires the distribution equation). We must now formulate a recursive system to incorporate the presented models, we start with Bayes theorem at any time t.

$$Posterior = \frac{Likelihood * Prior}{Evidence} \tag{3.3}$$

In this application, the likelihood is represented by our measurement model and the prior by the initial prior distribution for the first time step. This can be represented in terms of the state and measurement in time t.

$$P(x_{0:t}|y_{1:t}) = \frac{P(y_{1:t}|x_{1:t})P(x_{0:t})}{P(y_{1:t})} \tag{3.4}$$

This leaves the posterior $(P(y_{1:t}))$ remaining as the only unknown. This represents the probability of producing the data and , in practical cases, is difficult to calculate and conceptualise. Therefore, it is beneficial to describe this term in a different way; to do so, first consider that we can remove it from the equation and express the posterior in terms of proportionality:

$$P(x_{0:t}|y_{1:t}) = \frac{P(y_t|x_t)P(x_{0:t})}{\int P(y_t|x_t)P(x_{0:t})\mathrm{dx_{0:t}}} \tag{3.5}$$

This can only provide a posterior prediction given the uninformed prior distribution $P(x_{0:t})$, in order to integrate the results from the previous time step calculation and hence provide an informed prior, allowing greater efficiency of prediction. To do this, we can develop a recursive formulation of the above terms, starting with a basic conditional probability law applied to the posterior:

$$P(x_{0:t}|y_{1:t}) = \frac{P(x_{0:t}, y_{1:t})}{P(y_{1:t})} \tag{3.6}$$

we can now separate the variables within the distribution and apply the chain rule multiple times to give:

$$P(x_{0:t}|y_{1:t}) = \frac{P(y_t|x_t, x_{0:t-1}, y_{1:t-1})P(x_t|x_{0:t-1}, y_{1:t-1})P(x_{0:t-1}|y_{1:t-1})}{P(y_t|y_{1:t-1})} \tag{3.7}$$

By applying the principle of the Hidden Markov Model, we can determine conditional independence from the Markov property of the above variables. This dictates that the state variable at a given time (x_t) is only dependent on the previous time step state (x_{t-1}), and the observation, or measurement, at a given time (y_t) is only dependent on the state at that time (x_t). Through this, we can simplify as:

$$P(x_{0:t}|y_{1:t}) = \frac{P(y_t|x_t)P(x_t|x_{t-1})P(x_{0:t-1}|y_{1:t-1})}{P(y_t|y_{1:t-1})} \tag{3.8}$$

We can now re-define, as before, the normalising factor (denominator) as the integral of the numerator for simplification purposes.

$$P(x_{0:t}|y_{1:t}) = \frac{P(y_t|x_t)P(x_t|x_{t-1})P(x_{0:t-1}|y_{1:t-1})}{\int P(y_t|x_t)P(x_t|x_{t-1})P(x_{0:t-1}|y_{1:t-1})\mathrm{dx}} \tag{3.9}$$

It is now clear that the prior represents the estimation of state incorporating the measurement $P(y_t|x_t)$ and the posterior from the previous time intervals $P(x_{0:t-1}|y_{1:t-1})$, advanced in time through the dynamic model $P(x_t|x_{t-1})$; the formula has now become recursive. In order to calculate the normalising constant and the marginals of the posterior we must apply the Monte Carlo method to the probability distributions as a numerical strategy. This is achieved by first considering the probability density function $p(x)$ for which we can sample the random variable x from.

$$x^i \sim p(x), i = 1, 2, ..., n$$

With these samples, we can form a discretised probability mass function $\hat{p}(x)$which acts as an approximation of the continuous function $p(x)$ when expressed in terms of the dirac delta function:

$$\hat{p}(x) = \frac{1}{n}\sum_{i=1}^{n}\delta(x - x^i) \tag{3.10}$$

And by using the law of large numbers:

$$P(\lim_{n\to\infty} \hat{F}_n(x) = F(x)) = 1 \tag{3.11}$$

It is obvious that as $n \to \infty$, the approximation approaches the real distribution. This however, can only be applied if we can sample from the distribution we want to obtain, which is not the case in most applications. This then requires a further sampling strategy, with Sequential Importance Re-sampling (SIS) the most widely used. This provides the posterior distribution from eq. 3.9 in terms of a normalised weight function.

$$P(x_{0:t}|y_{1:t}) = \sum_{i=1}^{n} \frac{W(x)\delta(x - x^i)}{\sum_{j=1}^{n} W(x^j)} \tag{3.12}$$

where:

$$W(x) = W(x_{t-1}) \frac{P(y_t|x_t)P(x_t|x_{t-1})}{q(x_t|x_{0:t-1}, y_{1:t})} \tag{3.13}$$

and:

$$W(x_{t-1}) = \frac{P(x_{0:t-1}|y_{1:t-1})}{q(x_{0:t-1}|y_{1:t-1})} \tag{3.14}$$

We now have a recursive formula for calculating the new weight function from the previous time step weight and can recursively predict the posterior distribution in time as new measurements become available.

The final stage is to add an additional re-sampling step. This is done simply by using the weights to define a discrete cumulative distribution, by sampling randomly from this distribution, we can obtain N new particles by interpreting the previous particles weight as the probability of obtaining a given particle with index i. We then replace the old particles with the new ones and assign each of them an equal weight $1/N$. This works to remove particles with very small weight, and duplicate particles with large weight and hence removes the problem of degeneracy. All that remains for this to be applied, is the definition of the importance distribution $q(x_{0:t}|y_{1:t})$, which can be obtained through multiple methods, though the simplest Bootstrap algorithm will be described here.

3.2.1.1 *Bootstrap algorithm*

The Bootstrap particle filter was the first functional method, as proposed by Gordon *et al.* [49]. As mentioned previously, this provides a way to to define the importance distribution, for which a range of techniques exist, including mixes of non-linear Kalman filters, or developed particle filter methods.

In the Bootstrap algorithm, a variation of sequential importance re-sampling is used, where the importance distribution is described

by the dynamic model $P(x_t|x_{t-1})$. Recalling eq. 3.9, and substituting the dynamic model for the importance distribution, we arrive at:

$$P(x_{0:t}|y_{1:t}) = \frac{\frac{P(y_t|x_t)P(x_t|x_{t-1})P(x_{0:t-1}|y_{1:t-1})}{P(x_t|x_{t-1})}P(x_t|x_{t-1})}{\int\frac{P(y_t|x_t)P(x_t|x_{t-1})P(x_{0:t-1}|y_{1:t-1})}{P(x_t|x_{t-1})}P(x_t|x_{t-1})\mathrm{dx}} \tag{3.15}$$

we can now cancel terms and represent the previous posterior distribution as a discretised mass function of samples.

$$P(x_{0:t}|y_{1:t}) = \frac{P(y_t|x_t)P(x_t|x_{t-1}^{(i)})}{\int P(y_t|x_t)P(x_t|x_{t-1}^{(i)})\mathrm{dx}} \tag{3.16}$$

We must now define the probabilistic model of state evolution $P(x_t|x_{t-1})$ as a discretised mass function, which is described by the system dynamic model and the statistics of the corresponding noise:

$$P(x_t|x_{t-1}^{(i)}) = \int\delta(x_t - f(x_{t-1}^{(i)}, w_{t-1}^{(i)}))P(w_{t-1}^{(i)})dw_{t-1} \tag{3.17}$$

considering that both $x_{t-1}$and $w_{t-1}$are known, then we can determine x_t from the deterministic relation in eq. 3.1, giving:

$$P(x_t|x_{t-1}^{(i)}) = \int\delta(x_t - x_t^{(i)})dw_{t-1} \tag{3.18}$$

where:

$$x_t^{(i)} = f(x_{t-1}^{(i)}, w_{t-1}^{(i)})$$

Continuing from eq. 3.16 and substituting the new relation in eq. 3.18, we arrive at:

$$P(x_{0:t}|y_{1:t}) = \sum_{i=1}^{n}\tilde{W}(x)\delta(x_t - x_t^{(i)}) \tag{3.19}$$

where:

$$\tilde{W}(x) = \frac{P(y_t|x_t)}{\sum_{j=1}^{n}P(y_t|x_t^{(j)})} \tag{3.20}$$

and:

$$P(y_t|x_t) = \int\delta(y_t - h(x_t, v_t))P(v_t)\mathrm{dv_t} \tag{3.21}$$

This then describes a functioning particle filter system with a simplification for the importance distribution. The main disadvantage to this simplicity, is the possible requirement of high number of Monte Carlo samples due to the importance distribution inefficiency. Despite this, the Bootstrap algorithm provides a simple and proven implementation.

3.3 ADVANCED PARTICLE FILTERS

Some inefficiencies exist within the original bootstrap algorithm [49] which have been pointed out previously, and hence much research has been conducted in order to provide more effective algorithms; allowing alleviation from some of these issues and hence producing viable methods for specific applications. This section aims to highlight some of these advanced particle filtering algorithms, and further describe the benefits and disadvantages posed during their application, with the aim of reasoned decisions to be made as to the viability of applying such techniques to flow measurement applications.

3.3.1 *Kernel Particle Filter*

The Kernel particle filter was introduced by Chang and Ansari [18] in order to provide a more efficient algorithm for typical particle filtering applications such as visual tracking, with experiments carried out specifically for human face / body tracking and simulated trajectory [19]. The idea behind this formulation is to improve sampling efficiency, pointed out as one of the main issues with the bootstrap algorithm, and hence increase the performance of the filtering system. This is specifically relevant in complex tracking applications, as their high dimensional nature requires a large number of particles, hence computations tend to take considerable time and are generally conducted offline, which limits their applicability for many desirable applications.

The strategy to produce this increase of efficiency is achieved by adjusting the procedure for identifying modes in the likelihood function. This is done by employing an iterative based sampling method, where the particles are represented as kernel densities and a mode seeking method of mean shifting is employed to encourage particles to move towards the modes, while maintaining a reasonable representation of the likelihood function. This highlights a fundamental issue when working in high dimensions, where obtaining a suitable set of samples which give a good portrayal of the posterior density becomes increasingly difficult, without the use of an excessive number of particles. To implement this method, the particle filter algorithm is performed similarly to that portrayed in the previous section, until the last stage where normally the mean / maximum likelihood is extracted for the current time and particles re-sampled. At this point, we have a set of samples and their corresponding weights $\{x_i^t, W_i^t$, from here the kernel density must be constructed as:

$$\hat{p}_K(x) = \sum_{i=1}^{n} \frac{1}{n\lambda^d} K\left(\frac{x - x_t^i}{\lambda}\right) W(x^i) \tag{3.22}$$

where K represents the kernel profile, varying with choice of distribution (square of Euclidean norm used so as the kernel acts as a form of interpolation), d is the dimensionality of the system and λ being the window radius or bandwidth which dictates the smoothness of the kernel (designated a value relating to both the original radius and number of iterations).

Once complete, the samples are shifted using a mean shift procedure using properties of the kernel, described by:

$$m(x) = \frac{\sum_{i=1}^{n} \frac{1}{n\lambda^d} K\left(\frac{x-x_t^i}{\lambda}\right) W(x^i) x_t^i}{\sum_{i=1}^{n} \frac{1}{n\lambda^d} K\left(\frac{x-x_t^i}{\lambda}\right) W(x^i)} \tag{3.23}$$

This provides new samples which have been coerced towards the modes, and after perturbation, the weights can be re-calculated to represent the new samples. This procedure can then be repeated for a given number of iterations (with the original work proposing 3 as a suitable number [19]). Once the iteration is complete, the estimation and re-sampling stage continues as with the original method.

The results from this work have shown that, for the applications tested, it is possible to achieve the same accuracy as the original particle filter algorithm but with a reduction of the number of particles by 60%; allowing a 10Hz implementation. In addition, it is found that, the kernel filter can provide a greater performance in its state prediction when the system noise is particularly small or large. In such situations, a basic implementation will tend to lose accuracy as the noise heads towards either extreme, and hence highlights an important benefit of this method. A further advantage of using the stated mean shifting technique, is that the system becomes more capable of recovering from failure, referring to when, at some point, the posterior distribution is clearly not representative of the true state. In this situation, the bootstrap algorithm may struggle to reposition the particles into effective positions, but the kernel filter will shift them in the appropriate direction during the iterative process. This is particularly effective when faced with abrupt changes of direction, or sudden acceleration of the state. Overall, this algorithm has presented some key benefits, in particular, when applying to problems with high dimensionality where efficiency and reduction in particle numbers is critical.

Despite the observed advantages of the kernel particle filter, there exists some shortfalls to implementing this method. Firstly, it seems counter-intuitive to apply an iterative based technique when seeking an increase in efficiency, due to the additional computational cost of iterating working against any improvement. though, this is pointed out by the author [19], stating that for a given computational requirement, the kernel filter will still provide a more efficient system despite any losses. Also, it is possible to further increase efficiency if sub-optimal

results are satisfactory. Another issue faced with the kernel filter is regarding its preference to a single definitive mode. For applications where a single value prediction of the state is preferred, this poses no problems. However, it is beneficial in many applications to retain this information as it may be used to provide an overall probability, and may hold valuable information which could be lost in using this algorithm.

3.3.2 *Condensation algorithm*

The condensation, or conditional density propagation algorithm proposed by Isard and Blake [66], is a method for improving the accuracy of the particle filtering algorithm; specifically for visual tracking applications where much visual clutter exists, such as tracking people in crowds or partially camouflaged objects. This technique has been used in much work, and consists of a relatively simple adjustment to the original algorithm when applied generally. Some parts of this algorithm are specifically concerning its application, such as the 'learned' dynamic model, and the definition of the observation model which will not be considered here. However, the iterative based approach to sampling at each time step is particularly interesting, and hence is further assessed.

The employed iterative approach is applied directly to the re-sampling stage, where the cumulative distribution of the the particle weights does not come directly from the particle weights at each time step. Instead, it is related to both the particle weights at current time, along with the cumulative distribution from the previous time step. This is, in effect, to strongly relate temporally related image sequences as encountered in the application, whilst maintaining multi-modal predictions. To describe this approach, we assume that at a given time, the appropriate weights have been calculated according to the current posterior distribution approximation, then assuming c_{t-1}^n represents the cumulative distribution at time $t-1$ for particle n, the newly derived cumulative distribution c_t^n is expressed as:

$$c_t^n = c_{t-1}^n + W_t^n \tag{3.24}$$

and hence the distribution is iterated during each time step of the system. The remaining issue faced here now is the re-sampling stage, as the typical methods need development due to the fact that the cumulative distribution is no longer fully representative of the particle weights, and hence direct sampling cannot take place. Instead, a random number R is generated between 0 and 1, then by binary subdivision a particle is chosen for re-sampling by choosing the lowest possible sample which satisfies the condition $c_{t-1}^n \geq R$, which is repeated for the chosen number of particles. This is seen to be effectively the same as re-sampling procedures presented previously, except for accounting

for the fact that a sample value from the cumulative distribution may not have a corresponding particle match.

The main effect of implementing this algorithm is to retain more influence of the prediction from the previous time step than in the original system. This is intuitive for visual tracking as, assuming a high enough frame rate, the tracked object should uphold its motion reasonably steadily. In the original algorithm, the required noise variance could cause too much variability, and hence the prediction may 'jump' to the wrong conclusion; a prime example being when a different person passes close to the tracked individual, causing the system to switch to the passer-by. Although this seems quite application specific, it could be assumed that as long as the process was relatively steady, this iterative process could be developed to be beneficial, without losing the multi-modal ability of the particle filter algorithm.

One of the key disadvantages of using the condensation algorithm is with regards to computational efficiency. Due to the additional stage of iterating the cumulative probability of each particle, the computational complexity formally increases to $O(N \log N)$. Though it is possible to reduce this with minor modifications to the sampling procedure [66]. The gain in efficiency could counter this effect by reducing the required number of particles for a suitable result, though it is clear there remains some difficulty in implementing this method in real-time. It could be argued that due to the high degrees of freedom associated with visual tracking, that this inability can be put down to application, and hence a less intensive application could be feasibly operated in real-time.

3.3.3 *Annealed Particle Filter*

With the aim of reducing computational complexity in high dimensional problems, the annealed particle filter acts as a stochastic search algorithm. Developed by Deutscher et al. [28], this method gradually introduces the effects of narrow distributions without the loss of generality, and without over focussing on local maximum. This then permits a greater focus on the global maximum whilst maintaining information on other prevalent modes, which is a crucial attribute for the initial application of body motion capture with high degrees of freedom. Furthermore, this algorithm is developed with real time functionality as a significant feature.

This technique employs a simulated annealing [75] approach to particle filtering, allowing an optimised system for handling multiple modes. It is implemented during the posterior prediction stage where the particles are weighted, and effectively changes the weighting and particles positioning to permit a global mode focus during the re-sample stage. Considering first, a distribution with two significant modes, both of which are similar, though with one more prevalent

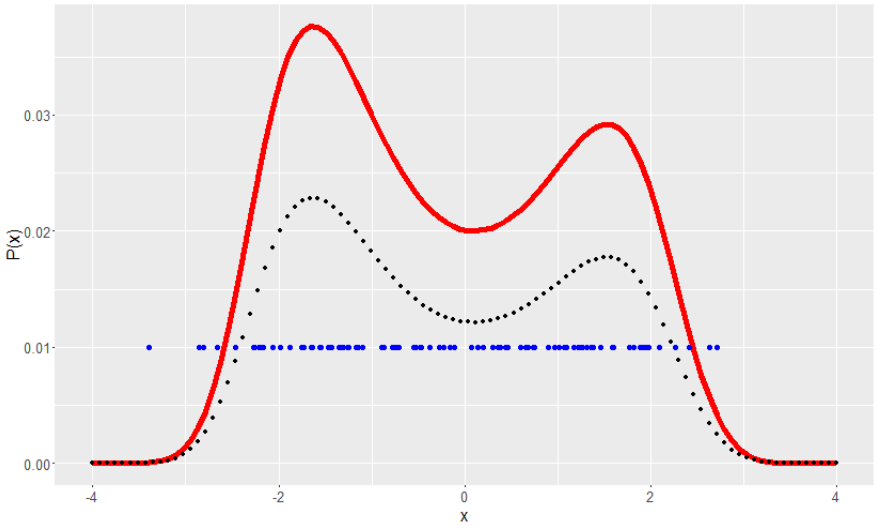

Figure 3.1: Approximation of the posterior distribution (red), with uniform prior and resulting weighting (black) and re-sampled particles (blue). Showing similar distribution of particles under both modes.

than the other. Figure 3.1, portrays such a distribution, along with the developed weighting when a uniform particle distribution is applied as a prior, and using an importance sampling based approach. It is noted that this represents an overly simplified problem for demonstrative purposes, with a real application likely to contain more than two significant modes of higher complexity. Also portrayed in Figure 3.1 is the re-sampling stage, consisting of deterministic re-sampling along with added noise to diversify the particles. By observing the re-sampled particles, it can, where

$$W(x) = \frac{P(y_t|x_t)P(x_t|x_{t-1})P(x_{0:t-1}|y_{1:t-1})}{q(x_{0:t}|y_{1:t})} \tag{3.25}$$

be seen that there is no significant difference between the density of particles under both modes, despite the dominance of one of the modes. This highlights the main issue that the annealed particle filter wishes to address, as preferably, we would like higher density of particles under the most prevalent mode, while maintaining some representation of the remaining mode.

To improve on this, the annealing procedure consists of employing a series of distributions which differ slightly from the originally derived weighting. We start with the original set of particles and their corresponding weighting:

$$S_t = \{x_t^N, W_t^N\} \tag{3.26}$$

We then create some annealing layers of the weight distribution for M layers:

$$S_{A,W} = \{(W_{t,1}^N)^{\beta_1}, (W_{t,2}^N)^{\beta_2} ... (W_{t,M}^N)^{\beta_M}\} \tag{3.27}$$

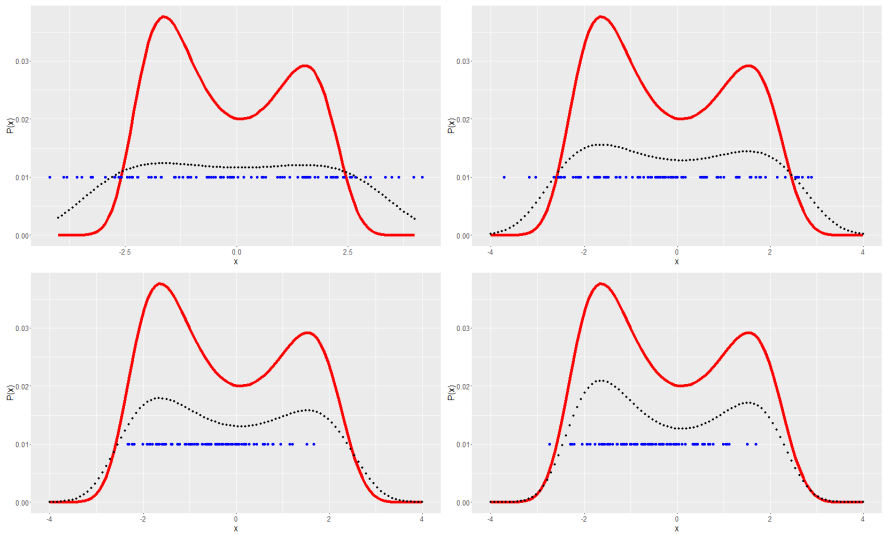

Figure 3.2: Approximation of the posterior distribution through a number of annealing layers, with β = 0.1,0.3,0.5,0.8 for images left to right, top to bottom respectively. Displays particles concentrating more on the most prevalent mode whilst still representing the other.

where all $\beta < 1$, and $\beta_1 > \beta_2 > ... > \beta_M$.

Then, beginning at layer M, the annealed weighting distribution is calculated, and once complete, the particles are re-sampled and have a noise distribution applied. The new particles are then fed into the next annealing layer and this is repeated for all layers; the final re-sampling stage consists of applying a noise distribution with a higher variance to ensure that the particles are redistributed fairly prior to the next time step, and after the information regarding the most prevalent mode is extracted. This process is demonstrated in Figure 3.2 for the simple problem described earlier. By observing the results from the annealed simulation, it is clear that the particles are coerced towards the most prevalent mode, but the remaining mode still maintains representation. It is important to note that this simulation only highlights the idea of annealing, and that the original prediction without annealing is already sufficient due to simplicity.

The only remaining area of discussion is with regards to parameter selection, considering the following:

- Number of annealing layers
- Range of annealing (β_1, β_M)
- Rate of annealing $(\triangle\beta_{1:M})$

Firstly, the number of annealing layers is dictated by the added computation require for additional layers, assuming that the other parameters are chosen appropriately, a higher number of annealing layers will generally produce more accurate results. As for the remaining parameters, some available mathematical definitions for choosing these

values are presented as a function of survival diagnostic [84], number of particles / annealing layers, as well as system parameters, such as noise variance and expected movement corresponding to the model. The parameter values used in the simulation presented in Figure 3.2 are merely chosen to exaggerate the algorithm features and hence would not be appropriate for use in real applications.

Overall, this algorithm achieves its aim of a general solution to reaching a global maximum while retaining enough information of the remaining modes. As for efficiency, it has been reported [28] that, for the articulated body motion tracking application, a reduction of particle size by a factor of 10 can achieve suitable results, and thus increase efficiency. With the available adjustment of the number of annealing layers, it is feasible that a variant of this system could be applied to real time systems if the resulting sub-optimal results were acceptable.

Despite this, there still remains an issue with computational efficiency in a general application sense, with any implementation of multiple weight calculation and resampling adding to the computational complexity. Although, with the reduction in required particles, further application specific experiments would be required in order to establish whether or not this would create a system viable for real time applications; dependent heavily on the required accuracy and the most intensive procedure present in the specific application (for body motion tracking this refers to the likelihood evaluation, though is not always the case). Finally, the additional job of assigning rate and range of annealing could be problematic if the application causes the most efficient values of these parameters to change.

3.3.4 *Auxiliary Particle Filter*

The Auxiliary filter aims to tackle some of the shortfalls encountered during a general particle filter simulation. These are defined as; the ability to implement adaption efficiently, meaning to incorporate the newly gathered measurement at time $t+1$ into the re-sampling procedure between times t and $t+1$. Also, a better representation of the distribution tails is an aspect tackled with the Auxiliary filter, with both of these issues strongly related to the presence of outliers within the system. This method was developed by Pitt and Shephard [96], who argue that these issues can all be improved, without severely affecting the computational cost, by introducing an additional dimension to the system, and subsequently removing it as required; hence the term ‘auxiliary" given to this additional dimension to indicate that it exists purely to aid the simulation and not to directly influence the prediction. An important aspect of this algorithm is that the importance distribution is not defined as the state evolution model or transition density, seen in the bootstrap method [49], and is given a

suggested definition which can be changed at the researchers discretion. Overall, it can be seen that this method is fundamentally closer to the SIR algorithm than previous examples.

As mentioned, the main strategy involved in Auxiliary particle filtering is the increase of dimensionality, without the additional computational cost. The sampling method demonstrated in the original work [96] uses the SIR framework, although it is pointed out that it can be easily adapted to either rejection or Markov Chain Monte Carlo (MCMC) based sampling. It is adapted by changing the posterior density, (from which we wish to sample) to a joint density with the inclusion of the auxiliary variable k.

$$P(x_{t+1}, k|y_t) \propto P(y_{t+1}|x_{t+1})P(x_{t+1}|x_t^k)W(x_t^k) \tag{3.28}$$

where k=1, .., N

If samples were then generated from this distribution, and the auxiliary variable k discarded, the samples represent the empirical density $P(x_{t+1}|y_t)$. In order to generate such samples, we can approximate the previous distribution as:

$$\hat{P}(x_{t+1}, k|y_t) \propto P(y_{t+1}|\mu_{t+1}^k)P(x_{t+1}|x_t^k)W(x_t^k) \tag{3.29}$$

where μ_{t+1}^k represents a value of high likelihood from $P(x_{t+1}|x_t^k)$, the mean for example.

For the distribution of the auxiliary variable, the following definition can be made:

$$\hat{P}(k|y_{t+1}) \propto P(y_{t+1}|\mu_{t+1}^k)W(x_t^k) \tag{3.30}$$

and hence by simulating the probability of this distribution, and sampling, we obtain what is known as the 'first stage weights' λ_k for each sample k. Once complete, we draw R samples from indices k (with corresponding weight λ_k) to form k^r. Then finally, draw x_{t+1}^r from the density $P(x_{t+1}|x_t^{k^r})$; with the idea being that, the particles sampled represent areas of particularly high likelihood. The final stage of this process is to develop the 'second stage weighting', which is used to form the prediction at each time step. This is achieved using the following:

$$W(x_{t+1}^r) = \frac{P(y_{t+1}|x_{t+1}^r)}{P(y_{+1}|\mu_{t+1}^{k^r})} \tag{3.31}$$

$$\widetilde{W}(x_{t+1}^r) = \frac{W(x_{t+1}^r)}{\sum_{j=1}^{n} W(x_{t+1}^r)} \tag{3.32}$$

If required, particles can be re-sampled from this discrete distribution, as seen in other algorithms. Referring back now to the aims of this

method, it can be seen that they have, to a degree, been improved by the auxiliary particle filter. Firstly, adaption is now implemented in the SIR method, where the first stage weights provide a link between the weights in the previous time step to the newly gathered measurement; the effect of this is to focus on high likelihood areas, and avoid wasting computation on particles with unlikely positioning. The other notable issue is with the representation of distribution tails, which is improved due to the increase in dimensionality, despite not severely increasing computational cost due to the removal of the auxiliary variable. This assists in providing an overall better representation of the distribution.

When implementing the auxiliary particle filter, there remains some issues that require consideration during application. Firstly, the number of particles chosen for each of the two re-sampling stages must be sufficient to provide adequate results, while low enough to ensure that the overall efficiency is not degraded by the additional resampling stage. It is suggested [96] that fewer particles can be used in the second stage of sampling due to the greater focus on the distribution modes, although the optimum ratio can only be attained through rigorous testing. Furthermore, it is pointed out that, with increasing numbers of particles, the gain in efficiency from this method will eventually plateau. Therefore if, for a given application, this maximum efficiency gain is calculated, it may be the case that such efficiency could be achieved through a simpler method with more particles if the computational resource is available; hence this method would not be required. A final point is regarding the selection of the importance distribution, although an option is presented here, this will not be the optimum solution for all applications and many possibilities exist. Careful consideration must be given to this assignment and would likely require application specific analysis to ensure the selection is suitable.

3.4 MULTIPHASE COMPUTATIONAL FLUID DYNAMICS

CFD has provided a breakthrough in simulation based studies for a considerable range of practices. In recent years, the potential of CFD in terms of applicability and accuracy has improved significantly with the ever increasing computational resource readily available, and its subsequent reduction in cost. CFD is a numerical methodology of solving complex equations, with specific reference to the governing fluid equations. As expected from a numerical methodology, it includes a mathematical representation, or model (in this case the Navier Stokes equations), of a phenomena (fluid flow), simplified, to varying degrees, by way of assumptions made about the specific system in question. The motive for using CFD is to provide an approximate numerical solution to a set of coupled differential equations by representing them as a large number of algebraic equations, which can be solved in

a reasonable time by use of a computer; this procedure is known as discretisation.

The typical procedure for conducting a CFD simulation can be split into three stages, each with specific steps, being:

1. **Pre-processing:** Problem definition, Assumptions, Fluid domain definition, Meshing
2. **Solver:** Model selection, Fluid/system properties, Boundary/initial conditions, Algorithm
3. **Post-processing:** Convergence analysis, Data extraction, Graphical representation, Validation

The most progress made in CFD application is that of single-phase flows, with numerous examples in aerospace, automotive and fluid handling machinery. In such examples, the fluid models are further developed and relatively simple to implement compared to multiphase systems, and may only require models for continuity and momentum, with more focus on describing boundary conditions. These flow models can then be applied to very complex geometries using Computer Aided Design (CAD) tools, which have provided invaluable research capabilities in the industries previously described. However, in the field of multiphase systems, the existence of deformable interfaces between the fluids and the greater magnitude of turbulence which occur, significantly increases the system complexity [125].

For multiphase CFD, a large range of both model frameworks and their corresponding closure equations have been proposed. For simplicity, we will consider briefly, two multiphase CFD models broadly applicable to flows in a pipeline:

1. Volume of Fluid (VOF) (Interface tracking) method
2. Multi-fluid (Euler-Euler) method

The VOF method has become one of the most popular strategies due mainly to its simplicity, and is applicable specifically for segregated flows, where interfaces between phases are sharp; it is accepted that such methods are suited to relatively simple interfaces [125], such as that encountered in annular and stratified wavy flows, as opposed to churn flow, for example. In this method, the most significant property is that the flow is represented as a mixture of fluid, meaning that both phases share a common velocity at any specific point in the flow domain. This is described in the model with a single momentum equation, along with an additional surface tension force parameter which acts at the phase interface. This model was developed in the early 1980's by Hirt and Nichols [57] based on multi-fluid simulations using the Marker and Cell (MAC) method, and has been further developed since, with particular focus on improving the interface tracking algorithm [50].

The Multi-fluid model provides a more robust and complex solution compared to VOF. In its most basic form, it is used specifically for inter-dispersed flows with high volume fraction of either phase, although a hybrid VOF/Multi-fluid is available, which is capable of handling both segregated and dispersed flows by the addition of interface tracking between phase pairs, as in VOF [125]. This model can solve for n phases, each with its own separate flow equation. In this sense, the phases are initially independent, and are then coupled by their transfer of mass, momentum and energy. With the multi-fluid models greater complexity, comes both a larger range of flow applicability, as well as computational cost compared to an equivalent VOF simulation. Furthermore, the derivation of generalised closure relations become more difficult [125].

3.4.1 *Volume of Fluid model*

The following describes the VOF method with interface sharpening using the homogeneous mixture assumption, and representing two phases as a single fluid system by means of averaging. Starting with the continuity equation (incompressible):

$$\nabla \cdot \bar{u} = 0 \tag{3.33}$$

and the (incompressible) mixture momentum equation presented by Hirt and Nichols [57]:

$$\frac{\partial \bar{u}}{\partial t} + \bar{u} \cdot \nabla(\bar{u}) = -\frac{1}{\bar{\rho}}\nabla p + \frac{\bar{\mu}}{\bar{\rho}}\nabla^2 \cdot \bar{u} + g + \frac{F_{st}}{\bar{\rho}} \tag{3.34}$$

where: $\bar{u}$ is the averaged velocity of present phases $\bar{u} = \alpha_l u_l + (1 - \alpha_l)u_g$

$\bar{\rho}$ is the average density $\bar{\rho} = \rho_l u_l + (1 - \alpha_l)\rho_g$

$\bar{\mu}$ is the average viscosity $\bar{\mu} = \mu_l u_l + (1 - \alpha_l)\mu_g$

g is the gravity vector

F_{st} is the force due to surface tension

It is worth noting that, as intended, the previous equations only include a single phase fraction term α_l, allowing the model to be treated as a single fluid using the definition: $\alpha_g = 1 - \alpha_l$, and hence the gas phase fraction becomes a secondary term. The only remaining term in eq. (3.33) and (3.34) is that of surface tension force (F_{st}), which, although different definitions exist, such as the Level Set method (LS) [109], the VOF method uses the Continuum Surface Force (CSF), proposed by Brackbill et al. [14]. Which, in the absence of density weighting, is as follows:

$$F_{st} = \sigma\kappa\nabla\alpha_l \tag{3.35}$$

where σ is the surface tension co-efficient, and κ is the interface curvature, given by the following.

$$\kappa = \nabla \cdot \left(\frac{\nabla \alpha_l}{|\nabla \alpha_l|} \right) \left(\tag{3.36}$$

The final stage for describing the VOF method is to define the interface sharpening technique, which is provided as part of the advection equation for the liquid phase fraction. Many Interface sharpening schemes exist, of which many have been extensively reviewed and analysed by Gopala and van Wachem [48], for a range of CFD codes. Here, we will consider the most commonly used method in commercial CFD software, based on the proposal by Weller [40]:

$$\frac{\partial \alpha_l}{\partial t} + \bar{u} \cdot \nabla(\alpha_l) + \nabla \cdot (u_c \alpha_l (1 - \alpha_l)) = 0 \tag{3.37}$$

where $u_c$is an artificial compression velocity which is applied normally to the interface, thus compressing the volume fraction and creating a sharp structure [121], and is given by:

$$u_c = C_\alpha |\bar{u}| \frac{\nabla \alpha_l}{|\nabla \alpha_l|} \tag{3.38}$$

where C_α is the compression indicator, a binary indicator for turning the interface compression on (1) or off (0). The term $\alpha_l(1 - \alpha_l)$ in eq. (3.37) ensures that the remainder of the term is only active during intermediate values of α_l (i.e. at the fluid interface).

3.4.2 *Multi-fluid model*

This section describes the Euler-Euler multi-fluid model for incompressible, isothermal flow, in its developed form to include interface tracking as seen in the VOF method. For each phase k, the conservation of mass equation is given, in a similar form as seen in Section 3.4.1 for VOF:

$$\frac{\partial \alpha_k}{\partial t} + u_k \cdot \nabla(\alpha_k) + \nabla \cdot (u_c \alpha_k (1 - \alpha_k)) = 0 \tag{3.39}$$

this again includes the additional term to include interface compression as seen in Section 3.4.1, with the same form used for the artificial compression velocity.

The momentum equation is described as follows, for each phase k:

$$\frac{\partial \alpha_k u_k}{\partial t} + u_k \cdot \nabla(\alpha_k u_k) = -\frac{\alpha_k}{\rho_k} \nabla p + \nu_k \nabla \cdot (\alpha_k \nabla u_k) + \alpha_k g + \frac{F_{b,k}}{\rho_k} + \frac{F_{st,k}}{\rho_k} \tag{3.40}$$

where: ν is the kinematic viscosity and F_{st} is the force due to surface tension, solved as in VOF by use of CSF [14]. $F_{b,k}$ is the summation

of forces which act on bubbles and drops for phase k, which are constrained to $\sum F_{b,k} = 0$ in order to satisfy momentum conservation. For a given phase, this term is made up of the following force terms [121]:

$$F_b = F_d + F_l + F_v \tag{3.41}$$

where: F_d and F_l are the drag and lift forces respectively, and $F_v$is the force due to virtual mass.

It is important to note that the force term F_b can include additional forces to the ones stated, if required for a specific simulation. eq. (3.41) displays the most commonly used force terms in CFD simulations. In order to prescribe relations to these force terms, the distinction must first be made between a continuous and a dispersed phase. Depending on the system to be simulated, the relative phase contents, and expected topology, the phases within the simulation must be designated either continuous or dispersed in order to correctly define the drag type forces acting on bubbles and droplets. Despite this presenting a possible problem if this definition may switch during a single simulation, in most cases the correct choice is clear.

The drag force can be defined by the following equation, developed from the single phase drag equation, for a specific phase:

$$F_d = \frac{3}{4}\rho_c \alpha_c \alpha_d C_d \frac{|u_d - u_c|(u_d - u_c)}{d_d} \tag{3.42}$$

where subscripts c and d represent continuous and dispersed phase respectively, C_d is the drag co-efficient, and d_d is the droplet diameter of the discrete phase which can be varied if required, or, as is most common, a single value estimation can be prescribed based on system geometry. For the drag co-efficient C_d, a multitude of models are available, including: Gidaspow [44], Syamlal-O'Brien [110], and Schiller and Naumann [99], each with their own advantages and limitations. The Schiller and Naumann model is a typical choice for many simulations, and is given as:

$$C_d = \begin{cases} \frac{24(1+0.15Re_d^{0.683}}{Re_d} & Re_d \leq 1000 \\ 0.44 & Re_d > 1000 \end{cases}$$

where the droplet Reynolds number is defined as: $Re_d = \frac{|u_d - u_c| d_d}{\nu_c}$.

Continuing now to the lift force, as before the equation is a multiphase equivalent to the single phase lift equation, for a specific phase:

$$F_l = -C_l \rho_c \alpha_d \left(u_c - u_d\right) \times \left(\nabla \times u_c\right) \tag{3.43}$$

where C_l is the lift co-efficient.

As with the drag co-efficient, many examples of lift co-efficient definitions exist, suited with particular applications. Specifically for

fluid-fluid systems, examples include: Legendre-Magnaudet [78], Tomiyama [115] or simply the value: $C_l = 0.5$ as described by Auton [8], derived for a spherical body in rotational flow.

The final term to be described is the virtual mass force, which models the force exerted on the fluid surrounding an immersed bubble as it accelerates, causing it to also accelerate, with this effect being greater when the density difference between phases is small, and negligible when large. Through Newton's second law we arrive at [34]:

$$F_v = C_v \rho_c \alpha_d \left(\frac{Du_c}{Dt} - \frac{Du_d}{Dt} \right) \Bigg(\tag{3.44}$$

where: $\frac{D}{Dt}$ is the material derivative of a variable, and C_v is the virtual mass co-efficient, given as $C_v = 0.5$ [42].

The next chapter describes both the outline of research, along with the 3 experiments undertaken in this work, including information on the flowloops, instruments, fluids, and flow ranges. Additionally, a detailed description of the ECT system used in all experiments is provided.

Part II

EXPERIMENTS, STUDIES AND DISCUSSIONS

4

RESEARCH OUTLINE, EXPERIMENTAL SETUP AND DATA COLLECTION

4.1 OUTLINE OF RESEARCH

The first section in this chapter provides a clear definition of the research carried out in this work and the resulting contributions and achievements that are gained. Furthermore, the scope of the work will be provided by describing any assumptions made and the subsequent limitations. This begins by summarising the findings of the literature survey, as defined in the previous two chapters, which assisted in determining the most appropriate research area.

4.1.1 *Summary of Capacitance tomography and its place in multiphase flow measurement*

Chapter 2 has highlighted the journey of ECT as an instrument, from its early development up to its current use in advanced measurement, encouraging many areas of research in improving its capability. It is clear that for both flow regime identification, and the flow measurement of slugs flows specifically, ECT is currently capable of contributing to multiphase flow measurement. Despite flow regime identification already being at a reasonable development stage, the increase in the computational efficiency of the method, and its capability in online identification of intermittent flows are the most vital areas for further research. For flow measurement of slug flows, the reliability and stability of using slug translational velocity along with the derived correlations, has provided a viable tomographic based measurement strategy within a reasonable accuracy. However, increasing the achievable accuracy, particularly for less stable slug flows, would be required in order for multiphase ECT measurement to become a profitable substitute to phase separation, and single phase flow measurement.

The biggest limitations in proposing ECT as a multiphase flow measurement device have been found to be in the application to conductive fluids, and to segregated flows such as annular and stratified-wavy. Considering that, in oil and gas applications and particularly in maturing oil fields, a water phase is present and thus must be accounted for. It would seem that development in this area must focus on the construction of measurement systems and their surroundings to be resistant to 'stray capacitance', and more importantly, the development of online dual modality systems. For segregated flows, assuming, as is the case for ECT, that the inter-facial wave properties are all that can be

measured, it is clear that the current proposed methods of correlation are simply not reliable for a large range of flows, and specifically high viscosity oils. As well as this, there remains a significant issue in determining the liquid superficial velocity. It is therefore apparent that a more complex strategy is required to allow ECT, and similar devices, to conduct flow measurement on these flow types.

From the literature reviewed, it is clear that there exist some areas within this field from which to conduct further research with the goal of improving the effectiveness of ECT as a multiphase flow measurement device. The chosen areas of focus are as follows:

1. On the basis that the current method of slug translational velocity and correlation used in slug flow measurement is effective; further investigation into the effect of velocity discontinuities at the slug front, (as discussed by Reis and Goldstein [33]) on the cross-correlation measurement accuracy will be investigated through observation of slug structures, and analysis of their representativeness. This is presented in Section 5.2.

2. Using the proposals of methods to counter the effect of conductive fluids on ECT measurement, analysis of their capability can be assessed on the multiphase flowloop at NEL. This concentrates only on the technique of effectively making the oil and water phases indistinguishable form each other in ECT, and therefore does not include the application of dual modality imaging, due to restrictions in available technology and the project scope overall. This work was conducted jointly between Coventry University and NEL, and is shown in Appendix B.

3. Considering the conclusion made previously that the wave correlation method, used currently in the field of measuring segregated flows, is insufficient in providing a basis for tomographic measurement of such flows, a new method will be investigated. This involves using historic data slug flow data from the instrument, to infer the flow parameters of segregated flows through similarity in wave properties. This is presented in Section 5.1.

4.1.2 *Summary of Particle filtering methods and multiphase CFD*

This chapter has highlighted the benefits and potential of a particle filtering based multiphase flow measurement system, facilitated by ECT as the primary measurement device, and a CFD model to provide state transition. The first half of the chapter has demonstrated that the original Bootstrap filter can provide a simple yet effective solution to implementing particle filtering in flow measurement. As well as this, the review of advanced methods has provided alternative particle filtering algorithms which may be suited to the proposed system.

The second half of the chapter has described two applicable CFD models for this application, the VOF and Multi-fluid model. The advantages and disadvantages of each was described, with the VOF method providing the simplest and fastest method, although restricted in modelling dispersed flows when compared to the multi-fluid model.

From the literature reviewed, the following was deduced, with respect to the studies to be conducted:

- A particle filtering system will be developed in line with the Bootstrap algorithm, as this will provide the simplest implementation, considering the other difficulties involved in applying CFD, whilst acting as a benchmark for future developments. The implementation of this system is provided in Section 5.3, and the proposal for advanced methods is given in the future system proposal in Section 6.1
- The model used in the particle filtering system will be the Euler-Euler multi-fluid model. Despite the VOF method being suitable for modelling the experiment described in Section 4.1.6, using the multi-fluid model provides reassurance of the applicability of the method to a greater range of flow regimes.

4.1.3 *Research scope and contributions*

Prior to outlining the main studies conducted in this work, this section aims to clearly describe the intended practical and theoretical contributions, as well as highlighting the scope of the work, and assumptions made. Firstly, by applying the knowledge gained through the literature survey, and the proposed research challenges, five research questions have been produced, defining what is required as an outcome to the following studies. After this, a description of the research scope is provided in the research definition, including the expected contributions, achievements and assumptions made.

4.1.3.1 *Research questions*

From the knowledge gained in Chapters 2 and 3, five research questions have been developed, specifying the desired outcomes of the main research conducted in Chapter 5 using the experimental data produced, as outlined later in this Chapter.

Q.1 *How capable, in terms of viability and accuracy, is a standalone ECT system of flow measurement when applied to flow regimes that could occur in pipelines in the oil and gas industry?*
It is believed that although ECT can be applied successfully to certain flow types found in industry, it remains limited as a standalone meter. To successfully operate as a FRIMM meter, other techniques would be required to ensure it is capable of achieving the needs outlined by

the oil and gas industry. Furthermore, by prescribing and developing such techniques to assist ECT, a better understanding of the extent to which these devices can accurately measure multiphase flows is required. The work conducted in relation to this question is covered in Sections 5.1 and 5.2.

Q.2 *Can the multiphase flows that tomography is currently capable and suited to measure (specifically slug flows), be improved in terms of its achievable accuracy?*
Considering the multiphase flows which tomography is currently suited to, it is assumed that in by identifying the causes of inaccuracies highlighted in other research, and proposing a developed measurement method incorporating the imaging ability of ECT, an improvement in the systems capability can be achieved. This is addressed in both Sections 2.4.4 and 5.2, with respect to identifying the cause, and proposing a solution respectively.

Q.3 *On the basis that currently, a standalone tomographic measurement device is not a viable solution for metering all flows that occur in industry, can the incorporation of a Computational Fluid Dynamics (CFD) model in the measurement system, using Bayesian Particle filtering, improve their applicability*?
Particle filtering has been shown to provide many benefits in other applications, where a measurement related to a state variable is combined with a model of the state. Assuming that such a technique can be applied to multiphase flow metering, considering the model complexity for instance, it is believed that this would alleviate the current limitations involved with a standalone ECT system. This question is addressed in Section 5.3.

Q.4 *Can such a system operate without relying on empirical correlations, that are limited in their flow range and applicability to flow regimes?*
Measurement systems based on empirical correlation are limited significantly in their applicability, as the correlation parameters are typically functions of the system, fluids or flow range. It is therefore assumed that any general solution to FRIMM must not rely on such correlations to be an effective solution. By providing evidence that this can be achieved, the potential for a new type of metering solution would be achieved. Work related to this question is found in Sections 5.1 and 5.3.

Q.5 *What further research and developments in technology would be required to produce a flow regime independent multiphase flow measurement (FRIMM) system to be used in large oil and gas pipelines in the context of process now-casting, and how could such a system operate*?
On the basis that the foundation of a FRIMM system is gained during this work, the developments and research required to create an industry-ready solution can be outlined. This can also include the variations in the way that it can be implemented, particularly for large

scale pipelines in the oil and gas industry. This is demonstrated in the system proposal in Section 6.1.

4.1.3.2 *Problem statement*

The problem that this research attempts to overcome is that the reliance on single phase flow metering in the oil and gas industry is limiting the efficiency of distribution. Furthermore, current multiphase flow meters are not appropriate for the environment and all flow types which are encountered in oil and gas pipelines, and therefore require development.

The scope of this research can be defined as:

- The development of ECT as a standalone multiphase flowmeter, specifically focussing on data processing with regards to commonly encountered flow regimes in the oil and gas industry.
- Development of a flow metering system, using ECT, a CFD model and Particle filtering, to be applied to a simplified multiphase flow, but with the potential to be flow regime independent.

4.1.3.3 *Assumptions / simplifications*

The main assumptions and simplifications used in this work, along with their validity and drawbacks are as follows.

- Multiphase flows in this work consist of only oil and gas.

Flows encountered in the oil and gas industry typically include a mixture of oil, gas, water and solids, and therefore any system developed would require further work to account for these additional phases. Although this additional work could pose significant difficulties and challenges, it is accepted that in order to test and develop a new method, as is the case with this work, a more stable benchmark is suitable. Furthermore, specific limitations of ECT cause testing with conductive fluids difficult, thus multiple measurement systems may be required for such a task which could interfere with the primary research goal.

- Linear Back Projection

The tomographic images produced in Section 5.2 are produced using LBP as an image reconstruction algorithm. Due to its assumption, outlined in Section 2.1.5, it is limited in accuracy compared to other methods. This limitation is particularly prevalent when imaging complex interfaces. Considering that the structures identified in this work have relatively simple interfaces, this simplification is deemed suitable.

- Gas flow through a liquid column

In Section 5.3, the multiphase flow used in the experiment and modelled using CFD, consists of gas being pumped through a vertical column of oil. Despite this flow simplification not representing the more complex flows encountered in industrial flows, it acts as a suitable test case to prove the principle of the proposed method, on the assumption that it remains representative and could be extended to more complex flows. Furthermore, this simplification allows for a straightforward implementation, and reduction in computational costs of the CFD model.

- Offline particle filtering system

The main study in Section 5.3, outlining the particle filtering system is conducted offline by using a database of pre-simulated results, as opposed to being a real-time system which would simultaneously simulate large numbers of possible states at each time step. This therefore does not allow the system to operate in a real application, though this was not an expected outcome of the work. Furthermore, the computational resources required to implement a real-time system would be considerable and outside the scope of this work, being more suitable for a later stage of development.

- Bootstrap algorithm particle filter

The simplest implementation of a particle filter is used during the implementation in Section 5.3, without the use of the discussed advanced methods described in Section 3.3. As demonstrated in the review of these advanced methods, considerable increases in efficiency, and thus performance, could be gained with a more complex algorithm. Considering that the study in question was also simplified to operate offline, computational requirement and sampling efficiency are not a primary concern and could be developed at a later stage.Experimental setup

This section outlines the experimental system set-up and all additional equipment and instrumentation used to collect data for the studies in this work, along with a description of the data acquisition and processing procedure. The analysis and studies outlined in Chapter 5 require data from three separate experiments, two of which were carried out on the multiphase flow loop at the NEL Glasgow, UK; an industrial partner of this project; providing industrial scale flow data, using equipment which is currently utilised for calibration and testing services by companies in the oil and gas sector. The third test was carried out on a lab-scale three phase flow loop, situated at the flow measurement research centre at Coventry University. This chapter will describe the stated experimental equipment, associated technology, and the specific phase flowrates for which tests were conducted, along with any additional procedures taken.

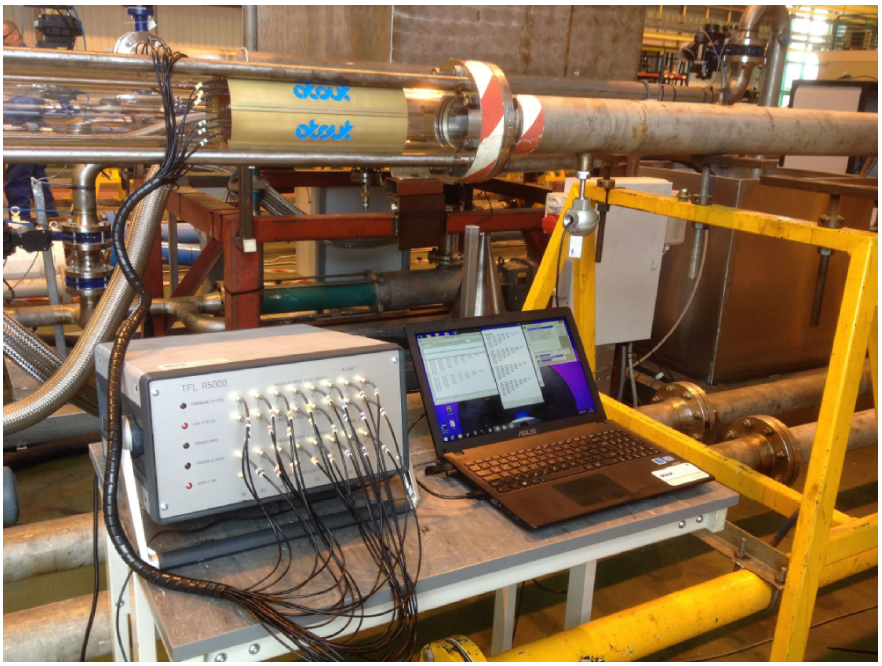

Figure 4.1: ECT system installed on a horizontal sight tube test section on the NEL multiphase flowloop.

4.1.4 *Experimental setup 1 - horizontal two-phase flow*

4.1.4.1 *Overview*

This experiment was conducted on the multiphase flowloop at NEL, depicted in Figure 4.1 with the ECT system installed, and the corresponding schematic in Figure 4.2. The test section, where the ECT measurement device is located, is a 10.2cm internal diameter, transparent Acrylic pipe, with a 20mm wall thickness and with a horizontal orientation. The flow loop itself, consisted of a large gravity separator, reference flowmeters and valves as portrayed in Figure 4.2. The flowloop is capable of delivering oil, water and gas, though for this experiment, only oil and gas was used. The horizontal length of the flowloop is 60m, including test section.

4.1.4.2 *Instrumentation and fluid delivery*

Both oil and water (only oil in this experiment), were transported around the flow loop via centrifugal pumps, and the gas was delivered through use of valves and a pipe expansion. Prior to mixture, both the oil and gas were metered using the reference turbine flow meters, which are calibrated and traceable to the UK national standard. The system is capable of delivering refined oil at rates up to $140 m^3/hr$ with an uncertainty $< 1\%$ and gas at rates of up to $600 m^3/hr$ with an uncertainty of $< 1.5\%$. The line pressure within the flow loop can operate within a gauge pressure range of between 0 and $15 bar(g)$, and

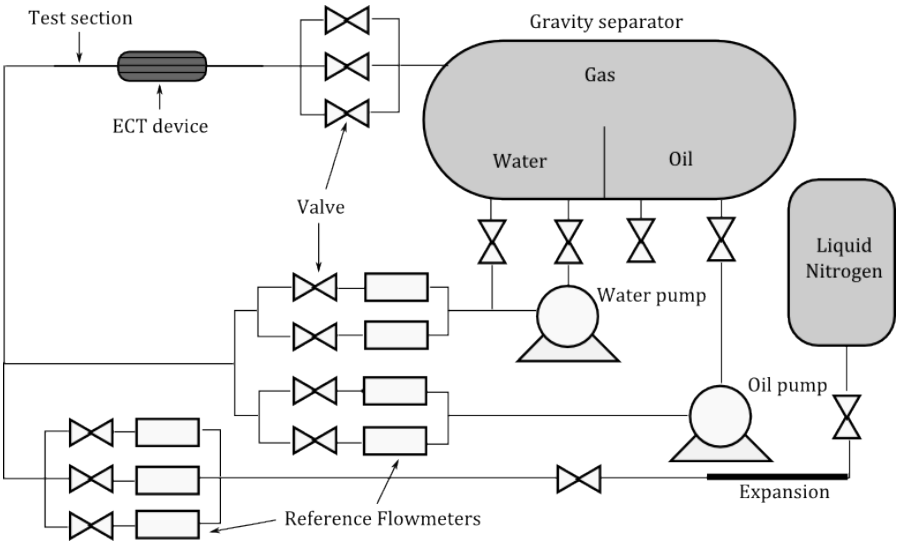

Figure 4.2: Schematic diagram representing the multiphase flowloop at NEL with a horizontal test section.

the line temperature can be maintained at temperatures within the range of 5 to 55°C. The line pressure, temperature, and the corresponding fluid properties affected can be monitored during testing at multiple points along the flowloop.

4.1.4.3 *Fluid properties*

In these experiments, the oil used was ParaFlex HT9, with a (Normal Temperature and Pressure (NTP) condition) density of $\rho_l = 830 kg/m^3$, along with a dynamic viscosity of $\mu_l = 18cP$. As for the gas, Nitrogen was used, with NTP properties of density $\rho_g = 1.165 kg/m^3$ and of viscosity $\mu_g = 1.76 \times 10^{-5} Pa.s$. During the range of tests conducted in this experiment, the reference data showed that the temperature within the flow loop varied between 20.7°C and 23.5°C, which caused the oil density to vary between the range of 829.1 to $831 kg/m^3$, and the corresponding viscosity to range between 15.88 to $17.87cP$. This variation was deemed low enough to have no substantial negative effect on the results, in terms of maintaining flow regime and fluid consistency.

4.1.4.4 *Tests conducted*

The objective of this experiment was to sample various test points within the slug flow regime range for these fluids, some of which are, close to, or at the flow regime transition boundary between slug flow and stratified wavy flow. This was conducted at a single maintained temperature, and hence fluid property. In order to accomplish this, the chosen range of component velocities used were between 1 to $3m/s$ for oil superficial velocity, and between 0.4 to $3m/s$ for gas superficial

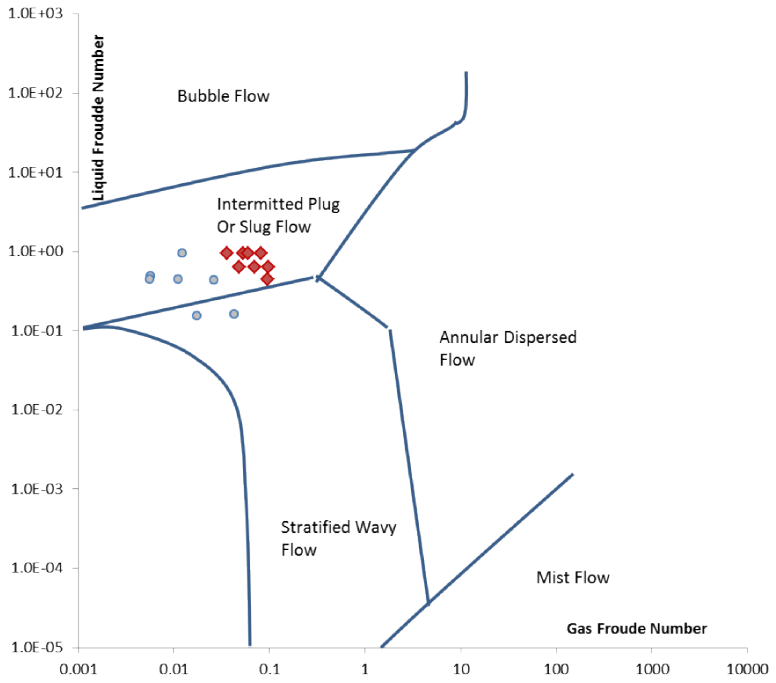

Figure 4.3: Horizontal flow map based on Shell DEP 31.22.05.11 [22], with blue data points displaying the specific data points used in this work.

velocity. This is outlined with respect to the points located on the flow regime map portrayed in Figure 4.3. These test points represent the reduced data from the experiment, although other test points were conducted, they will not be considered here as they are beyond the scope of this study. For each test point, the correct flow rates of oil and gas were applied using the flow loop control PC, once achieved and settled, the system was maintained for around 1minute prior to conducting the measurement to ensure consistency.

4.1.5 *Experimental setup 2 - vertical two-phase flow with heavy oil*

4.1.5.1 *Overview*

The second experiment was conducted on the same flowloop at NEL as the experiment described in the previous section, with the main difference being that the orientation of the test section (mounted with the ECT sensor) was changed from horizontal to vertical. This test section and the flowloop are portrayed in Figure 4.4, with the ECT sensor installed, and the separator in the background. The test section itself, is of the same composition and size as that described in Section 4.1.4. For these tests, due to the nature of the fluids used and only the requirement for oil and gas flow, the water within the gravity

Figure 4.4: ECT sensor installed on a vertical sight tube test section on the NEL multiphase flowloop.

separator system was removed, hence the new system schematic can be seen in Figure 4.5.

4.1.5.2 *Flow loop instrumentation*

The instrumentation used in this experiment is comparable to the Experimental set-up 1 except for slight modifications to account for the heavy oil used. The most significant change is that of the reference flowmeters. Turbine flow meters were used, as previously, for the reference measurement of the nitrogen phase, whereas for the oil phase, Coriolis reference meters were used instead. Other than this, the stated capabilities outlined in Section 4.1.4 hold for this set-up, with the exception of a reduced maximum oil flow rate, due to the creation of high stresses on the component from the high viscosity fluid.

4.1.5.3 *Fluid properties*

For these experiments, the oil used was Regal 460, considered a "heavy" oil with a stated density $\rho_l = 896.1 kg/m^3$ and dynamic viscosity $\mu_l = 412 cP$ when tested at 40°C. Nitrogen was again used for the gas phase, with relevant properties described in the previous section. During these tests, two different line temperatures were tested to provide results for changing the viscosity of the oil. The first set of

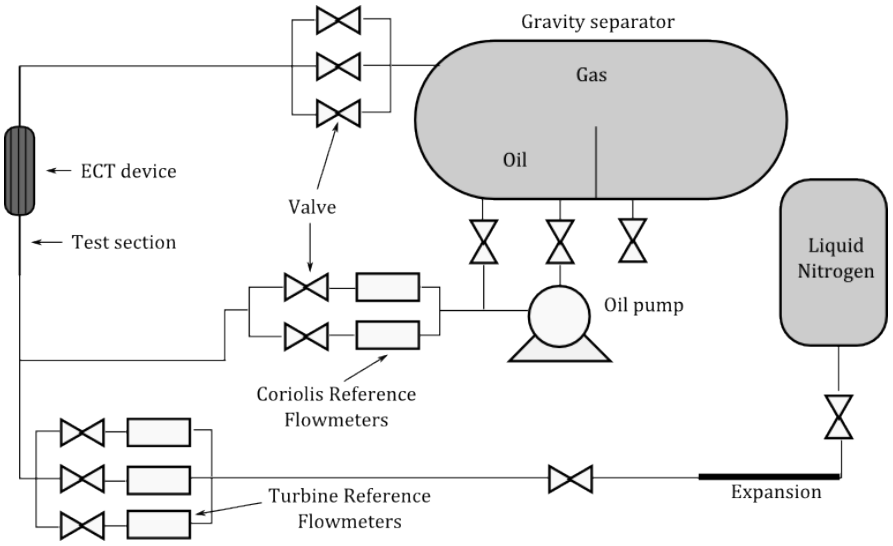

Figure 4.5: Schematic diagram representing the multiphase flowloop at NEL with a vertical test section.

tests were conducted at a temperature of 23°C, which produced an oil viscosity of around 1500cP. After this, the temperature was increased to 32°C, which subsequently gave an oil viscosity of around 1000cP, and the tests were repeated. The change in oil density with respect to line temperature was neglected as the change was minimal.

4.1.5.4 *Tests conducted*

The objective of these tests was to sample both annular and slug flows, and by increasing the line temperature and repeating the tests, the comparison can be made from two different viscosity conditions. The range of phase superficial velocities used were: between 0.23 and 6.15m/s for oil, and between 0.784 and 32.68m/s for gas. The test points are illustrated on the flow regime map for vertical flows, in Figure 4.6 (red data points were conducted but not used in this work). As in Section 4.1.4, each test point was achieved using the control PC and maintained for 1 minute prior to measurement to ensure consistency.

4.1.6 *Experimental setup 3 - bubble column - lab scale flow*

4.1.6.1 *Overview*

The final experiment was conducted on a 3 phase lab-scale, vertically orientated flow loop. The flow loop is depicted in Figure 4.7, and a schematic diagram of the entire flowloop is portrayed in Appendix C. The test section used was the smaller section with an internal diameter of 80mm and length of 1.41m, constructed of transparent

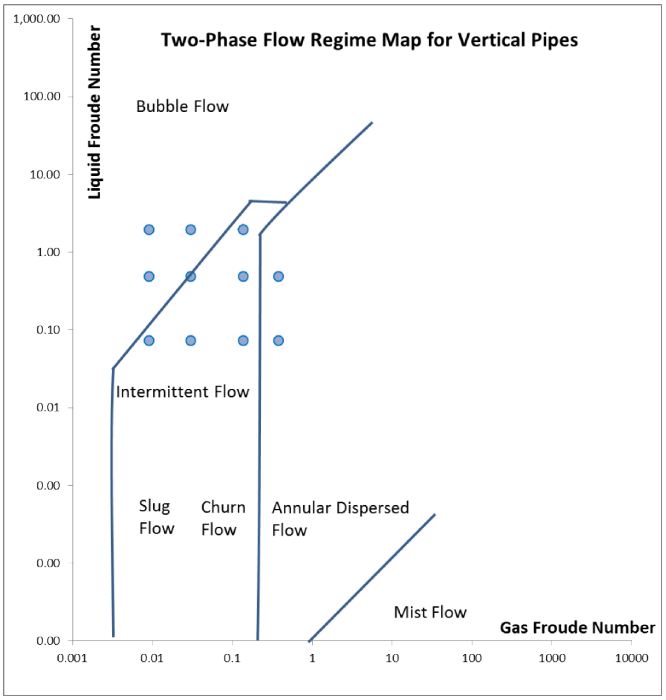

Figure 4.6: Vertical flow map based on Shell DEP 31.22.05.11 [22].

Acrylic. Despite the system being capable of delivering oil, gas and water, only two phase oil gas flows were used.

4.1.6.2 *Instrumentation*

The flow loop consisted of a centrifugal pump for oil delivery, with a maximum head of $35m$, maximum flowrate delivery of $35l/min$ and a maximum liquid operating temperature of $40°C$. As for the reference flowmeters, for the measurement of compressed air, a thermal flow speed sensor was used with an overall accuracy of $+/-3\%$, with an operating flow range of 0 to $200l/min$, and a gas temperature range of -10 to $60°C$. As for the oil reference flowmeter, rotary vane type meters are used to monitor oil flow. Along the test section, multiple pressure transducers, along with a single differential pressure measurement, allowed pressure profiles to be obtained; these transducers have an operating range of $0-3bar$. The rate at which fluids were delivered to the test section was controlled via variable valves, which could be controlled through the flowloop PC.

4.1.6.3 *Fluid properties*

The gas phase used in this experiment was compressed air and therefore properties at standard conditions are used to describe it. As for the oil phase, a clear silicone oil was used (SeraSense SF2), specifically a synthetic fluid called Dimethicone. The viscosity of this oil is given as $2cSt$, at an operating temperature of $25°C$, and a specific gravity of

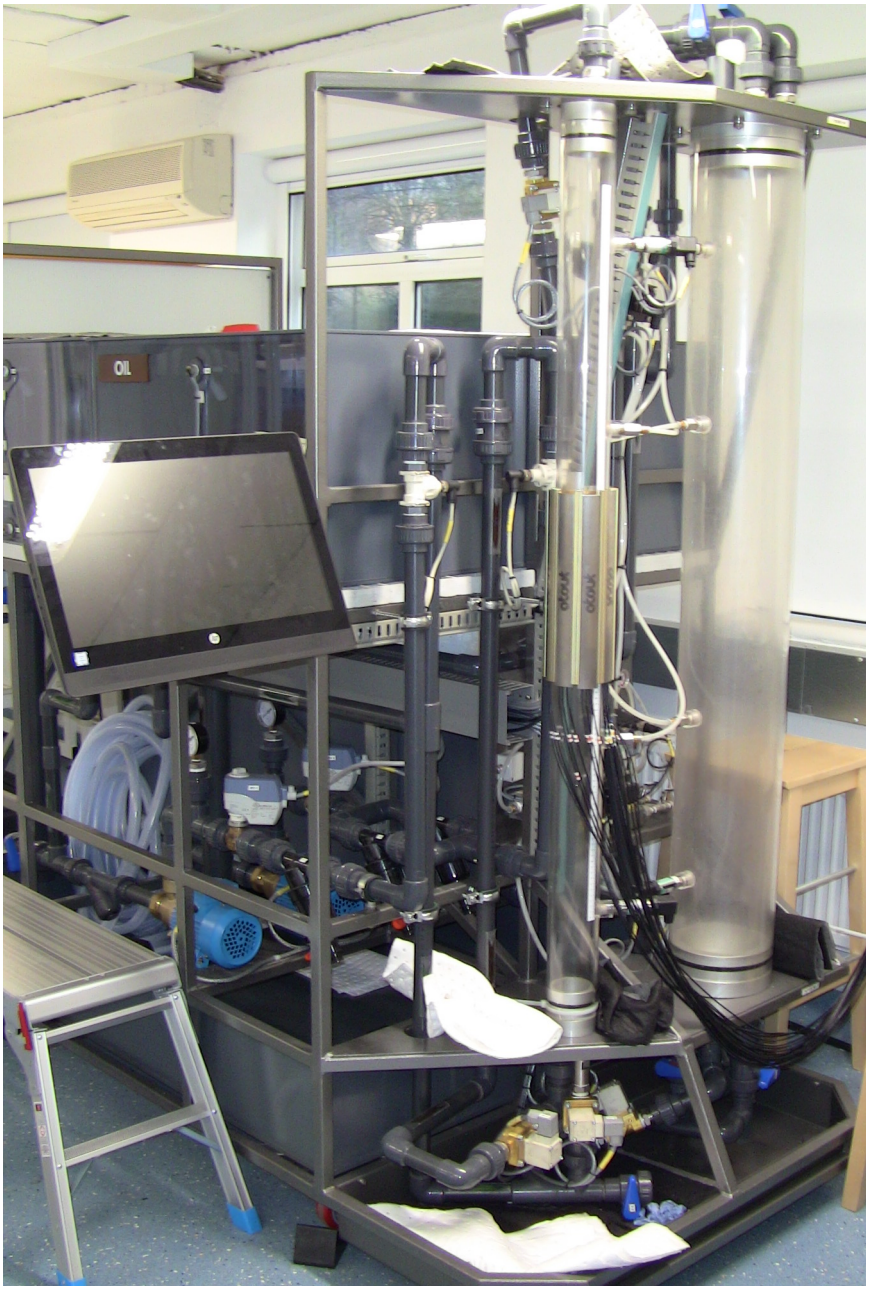

Figure 4.7: 3-phase flowloop at Coventry University with ECT sensor installed.

0.873 at the same condition. The surface tension of this oil is stated as: $18.3mN/m$. The manufacturer provided datasheet for this oil is included in Appendix E. The tests were conducted at room temperature as the flowloop has no temperature control, therefore the provided fluid properties are used for definition.

4.1.6.4 *Tests conducted*

Tests were conducted on this flowloop using a range of both gas and oil flowrates. However, the data collected for use in Section 5.3, for purposes outlined there, only applied a gas flowrate. The entire test section was initially filled with oil, once complete, gas was applied at different rates and data collected. The gas flow range for these experiments ranges between a gas superficial velocity of $0.0435m/s$ and $0.2675m/s$. For each test point, the designated valve position was set, the flow was allowed to settle by observations of the reference flowmeter reading, then subsequently around 1 minute of data was measured by the ECT system, and finally the reference flowmeter data was outputted.

4.2 ECT SYSTEM - DEPLOYMENT AND CALIBRATION

For all the experiments described in the previous section section, an ECT device was deployed on the relevant test section and thus was used as the measurement device for the studies. This section provides a description of the main measurement instrument (ECT), along with operational procedures undertaken in the previously mentioned experiments and subsequent data analysis.

4.2.1 *Overview of system design*

The ECT system can be categorised into three main components. Firstly, the sensor head, consisting of the concentric electrodes and supporting frame which can be clamped onto the pipe test section, where its circumference can be adjusted via tightening screws, to allow the sensor head to fit a reasonable range of pipe diameters. Secondly is the capacitance measurement system, attached by cables to the individual electrodes on the sensor head, which provides the voltage to the electrodes and hence interprets the measurement at each point in time. Finally, the capacitance measurement system is attached to a control PC, where bespoke software for the instrument allows both data collection along with data analysis. Table 4.1, gives a technical summary of the sensor itself, whereas Table 4.2 gives a technical summary of the capacitance measurement system. The electrode laminate material used is a GTS77012ED copper polymide

Property	Value
Type	APL-S-SL-140
Nominal sensor I.D	0.14m
Number of measurement planes	2
Number of electrode segments	8
Total electrically guarded length	0.225m
Axial length of measurement electrode	0.032m
Axial separation of measurement planes	0.068m

Table 4.1: Technical summary of the ECT sensor.

Property	Value
Type	TFLR5000
Capacitance measurement range	6fF - 400fF
Maximum image capture rate	1500 fps
Measurement resolution	< 0.1fF
Measurement noise level	< 0.03fF RMS
Communication	Ethernet
Excitation frequency (square wave)	2.5MHz

Table 4.2: Technical summary of capacitance measurement system (data acquisition hardware).

(Kapton), with a 50 micron film of plastic, coated with a copper layer of thickness 35 microns.

4.2.2 *Deployment*

The ECT sensor was attached to the exterior of the relevant pipe test section. This included removing the screws at two opposite locations on the sensor, allowing it to be split in half. Once achieved, the sensor was clamped into place by re-inserting and tightening the screws once placed on the pipe section. From here, the remaining screws were adjusted, if required, to ensure that the electrodes are equally spaced concentrically around the pipe. Once complete, the sensor head was attached to the ECT measurement system via three connecting wires for each electrode (two measurement, one guard), which was then connected to the control PC via an Ethernet cable.

4.2.3 *Calibration*

The calibration procedure for the ECT system is relatively simple, and involved taking a controlled reference measurement of the pipe when it was full of high permittivity material (oil) , followed by the same process for the low permittivity material (gas); the low permittivity calibration was conducted first, as the process of removing oil from the pipe, which would have a detrimental effect on the calibration, adds difficulty to the process. Once the pipe section was filled with the relevant material, the bespoke ECT software (Sensor Toolkit) provided by Atout Process Ltd. allowed a measurement to be taken and averaged over a short time period (~5 sec), which ensured that the calibration data was not affected by small inconsistencies in the fluid within the pipe. A summary of the output from the calibration of the 3 experiments is displayed in Figure 4.8, and the raw calibration data is provided in Appendix D.

4.2.4 *Correlation zone maps*

When analysing tomographic data using the post-processing software (Flowan) provided by Atout Process Ltd., the two main variables which can be assessed, being the phase fraction data and the obtained cross-correlation velocity, can be localised to certain areas of the cross-section by the use of correlation zone maps. These correlation maps define different areas within the cross-section and can be user-defined to take a variety of different shapes and sizes, some of which are displayed in Figure 4.9. These zones can then be used to analyse the phase fraction or cross-correlation data specifically in the defined area. This therefore allows more intuitive information to be gained. For instance, inter-facial waves in stratified wavy flows can be focussed

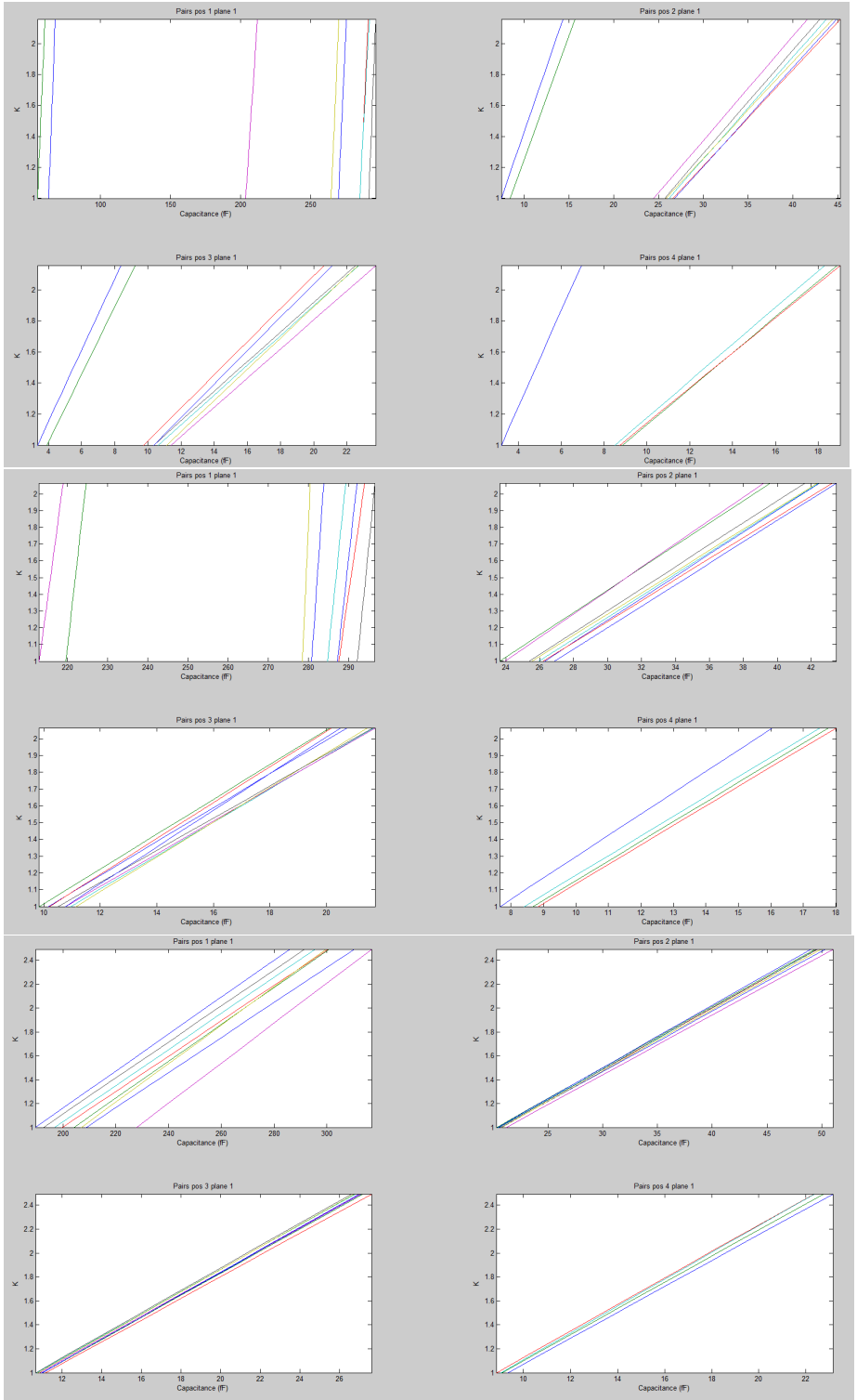

Figure 4.8: Summary of ECT calibration showing capacitance-permittivity relationship based on electrode pair position. For experiment set-up 1 (top), 2 (middle), and 3 (bottom).

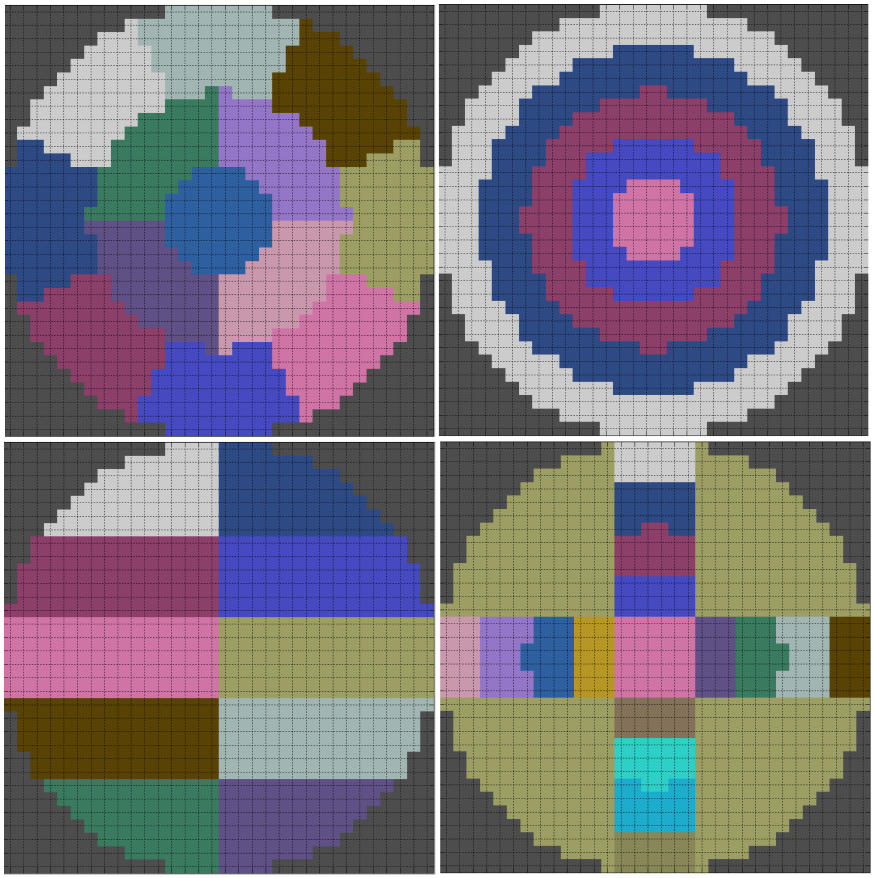

Figure 4.9: Examples of pre-defined correlation zone maps available in the Flowan software for localised analysis, where different coloured areas represent different zones.

on by using a stratified zone map covering the fluid interface. Gas entrainment can be isolated from the main gas body by applying a zone map which only includes the liquid body of interest, and the velocity of a passing liquid slug can be measured along an axis, providing a velocity profile, by defining multiple correlation zones along this axis which matches the liquid motion change along the aforesaid axis.

4.3 SUMMARY

By conducting tests for three separate experimental set-ups, a diverse range of data was achieved. This included both industrial scale data, providing flows which are directly comparable to those faced in the oil and gas industry. Along with laboratory scale data, which being more accessible and easily repeated, allowed the more complex methods to be applied to it. Furthermore, these experiments included both horizontal and vertical test sections, providing a greater span of flow types and hence better represented the range of flows encountered in

industry. Finally, the oil types used included a light oil, as typically applied in laboratory scale tests, a typical mid-range oil and a heavy oil which better represents those encountered in oil fields. This diversity in fluids used added to the applicability of the methods applied to these experiments.

The next section outlines the main studies undertaken during this work. This incorporates the knowledge taken form the literature survey, and the data gained from the experiments outlined here, and attempts to apply new methods in determining the phase flowrates in multiphase flows from the use of ECT.

5

FLOW REGIME INDEPENDENT TOMOGRAPHIC FLOW MEASUREMENT

This Chapter outlines the main studies conducted in this work to answer the questions posed both in the stated research questions, and specifically those outlined in the summary of the literature review. This chapter is structured in the following way, with regards to the three studies undertaken:

5.1 Proposal of a method to link slug and annular flows via similarities in inter-facial wave properties, allowing flow measurement of annular flow data.

5.2 Development of cross-correlation flow metering for slug flows by measuring selectively, based on differences identified between slug front structures.

5.3 Implementation of a particle filtering system, using ECT and a CFD model to determine the gas flowrate in a two phase flow system.

For each section, a justification with regards to its application to the overall scope of this work will be given, along with its specific application to a FRIMM system.

5.1 SIMILARITIES WITH INTER-FLOW REGIME WAVE PROPERTIES

5.1.1 *Justification*

To provide a single multiphase flow measurement system, one of the most crucial aspects is the requirement to operate on any flow regime that occurs. For tomography, the difficulty varies depending on the specific flow regime in question. Referring to Chapter 2, it can be said that the accurate metering of slug flows is more achievable currently than annular and stratified-wavy flows, due to the limitation of measuring the interface wave properties in segregated flows. Therefore, the measurement principle applied to segregated flows by ECT must be developed in line with what is achievable for slug flows, by incorporating a more complex methodology.

The main issue encountered in annular and wavy flows, as demonstrated in Section 2.5.1, is the reliance on wave property correlations. The correlations lack the accuracy potential seen in the slug translational velocity correlations for slug flows, but more importantly, they are highly unstable with respects to system and fluid properties. Furthermore, the correlations are better suited for obtaining the gas superficial velocities, whereas the liquid superficial velocities are difficult to recover within a reasonable accuracy. For this reason, the reliance on conventional wave property relations would not suffice in allowing tomographic measurement for these flows, due to the large amount of correlations and their parameters required to cover the flow ranges encountered in the oil and gas industry. Such a requirement would mean unprecedented testing prior to meter installation and would thus undermine any attempt to create a general purpose, self-reliant multiphase meter. This issue would be a particular problem in terms of fluid properties such as viscosity, where its effect on correlation accuracy is prevalent [46] and the required test range would be untenable.

5.1.2 *Application to FRIMM*

For the reasons outlined in the previous section, a new methodology is required for annular and stratified-wavy flows, in order to provide a flow regime independent metering system. The method proposed in this study is to use information from flows which are susceptible to tomographic flow measurement (slug), that have been previously measured with the device, in order to assist the measurement of flows which are less susceptible to this form of measurement (annular, stratified-wavy). This concept is outlined in Figure 5.1, where the primary state represents the phase flowrates (or phase superficial velocities), which can be directly measured for slug flows. In order to

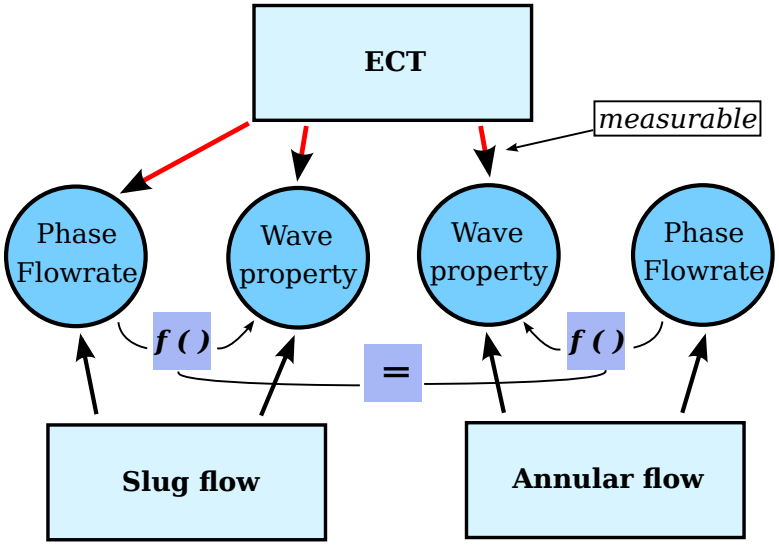

Figure 5.1: Diagram representing the proposal of comparing wave properties between slug and annular flows to assist in measurement.

measure the primary state for annular flow, we assume that the relationship between a wave property (secondary state) and the primary state are equal for both annular and slug processes. To achieve this, the first milestone is to find a distinctive similarity between the susceptible and non-susceptible flow regimes, with the wave properties proposed as a suitable candidate. If achievable, then such information can be utilised to update the parameters of certain correlations, allowing not only the self-derivation of correlations, but also creating an environment where the correlations used can adapt to certain conditions; for instance with a measured temperature of the flow, related to the liquid viscosity. In this case, over time, the metering device can reference the most suitable correlation from the current state of the system, and apply it to annular and stratified-wavy flows. Finally, it is reasonable to assume that this could integrate some machine learning principles and algorithms as a way to implement this methodology, although this is not necessarily the focus of this study, but may be used in future developments. This therefore would allow this system to be applied successfully to segregated flows, without the reliance on empirical correlations.

5.1.3 *Method*

To collect the necessary data for this study, the multiphase flowloop at NEL is used as described in Section 4.1.5. This provided flows at a range of phase velocities covering both slug and annular flow regimes in a vertical pipe. As well as this, the tests were repeated at a different temperature to provide a comparison for measuring two distinct oil viscosities, high viscosity in particular. Prior to the

experiments, the ECT system described in Section 4.2, was firstly installed and calibrated, as outlined in Sections 4.2.2 and 4.2.3. For each test point, the ECT measurement system recorded around 1 minute of raw capacitance data from each electrode pair at around 1400 fps, and logged them to the control PC; once the data is checked to ensure no significant error occurred, the process is repeated for the next test point.

After the raw capacitance data has been collected for each test point, the data analysis stage is conducted offline using the sensor software. The first stage in the analysis is to differentiate between flow regimes for each data set. Although this could be carried out with reference to the flow regime maps depicted in Section 4.1.5, the effectiveness of ECT imaging in providing fluid structural information, using the images themselves, is a much more effective means to distinguish each data set. Once complete, the main data can be extracted from each test point. Firstly, the phase fraction data change with time is extracted, requiring only the input of the permittivity ratio between the two fluids, in this case ~2.6. For the annular flow points, this is a simple average of all data points, whereas for slug flow, it is specifically within the annular region, which will be discussed further. Secondly, the cross-correlation velocity of the inter-facial disturbance waves must be obtained, which requires more information. In order to recover the most representative cross-correlation measurement, a correlation zone map must be chosen which isolates the appropriate area within the cross-section. For both flow regimes, a single correlation zone map is selected which satisfies this criteria. This consists of a central core zone, which isolates the area where the liquid body occupies when a liquid slug passes the sensor, excluding the liquid annulus. This is then surrounded by multiple rings, which specifically capture the area covering the fluid interface where the waves occur. By having multiple ring zones, the appropriate zone can be selected regardless of the size of the oil annulus; this correlation zone map is portrayed in Figure 4.9.

Once the correlation zone map is selected, the cross-correlation parameters are chosen. For the annular flow test points, it is advantageous to obtain a single averaged value for each test point, on the basis that the flow is stable (achieved through the sufficiently long flow loop). For this reason, a relatively large integration window is selected ($\sim 1.5s$) which is long enough to achieve a stable value, but short enough to detect significant changes if they occur. For the slug flow tests, this integration window may require shortening slightly to ensure that the annular sections of the flow (when a gas slug is present) is sufficiently isolated from the liquid slug front, as the disturbance waves that occur during the annular regime are the focus for this study. This procedure overall, produces both the phase fraction as a function of time and the average correlation velocity of the disturbance waves, for both slug and annular test points.

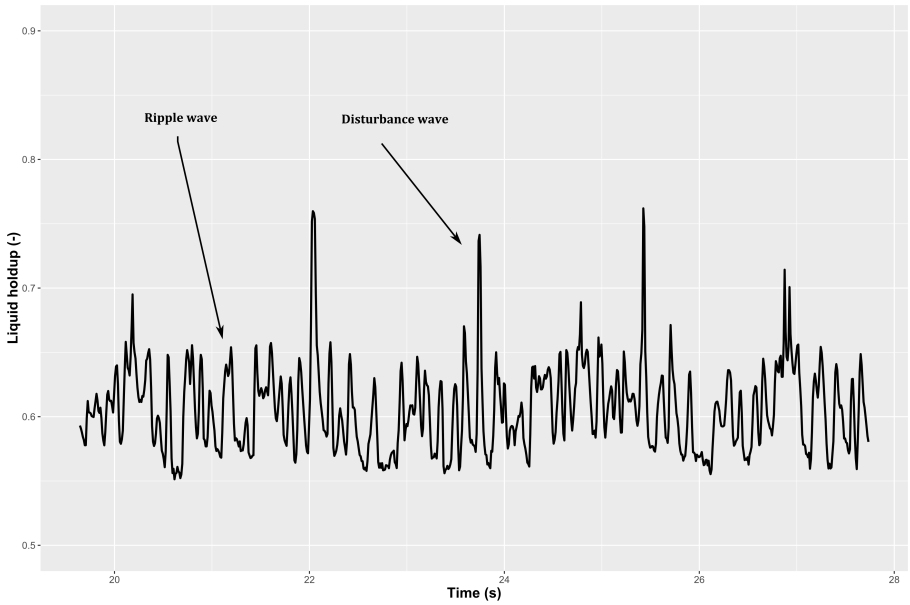

Figure 5.2: Example output from ECT of liquid holdup over time, for an annular flow test point, outlining the difference in ripple and disturbance waves.

From here, the objective becomes finding a suitable relation which applies to both annular and slug flows, linking the wave properties and the flow properties. This relation must show minimal disparities between changes in phase flowrates (both liquid and gas), as this would be required to ensure the method can be applied to any flow range. However, disparities from changes in the liquid viscosity are acceptable, as over time, and with the inclusion of temperature measurements, the relation parameters can change. The final stage requires the use of only the slug flow data (which can be obtained through other measurement methods), to derive the parameters for the relation. These parameters can then be used to predict the flow properties for the annular data, and hence the obtainable accuracy can be analysed.

5.1.4 *Results*

By observing the raw phase fraction data, obtained for both the annular and slug flow points, we can ensure that the disturbance waves, those of which velocities we want to measure, exist for both annular and slug data. Figures 5.2 and 5.3, display an example output for both annular and slug flows.

For annular flow, Figure 5.2 clearly distinguishes between ripple waves, with a small amplitude and high frequency, and disturbance waves, with a high amplitude and lower frequency. For this study, the velocity measured through cross-correlation will reflect the wave speed of disturbance waves only. This is due to the fact that they

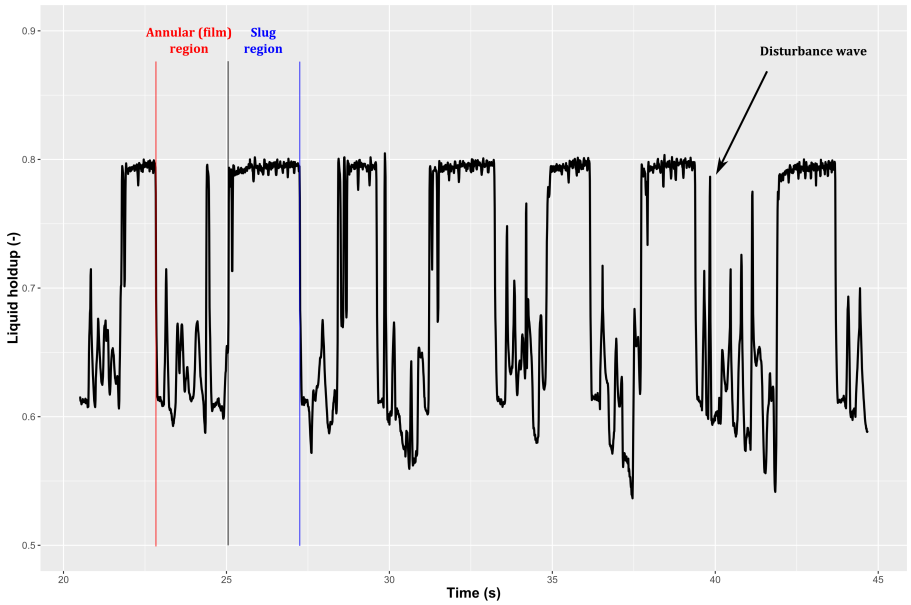

Figure 5.3: Example output from ECT of liquid holdup over time, for a slug flow test point, outlining the two defined regions and an example disturbance wave.

are susceptible to cross-correlation as they are distinct and stable, compared to ripple waves which are far harder to correlate; for this reason, the results from cross-correlation, considering the size of the integration window, will reflect this, which would not be true if it was reduced significantly. Furthermore, ripple wave properties have not yet proven to provide useful and stable information on the flow, due mainly to not appearing to carry mass [100] and being short lived [112].

For the slug flow data in Figure 5.3, it can be seen that we must distinguish between periods where the cross-section is effectively full of oil (oil slug), and when it appears that the flow structure is the same as for annular (film region). By focussing on the annular film region, we can make the comparison between the annular and slug data, on the basis that they are linked, with the main difference that for slug flows, the Kelvin-Helmholtz stability criteria has been reached [35]. The data shows the same behaviour in the annular film region as previously seen for annular flows, with a distinct difference between ripple and disturbance waves. It is important to note that there are fewer disturbance waves in the slug flows, and hence less data to work with, though it could be argued that the oil slugs themselves could be included as they are themselves developed disturbance waves.

For interpreting the phase fraction data, assuming that it is advantageous to obtain a single value for each test point, some consideration must be given to the effects of simple averaging, considering that the frequency and amplitude of disturbance waves and oil slugs would increase this average value regardless of the remaining data points. In

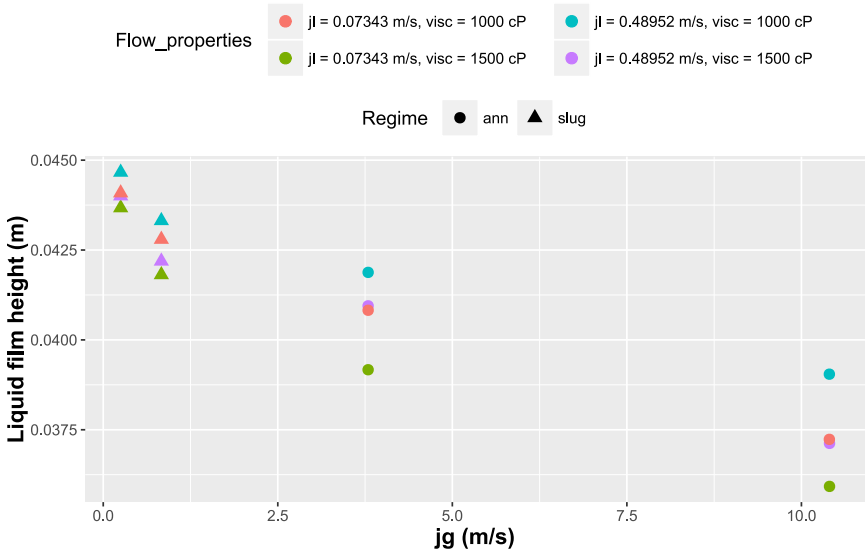

Figure 5.4: Effect of gas superficial velocity on the liquid film height, for annular and slug data for two separate liquid superficial velocities.

order to counter this effect, and provide a simple and quick method of providing a phase fraction value, representative of the liquid film, the following threshold is set, as used by Zhao et al. [132], for the liquid holdup α_l:

$$\alpha_{l,thresh} = \frac{1}{2}\left(max(\alpha_l) + min(\alpha_l)\right) \tag{5.1}$$

on top of this, due to the axis-symmetric nature of annular flow, the liquid holdup, or phase fraction, can be simply converted to a liquid film height (H), which has been successfully used in other work [46, 132].

5.1.4.1 *Wave velocity*

The first result is to compare the liquid film height to the measured gas superficial velocity, obtained from the reference flowmeters. This is carried out for both annular and slug flow points in the same graph, displayed in Figure 5.4. The results suggest that the comparison between slug and annular flows can be made, although if assuming a linear relation, it can be said that the film height reduces at a greater rate with gas superficial velocities when considering slug flows as opposed to annular. However, one can also suggest that a non-linear relationship could be used to compare the results, independent of flow regime. This suggestion will be assumed for the basis of this work, though a finer resolution of data points, especially close to the flow regime transition zone would be desirable to confirm this. As for liquid superficial velocity, an increase does not affect the overall

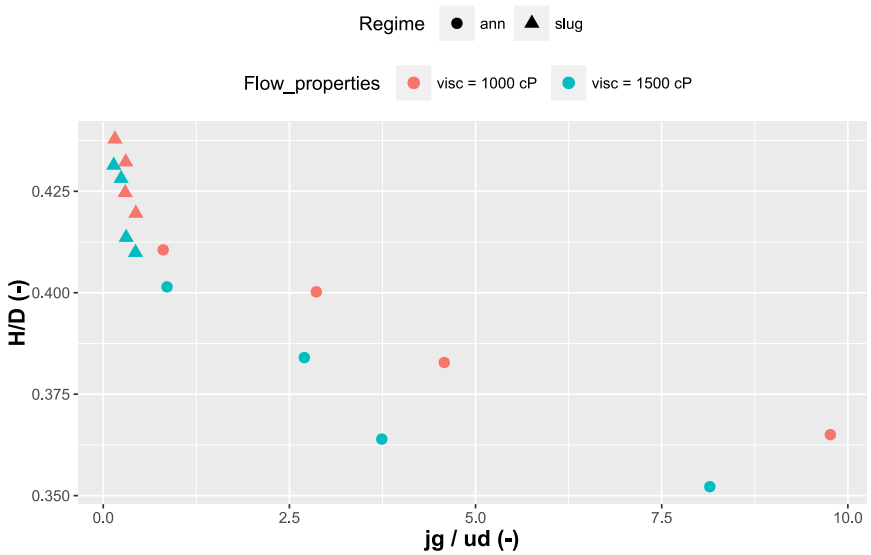

Figure 5.5: Relationship between normalised liquid film height and normalised wave velocity, for slug and annular data.

trend, though it shifts the data points higher, showing a general increase in liquid film height with increased liquid superficial velocity, as is expected when compared to the work of Waltrich et al. [119]. Furthermore, a decrease in viscosity seems to have the same effect, and can also attribute to a reduced correlation between slug and annular test points.

The previous data can be developed further by introducing the disturbance wave velocity. The purpose of doing this is to reduce the disparity caused by the difference in properties, by the assumption that the disturbance wave velocity is related to said properties. In this case, the superficial gas velocity is normalised by the disturbance wave velocity, and for completeness, the liquid film height is normalised by the pipe diameter; the results for this are shown in Figure 5.5.

The data suggests that the assumption made previously is justified. The effects contributed by different liquid superficial velocity has reduced significantly, leaving the main distinguishing factor as the liquid viscosity. Although a small difference can still be seen for the two superficial liquid velocities, it remains minimal, despite the fact that the velocity difference is relatively large (referring back to Figure 5.4).

5.1.4.2 *Wave Frequency*

Considering now the relation between disturbance wave frequency and flow parameters. The frequency measurement for the flow data is calculated manually by counting the total number of disturbance waves in each data set, divided by the total time. For the annular data points, this procedure is simple, for the slug flow data, only the

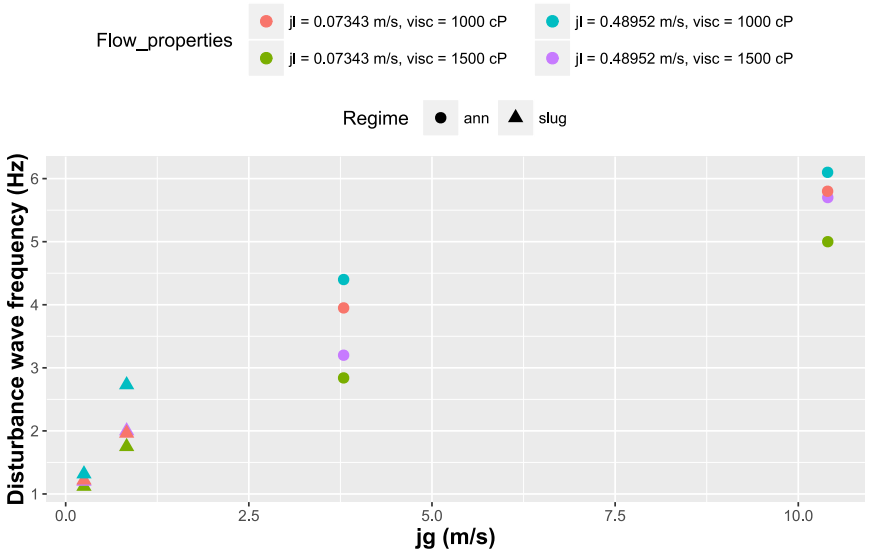

Figure 5.6: Relationship between disturbance wave frequency and superficial gas velocity, for slug and annular data.

annular regions are considered, hence the annular region disturbance waves are counted and are then divided by the total annular region time of each slug flow data set. Figure 5.6 displays the result of this compared to gas superficial velocity.

As expected, from comparison with other studies [101], the disturbance wave frequency increases with increasing gas and liquid superficial velocity and decreasing liquid viscosity. As seen previously in the results from Figure 5.4, this relationship is clearly a function of liquid superficial velocity from the apparent differences displayed, and hence must be developed to mitigate the effect. By referring to Eqs. 2.22 through 2.27 in Section 2.5.1, we can test other relations which include disturbance wave frequency, as well as wave velocity, to attempt to improve on this. This starts with the assessment of Strouhal number with respects to: the Lockhart-Martinelli parameter (X), and the modified Froude number, as depicted in Figures 5.7 and 5.8.

The results from Figures 5.7 and 5.8 show a mixture of performances. Firstly, Figure 5.7 displays the relationship between Strouhal number and the Lockhart-Martinelli parameter (X). The most striking feature of this graph is the minimal effect of viscosity, with only a small increase in Strouhal number for lower viscosities. This is somewhat surprising considering that there is no explicit viscosity term in the formulation, though this could be somewhat explained considering that the inclusion of liquid superficial velocity and phase densities could contribute in lessening the effect on the overall result. It is also clear that, the effect of liquid superficial velocity is prevalent, where two significantly separate trends are observed, which would render this relation unfit for the proposed method, as the additional variable

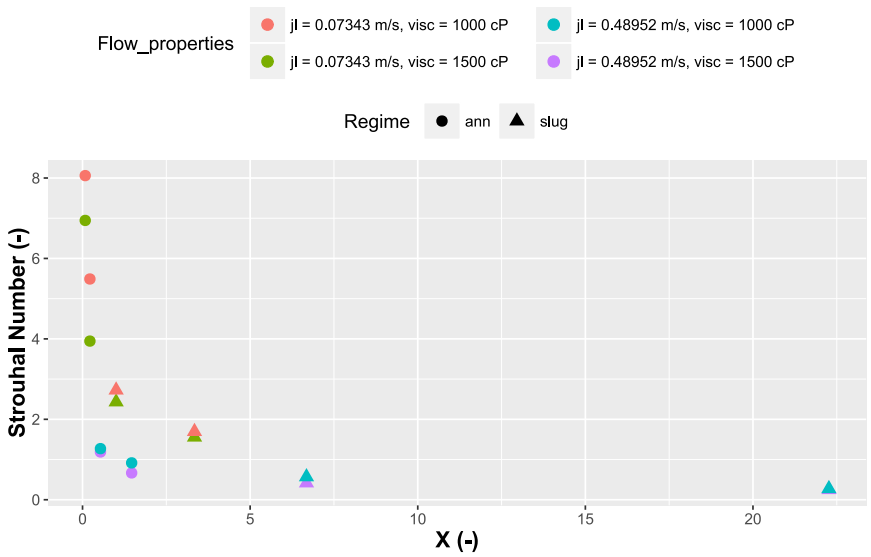

Figure 5.7: Relationship between Strouhal number and Lockhart-Martinelli parameter, for slug and annular test points.

Figure 5.8: Relationship between Strouhal number and the modified Froude number, for slug and annular test points.

would be required to be supplied from the slug flow data; making the number of data points initially needed too large. Despite this failing, the relation between slug and annular points on the graph show a reasonable relation, though the function itself would be too sensitive to changes in the Lockhart-Martinelli parameter (X) to predict an appropriate trend (especially considering data at the lower liquid velocity).

Considering now Figure 5.8 and the relationship of Strouhal number and the modified Froude number, a more optimistic result is present. The result clearly shows that, overall, the data is much tighter in terms of all data points than the previous results. The main differences in the data in this result is between the different liquid viscosities, which is far more desirable for the proposed method as the databased slug data could easily account for changes in viscosity by referencing the temperature. The differences with respect to liquid superficial velocity are noticeable, though remain small and would not pose a significant problem if the same trend was applied to both data types. Furthermore, not only do the slug flow points seem to have a power law relation to the annular flow points, but the trend does not suffer the same sensitivities compared to that of the previous results. This relation is therefore a suitable candidate for the proposed method due to the fact that the effect of liquid superficial velocity has been reasonably reduced and the inter-flow regime trend is relatively stable.

5.1.4.3 *Prediction of annular flow data from slug flow data*

We now progress to the next stage of assessing the proposed method, by using the two relations deemed appropriate (normalised wave velocity- normalised wave height in Figure 5.5, and Strouhal number - Modified Froude number in Figure 5.8). This consists of firstly, using only the slug flow data points (where the critical flow parameters are achievable through other conventional means of measurement), to produce the parameters for a power law relation in the chosen formulations. Once obtained, the newly developed power law approximation can be used, alongside the annular wave properties, to predict the gas superficial velocity for the annular flow data points. Beginning with the prediction of the normalised waves speed, from using the slug flow data points only, the following approximation is derived using the logarithm of the data.

$$\frac{j_g}{u_d} = 4.47 \times 10^{-8} \left(\frac{H}{D} \right)^{-17.238} \tag{5.2}$$

Now using this power law relationship, we can predict the normalised wave speed for the annular flow points, as shown in Figure 5.9.

The result shows a prediction within $+/-50\%$, with a relatively consistent variation for the range of normalised wave velocity values. Although this achieved accuracy is relatively large, it is important to

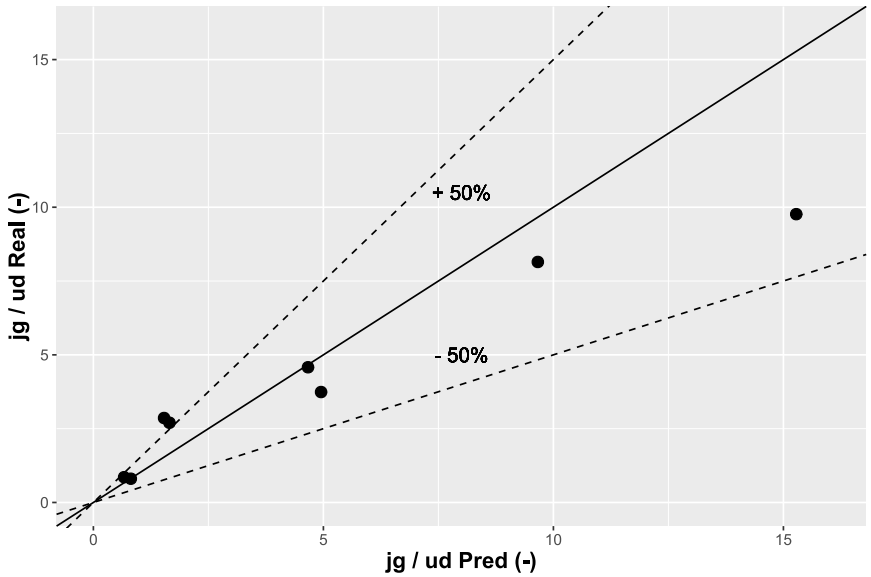

Figure 5.9: Prediction of dimensionless wave velocity from correlation produced solely from slug flow data.

remember that this reflects what is achievable for any flow variation that may be encountered, assuming that sufficient slug flow data points have been attained previously. Therefore, although accuracy is low, the method is somewhat robust in comparison to a single correlation which would potentially deviate more when confronted with large flow variations such as viscosity.

Continuing now to the prediction of the Strouhal number. As before, the power law approximation is derived from the slug flow points only giving:

$$Sr = 6.2244 \times 10^{-3} \left(Fr_{mod}\right)^{-0.5445} \tag{5.3}$$

again using this relationship, the Strouhal number for the annular flow points is predicted, as shown in Figure 5.10.

As seen previously, the power law approximation predicts the Strouhal number with a similar accuracy, this time well within $+/-$ 50%. In this case, the approximation does seem better in its performance when compared to that of the normalised wave velocity, this is likely due to the lower effect of liquid superficial velocity on the trend for predicting Strouhal number, though more data would likely be required for confirmation. Despite this, it is likely most productive to use both of the relations combined as opposed to the one that performs highest, as in this case the measurement would incorporate both the wave velocity and the wave frequency, and hence may provide benefits for flow cases where a certain measurement may be compromised.

The result of this work so far has provided an estimation of the superficial gas velocity from the annular flow data, incorporating knowledge from the slug flow data, within $+/-$ 50%. However, not

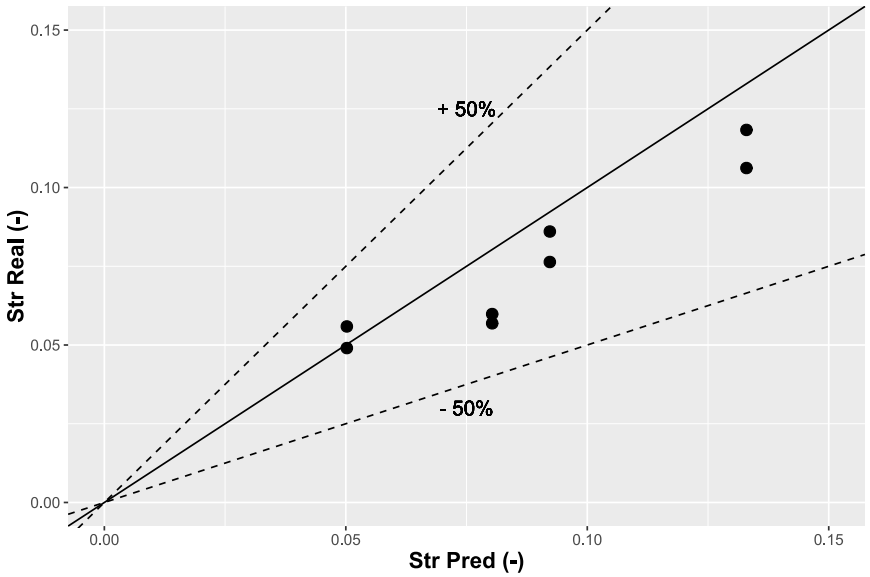

Figure 5.10: Prediction of the Strouhal number from correlation produced solely from slug flow data.

only does this achievable accuracy require improvement, it does not take account of the liquid superficial velocity, which would also be required to satisfy the flow measurement criteria.

5.1.5 *Discussion*

From the results of this study and the application of the proposed method we can deduce the following. Firstly, through the relationships displayed in Figures 5.4 through 5.8, the stable trends which were produced, and their similarity to results from other researchers [132, 101], we can state that the application of the current ECT system is a viable technique of measuring wave properties for vertical annular and slug flows. This is particularly the case for the wave velocity, which was seen to be stable and reproducible for all the tests conducted, due to the high resolution of the disturbance waves produced from the high temporal resolution attainable through this particular ECT system. However, though acceptable, not such a high level of reliability is achievable for the disturbance wave frequency. The reason for this is firstly with regard to the length of the data set used. For a real time system, the time frame may cause complications with respect to its selection, as too long a time frame may cause the system to be less sensitive to changes, or even data storage/computational issues, whereas too short a time frame may produce unrepresentative results; this is particularly problematic for slug flows, where the annular film region restricts the length of the considered data. Secondly, the identification of disturbance waves causes more issues with wave frequency, compared to wave velocity, as the velocities tend to be

similar, though the effects of a wrongly identified disturbance on the overall frequency calculation can be higher. Despite this, the results indicate that the current method is reasonable for obtaining both these properties.

For the relationships tested, it was found that the correlation between both normalised wave velocity and normalised wave height, as well as Strouhal number and Modified Froude number were viable in producing trends which differ in terms of viscosity, but not liquid superficial velocity. Both relationships showed a possible power law relationship between slug and annular data points, however, other researchers such as Zhao et al. [132], have suggested that they are in fact separate linear relationships, and furthermore, state that the observed differences in gradient is lessened at lower viscosities. This may in fact be the case and would require further testing, particularly at the transition region between slug and annular flow to determine this, though it is noted that the unstable nature of data at this transition period could in fact hinder reliable measurements.

Considering the achieved final accuracy of predicting the phase superficial velocities in this study, it can be reasonably assumed that such a method could be successfully applied to both annular and stratified-wavy points in both horizontal and vertical flows, given that the relationships are tested to ensure their individual applicability. The prediction method could never realistically be applied alone, as the inaccuracies are simply too large, and any attempt to predict the liquid superficial velocities using drift flux correlations would also fail to satisfy measurement requirements. However, by applying an additional method, based possibly on machine learning principles, it may be possible to improve on this. The main benefit of using this self-deriving correlation method is with respect to its flexibility. Over time, when the flow changes, as well as the possible addition of temperature measurements for example, the correlation parameters can change to suit flow properties such as the liquid viscosity presented here. This is particularly useful for high viscosity flows, where correlations fail significantly to model the changes. Therefore, although the accuracy of this method is limited currently, it represents an alternative strategy to the flow measurement of segregated flows with tomographic instruments.

5.2 SLUG FLOW STRUCTURES AND SELECTIVE TRANSLATIONAL VELOCITY MEASUREMENT

5.2.1 *Justification*

Due to the topology of slugging flows, with large stable liquid and gas structures moving in accordance with each other, the application of non-invasive measurement through tomography can be more easily applied in comparison to other flow patterns. One of the main assumptions that can be made to this flow type is that of the unit cell method, a description which can be traced back to the early work by Nicklin et al. [92] and Dukler et al. [35], in the study and modelling of slug flows. The basis for this method is the assumption that, if stable, the flow can be simply described as a repeating unit cell, of which is the volume of fluid which spans both the oil and gas slug. Another significant feature is, excluding gas entrainment in the liquid slug, that the liquid slug acts like a piston on the gas slug, therefore implying that the averaged liquid slug velocity should equal that of the gas slug, although this is not necessarily always the case.

By obtaining the liquid slug wave velocity from cross correlation, it becomes possible to obtain both the gas and oil flowrates. The first step in this is to use the relations described by eqs. 2.17 through 2.20 in Section 2.4.3 to determine the mixture superficial velocity from the cross-correlated velocity. Secondly, the gas flowrate can be estimated by the assumption that the wave velocity must, within reason, represent the mean gas velocity (assuming the liquid slug acts as a piston when excluding gas entrainment). Thus by knowing the gas phase fraction and the cross-sectional area, the gas flowrate can be calculated. Additionally, the gas flow through entrainment in the liquid slug can be added to this value by careful application of cross-correlation and tomography, producing greater accuracy. Finally, the mixture and gas superficial velocities together, allow the calculation of the liquid superficial velocity. Despite this method being already capable of providing good results, any improvements in reliability and achievable accuracy is advantageous. One area where this can be improved is in the first step of estimating the mixture superficial velocity. Despite a large number of studies concentrating on providing accurate correlations for this relationship, in which many succeed in modelling the linear trends, the variation of the data is still reasonably large, at around $+/-10$, and particularly bad at flow regime transitions. As pointed out in Section 2.4.4, one reason proposed for this variation is due to velocity discontinuities at the fluid interface [33]. Due to the nature of tomography, such discontinuities are harmful to the measurement accuracy. Therefore, the identification, and if possible mitigation, of such discontinuities could provide significant improvements to the potential accuracy of tomographic based flow measurement of slug

flows. By studying the structures of slug interfaces, it may be possible to categorise certain discontinuities, then, by assessing their effect to the overall measurement, a suitable treatment method can be proposed which can be implemented in a real time tomographic sensor when the specific structure is identified.

5.2.2 *Application to FRIMM*

Despite slug flow representing the most susceptible flow regime to tomographic measurement, and the obvious need for a flow regime independent meter to measure these flows, more accurate metering of slug flows could benefit such a system in additional ways. Considering the work outlined in Section 5.1, where it is proposed that slug flow data could, in some way, be used to assist in metering other flow regimes over time when information (on wave properties) is collected, it is reasonable to suggest that such measurements can be used as a reliable standard. One of the reasons for this is that, the method of tomographic slug flow measurement is based solely on the movement of inter-facial structures, and therefore is independent of properties such as viscosity, unlike the methods presented for annular flow, for instance.

Despite the discussed preference for a FRIMM based system which does not rely on empirical correlations, due to their nature of limited applicability; a high accuracy correlation for slug flows, seemingly achievable by the development of current measurements as proposed here, could be used as a continuous validation for such a system. This would entail the referencing of results gained through the integration of fluid models (as proposed in Section 5.3), being compared to the translational slug velocity correlations, along with integrating the method proposed here, to ensure the system validity, or perhaps to use as a substitute, or simply integrated to improve the overall measurement.

5.2.3 *Method*

The method used in this study uses data collected from the multiphase flowloop at NEL, as described in Section 4.1.4. The phase flowrates applied provide data sets within the slug flow regime, including some close to the flow regime transition zone. Prior to the experiments, the ECT system was firstly installed and calibrated, as outlined in Section 4.2. For each test point, the ECT measurement system records around 1 minute of raw capacitance data from each electrode pair at around 1400 fps, and logs them to the control PC; once the data is checked to ensure no significant error occurred, the process is repeated for the next test point.

For this study, two main properties require measurement using ECT. Firstly, the tomographic images themselves are required at the slug front and tail fluid interface in order to identify, assess, and if possible categorise the structures based on their features. The analysis of the slug front and tail structures will be conducted by manual investigation of the tomographic images during the very short period of time that the fluid body passes the sensing region. Secondly, the wave, or translational velocity of the liquid slug is measured through cross-correlation, with respects to the method outlined in Section 2.1.3, where small integration windows are used at the slug front and tail fluid interface, obtaining separate measurements which are then averaged to get the desired value. Considering that, differentiating between slug and tail velocities involves the correlation of a signal which is not a pulse (instead just a sudden increase or decrease), the derivative of the signal is used to ensure the cross-correlation procedure is optimal. On top of this, for the analysis of specific structures, a range of correlation zone maps will be utilised to assess a specific structures effect on the overall measurement, with the type of correlation zone map dependent on the structures topology. The cross-correlation velocity will be used to obtain the mixture superficial velocity using the correlations outlined in Section 2.4.3, which can then be compared to the equivalent measurement from the reference flowmeters installed on the flowloop for comparison. This will also include any variation in measurement strategy (correlation parameters or zone maps), or method which results from the analysis of the slugs front tomographic images in order to assess its usefulness.

5.2.4 *Results*

5.2.4.1 *Slug front and tail structures*

By manual analysis of the tomographic images at the fluid interface, different structures have been identified and categorised based solely on their topology; the resulting structure groups are depicted in Figure 5.11. To obtain the images, the segment of data covering the evolution from stratified flow to the main slug body (cross-section of oil with some entrainment) is isolated for the selected slugs. The 2D images for each time step within this segment are stacked on a 3D axis, and finally the number of images are reduced to display the most significant transitions. The spacing between each image is adjusted to ensure a clear image of the structures. It is therefore important to note that the aspect ratio of the images are exaggerated, and do not represent a comparable length of the different structures, hence no units along the time axis are given. The colour gradients for the images are chosen to provide clear distinctions between each stacked image as well as intermediate values. Areas of high permittivity fluid (oil) are shown in blue, whereas low permittivity fluid (gas) areas are

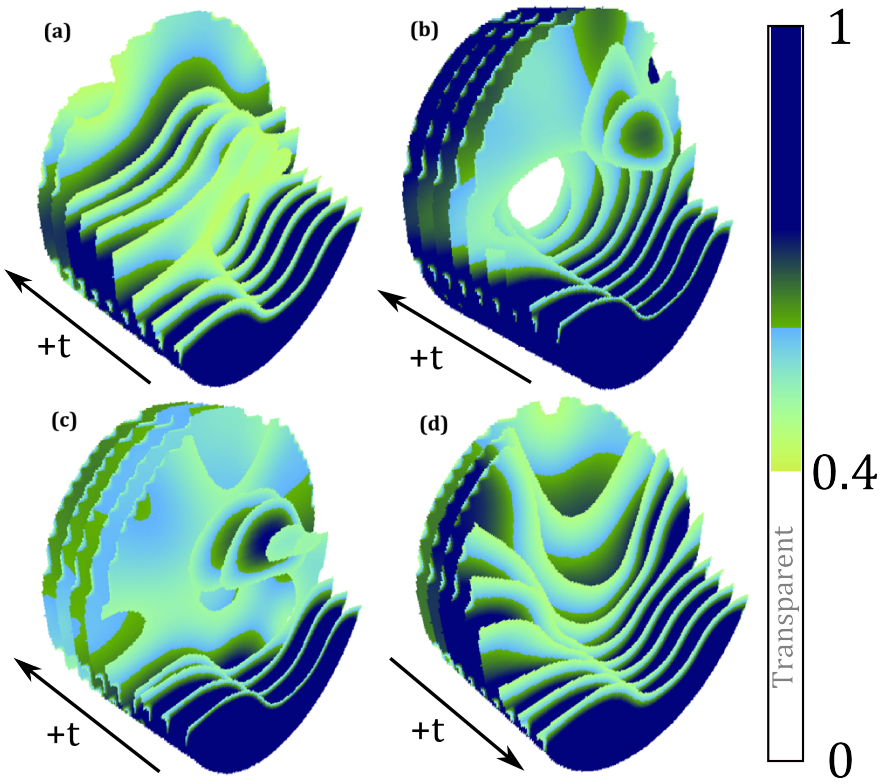

Figure 5.11: Temporally stacked tomographic images of three slug front structures (a,b,c) and one slug tail structure (d).

transparent, which is required when images are presented in this way, in order to observe the change in structure over time. As is typical in ECT images, the interface between the two fluids is represented by the green area, and defines a point in the cross-section where neither only oil or only gas is present. This exists for two main reasons: firstly, the electrodes measure over a small volume as opposed to just a 2D plane as the images suggest, therefore the sensor can measure axially separated oil and gas at the same point in the cross-section. Secondly, blurring of the interface is a common trait of LBP image reconstruction, due to the assumptions made in the algorithm to solve the ill-posed problem.

Beginning with Figure 5.11 (d), which displays the structure of a liquid slug tail. This structure was seen to be consistent in practically all viewed images of the data, which could be explained as they are not subject to the sudden pressure change that is observed at the oil slug front. The observed transition at the slug tail is what would be expected, with a relatively stable and gradual incline between full oil condition to the stratified region, with a noticeably faster drop at the centre of the cross-section, which, due to surface friction at the pipe wall would also be expected. It is important to note that the LBP image reconstruction method would incur blurring at the interface, and thus may contribute to this shape, however the prominence of this central

zone's behaviour is consistent with that seen in industrial stratified flow, and thus will be assumed to be valid. The slug front structures, however, are not so consistent, and have been broadly categorised into three main groups, again based solely on their topology.

- Steady rising structure

Starting with the structure depicted in Figure 5.11 (a), where a similar structure to that for the slug tails is observed, but inverse. For this structure, a steady incline from stratified to a full oil condition is apparent, with this beginning at the centre of the cross-section, then spreading to the outer regions. This steady rising slug front structure was the most commonly observed out of the three defined groups, and is typical of what we would have expected the slug front to be.

- Gas core structure

The second group, as depicted in Figure 5.11 (b), displays a very different topology, with a distinct central core of gas, surrounded by an annulus of oil initially, then eventually the gas core is filled with oil. The structure is reminiscent of the initiation of a gas core slug, described by Hunt and Millington [64], where the oil slugs have a continuous gas core, which has important implications with respect to assumptions made when modelling such flows.

- Unstable structures

The final category, as displayed in Figure 5.11 (c), is that described as unstable. The main identifier in this case is a generally chaotic or non-uniformity of sections of the cross-section where oil packets separate from the main slug body, as well as a non-conformity to either of the previous two categories. It is important to note that the image presented in Figure 5.11 (c) is merely an example of what has been described as an unstable structure, with other examples varying significantly in their appearance. Additionally, there is a noticeably large amount of gas entrainment in the slug front for these structures, identified by the large areas of intermediary (green) values.

The assumption made here is that, for gas core and unstable structures, the distinguishing liquid features (oil annulus for gas core structures and the oil packets for unstable structures) are travelling at a velocity greater than that of the overall liquid body. Therefore, conventional cross-correlation when applied, will measure the velocity of these discontinuities, and thus over-estimate the actual translational velocity. Hence it is necessary to find methods to alleviate this or, if possible (i.e. if their frequency is reasonably low) exclude them from the measurement in an attempt to improve the overall measurement accuracy.

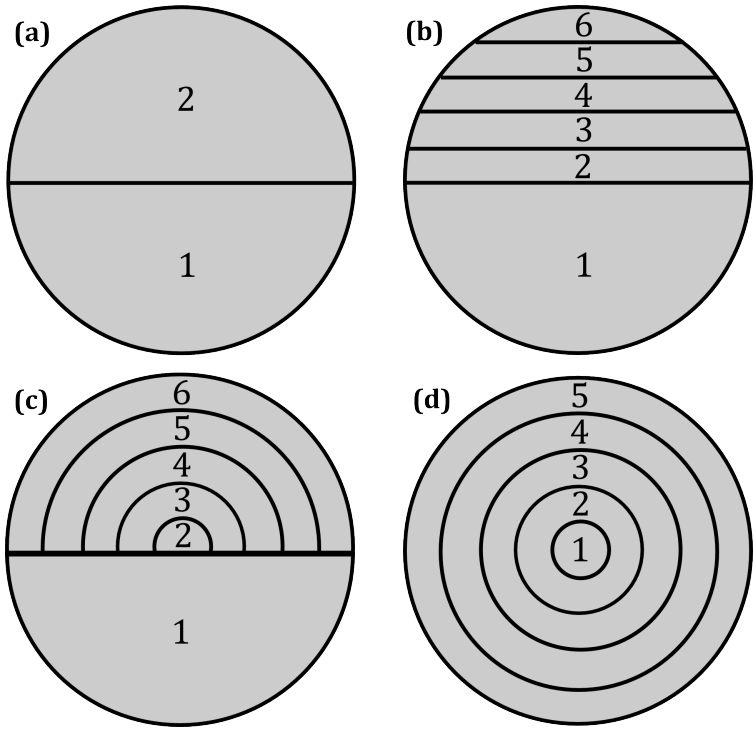

Figure 5.12: Correlation zone map examples for representing fluid structures as they pass through the sensor.

5.2.4.2 *Analysis of steady rising slugs*

As mentioned in the previous section, the named 'steady rising' slug represents the most typical slug structure encountered. For this reason, we begin by analysing this simple slug type to assess the normal validity of the ECT measurements taken. The first step in this procedure is to designate suitable cross-correlation zone maps in order to specifically designate areas within the cross-section which match the progression of the particular structure as it passes through the sensor, which in turn will reduce the influence of gas entrainment and isolate specific structures if necessary. Figure 5.12 depicts 4 correlation zone maps which have been applied in this work.

By observing Figure 5.11 (a), we can see that a suitable correlation zone map for ECT would be either Figure 5.12 (b) or (c) if a velocity profile is desired, as opposed to a single averaged value. Using either of these correlation zone maps will suffice in providing a reasonable result, due to firstly the lower half of the cross-section being excluded to remove any influence of gas entrainment, and the topology of the top half roughly matching the structural movements at the slug front. For a single average velocity value, the correlation zone map depicted in Figure 5.12 (a) would suffice, as it excludes the stratified section at the lower half of the cross-section, and would not require multiple zones in the top half as the fluid structure moves as a single entity.

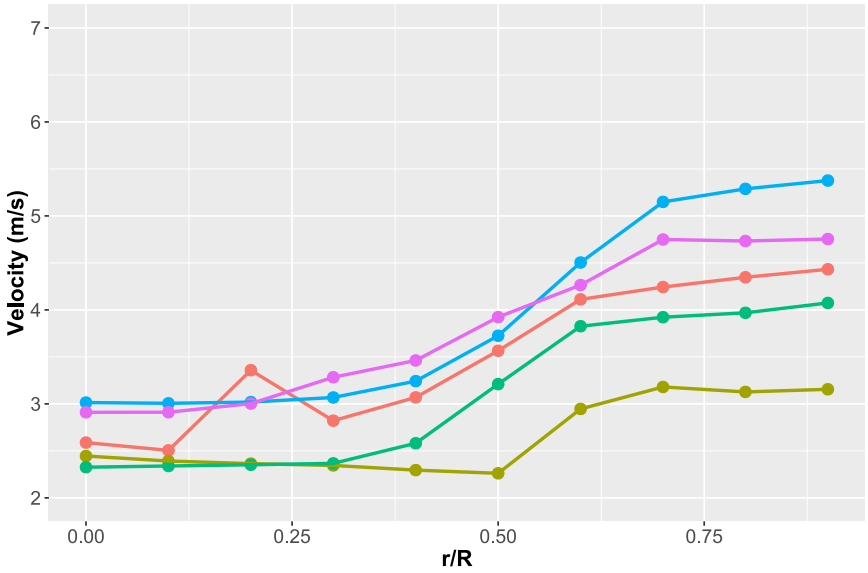

Figure 5.13: Measured axial velocity profile (top half of pipe only) of slug fronts. With different colours representing separate slugs in a single test, with slug fronts of type shown in Figure 5.11 (a), encountered during experiment at $J_g = 2.19m/s$ and $J_l = 1.37m/s$.

5.2.4.3 *Velocity profiles - slug front*

The first validity test can be the measurement of velocity profiles for the stable rising slugs. By following the method described in the previous section, and obtaining a velocity measurement for each vertical segment of the correlation map depicted in Figure 5.12 (c), the velocity profiles that are measured for steady rising slugs in a single test at $J_g = 2.19m/s$ and $J_l = 1.37m/s$ can be observed in Figure 5.13. This specific correlation zone map (as opposed to that shown in Figure 5.12 (c)) was chosen due to the noticeable difference in the appearance of the structure between the centre and the outer regions of the pipe. It is noted however, that the use of correlation zone map shown in Figure 5.12 (c) produces a very similar outcome. The result, therefore displays the velocity profile along the vertical axis, from the centre to the top of the pipe, and does not suggest axissymmetry. The results are viable due to the known occurrence of wave structures in liquid slugs for industrial flows, where velocity increases when approaching the top or outer regions of the pipe, and levels out near the pipe wall. It is noted that the zone map area at the wall of the pipe will not portray the effects of wall shear stress due to the nature of the cross-correlation method.

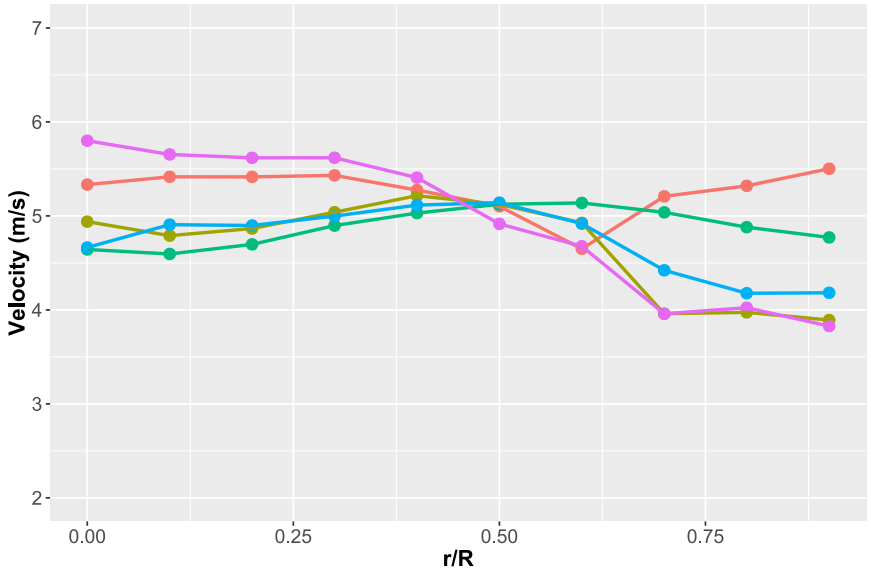

Figure 5.14: Measured axial velocity profile (top half of pipe only) of slug tails. With different colours representing separate slugs in a single test, with slug tails of type shown in Figure 5.11 (d), encountered during experiment at $J_g = 2.96m/s$ and $J_l = 1.025m/s$.

5.2.4.4 *Velocity profiles - slug tail*

Due to the similarities in structure, mentioned previously, between steady rising slug front and tails, the same method used previously can be applied to obtain the slug tail velocity profiles. For these tests a different data set is used, with flow parameters: $J_g = 2.96m/s$ and $J_l = 1.025m/s$. The results, though not as stable as the previous test, seem to show an opposite behaviour, with the fluid in the top or at the walls of the top half of the pipe travelling relatively slowly, then accelerating as the centre point is approached. This is displayed in Figure 5.14. As with the previous velocity profiles, the results describe that which is measured along the vertical axis from the centre to the top of pipe only.

5.2.4.5 *Behaviour of slug fronts and tails*

A further way of analysing slug structural effects, is through the comparison of slug front and tail velocities. As pointed out by Abdulkadir et al. [2], relatively close values of slug front and tail velocity can be used as an indication of good flow development. Therefore, by categorising the different slug structures within a developed flow, the variation present for the different structures can be used as an indication of their stability, or degree of representation. Figure 5.15 shows a comparison between front and tail velocities of slugs chosen from four separate test points (with flow range indicated in caption), covering the 3 slug front structures defined in Figure 5.11 (a), (b) and

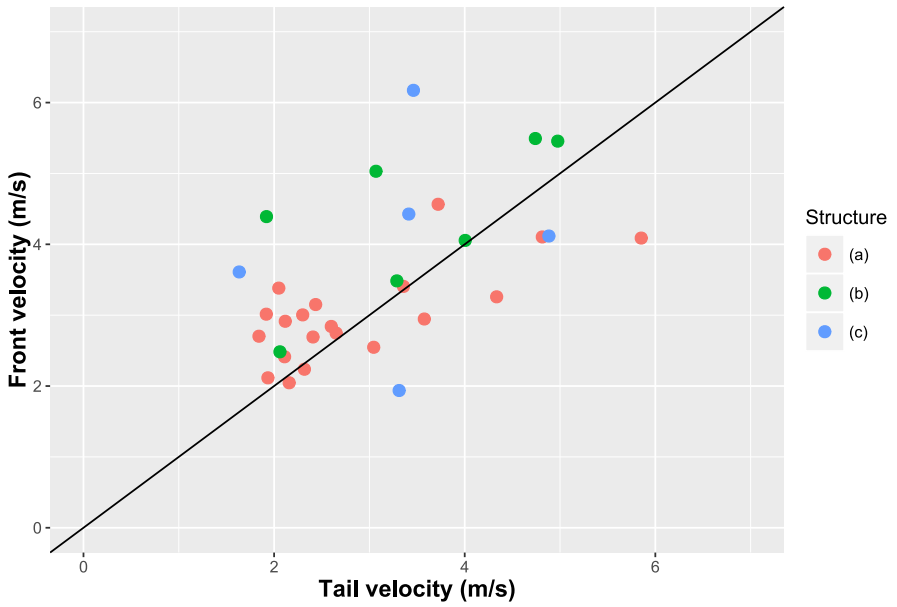

Figure 5.15: Comparison of slug front and tail velocities for different slug front structures in 3 separate test points covering flow range of $J_g = 0.47m/s$ to $2.19m/s$ and $J_l = 1.37m/s$ to $1.522m/s$. Structure titles refer to those seen in Figure 5.11.

(c). The plot also gives an impression of the frequency of each structure type observed during testing. The results were gathered using the correlation zone map depicted in Figure 5.12 (a) (providing an average velocity of the top half of the cross-section, hence not affected by gas entrainment), with a small correlation window and by correlating the differential of the time series. This allowed individual slug velocity measurement, differentiation between front and tail velocities, as well as representing conventional cross-correlation, in terms of correlation zone map. The black line in Figure 5.15 indicates where the front and tail velocities of a certain slug are equal, therefore, points above this line represent instances where the front is higher than the tail velocity (i.e. increasing in length). The results show that the most frequent structure type (stable rise (a)) produces the most consistent similarity between slug front and tail velocity. Although they indicate that the majority of slugs within this category are accelerating, this is not considered a problem with respect to flow development, as the differences in values are relatively small. Furthermore, providing fully developed flow is not a necessity for this work, as the main focus is to measure the flow as opposed to providing a basis for modelling. Structures with gas cores (b) have a larger variation, with a clear bias for higher front velocities, as expected. Finally, the unstable structures also produce a higher variation between front and tail velocities, with no clear bias.

5.2.4.6 *Method for analysis of structures*

Now that these structures have been identified and the stable structures validated, the remaining slug front types must undergo analysis to asses the effects of using cross-correlation to measure their corresponding interface wave speed. With the goal of understanding how representative they are of the actual oil body translational speed. The method proposed for judging representativeness will be based on the correlations described in eqs. 2.17 and 2.20 in Section 2.4.3. By obtaining the true mixture superficial velocity from the reference flowmeters, and using the parameters from the work of Bendiksen [13], we can obtain an expected value for the measured translational velocity. This expected value can be used as a guide, not for single measured slug waves due to the varying nature of slug speeds, but as an averaged overall goal when many slugs of a certain structure are tested. This should be sufficient in analysing the effects of each structure and their corresponding measurement method.

5.2.4.7 *Analysis of gas core structures*

As mentioned previously, slug fronts with a gas core, when measured using the correlation zone maps used for other structures, tend to overestimate the translational velocity significantly. This can be explained because the cross-correlation includes the oil annulus as the majority of the measurement, where this structure is propelled around the pipe circumference at a greater velocity. In order to counter this, it is assumed that the only part of the structure at the fluid interface which is truly representative of the slug, is the central core zone, when it eventually fills the cross-section. Therefore the most suitable zone map to apply to these slug types would be a conventional annular type, as shown in Figure 5.12 (d), whilst only considering the zones which encompass the core area. The results in Figure 5.16 are measurements of gas core structure slugs using both the annular zone map, only considering zone segments that encompass the core area (annular - centre zones) as well as cross-correlating the entire cross-section, named as conventional.

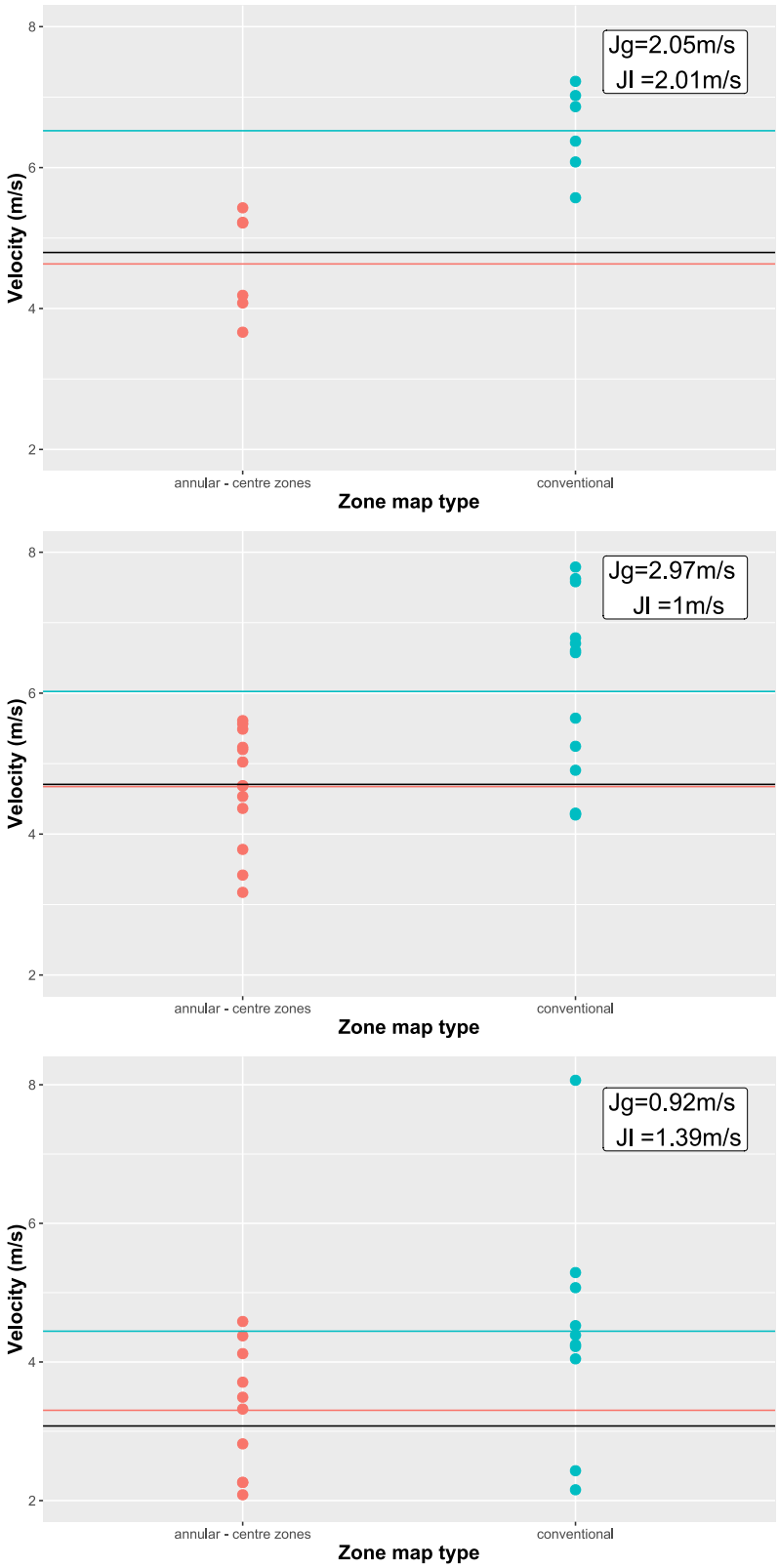

Figure 5.16: Comparison of individual gas core structure slug front velocities observed during the three separate experiments indicated in each plot. Measured through conventional averaged cross-correlation and using an annular based zone map whilst only taking measurements from the central core zones. Horizontal lines represent: predicted translational velocity (U_T) (black), averaged values (red and blue).

The results show that the average velocity value obtained when only using the central zones decreases, and obtains a figure much closer to the expected. This is due to the reasons explained previously and provides a viable solution to measuring the slug translational velocity for these slug types. However, an important point is that, due to the smaller region of measurement, it is reasonable to assume that the reliability of the measurement is somewhat reduced, due to the possibility of some discontinuity or instability within the core region having more effect during such measurements. Despite this, the presented method displays a better measurement potential in comparison to the conventional technique of cross-correlation of the entire measured cross-section.

5.2.4.8 *Analysis of unstable slug front structures*

In order to understand the effects of each slug structure type on the overall measurement, in particular the unstable slugs, which, unlike the gas core slugs do not allow a simple method of distinguishing between discontinuities, it is necessary to analyse each individual slug velocity (both front and tail) for a particular data set. This data can then be compared to the prediction of translational velocity from correlations, as before. It is noted that the theoretical prediction, although based on the reference measurements, is only expected to serve as a guideline of the true value, due to the inaccuracy present in the correlations. Also, due to the industrial scale flow experienced within the testing, reasonable deviation of the slug translational velocities with respect to their mean values is expected. Figure 5.17 (top) shows an example test point where the front and tail velocity (red and blue points respectively) of every slug encountered are plotted against time (as observed in the test), using the zone map depicted in Figure 5.12 (a). The mean of both front and tail velocities separately are also displayed by their corresponding coloured line, along with the theoretical prediction of slug translational velocity, displayed by the black line. It is assumed that the more representative the measurements are, the theoretical prediction (black line), will be closer to the centre between the mean front and tail velocities (red and blue lines).

Figure 5.17 (bottom) shows the same data as previously, except only slugs which exhibit stable rising structures (Figure 5.11 (a)) are included (selective measurement), with mean values adjusted to only include the measurements present. The results clearly show an improvement when selective measurement is conducted, where the prediction line sits closer to the centre of the front and tail mean velocities. This is mainly achieved, through the reduction in mean slug front velocity, which confirms the previously made statement that the inter-facial instabilities move faster than the true translational velocity. Another observation which can be made is the benefit of averaging the front and tail velocities, as opposed to using either individually. This

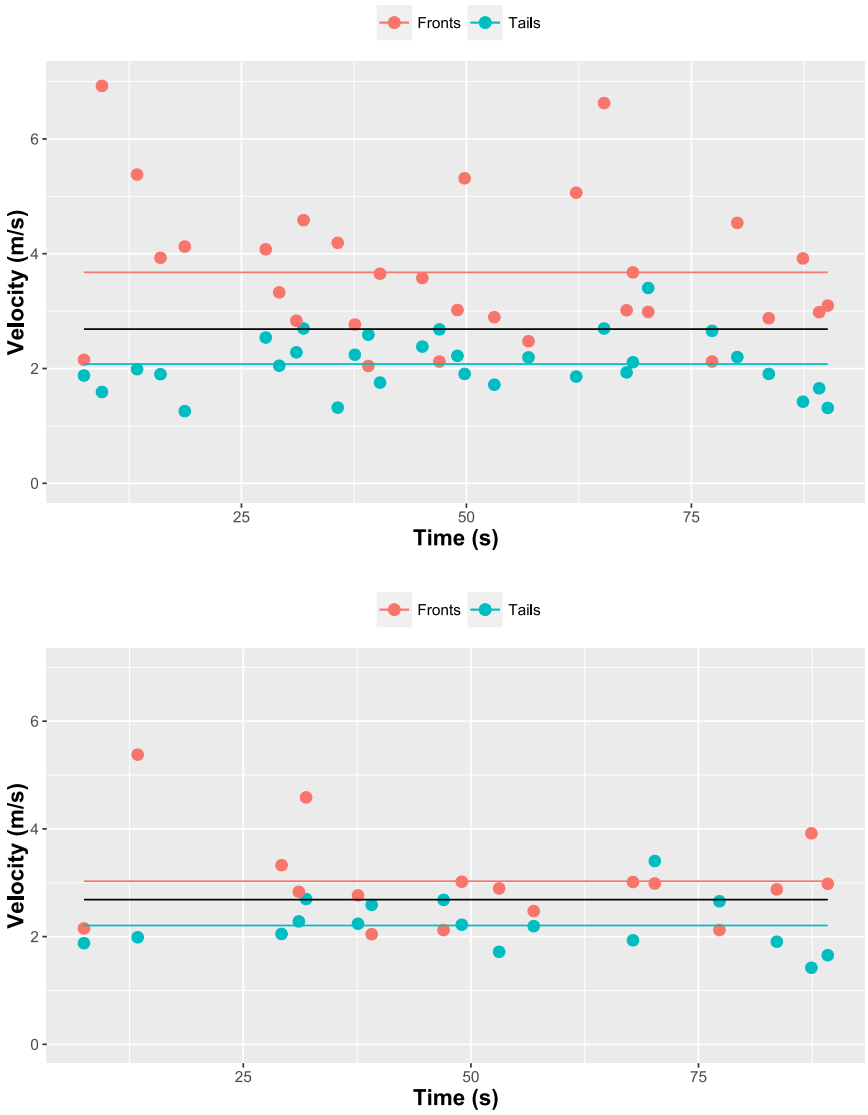

Figure 5.17: Slug front and tail velocities of multiple different slugs encountered at $J_g = 0.98m/s$ and $J_l = 1m/s$, for both: inclusive of all slugs (top) and inclusive of only slug fronts of type Figure 5.11 (a). Horizontal lines indicate: predicted translational velocity (U_T) (black), mean slug front velocity (red) and mean slug tail velocity (blue).

is important in reference to the tail velocities, as they are consistent in their structure, and thus obtaining a reliable measurement is easily achieved. It is therefore assumed from these results that, removing unstable slug types from the overall measurement, in the absence of a suitable bespoke method as was proposed with gas core structures, increases the overall accuracy capability and representativeness of the true slug translational velocity.

5.2.4.9 *Outline of Selective cross- correlation method*

This section outlines the method of selective measurement of slug flows using ECT. This takes the results from the previous section as justification in improving the overall measurement potential of ECT as a cross-correlation flowmeter for slug flows. The steps involved in this method are as follows:

1. Categorise slug structure

The first step in a selective based cross-correlation flowmeter is the detection of structure type. This can be implemented using techniques defined for flow regime detection, outlined in Section 2.2. For instance, with gas core type structures, the relative difference between neighbouring electrode pairs and opposite electrode pairs can be used to distinguish this feature. As for stable structures, either the relative difference between electrode pairs covering the lower and upper parts of the cross-section can be used, or the same principle can be applied to the resulting reconstructed image. Unstable structures could be identified by non-uniformity in the resulting image, or simply by not being categorised by the previous identifiers. This method can be implemented efficiently by isolating a data segment once a certain threshold of oil holdup has been reached, this would reduce the number of images, or data points, that would require analysis, and hence would be viable with respect to computational resources.

- ***If stable rise: use half zone map***

If a stable rise type slug is detected, the correlation zone map depicted in Figure 5.12 (a) can be applied, as normal (but excluding gas entrainment effects), in order to obtain the slug front velocity. This is then repeated for the slug tail velocity, and the average of front and tail velocity is used as the translational velocity.

- ***If gas core: use core zone map, only include central zone***

When a gas core structure is detected, the method described in Section 5.2.4.7, where the correlation zone in Figure 5.12 (d) is used, with only the central zone to obtain the front velocity. The tail velocity is measured as with stable rising structures, and the average of the two are used.

- ***If unstable: ignore***

When an unstable slug is detected, the result is ignored. This is suitable for the flows tested in this study, however, if it was the case that such slug structures were very common, this method would need to be replaced with a more complex method, as applied with gas core structured slugs.

2. Determine mixture superficial velocity

Once the translational velocity of a particular slug is obtained, by applying the correlation proposed by Bendiksen [13], and described by Eqs 2.17 and 2.20 in Section 2.4.3, the mixture velocity can be obtained.

3. Determine the phase superficial velocities

To obtain the gas superficial velocity, the translational velocity found previously is assumed to represent the mean gas velocity, and hence, with the use of the measured gas phase fraction and timescale (from tomography), the gas slug flowrate is calculated. This value is then added to the gas entrainment flowrate, obtained by conventional cross-correlation on the oil slug, and the corresponding gas entrainment phase fraction. The addition of these two measurements provides the overall gas flowrate for a unit cell slug. Finally, the mixture and gas superficial velocity is utilised to obtain the oil superficial velocity ($j_l = j - j_g$). This process then repeats for every "unit cell" of slug flow.

5.2.4.10 *Accuracy comparison for selective method*

To determine if an improvement in accuracy is possible through the selective based measurement method presented here, the mixture velocity can be determined from the measurements for the following different methods:

1. Conventional cross-correlation is tested by applying the zone map presented in Figure 5.12 (a), with a large integration window, giving a single velocity measurement for the data set.

2. Method 1 except with the correlation window reduced to allow individual slug velocity measurement (inclusive of both front and tail), with averaged values.

3. A small correlation window is combined with cross-correlation of the time series differential, use of the zone map depicted in Figure 5.12 (b), measuring only front structures within category Figure 5.11 (a), and the front velocities are solely used.

4. An average of front and tail velocities of Method 3.

Figure 5.18 displays the results for this test, along with predictions outlined in Eqs 2.17 through 2.20. It is noted that the more complex zone map used previously for obtaining velocity profiles (Figure 5.12 (c)), is not included here. This is due to results for the selective based methods (3 and 4), (referring to methods which exclude slugs based

on their front structures), giving similar averaged results when using either zone map depicted in Figure 5.12 (a) or (c).

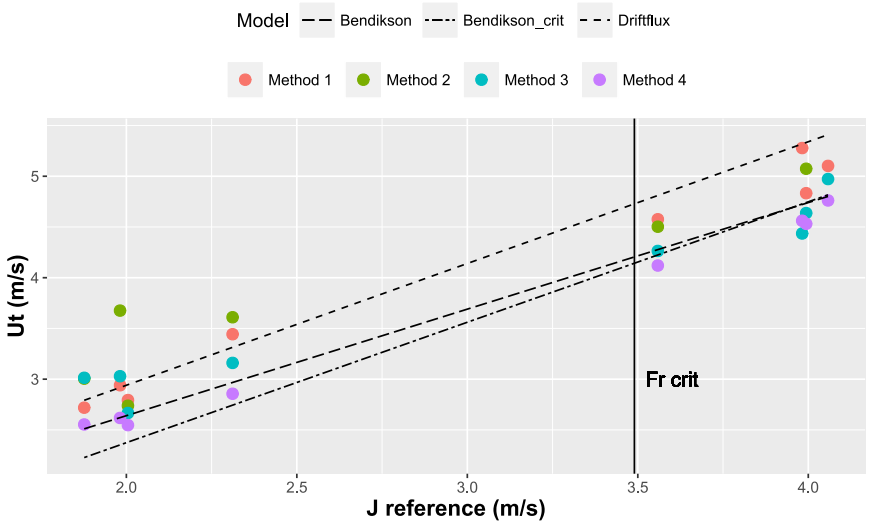

Figure 5.18: Comparison of accuracy encountered for the different methods of cross-correlation and zone maps covering all experiments. Along with previously derived predictions.

Both axis ranges have been restricted to only cover the values observed in the tests, this is to ensure that the results from the different methods can be compared easily, considering that the differences are relatively small. The results, overall, show correlation between measurements and theoretical predictions for all methods, with method 4 producing the most reliable linear trend. Firstly, the conventional method (1) gives a relatively good linear trend, though variation is reasonably large, and comparable to results from other non-intrusive devices [130, 129]. Method (2) gives a similar trend but with some data points with larger variation, this can be explained due to unstable slugs having a more profound effect on the measurement when considered individually. Both method (1) and (2) give slightly higher results than the others, due to the inclusion of less stable structures with larger velocities at the slug front. They may also be affected by not distinguishing between front and tail. Method (3) shows overall lower values but with similar variation to method (1). Finally, the selective method with average front and tail velocities (4) gives the best results. The linear trend is strong with reduced variation, the data points suggest good correlation with the prediction of Bendiksen [13], including the critical Froude number boundary.

Method (4) can now be presented in terms of measurement and reference as illustrated in Figure 5.19. In this plot, the reference mixture superficial velocity is obtained from the reference flowmeters as in Figure 5.18 ($J_{ref} = \frac{Q_{g-ref}+Q_{l-ref}}{A}$), and the measured mixture superficial velocity is obtained by rearranging eq. (2.17), and using values of the

distribution parameter C_o and drift velocity U_{dj} from eq. (2.20), with reference to eq. (2.21).

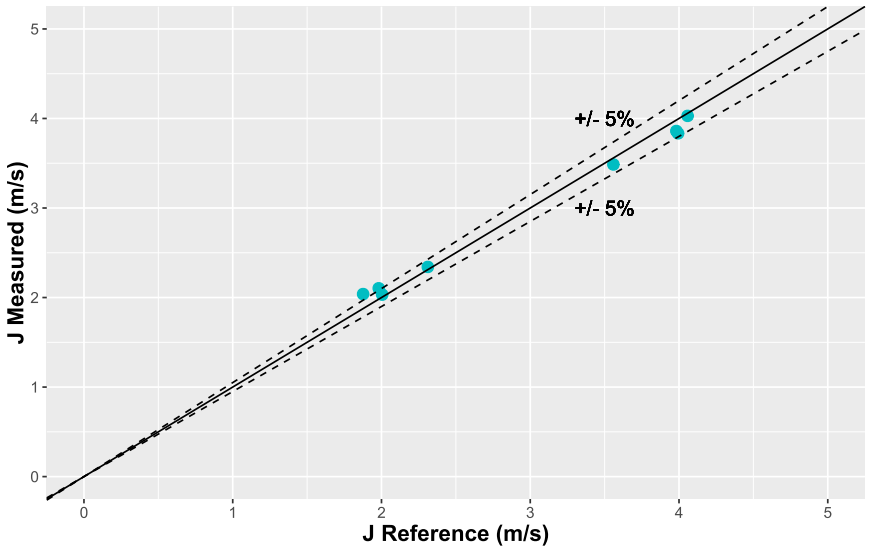

Figure 5.19: Results of applying method (4) and prediction of Bendiksen [13] to the measurement of the mixture velocity for all test points. Compared to reference measurements of the mixture velocity recorded during testing.

The result overall shows a high measurement accuracy potential, where the majority of data points are well within a $+/-5$ error range, and close resemblance to the prediction. Measured points at the lower values of mixture superficial velocity ($< 2m/s$) appear to have slightly higher error margins, as seen by Zhang and Dong [130], though more data would be required to confirm this. Such results are comparable to advanced metering methods such as Ultrasonic Doppler sensors [32] which measure the actual velocity of fluid particles. The method represented, therefore, provides a basis for ECT cross-correlation flow-meters to compete with other methods which are less suitable to oilfield applications.

5.2.5 *Discussion*

From the results for velocity profiles of the stable rising slugs, we can assume validity of measurement. The trends displayed in Figure 5.13, resembles that obtained by Gopal and Jepson [47] specifically for slug fronts as well as Belt and Leinan [12], for the reasons discussed previously. By also considering the conventional cross-correlation results depicted in Figure 5.18, it can be justified that the measurements obtained from ECT, with the application of conventional correlation zones and parameters, resembles that of work carried out by a large number of researchers [2, 129], with regards to the variation of data around the prediction, being close to or slightly exceeding $+/-10\%$,

with the exception of test undertaken close to, or at, the regime transition zone. Hence, any improvement on this capability can be validated by this work, and that of others.

From the results comparing front and tail velocities in Figure 5.15, some interesting points can be made. Firstly, the gas core structured slugs (b), as pointed out, vary more in comparison to the stable rise slugs, due to the increased velocity in the oil annulus. This is confirmed by the fact that, for all gas core structured slugs, the front velocity is greater than that of the tail, as would be expected. However, this is not the case for unstable structured slugs, where two out of the five slugs showed the tail velocity moving faster than the front. One possible explanation for this would be that the instability, or discontinuity, of velocity at the slug front has caused a substantial breakdown of the slug front, causing deceleration to a degree where the tail is actually moving faster. Alternatively, it could be assumed that in these cases, the slug is simply decelerating slightly, and the unstable structure is having a minimal effect, considering that the decelerating data points are closer to the steady state line (front velocity = tail velocity) than the accelerating points. Looking now at the stable rising slugs, it is clear that the results suggest that most slugs are accelerating. This is not necessarily expected, due to the fact that the flow loop is relatively long (60m), much longer than the 60 - 100 diameters in length (dependent on phase velocity) seen in other work [29], which should allow sufficient flow development to produce a steady state condition, i.e. when the liquid taken up at the front is equal to that shed at the back [24, 72]. It is also noted that this is prevalent only in the lower end of slug translational velocities (< 3m/s) which could be relevant.

Results for the analysis of gas core structure slugs suggest the proposed method is a viable solution in obtaining a more representative velocity from such liquid slugs. However, the reduction of the correlation zone to the core area has its own disadvantages. Firstly, the size of the core itself will vary, likely dependent on relative phase velocities, and hence there may not be a single sized correlation zone which would be suitable for all scenarios. Despite this, it can be assumed that the range of core sizes is somewhat limited, and in the case where the correlation zone includes areas outside the gas core, the overall effect is likely to be limited. As briefly mentioned in Section 5.2.4.1, these structures are reminiscent of the recently discovered gas core slugs, first reported by Hunt et al. [65], and further described by Hunt and Millington [64] as high speed slugs with an annular wave structure, comparable to “huge waves” as defined by Sekoguchi [102].

The unstable structured slugs, though seemingly rare, are likely created by the same mechanism in which gas entrainment exists within the liquid slug. This is due to turbulence in the shear layer and wall jet, formed at the gas wake as liquid penetrates the slug

front [15]. Considering that it has been shown here that the removal of unstable and gas core structured slugs, improves measurement accuracy, we can assume that both these slug types are detrimental and require further consideration. If the proposal in the previous section is implemented, then gas core slugs may be included. However, the exclusion of discontinuities from the measurement of unstable slugs is not straightforward. It would require a bespoke correlation map for each slug type, due to their inconsistency, to ensure only the main oil body is included in cross-correlation. Though this may well be possible through image processing, the requirement for this to be implemented in real time for each occurrence is not viable. Furthermore, referring to Figure 5.15, it can be assumed for now that unstable slugs are relatively uncommon, and hence their exclusion from measurement is deemed more appropriate, however, further tests at different flow ranges would be required to be certain.

Looking now at the comparison of methods and their effect on the relationship between the measured translational velocity and the reference mixture superficial velocity, displayed in Figure 5.18. Method 1 represents the most common technique in this application of cross-correlation measurement, and the results match, in terms of variation, that found by other researchers. The data points are best described by the drift flux correlation, which may be relevant, as this correlation predicts a higher translational velocity, which would be expected if the velocity discontinuities from certain structures are not accounted for. The same can be said for method 2, except as explained previously, the detrimental effects on variation due to individual slugs with velocity discontinuities having greater influence on the result. When we consider the selective methods, in particular method 4 (as the results suggest an averaging of front and tail velocities is beneficial), not only is the variation improved, but the best fit correlation is that proposed by Bendiksen [13]. It may be the case that the experiments conducted by Bendiksen, along with those who have found this to be the closest correlation, produced a greater number of stable rise type slugs, likely due to their position on the flow regime map, and hence the correlation better matches that found in this work .

The final graph for estimating the mixture superficial velocity in Figure 5.19, overall suggests that the selective method of cross-correlation can improve the overall accuracy potential. However, the final stage of recovering the gas and liquid superficial velocities relies not only on this prediction, but also on the instruments ability to measure the gas slug flowrate and gas entrainment in the oil slugs. Considering this, the improvement gained through selective measurement should work two-fold, firstly the estimation of gas flowrate should be improved by a more representative gas slug velocity (assuming its equality to the measured translational velocity of the oil slug), as well as the

improvement in predicting mixture superficial velocity (used with the gas superficial velocity to predict the oil superficial velocity).

5.3 PARTICLE FILTERING APPLICATION TO TOMOGRAPHIC FLOW MEASUREMENT

5.3.1 *Overview*

To attempt to provide a foundation for which to build a general purpose, flow-regime independent, multiphase flow metering system using tomography, the Bayesian recursive method of Particle filtering will be employed. Essentially, this consists of using the data from ECT systems to update the relative likeliness of a large set of CFD simulations. By testing statistical noise parameters of both the measurement and the CFD model, and subsequently inputting this into the system, a probability density can be developed at each time step of the systems operation, providing information of the probability of values that the relevant flow parameters (phase superficial velocities) take. By using this method, we incorporate fluid modelling and tomographic measurements to produce a superior method of tracking the state of flow within a pipe.

5.3.2 *Justification*

The application of the recursive Bayesian method of particle filtering to the tomographic flow measurement of multiphase flows is deemed a viable solution to flow regime independent metering for many reasons. Firstly, the integration of information from a CFD model is beneficial to a measurement system as it can be used to simulate the conditions for which the tomography sensor would measure, from a wide range of flow situations, and hence would inevitably provide better judgement to the state of flow in situations where the tomography measurement would seem similar. This also assists in the idea of a process now-casting approach to multiphase flow measurement where, like that seen in weather prediction, an overriding model is used to predict the flow state at any point along a pipeline, which is continuously updated when new information from individual measurement systems (tomography) is provided. Such an approach would provide an invaluable tool to flow operators, in providing far more information than the equivalent individual measurement systems.

Another important factor with the implementation of this method is the handling of both measurement and model noise. Particle filtering provides a basis to which the known measurement noise of tomography (though small in phase fraction, higher in velocity), and the inaccuracies present in CFD modelling can be tested, inputted into the system, and incorporated into the measurement prediction of the flow state. This not only works to remove errors, but also provides the end-user information on the probability or likeliness of the resulting measurement.

One of the main advantages of particle filtering is in its ability to handle non-linear and high dimensionality systems, which multiphase flow metering requires. Firstly, tomography itself is a non-linear measurement and although not the focus in this work, particle filtering could be applied on a more fundamental level in tomographic image reconstruction. Whereby the process between raw capacitance data to informative phase fraction and velocity data is itself included in the filtering system, as seen in the work of Liu et al. [80] for example, where it is used to solve the inverse problem. As for this work, the conventional tomographic process is used, and the resulting data is fed into the particle filter system as the focus and scope of this study is on providing flow measurement rather than improving the current potential of ECT. Along with this, the CFD model, which is required to be suitable for all possible flows encountered in industry, would of course be non-linear. As for dimensionality, despite this study restricting dimensionality due to the available data from a single experimental apparatus, the ideal final system could integrate high dimensionality when considering the large number of fluid properties, as well as the parameters related to flow regimes, which could be integrated into the system in industrial application.

5.3.3 *Simulation validation*

The first main stage of this study is to develop a CFD model of the experimental set-up described in Section 4.1.6, along with fluid properties and flowrates. Once complete, this must be validated against experimental data initially, to ensure the model is representative of the flow. This will be achieved by the comparison of average phase fraction from both experiment and simulation for a range of supplied gas superficial velocities. As mentioned previously, for simplicity, the test section will be filled with oil, and a range of gas flowrates are applied, being itself a multiphase flow, though no oil will be supplied via the pumps.

5.3.3.1 *Model*

The CFD model applied in this work will be the Euler-Euler model described in Section 3.4.2, applied using the OpenFOAM software. The reason for the use of this model, as opposed to the VOF model for instance, is due to application. In order for this system to have the potential to be applied in all the flow regimes and situations encountered in the oil and gas industry, the CFD model must be capable of achieving this, unlike the VOF model, which is specifically suited for segregated flows. Therefore it can be said that this approach is more viable to the end application of the system if the Euler-Euler model is used, despite the increase of computational resource required. All OpenFOAM C++ files used to conduct this simulation are included in

Appendix H, including files defining: flow geometry, initial/boundary conditions, model, and simulation set-up.

5.3.3.2 *Simulation validation results*

This section now describes the system and fluid parameters used in the simulation along with the model description, with respects to the experimental set-up described in Section 4.1.6 and the CFD model described in Section 3.4.2.

5.3.3.3 *System properties*

Property	**Value**
Pipe Diameter	0.08m
Pipe Height	1.41m
Instrument	Pressure transducer x2
	ECT system
	Reference air flowmeter

5.3.3.4 *Fluid properties*

Gas - air

Property	**Value**
Density	1.225 kg/m3
Viscosity	0.148 St

Liquid - silicone oil

Property	**Value**
Density	870 kg/m3
Viscosity	0.02 St
Surface tension	0.0183N/m

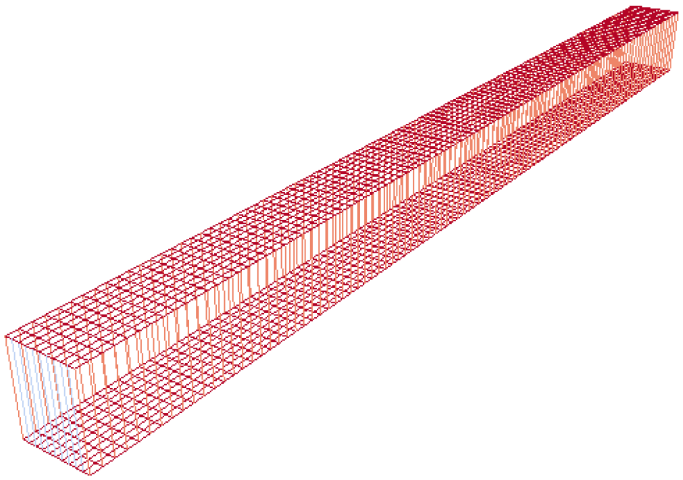

Figure 5.20: Image of the flow domain, including mesh, used in the simulation.

5.3.3.5 *Simulation set-up*

Property	Value
Software	OpenFoam
Solver type	MultiphaseEulerFoam
Dimension	2D
Mesh density	10 x 100
Time step simulated	0.0001s
Time step recorded	0.05s
Turbulence	Laminar
Duration	30s
Interface compression (IC)	1

Figure 5.20 shows the geometry of the flow domain, in accordance with the system properties defined previously. The geometry is displayed as a wireframe, allowing an observation of the mesh, with respects to the mesh density also defined previously. Despite the fact that the flow domain is shown here in 3D, the simulation itself is conducted as a 2D analysis, which can be observed by only a single cell visible in the z-plane.

Boundary conditions

Table 5.1 indicates the boundary conditions set for each main fluid property, with respects to the conditions at the wall, inlet and outlet[1].

The majority of conditions used here are self explanatory, except with the reference velocity and pressure, which is obtained from

1 The boundary condition description relates directly to the term used in the OpenFOAM software, a more general description can be found with reference to [23]

Property	Inlet	Outlet	Walls
alpha.oil	fixedValue: uniform 0	zeroGradient	zeroGradient
alpha.air	fixedValue: uniform 1	zeroGradient	zeroGradient
U.oil	fixedValue: uniform 0	zeroGradient	noSlip
U.air	fixedValue: uniform (0 u_{ref} 0)	zeroGradient	noSlip
Pressure(rgh)	zeroGradient	totalPressure: P_{ref}	zeroGradient

Table 5.1: Boundary Conditions for simulations

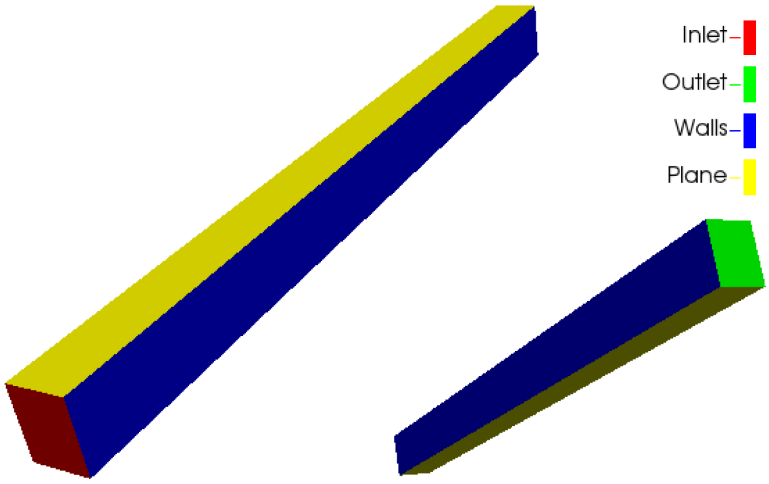

Figure 5.21: Image of the flow domain, along with indication of the boundaries within the simulation.

measurement by the reference flowmeter and pressure transducer respectively. The boundaries defined here can be observed as part of flow domain, and are displayed in Figure 5.21. The boundary designated as 'Plane' refers to an observation plane, considering the simulation is 2D, and therefore has no conditions assigned to it.

5.3.3.6 *Validation plots*

Now the simulation is prepared, 5 separate simulations (with respects to pressure and velocity conditions) are conducted, in line with the flow conditions outlined in Section 4.1.6. Providing a reasonable range of test points across the flow range that the flowloop is capable of. From the experiments, an average gas phase fraction is obtained for each test point, along with the time trace of the gas fraction to be used in the validation process. For each simulation, once complete, the post-processing stage consists of creating a "slice" plane at the geometry location which matches the central position of where the ECT sensor is located on the flowloop. The gas phase fraction in the slice area is then averaged and the data stored for all time steps, thus providing the simulated equivalence of the ECT time trace, along with

the averaged value. Now complete, the two outputs of the simulation can be compared to their equivalent experimental results, as shown in Figures 5.22 and 5.23.

Average gas phase fraction (alpha)

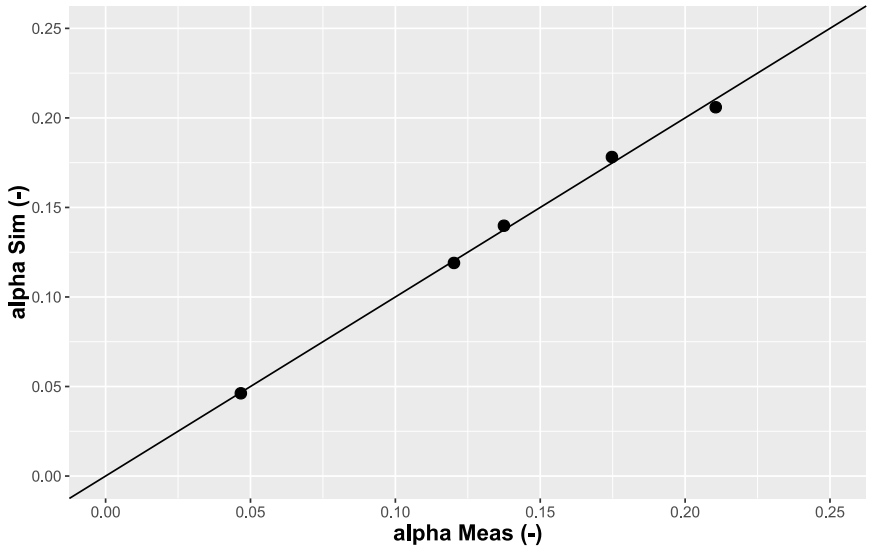

Figure 5.22: Average gas phase fraction validation plot.

Alpha time trace

The results overall validate the CFD simulations with respect to the conducted experiments. The data from the average gas phase fraction in Figure 5.22 show a strong comparison between simulation and experiment, with the variation particularly minor and thus not requiring consideration. As for the time trace validation plots, the comparison shown in Figure 5.23, show a distinct similarity in terms of the signal amplitude, frequency and range, hence the results also provide validation for the simulations. Despite the average gas fraction result providing reliable and clear validation, the time trace data is in fact more relevant, as the particle filtering system operates on a recursive basis of each data point in time, thus the similarity in the signals over time is particularly vital to the overall system.

5.3.4 *Particle filtering system application*

With the chosen CFD model and set-up validated, the work can now focus on constructing a particle filtering system suitable for application in measuring the state of the system described. This includes determining parameters and models which are used in the system, along with creating a method to allow the sampling of a range of CFD models without the requirement to simulate in real time.

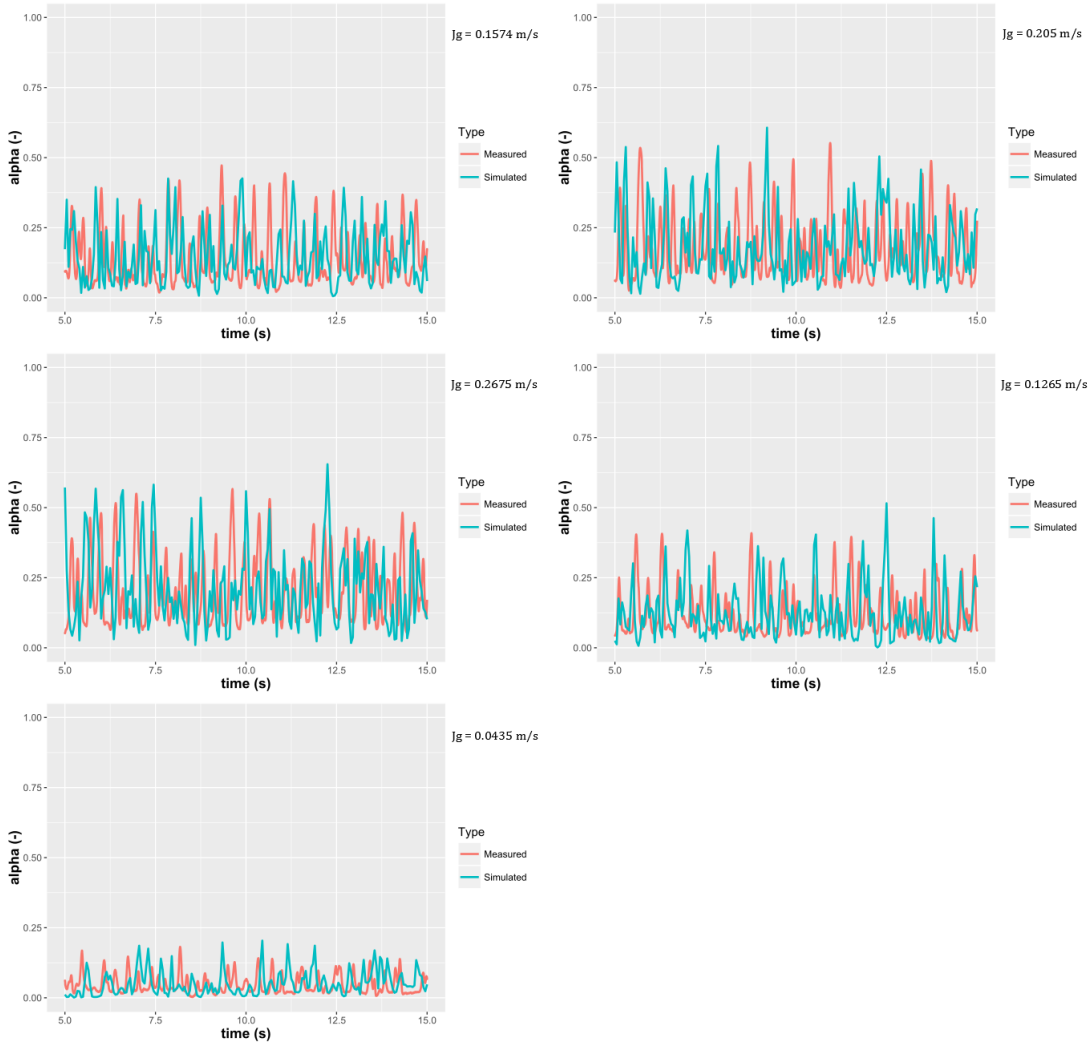

Figure 5.23: Alpha time trace validation plots.

5.3.5 *Method*

Due mainly to the requirement of a large number of simulations for every time step encountered within the system, it is deemed necessary to conduct a large scale of simulations prior to the operation of the particle filtering system, as in terms of computational resource, computing simultaneous simulations over time in a sensible timeframe (particularly when considering initial testing) is beyond the capability of the hardware available. Though this is the case currently, it is feasible to assume that for industrial application, not only would more expensive dedicated hardware be available, but the computational capacity available (at reasonable costs) is ever increasing, therefore making future applications more viable (according to Moore's law). The simulations must cover a large range of the system states to ensure that the simulation points represent that which would be available to a real time implementation. As well as this, sufficient density of simulations within this range is required to ensure a good accuracy is achievable. Once complete, an algorithm must be incorporated into the particle filter system which, in effect, feeds the simulation data into the system, as it would if the simulations were carried out during operation.

By choosing this method of creating a simulation database which the system refers to, some disadvantages are incurred, and must be considered. Firstly, a fixed number of simulations within the given range for the system states, does not represent the entire state space for which a full real time particle filter system would be able to sample from. Therefore it can be argued that the sampled state space would differ for the system being tested, and furthermore there will be a distinct limit to the convergence in positions of particles in the state space, limiting effectiveness. Despite this, by ensuring a reasonable number of simulations are carried out, and providing a bespoke re-sampling algorithm, which works to mimic what would be the case under a standard system, (in terms of both re-sampling procedure and regulation of the number of particles) the proposed system will operate to a close enough degree. Another difficulty with this proposal is in terms of the range of the simulations. A conventional particle filter system can effectively explore any region of the state space for which the model, along with any defined limits, allow. Therefore limiting the proposed system to a relatively small region of the state space can be considered unrepresentative. To alleviate this, the simulations will cover up to, and slightly beyond, the states encountered during the experiments. However, it is reasonable to assume that by limiting the state space, the system benefits from the fact that this entails a removal of possible states for which the system may, *incorrectly*, perceive the system to be operating at.

Once the simulation database is created, the particle filtering system itself must be developed. This involves firstly defining the measurements to be taken from the ECT measurement device, along with the corresponding measurement model, relating the measurement to a state variable, and finally the noise characteristics of the measurement. The system states must also be defined, and represent the variables which are being tracked in time. Despite there being no real limit to the number of states which can be prescribed, (as effectively any significant variable within the system could be included) for simplicity, the number of states are to be kept relatively low, but must include the vital flow parameters, which is the superficial gas velocity in this case. As mentioned previously, communication between the main program and the simulation database must be incorporated, along with a bespoke sampling strategy to mimic the re-sampling stage in a typical particle filtering system. Therefore, a range of functions are to be written in Python which achieve the goals described here, and will be called at each time iteration in the main script. As for the main operation of the system, other than the specific changes mentioned in this section, the system will be that of the bootstrap algorithm, mentioned in Chapter 3. The reason for choosing this particular particle filtering method is due mainly to its simplicity in application, allowing a baseline test of the system operating within this specific application which when complete, can be used as a justification for applying more complex algorithms, such as those described in Chapter 3.

With the system complete, initial testing will ensue, ensuring that the system is viable in its development, with any modifications or amendments added. Once complete, the system will be run for the five test flow points outlined in the simulation validation in Section 5.3.3.2. This will include providing the system with only the data produced from ECT and pressure transducers, and allowing it to track and predict the superficial gas velocity. The validity of the system will be based mainly on the resulting mean superficial gas velocity (or gas flowrate), compared to that obtained from the reference flowmeters. Furthermore, to test the systems ability to adapt to changes in the flowrate, the flow data (from ECT and pressure transducers) will be merged, thus providing an analysis of the systems capability in sampling the state space when presented with changing measurements. As commonly seen in particle filtering, a convergence analysis will be undertaken, where the resulting flowrate estimation will be obtained at variants of number of particles used. This is relevant as, from the law of large numbers, the estimation is expected to converge on the true result as the number of particles used increases. Finally, the results predicting the phase flowrate from the particle filtering system can be compared to that obtained from both empirical correlations for similar flow ranges, as well as from ECT as a standalone sensor.

State	Minimum	Maximum	In steps of
Superficial gas velocity, J_g (at inlet) [m/s]	0.02	0.3	0.01
Pressure, P (at outlet) [Pa]	850	950	5

Table 5.2: Description of the range of boundary conditions used for simulation database.

5.3.5.1 *Simulation setup and implementation*

The simulations for this study are implemented using the model, boundary conditions and parameters described previously in the simulation validation in Section 5.3.3.2 (using the corresponding OpenFOAM C++ case files included in Appendix H) with the only difference being the range of velocities and pressures used. These values must cover beyond the range of values tested and must be relatively small intervals to ensure a suitable resolution is achieved. These values are described in Table 5.2. Therefore, to achieve the determined suitable number and range of simulation states, we require 609 simulations to be conducted.

The simulations were carried out on a High Performance Computer (HPC) provided by Coventry University using the Message Passing Interface (MPI) included in the OpenFOAM software. The HPC system has 4 nodes each with 16 real processors available, allowing 4 jobs to be conducted at the same time with a specified number of processors. Prior to performing the simulations, a parallel processing test was undertaken to find the optimum number of processors to use for each simulation. Parallel processing of CFD simulations effectively works to separate the flow domain into multiple segments, which are computed separately on a single processor, then merged together in the attempt to reduce the overall processing time. The reason for undertaking a parallel processing test is due to the fact that the separation and calculation of regions, and re-joining, of the flow domain does itself produce an additional computational cost. This thus produces a limit of the number of parallel processes which, if reached, does not provide any reduction in processing time, and in fact may increase it. The result of the parallel processing test is portrayed in Figure 5.24, where a single simulation is timed and repeated for different numbers of processors used.

The result shows that, in fact, a very low number of parallel processes should be used. This is not surprising as, due to the relatively simple and coarse nature of the flow geometry, there is only a small benefit to be gained through parallel processing. Despite this, it is possible to perform 4 individual simulations (using 4 processors each) at any time, as 4 cores are available, which also contributes to producing the results in a timely manner. Finally, an option available during parallel processing is with regards to process binding, which gives

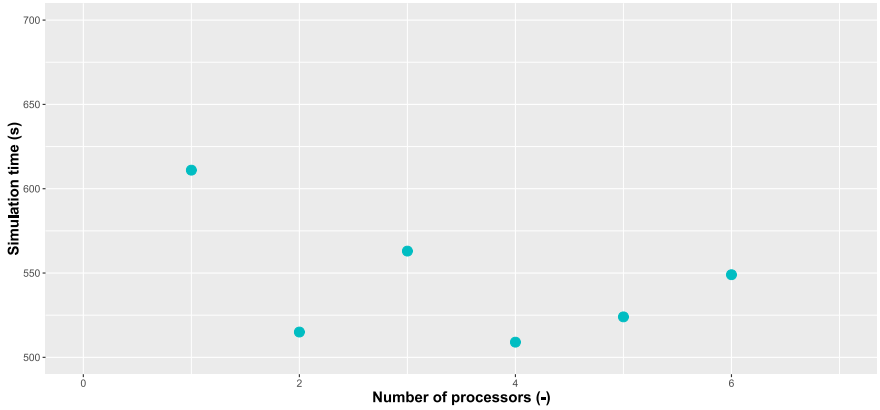

Figure 5.24: Parallel processing efficiency test for a single repeated simulation.

the user some control over the process distribution, so as to maximise communication between cores on the same CPU [74]. For the MPI provided, 3 options are available, being: No binding, Bind-to-core and Bind-to-socket. Tests showed that the Bind-to-Socket option produced the fastest simulation time and therefore is adopted.

5.3.5.2 *Simulation post-processing*

The post-processing procedure is undertaken on all 609 simulations of flows described in the previous section. Due to the large amount of files considered, it is necessary to automate this process in order to create the usable data in a reasonable time frame. To do this, a Python script was developed using a plug-in for Paraview (the post-processing software used in OpenFOAM), the script is outlined in Appendix G, along with the simulation run script. This procedure uses a Paraview state file, generated from a sample post-processed data set following the steps outlined in Section 5.3.3.6. The python script loads a particular simulation data file, then applies the state file through Paraview automatically, and exports the resulting data in standard format; this process is then repeated for all 609 simulations. This results in a simple data file, for each simulation, with the results of all averaged simulated properties at the measurement plane specifically.

5.3.6 *Outline of particle filter system*

5.3.6.1 *System states*

The two states of the system are chosen to be the superficial gas velocity j_g and the pressure P_{outlet}.

$$\mathbf{x} = \begin{bmatrix} j_g \\ P_{outlet} \end{bmatrix} \Bigg(\tag{5.4}$$

It is important to note that, the tracked states refer to those averaged at the measurement plane (j_g), and the outlet (P_{outlet}) in the flow geometry. However, the states for which the simulation boundary conditions refer to are those at the inlet (for j_g) and the outlet (for P), caused by the fact that the model is required to cover the defined flow domain. For a real time simulation system, this would cause a problem due to how the re-sampling procedure (which refers to the measurement plane) would reflect at the inlet/outlet boundary condition; this will be further discussed later. The main reason for the selection of these variables as the system states, is that they remain the two modifiable variables within the simulation. For instance, although the gas phase fraction α_g could itself be considered as a useful state within the system, due to the nature of the simulation set-up, this quantity is determined (at the point of simulated measurement), based on the interaction of the gas superficial velocity and outlet pressure. Therefore it cannot be assigned in the simulation conveniently when the system samples particles. If the simulation was set-up so that the flow domain was simply a segment of the cross-section (not including the whole length and thus the inlet), it could be feasible to include α_g as part of the state, however, this would itself have implications on the superficial gas velocity at the modified inlet, as it would become more complex in terms of its cross-sectional profile. For the states defined, the Pressure P_{outlet} is simply used firstly to assist us in applying the simulation database defined previously, but also to outline how additional states in future developed systems would act, providing greater state possibilities and accounting for the possible inaccuracies in the pressure transducer measurements. Alternatively, the gas superficial velocity j_g is the state of interest, and therefore is what is used to define the overall measurement, and thus the validity of the system.

5.3.6.2 *State transition model*

The state transition model in this work is pre-defined in the results from the simulation database, described as:

$$P(x_t|x_{t-1}^{(i)}) = f_{cfd}(x_t^{(i)}) + \omega_{model} \tag{5.5}$$

Outlining that, to obtain a particular state value of a particle (i), propagated through time (from $t = t - 1$), the simulation database is accessed for that particular particle at the new time (t), defined as the function $f_{cfd}()$. In addition, as stated in typical particle filtering algorithms, the model noise is included which, will be described as a non-zero Gaussian function, with variance value discussed later. The inclusion of the noise function is less straightforward with the simplified system, as the use of a simulation database means that only a limited discrete number of states are available. This issue is addressed in the algorithm presented later.

5.3.6.3 *Measurement models*

The measurements which are considered in this system are firstly the gas phase fraction α_g, along with the cross-correlation velocity u_{cc} and the outlet pressure P_m. The gas phase fraction must be included due to it being the most fundamental and useful measurement which can be obtained from ECT, as well as having a strong relationship with the system states. As for the cross-correlation velocity, it could be said that it is not necessary, due to the fact that it is essentially a secondary measurement and could be replaced by an additional gas phase fraction measurement at the second measurement plane. However, due to the very small gap between measurement planes, extracting the equivalent information, by comparison to the model, is difficult, and furthermore, the addition of a velocity measurement could significantly improve the system capability, as it has a separate measurement model, and thus can be treated independently. For the gas phase fraction α_g, the relation to the system state is handled by the CFD model itself. In this sense, we can describe the measurement model simply as:

$$\alpha_g = f_{cfd-meas}(\mathbf{x}) + \omega_\alpha \tag{5.6}$$

where: $f_{cfd-meas}()$ is the function of determining α_g from the CFD model, and ω_α is the noise associated with the measurement.

This is due to the gas phase fraction being modelled at each time step and therefore being related, through the model, to the system states. In addition to its relation to the states as described in the numerical model in Section 3.4.2, which describes the gas phase fraction at all points in the flow domain, the function $f_{cfd-meas}()$ also refers to the averaging process of value at the corresponding measurement plane in the flow domain, as described in Section 5.3.3.6. In this case, the measurement noise ω_α is described by a zero mean Gaussian distribution with variation of 0.1. This value is chosen by considering the high accuracy obtainable through ECT in measuring the gas phase fraction α_g, when compared to other methods such as wire mesh sensor as conducted by Azzopardi et al. [9], which suggests a value smaller than 0.1, though this value is deemed suitably small to describe its behaviour, but with some additional leniency.

For the pressure measurement model at the outlet, like the gas phase fraction, a zero-mean Gaussian distribution is used to describe the measurement noise, except here the measurement is directly representing the state P_{outlet}.

$$P_m = P_{outlet} + \omega_P \tag{5.7}$$

In choosing the value for the variance noise, taking into account the relatively low sensitivity of the pressure transducers, a value of

10 is used. Despite this value exceeding the expected noise of the instrument, it is selected also to allow a higher range of particles to be considered, and additionally reducing the influence of the pressure measurement. This will act to mitigate further some of the effects of using a simulation database, as it effectively permits a greater area of the state space to be areas of high likelihood. This assumption is backed up by trial and error testing of the system, but can also be justified due to the minimal effect of this pressure value on the simulation result when compared to the assigned rate of gas flow.

Considering now the measurement model for the cross-correlation velocity u_{cc}. It is decided that this measurement will be modelled with respect to the gas superficial velocity solely, based on the relation described by eq. (2.16) in Section 2.4.3. As the flows considered here including only gas flow through stationary oil, eq. (2.16) can be modified to the following, as the mixture superficial velocity term simplifies to the gas superficial velocity:

$$u_{cc} = \frac{\partial j_g}{\partial \alpha_g} = \left(C_o j_g + V_{gj}\right) + \alpha_g \frac{\partial \left(C_o j_g + V_{gj}\right)}{\partial \alpha_g} \tag{5.8}$$

In order to convert this to a direct relation between measurement and state, we can asses the difference between the kinematic wave speed and actual gas velocity $(\frac{\partial j_g}{\partial \alpha_g} - \frac{j_g}{\alpha_g})$, which, when re-arranged, gives:

$$u_{cc} = \frac{j_g}{\alpha_g} + \alpha_g \frac{\partial \left(C_o j_g + V_{gj}\right)}{\partial \alpha_g} \tag{5.9}$$

Referring back to Section 2.4.3, it is known that the term furthest on the right is both small in value but difficult to solve. Therefore, we can replace this term with a non-Gaussian noise function, as:

$$u_{cc} = \frac{j_g}{\alpha_g} + \omega_{u_{cc}} \tag{5.10}$$

Considering that this equation includes two measured variables, it is decided to group them together to give a superficial gas velocity measurement obtained through both the cross-correlation velocity and gas phase fraction measurement. This then provides a measurement model in the following form:

$$j_{g-cc} = u_{cc}\alpha_g = j_g + \omega_{u_{cc}} \tag{5.11}$$

We now have a defined measurement model for the cross-correlation velocity (combined with the gas phase fraction), leaving only the need to define the noise function $\omega_{u_{cc}}$ suitably. With reference to eq. (5.9), it

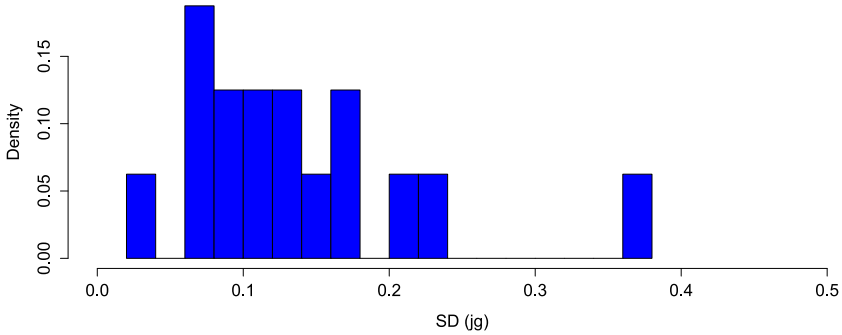

Figure 5.25: Histogram showing the standard deviation between measured j_{g-cc} and the referencej_g for both gas flow only, and oil and gas flow tests.

is known that the cross-correlation velocity multiplied by the gas phase fraction (j_{g-cc}) will always be lower than the actual gas superficial velocity, which is seen in all results in this work, and can justify a non-Gaussian noise being used. In order to choose a suitable noise function, we can analyse the difference between these two terms for both the test points used specifically for this work (gas flow only), along with some additional gas and oil flows which were conducted on the same flow loop. The results for this are depicted in Figure 5.25, which shows a histogram plot of the standard deviation between the measured term j_{g-cc} and reference term j_g.

By observing the results in Figure 5.25, along with considering that the optimum solution would also represent flows outside the tested range, an exponential noise distribution function is chosen. This distribution will always provide a positive value, for reasons explained previously, and is described by the following equation:

$$\omega_{u_{cc}} = f(x,\lambda) = \begin{cases} \lambda e^{-\lambda x} & x \geq 0 \\ 0 & x < 0 \end{cases} \tag{5.12}$$

With reference again to Figure 5.25, the value of lambda (λ) is selected as 0.3. This provides a reasonable description of the noise function at values close to 0, though over estimates the likelihood of values higher than this. Despite there being many other variations of noise distributions which could model this measurement noise, this function is deemed a reasonable solution for the flows considered in this work. It is likely that, if this system was to be applied for a larger, or entire, flow range, a more sophisticated approach may be necessary. However, it should also be considered that this measurement model would have to change to facilitate both oil and gas flows due to the assumption made for eq. (5.8).

Parameter	Value
Variation in Gaussian distribution for α_g	0.1
Variation in Gaussian distribution for P	10
Lambda value of exponential distribution for j_{g-cc} (λ)	0.3
Variation in Gaussian distribution for model noise ω_{model}	0.01
Number of particles (N)	3000
Time step (Δt) [s]	0.05

Table 5.3: Particle filtering system parameters.

5.3.6.4 *Parameters*

The parameters used in these tests, some of which have been defined in Section 5.3.6, are outlined in Table 5.3.

As mentioned, most of these values were defined in Section 5.3.6, except the model noise variation and number of particles used. Firstly, the model noise variation was based on results from initial testing, the value is arguably lower than would be expected, despite the high accuracy in the simulation validation results in Section 5.3.3.6. This is due mainly to the use of the simulation database, causing the relevance of this term to be undermined as there are a fixed number of simulation outcomes available. Furthermore, due to the large variation assigned to the pressure measurement model, initial tests showed that a suitable range of the state space was sampled at each time interval, and substantial increases in the model noise variance (needed to have significant effect), would include too many particles, and thus reduce the systems need to explore the state space when changes occur. As for the number of particles, despite only a small number being required, again due to the fixed number of simulations, a particularly large number was selected. This both ensures the system can operate at what is considered a normal number of particles used in typical particle filtering systems, but to also remove any effects from lack of samples; the effect of number of particles on the results is described in the convergence analysis in Section 5.3.8.4.

5.3.6.5 *Prior distribution*

The final consideration prior to implementation of the particle filtering system is with regard to the prior distribution. This distribution represents the likelihood of the states at the beginning of the process, when no measurement data is present, and thus defines the systems uninformed knowledge of the states. When considering the possible applications of such a system, it is assumed that, at this point, no value of state, or area within the state space, is more likely than another.

Algorithm 5.1 Particle filtering for the simplified system, based on the Bootstrap algorithm.

1. Initialisation

$t = 0$

For $i = 1...N$:

Sample $x_0^{(i)} \sim P(x_0)$

$t = 1$

2. Importance sampling

For $i = 1...N$:

Sample $x_t^{(i)} \sim P(x_t | x_{t-1}^{(i)})$

Replace $x_t^{(i)}$ with nearest values in $f_{cfd}(x_t^{(i)})$

Import measurements: $\alpha_{g,t}$, $P_{outlet,t}$ and $u_{cc,t}$

$j_{g,t} = u_{cc,t}\alpha_{g,t}$

Construct $y_t = \begin{bmatrix} \alpha_{g,t} \\ P_{outlet,t} \\ j_{g,t} \end{bmatrix}$

Evaluate importance weights $w_t^{(i)} = P(y_t | x_t^{(i)})$, (based on measurement models)

$w_t^{(i)} = \frac{w_t^{(i)}}{\sum_{i=1}^{N} w_t^{(i)}}$

Export results from $f_{cfd}(x_t^{(i)}(max(w_t^{(i)}))$

3. Re-sampling

Multinomial Re-sampling of $x_t^{(i)}$ with replacement N particles, based on $w_t^{(i)}$

Replace $x_t^{(i)}$ with nearest values in $f_{cfd}(x_t^{(i)})$

$t \rightarrow t + 1$

Return to step 2

Therefore, a uniform distribution will be assigned to the state space as the prior distribution.

$$P(x_o) = unif(x_{min}, x_{max}) \tag{5.13}$$

5.3.7 *Algorithm*

The particle filtering method used in this study is, for the most part, that described as the original Bootstrap algorithm, as outlined in Chapter 3. One of the main points of difference is the additional steps required to account for the fact that the simulations were carried out prior to the operation of the system. The procedure for implementing the proposed particle filter algorithm is displayed in Algorithm 5.1, and the Python code implementation is provided in Appendix G.

By comparing this to the Bootstrap method described in Chapter 3, the steps are essentially the same, except with some additions to ac-

count for the use of a simulation database. The differences include the state transition simplification, where the new state vector is essentially referenced from the simulation database at the new timestep. But also in how the data is exported, where the simulation which corresponds to the state with the highest weighting $max(w_t^{(i)})$, is accessed to export the state, and any additional variables, at the measurement plane. Finally, due to the discrete nature of the available simulations, the relevant sampling stages involved (state transition and re-sampling), are limited in which values they can take. Therefore a replacement step is included, where a simple function is introduced to assign any continuously sampled values to be converted to their closest neighbours which are present in the simulation database. It is worth noting that, because of this, the number of replacement particles (N) in the Re-sampling stage, varies depending on the number of samples that, when replaced, take on the same values. Therefore, when a sufficient number of particles are used initially, the effective value of N will reduce over time due to identical particles being present.

5.3.8 *Results*

With the particle filtering code and data communication developed, based on Algorithm 5.1, and with initial tests complete, the program can be run for each data set outlined in Section 4.1.6. Prior to showing the results of the particle filtering system, the results from the simulation output will be displayed, with specific reference to the simulations from the database which correspond to the experimental data. Starting with the gas phase fraction (α_g), Figure 5.26 displays the entire flow domain at different times during the simulation, with respect to the simulation with the boundary conditions: $j_g = 0.27$ and $P_{outlet} = 930$. Figure 5.27 displays the equivalent results, but for the gas velocity magnitude, over the same time periods and with the same conditions. The initial transient behaviour of the flow (~2.5s) is not included as part of the particle filtering system, as the tomography data is recorded at steady state. Visual inspection of the experimental apparatus during this period however, confirms that both the time period, along with the observable taylor bubble in Figure 4.1.6 is consistent with the experiments.

5.3.8.1 *Gas superficial velocity estimation*

With the algorithm parameters set, the system is run for all test cases. The first results to be analysed are that of the gas phase fraction obtained from the corresponding simulation at each time step, representing the assumed gas phase fraction after the filtering process. This allows us to ensure that the process is viable as, based on the system parameters, the simulated gas phase fraction should correspond with

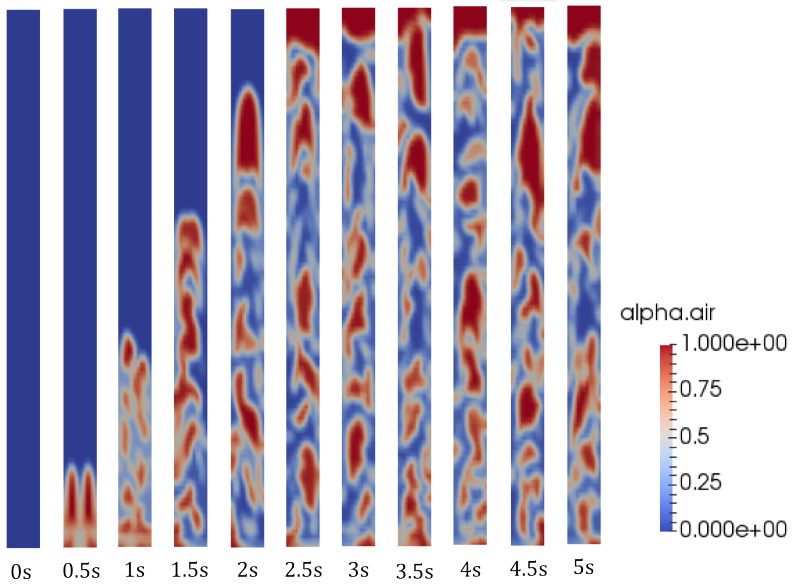

Figure 5.26: Snapshots of the simulated values of the gas phase fraction through time at: $j_g = 0.27m/s$ and $P_{outlet} = 930Pa$.

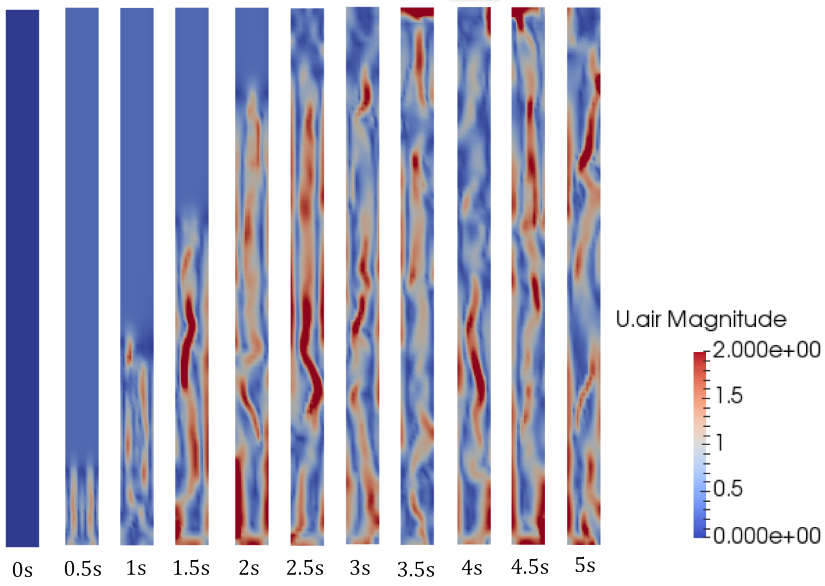

Figure 5.27: Snapshots of the simulated values of the gas velocity magnitude through time at: $j_g = 0.27m/s$ and $P_{outlet} = 930Pa$.

those obtained through tomography, but with small differences (equivalent of a variance of 0.1). Figure 5.28 displays both the simulated gas phase fraction and the measured (from tomography) for all test cases.

Overall the results suggest that the particle filtering process is viable in terms of the main measurement model. For all test cases, the results show a strong similarity between simulated and measured values, with differences corresponding to the assigned noise variance. A notable exception can be seen for the results for $j_g = 0.205$ and 0.2675, where at a specific point, the simulated gas phase fraction is displayed as 0 and is notably different to the measured value. This occurred during operation where, at those points, the set probability distributions have designated all active particles with a weighting of 0, therefore no specific result was assigned with the highest likelihood. This highlights a deficiency in the modelling of distributions, and will be further discussed later. Despite this, it is clear that within a short period of time, the system recovered and particles were sampled and weighted correctly. Overall, due to the minimal amount of time-steps affected, this issue did not have a significant effect on the overall results.

Moving on now to the corresponding results for the gas superficial velocity (j_g), which represent the systems ability to conduct flow measurement, and thus acts as the main indicator of performance. Firstly, as done previously with the gas phase fraction, the simulated results for j_g are plotted for each time step. As there is no reference measurement at the test section (where the ECT sensor is located), these measurements are compared to the gas superficial velocity at the inlet, obtained from the reference flowmeters. With the average of the simulated j_g expected to correspond to the reference measurements. These results are depicted for each test point in Figure 5.29. By taking the average values of the simulated gas superficial velocities, and comparing them to the reference measurements, a validation plot can also be produced, as shown in Figure 5.30.

The results from both Figures 5.29 and 5.30 show a strong performance in predicting the gas superficial velocity, and therefore the gas flowrate. Starting with Figure 5.29, for all test cases, the predicted j_g values follow the reference values well. As would be expected, the amplitude of the signals increase significantly with increasing gas flowrates, where larger bubbles, or slugs, coalesce prior to passing the ECT sensor. Furthermore, the frequency of the simulated signals seem to increase slightly with increasing flowrates, particularly in the test point with the largest gas flow ($j_g = 0.2675$), which corresponds to results of the gas phase fraction. As seen with the results from the gas phase fraction, where the weighting process fails and produces a zero result for two test cases, it is seen that these are repeated for the gas superficial velocity as would be expected. Again, due to their relatively short timespan, their effect is disregarded for now, which can be

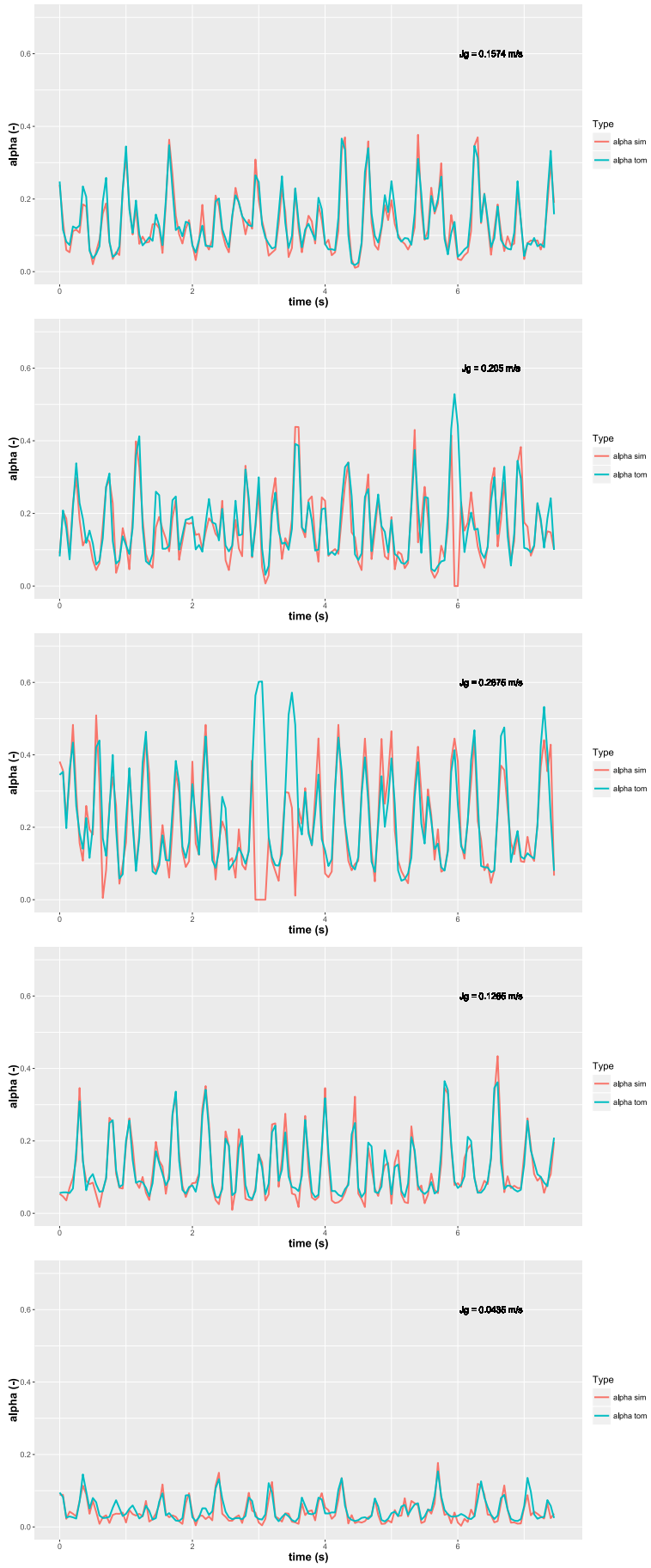

Figure 5.28: alpha time traces from both tomography and that of the state predicted by the particle filter system.

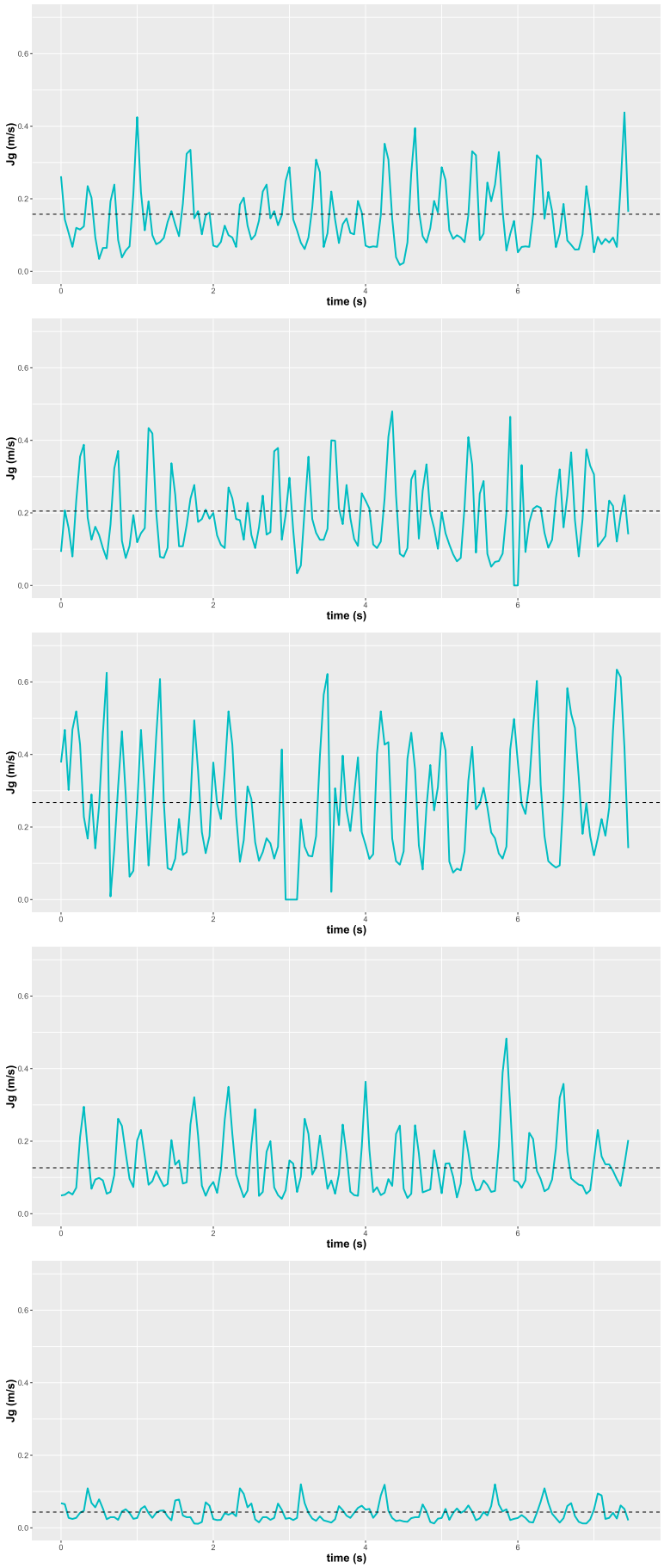

Figure 5.29: Result of superficial gas velocity state at each time-step, along with the corresponding reference measurement (dotted black line).

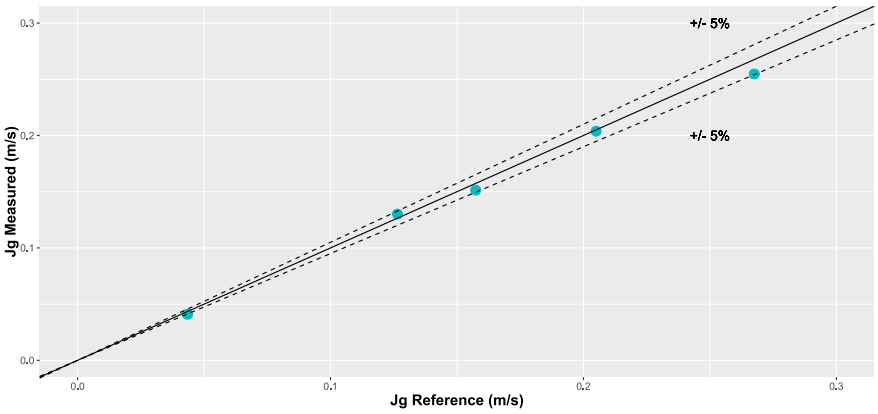

Figure 5.30: Validation plot for all test cases, comparing the reference measurements to the averaged state estimation form the particle filtering system.

justified by the overall accuracy obtained in Figure 5.30. The validation plot shows that the prediction of the overall gas superficial velocity, and therefore gas flowrate, is well within +/- 5% and is therefore a viable solution to flow measurement for the tests conducted.

5.3.8.2 *Accuracy comparison*

Now with the overall results from the particle filtering system, a comparison can be made to other flow measurement methods using ECT. Firstly, one method to obtain j_g using the mean gas phase fraction measurement from ECT is by use of empirical correlations as described by eq. (2.14) in Section 2.4.3. For this, as seen in the previous studies, values must be given for the distribution co-efficient C_o and the drift velocity V_{gj}. As mentioned previously, these depend on the specific flow range and type, flow regime for example. For the flowloop and flow range used in this work, the most suitable proposed correlations come from the work of Lemari [89], who suggests the following:

$$C_o = 1.06; \quad V_{gj} = 0.991$$

Which can be directly inputted into eq. (2.14) (with the mixture superficial velocity (j) exchanged with the gas superficial velocity (j_g) for gas flow only), therefore allowing the prediction of j_g from the ECT measurement of α_g. The results of using this correlation in predicting j_g are displayed in Figure 5.31.

Another comparison which can be made is by using ECT as a standalone measurement system, where the gas phase fraction and the cross-correlation velocity are combined to estimate the gas flowrate. Although this is not a robust method, due to the fact that the cross-correlation velocity represents a kinematic wave speed as opposed to the actual gas velocity (as discussed in Section 2.4.3), it represents the

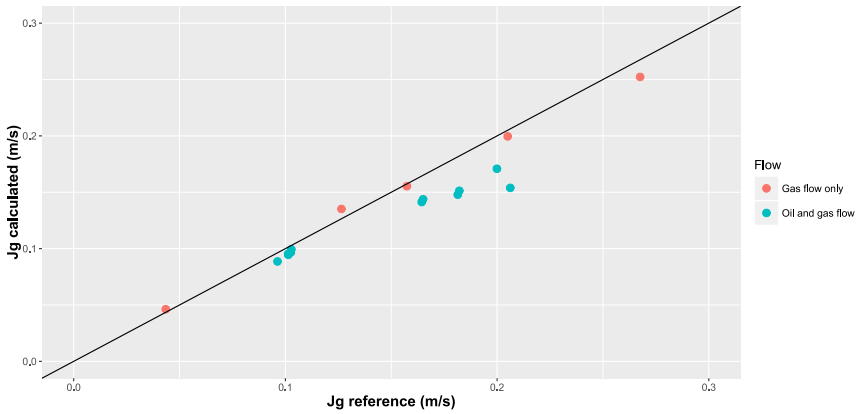

Figure 5.31: Comparison of results for superficial gas velocity from reference measurements and calculated from empirical correlations.

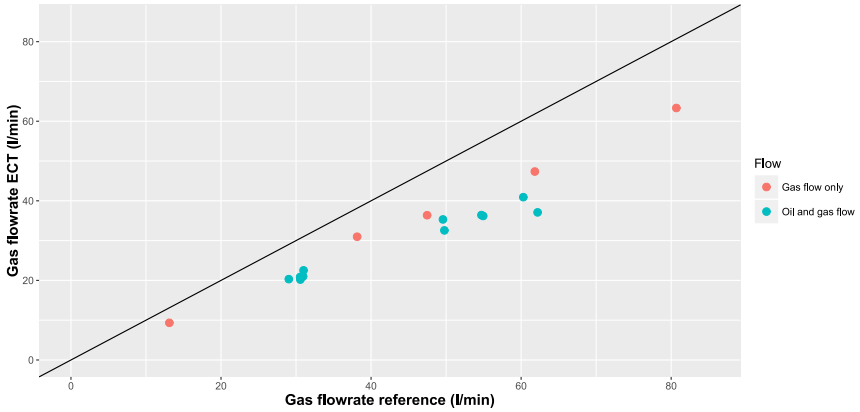

Figure 5.32: Comparison of gas flowrate estimation from reference measurement and conventional ECT measurement.

effectiveness of ECT as a multiphase flowmeter without the use of correlations. Furthermore, in gas solid flows for example, this method has been proven to be viable [63], as the cross-correlation velocity does represent the velocity of a solid discrete phase. The results from applying this conventional ECT flow measurement method to the flows considered is shown in Figure 5.32.

Starting with the results from the correlations depicted in Figure 5.31, it can be said that a very similar accuracy in measurement is obtained when compared to results from the particle filtering system, for gas flow only tests. This is somewhat expected as the tests for which the empirical correlations were based on [89], are very similar in terms of flow range to the experiments conducted here. Despite the similarity in accuracy potential, the most crucial point is that the correlations used are limited to a specific flow range, where the obtainable accuracy will reduce significantly with flows further from the specified range, therefore requiring changes to the parameters to maintain this performance. Whereas the particle filtering system can

operate effectively at any flow range if in a developed form, i.e. when the system simulates test points in real time (as with conventional particle filtering systems), thus allowing further exploration of the state space, or if the simulation database used covered a greater flow range.

Considering now the estimation of flowrate from conventional ECT method depicted in Figure 5.32. Looking firstly at the gas flow only tests, it is clear that the error margin is significantly larger than results from the particle filtering system. This is expected as it uses the assumption that the measured wave speed is equal to the actual gas velocity, thus the measurement under-estimates the true result as proven by eq. (5.9). Furthermore, at higher gas flowrates, the measurement error increases linearly as the ratio between wave speed and gas velocity increases, again suggested by eq. (5.9). As for the tests with both oil and gas flow, a similar trend is observed for the reasons pointed out previously, however, the error margin is slightly increased which can be explained by referring back to eq. (2.16) in Section 2.4.3 (inclusive of the mixture superficial velocity), where the effective difference between measured wave speed and gas velocity will increase with any addition to the mixture superficial velocity j, i.e. by the inclusion of an oil flowrate.

5.3.8.3 *Transient flow analysis*

A further test which can be carried out is the assessment of how the particle filtering system adapts to changes in the flow. This, of course, is vital in industry operation as the flows encountered can change both slowly and rapidly dependent on the application. Such operation of the system will test its ability to search the state space effectively and reposition itself at the correct gas flowrate. In order to accomplish this, the system is tested with data combined from two separate test cases. This is achieved by merging the measurement data of two test cases, including the gas phase fraction measurement and cross-correlation velocity from the ECT system, along with the pressure measurement from the transducers on the flowloop. Figures 5.33 and 5.34 show the resulting prediction of the gas superficial velocity state in time from the particle filtering system for two separate cases. The graphs also depict the reference gas flow measurement at the inlet and its subsequent change.

It is clear from the results that the particle filtering system successfully measures the gas flow when the change is applied, with the results showing a strong similarity to the corresponding individual results in Figure 5.29. During the transition, the time gap between moving from what was expected for the first half of data and the second, is relatively low at around 1 second. This represents the time in which the particles move to the higher likelihood regions of the state space and are well within reasonable timespans for the adjustment.

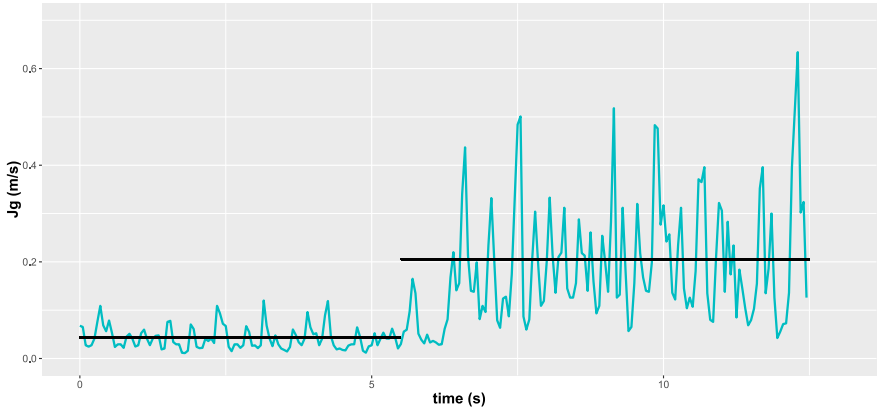

Figure 5.33: State estimation result from particle filtering system for data merged from two separate test cases, including reference measurement at inlet (black line).

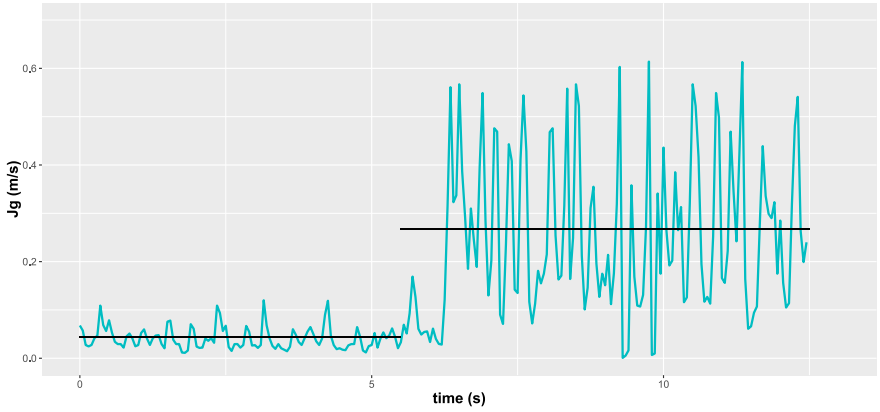

Figure 5.34: State estimation result from particle filtering system for different data merged from two separate test cases, including reference measurement at inlet (black line).

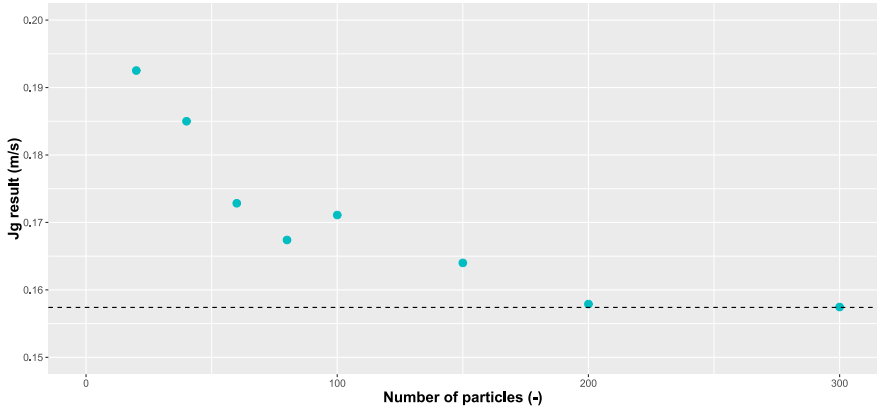

Figure 5.35: Convergence analysis of particle filtering system with increases in the number of particles used.

Overall the results suggest that the proposed particle filtering system would successfully meter such varying multiphase flows to a high degree of accuracy, therefore justifying the application of this method.

5.3.8.4 *Convergence analysis*

As pointed out in Section 5.3.5, a common analysis stage in assessing particle filtering systems is with respect to convergence. Due to the nature of the method, it is assumed that, with an increase in the number of particles used in the system, the law of large numbers dictates that the likelihood distribution will converge towards the actual distribution of the state. In order to test this, a single test point is chosen and the system is applied at multiple intervals of number of particles. The overall mean of the superficial gas velocity is collected from each iteration and then compared to the reference gas flow measurement at the inlet. The results of this test are displayed in Figure 5.35.

The result shows a smooth convergence towards the expected value of j_g, from the test using 20 particles up to using 300 particles. By between 200 and 300 particles, the result successfully converges on the true value, with all but one case of increases in particle number causing a reduction in the error margin. At 100 particles, the result produces a higher error margin than seen at 80 particles, though this can be explained as being due to degeneracy, where the lack of sufficient particles restricts the systems capability to cover sufficient areas of high likelihood within the state space. It is noted that convergence is reached at a relatively low number of particles, when compared to the number used in conventional particle filtering applications, as well as the number used in the previous tests. This is likely due to the use of a simulation database, which restricts the limit of resolution possible within a specific area of the state space, therefore limiting the benefits

of including more particles. Overall the convergence analysis assists in proving the viability of the method proposed for flow measurement.

5.3.9 *Discussion*

From the work carried out in this study, it has been shown that, by applying a particle filtering method to tomographic based flow measurement, by the method outlined, an accurate estimation of the flowrate can be achieved for the flow types considered. Furthermore, the results indicate that such a method can be applied to a much broader scale of flows, including multiple flow regimes if the corresponding simulation validation and amendments to the measurement models are applied. Therefore, this work acts as a basis for future developments in creating a FRIMM system based on tomography which could achieve suitable performance when applied in oil and gas applications.

In terms of parameter selection, a relatively simple analysis of data was used in order to define a suitable value for those described, and initial testing for the others in order to obtain the optimum values. To allow this system to further increase its potential in terms of flow range, larger data sets, tested at a range of flow types, would be beneficial in selecting parameters, and distributions, which can be applied to larger variations in flows. This, of course, also applies to the models themselves, which, in this application have been chosen specifically for the test cases used. The time resolution for both the simulation and particle filter system was chosen as it is small enough to ensure the significant changes in flow variables are measured/modelled while minimising the pre-simulation time. Considering the obtained accuracy, it is unlikely that a greater resolution would affect the results noticeably. If the resolution is reduced slightly, a similar outcome could be achieved at a smaller computational cost, which, for a developed system, may be relevant.

Considering now, the results from the transient analysis where the system reacted to a change in gas flowrate. It is notable that the process of merging data from two separate experiments is limited in representing transient behaviour, however, for this system specifically (in terms of flowloop sizing and liquid properties), the transition stage is minimal, and the new steady state is reached in a very small time period. An ideal test would consist of applying a sinusoidal wave input from the pump, where the rate of the systems convergence could be analysed, though hardware limitations restricted the gas flow input to a single value in this work. Alternatively, measuring the developed flow with an alternative multiphase meter, one which is specifically suited to these flow types, would allow a significant validation for transitions tests. This is due to the reference being specific to the

measurement area (with the flow developed), as opposed to relying on single phase references at the inlet.

Providing a suitable alternative method for comparison to the results gained by this system is difficult, considering that the potential ranges of flows for which it could measure must be considered. As seen in the comparison plots, the use of linear relations and empirical correlations can match the accuracy obtained through particle filtering, though they remain far more limited in their potential. Due to the lack of multiphase meters which can be applied, theoretically, to all flow types, it is a fair assumption that if the proposed method can match that gained through correlations, then the system has potential for industrial application. Alternatively, one could compare these results to that gained by single phase flowmeters, which can currently obtain accuracies which far surpass those gained in this work. However, in making such a comparison, the negative effects of the separation process (required for single phase metering) on the overall oil and gas processing must also be considered.

The two main simplifications made during this work, which could not be applied in a realistic application, were the application of gas flow only, and the use of a simulation database. Firstly, by introducing oil flow in addition to gas flow will have an inevitable effect on the outcome. It is assumed that the CFD models ability to represent the flow, observed through a simulation validation, will likely reduce as the flow becomes more complex. This would initially suggest that the achievable accuracy would be reduced, when compared to the results shown in this work. However, by including this uncertainty into the model noise of the system (affecting the re-sampling distribution), along with significantly increasing the number of particles used (on the basis that a simulation database is not used), the negative effects of introducing oil flow could be reduced, and hence still provide a satisfactory outcome. Furthermore, the addition of oil flow would require the measurement models and states to be amended to facilitate this, though it is unlikely that this change would cause any significant effects. The other simplification made by the use of the simulation database is more a case of technological restriction, where the computational resource required is particularly large. As for the effect on the results, a particle filtering system which simulated on a real time basis would have two major effects, both being positive. Firstly, the achievable accuracy for more complex systems would increase as the possible resolution of the state space is no longer limited, allowing the system to calculate the outcome of states in a highly focussed area. The other, more obvious, effect would be to lift the restriction of flow range, as the system can explore any part of the state space as it is not restricted to the areas which have been pre-simulated.

An error that occurred, and was pointed out, within the particle filtering system during this work was due to the active particles all

being assigned zero values due to inconsistencies in the comparison between ECT measurement and measurement models. Despite this issue being quickly addressed by the system and not affecting the results, it can be analysed further. Such a problem has been highlighted in work applying machine learning to robotics applications, where a suitable solution was proposed [113]. By introducing a low weighted uniform distribution to the applicable range in the measurement models, the zero value weighting can be avoided without influencing the calculated likelihood during normal operation, therefore alleviating the negative effect of random measurements or limited distributions.

A significant issue faced with applying a particle filtering system over a geometry, where a time delay exists between the system input (via a change in gas flowrate) of the state (as an initial condition of the model simulations), and the point of measurement (where the actual state is recorded), is with regards to sampling. In this work, as the simulations were conducted beforehand, the transient effect at the beginning of the simulation is simply disregarded for all state simulations, and thus at any point in time a specific state can be sampled from, in its fully developed condition. This, however, is a simplification which would not be possible in a real time implementation. For instance, for a specific distribution of states (at the measurement point) at a given time, the system needs to resample these states, and beyond them, for the next time step. This, however cannot be simulated instantly as any change to the simulation (via a change to the flowrate at the inlet), would require enough time for the effect to be noticed at the measurement area. This transient time is disregarded in this work as we already possess all the possible simulation states for all times. This then, may become a significant problem to be solved in a real implementation and comes about due to the fact that the model is required to develop over both space and time, as opposed to just time in typical particle filtering applications. One possible solution would be to not only sample over a larger range of the state space (in terms of the simulation conditions), but to also stagger the simulations, so that multiple versions of the same simulation exist but at a different time in their development. Though possible, such a problem would require further testing in a real time application and therefore will not be discussed further.

5.4 SUMMARY

This chapter has outlined the three studies undertaken in this work, with the aim of developing ECT as a multiphase flow measurement system. A method utilising similarities between annular and slug flow wave properties was proposed. By obtaining phase flowrates in slug flow through using ECT as a cross-correlation flowmeter, the information was used to determine the parameters for a power law

relationship, common to both annular and slug flows. This allowed the prediction of phase flowrates in annular flow without reliance on empirical correlations. The results were found to be limited in their achievable accuracy, although it is suggested that this method could be further developed. Additionally, this has provided further justification to the integration of a fluid model to ECT measurement to solve this problem.

Slug front structures were identified and categorised based on their shape, and assessed with regard to their representation to the true translational velocity. A bespoke measurement method was proposed for each structure type to account for the negative effect of velocity discontinuity. By applying this method, a considerable improvement in achievable accuracy was gained.

A particle filtering system was developed, integrating ECT and a CFD model to improve on the measurement capability of ECT. By using a simulation database to mimic online simultaneous simulations of particles within the state space, state tracking of gas superficial velocity was achieved. The results suggest that this method is valid and is capable of estimating the phase flowrate to a high degree of accuracy. Furthermore, this method could easily be applied to different flow types encountered ion the oil and gas industry.

The next section provides a conclusion to the work undertaken in this thesis. This includes a future system proposal, based on the knowledge gained throughout this work. This is followed by the individual conclusions for each of the three studies. Finally, a future work section is provided for each study, describing further developments which could be investigated.

Part III

CONCLUSIONS

6 FUTURE SYSTEM PROPOSAL

This chapter contains a proposal for the future development of a particle filtering based flow measurement system, using tomography and CFD modelling, with progression towards the concept of process now-casting.

6.1 PROPOSAL OF A TOMOGRAPHIC BAYESIAN BASED FRIMM SYSTEM

In this section, the work carried out and knowledge gained throughout this project, is now applied to propose a map to create a fully-fledged flow regime independent multiphase flow measurement system based on tomographic measurement and particle filtering. In doing this, it is conceded that the work carried out previously is merely the first stage, though necessary, in laying the foundation for providing a suitable measurement system. This is particularly the case for sub-sea oil and gas applications, in terms of providing a more efficient and sustainable solution to fuel extraction, processing and transportation.

Despite the belief that the proposals in this section could provide the desired outcome, it is important to conceive the limitations which restrict the immediate production of such a system. This firstly can be viewed from a limit in technology, particularly focused on computational resource. Despite the huge leaps in affordable computational power in recent decades, the notion of conducting simultaneous complex CFD simulations, which number in the thousands, in the context of a real time system is still untenable, especially at a reasonable cost. However, by assuming the continued availability of more powerful and cheaper processing ability, it can be reasonably assumed that such a system proposal could become feasible. The second obstacle, though much easier to overcome, is the level of development that is required. It must not be under-estimated as to the scale of work required to provide not only a working system, but one which can stand up to the levels of reliability, robustness and uncertainty which exists, and continues to be improved, in the realm of single-phase flow measurement.

6.1.1 *ECT sensor*

The Capacitance based tomographic instrument used in this work, as described in Section 4.2, has been developed over many years, and thus provides a stable and robust (in terms of the fundamental meas-

urement) technique to extract data from a pipeline in a non-invasive and non-intrusive manner. It is, however, worthwhile to assess whether any improvement to the instrument may be required to further the proposed FRIMM system of the future. With respect to the instrument itself, the current achievable image resolution from the stability and noise is suitable for the proposed application and the expectation of any significant further improvement may be unachievable due to physical limitations. This is also the case for the temporal resolution, achieving 5000 frames per second, which is enough to measure any significant fluid structure which would affect the overall system capability.

Outside of the instrument itself, a better case for development can be made. Throughout this work, the image reconstruction method used was the most simple LBP method, though huge focus of research in tomography in recent years has been on more complex image reconstruction methods, some of which are described in Section 2.1.5. The use of more advanced methods, such as iterative based, could provide a more quantitative image and hence would increase the overall performance potential of the system. Some researchers explicitly make this point, such as Ismail et al. [69], who suggests that LBP, due to its weaker formulation, can only produce qualitative data. From looking at the simplification proposed by LBP, this may seem a reasonable assertion, however, this does not take the structure to be imaged at an individual basis. Meaning that, the assertion made by Ismail [69] and other researchers is most definitely the case when imaging complex topology, but not necessarily when considering relatively simple structures, which, categorises those encountered in multiphase flows. A further point on the use of LBP is one which gives it an advantage over more complex methods, being that the overall mean quantity of relative density in the resulting image is precise in its representation of the actual media (useful for overall quantity measurement). Although its shape and interfacial limits, or particular segments in the image, may not. This may not be true in iterative methods when, for example, too many iterative steps are used which can be detrimental to the overall average. To conclude on image reconstruction, though not necessary, more complex algorithms could well be integrated to a FRIMM system and provide a net benefit, however, care must be taken to incorporate the fundamental imaging formulation into the measurement model, as has been attempted in very complex terms by Liu et al. [80], for example.

The final point to make on the use of ECT in a final FRIMM system is with regards to cross-correlation velocity. Throughout this work, this technique has been successfully applied to assist in both conventional tomographic flow measurement (as seen in Section 5.2), as well as in the application of the particle filtering system in Section 5.3, to incorporate the interfacial velocities. However, considering the fact

that this method is fundamentally a secondary measurement (with respects to the phase fraction measurement), it could be argued that it is in itself not required. Alternatively, the second measurement plane could, instead, be used as an additional independent measurement of the phase fraction at a different point on the geometry, where this is integrated as an additional state in the particle filter system. Due to the small distance between the two planes, this additional measurement may not, in itself, provide useful information to the system evaluation process However, the comparative similarity between how close the measurement is modelled at plane 1 and plane 2 may provide equivalent information close to that provided by cross-correlation, as the time difference in measurement and model would be analysed. Despite this, there is a reasonable argument for retaining cross-correlation due to its proven relation to vital flow parameters and its ease of implementation. The benefits of such a change are unclear and would require future testing to determine whether the stated advantages would exist, although it could also be argued that both the cross-correlation and the additional phase fraction measurement could both be applied.

6.1.2 *CFD modelling*

With regards to the use of CFD, as pointed out in Section 5.3.3, the Euler-Euler model applied would be suitable for flows encountered in the oil and gas industry, due to its ability to model both dispersed and segregated flows. Assuming this is the case, there are additional simulation parameters to be considered for the FRIMM system proposal. We will first consider these parameters with respect to a single tomographic system, such as that applied in Section 5.3, although as pointed out later in the section on process now-casting, a multi-instrument based system, spanning long pipelines, would suggest a need for both a small-scale model at each measurement system, as well as a large-scale overriding model for the entire pipeline (requiring different simulation parameters).

With respects firstly, to the determination of a suitable mesh coarseness, a value must be chosen that represents a balance between obtaining satisfactory simulation resolution (requiring a finer mesh), and reducing the computational cost (requiring a coarser mesh), although it is also recognised that the mesh coarseness, or density, is intrinsically linked to the simulation temporal resolution, with respects to the resulting Courant number, which is limited to assure simulation stability. The coarseness of mesh used in Section 5.3 seemed to satisfy both of these criteria to a reasonable degree (relative to the size of the actual domain), though it is noted that a small reduction in the numbers of cells could be applied without affecting the results substantially. Furthermore, this could be tested with relative ease by using multiple mesh sizes and determining the effect on a fixed test

case result. A further point, is the difference in mesh density along the pipe and along the cross-section. For the simulation used in the study, it could be argued that the cross-section requires only a single cell (thus reducing the model to a single dimension), due to the fact that the average values along the cross-section are used. However, this would heavily restrict the model potential in, for instance, distinct modelling of certain flow regimes, along with removing the ability of more complex states, such as velocity or phase distribution, to be used in a future system; something which would be easily achieved by the corresponding ECT measurement. For the mesh density along the length of the pipe, a much finer mesh would be necessary in order to obtain a suitable resolution in the simulated phase fraction to adequately equate to the high resolution tomography measurement.

The next simulation parameter which would require addressing, is the temporal resolution. As with the mesh density, computational resource would be a factor, though not necessarily as severe. As mentioned previously, for reasons of simulation stability, the chosen temporal resolution is linked to the mesh density. In the simulations carried out in Section 5.3, a timestep of 0.05s was used. Although this was sufficient in this case, it would be advantageous to reduce this figure. A simulation time step of around 0.01s should more than suffice in identifying the fluid structures of importance. But a further point is in regard to the simulation capability, where modelling very small fluctuations (those for which a smaller time step would be needed), is simply not reliable enough at the proposed flow resolution, and hence would be a waste of computational resources.

A final point on the use of CFD in a proposed FRIMM system is with regard to modelling turbulence. In the system developed in this work, a laminar assumption was made for simplicity, and was confirmed to be viable from the simulation validation in Section 5.3.3. In an ideal system, not only would the addition of turbulence modelling assist in more complex flows than that encountered in the study conducted, but could also play a bigger role in the overall system. It is conceivable that, turbulence, or some factor of it such as intensity, itself could be implemented as a system state in the particle filtering system, which could produce significant benefits, especially considering that this method is particularly suited for the modelling of random noise, a fundamental part of turbulence. In such a case, it is likely that the pre-defined turbulence function available in OpenFOAM could be easily adapted to implement this.

6.1.3 *Particle filtering method*

With reference to the literature survey describing advanced particle filtering methods in Section 3.3, a suitable algorithm for a future system can be proposed. Considering that, if suitable computational resource

was available to implement a real-time particle filtering system, the main objective of employing an advanced algorithm would likely still be in terms of computational efficiency. This is because it would allow a greater number of particles, along with a greater resolution with respects to time steps and how fine the model mesh could be, thus improving performance. Although, considering the significant size of the state space when all flows are considered, improvements to the representation of the actual probability density, therefore relating to accuracy, should also be considered.

With this in mind, the condensation algorithm would not be suitable, as despite giving the advantage of the posterior having more influence from the previous time step results, the loss of computational efficiency would not justify any benefit gained. As for the Kernel particle filter, some useful benefits are gained, including: an improved sampling efficiency and more suited for high dimensionality (which would likely exist with reference to suggestions made in this section). Despite this, the Kernel particle filters preference to single modality would cause significant issues when considering possible states such as flow regimes (described later), which would benefit greatly from multi-modal predictions; therefore, the Kernel particle filter is also not suitable.

Moving on now to two more suitable candidates. First, the Annealed particle filter, which can reduce computational complexity in high dimensionality, which would likely be relevant for the system proposed here, where the state could be extended to many flow properties. This, therefore presents a more suitable algorithm, with the only main downside being that additional parameters related to the annealing layers would need to be defined; relying on further tests to ensure the most efficient values are chosen. The alternative advanced algorithm which could be suitable is the Auxiliary particle filter. This is mainly due to the advantages of representation, particularly of distribution tails which may become more relevant in a system which covers all flow types. Furthermore, the loss in efficiency due to the additional dimensionality will not affect the system as severely as the condensation or Kernel particle filter. Despite this, a significant disadvantage of this method lies with the need to define an importance distribution (not required in the Bootstrap algorithm due to assumptions imposed), which could present serious difficulties. Overall, it can be said that the Annealed particle filter is the most suitable for future applications of this system as it benefits the efficiency without compromising other areas significantly.

6.1.4 *Acknowledgement of flow regime*

As discussed in Section 2.2, tomography provides an ideal platform for flow regime identification considering its first and foremost function

is as an imaging device. Due to the need for different measurement models with the particle filtering system dependent on flow regime, as discussed in Section 5.3.6, it can be assumed that an additional flow regime state would be required in the system, determined from the reconstructed tomograph, and subsequently used to switch between measurement models. For flows with a continuous and a distinctive structure, such as annular and stratified, the computationally efficient method of using the raw capacitance data, outlined in Section 2.2.2, would be a suitable choice. However, for non-continuous flows and those of which the structure is not so distinctive, i.e. slug and churn flows, it may be necessary to construct the image and conduct an image analysis algorithm to ensure a reliable outcome. This therefore, would entail image reconstruction and analysis during all operations to ensure all flow regime outcomes are accounted for. Despite incurring greater computational cost, it is deemed necessary, as the correct identification of flow regime is imperative in ensuring the correct models are applied.

Considering now the integration of flow regime identification into the particle filtering algorithm. This could be achieved as either a separate algorithm, with the result fed into the system, or alternatively, the processes flow regime could become a fully integrated system state. The first option would entail an algorithm running parallel to the particle filtering system, using the processing methods suggested previously, and signalling the main system of the current flow regime at each time interval, which then uses the corresponding model. Though simple to implement, this may cause an issue during periods where the prediction of flow regime is not definitive, such as during transition or unstable flows. By including the flow regime as a significant system state, not only does this make the determination of statistical likelihood more difficult, but it also puts additional computational need on the particle filtering system. Despite this, the benefit will be that for multi-modal probability distributions corresponding to the current flow regime, different measurement models can be applied to different particles. Therefore, not only will less likely flow regimes be considered, but by applying the separate models, the resulting estimation may help in determining the most likely outcome (as data which is calculated using the wrong measurement model is more likely to produce unreasonable predictions).

6.1.5 *Oil, gas and water flow*

For the studies conducted in this work, in particular the simplified system proposed in Section 5.3, the focus has been to measure two-phase oil and gas flows, for the reason of their suitability for measurement using ECT. However, the proposed developed system for oil and gas applications would be required to also measure the conductive water

phase that exists in industrial flows. As pointed out in Section 2.3, due to the measurement principle of ECT, the inclusion of a conductive phase, causes both the creation of conductive paths, as well as the contrasting permittivity issue, both of which have a negative effect on the instruments capability. As alluded to in Section 2.3, there are two main solutions to this problem, both of which introduce an additional tomography device (MIT in particular) for the conductive phase, proposed by Sun and Yang [108] and Zhang et al. [131]. If the assumption is made, that the more complex forward model updating method proposed by Zhang et al. [131] is developed and supplied with sufficient computational resource to operate in real time, this would be the obvious choice. The reason being, that despite this method itself being more complex, it would simplify the process once the data has been collected, as no further processing would be required, other than the inclusion of the MIT data, as the resulting data from ECT is left unaffected from the presence of a conductive phase. This is not the case necessarily for the simpler method proposed by Sun and Yang [108]. Although simpler in its method, it has been demonstrated that the accuracy of the phase fraction measurement, along with the oil and gas interface, is undermined, as the effect of the conductive phase is not accounted for in the forward model. Therefore, after the data is collected from ECT, the particle filtering system would need to be informed that the measurement model, or more relevantly the measurement noise characteristics, has changed in order to account for this effect. Despite the fact that the MIT, or a similar instrument, itself could be used to identify the conductive phase, and subsequently update the system, the measurement model / noise characteristics will most likely be affected differently depending on the amount of conductive phase present (and perhaps its location), increasing the complexity of the system processing of tomography data.

6.1.6 *Flow regime specific solutions*

6.1.6.1 *Slug flow*

Much focus on the implementation of the particle filter system in this work was focussed on slug flows. One of the advantages with these flow types is the significant phase fraction signals which come from the slug frequency, along with the two specific phase fraction values (during gas and oil slugs). This gives us the ability, as in Section 5.3, to apply the particle filtering algorithm for slug type flows, without the need for correlations such as that provided by Bendiksen [13]. Though useful, it is noted that for slug flows, the correlations available already provide a suitably accurate method to recover the vital flow parameters, as seen in Section 5.2, therefore disregarding their use may seem counter-intuitive.

6.1.6.2 *Annular and stratified-wavy flow*

In order to avoid the problems outlined in Section 5.1, where, for annular or stratified wavy flows, we rely solely on wave properties for their analysis, and even the complex method of using inter flow regime wave similarities which, as outlined has many problems, the particle filtering application seems appropriate. In order to successfully apply the particle filtering method for these flows, as we have previously with slug flows, we rely on a reasonably accurate modelling of wave properties specifically, from CFD, in order to successfully compare the results to the measurements from tomography. If this is the case, the method outlined for slug flows would easily apply to annular and stratified-wavy flows, except with a variation in the cross-correlation velocity measurement model, which could be adapted to provide a general relationship between wave velocity and flow parameters, or simply disregarded.

For annular and stratified-wavy flows, there is a further issue presented when considering the application of three-phase oil, gas and water flows. For such systems, the complexity increases significantly as there are not only an additional phase to be measured and modelled, but there must be significant differences in measurements when, for example, a constant oil and gas flow rate, but with changes in water flow rate (lowest stratified liquid due to density). .

6.1.6.3 *Stratified flow*

Stratified flow in its steady form has not been mentioned in this work, due mainly to the fact that tomography is very limited, except in its ability to measure the phase fraction, in its measurement capability, and therefore presents a particular issue to the proposed FRIMM system. By only knowing the phase fraction data at any time, it is not feasible to expect tomography alone to provide enough information for the particle filtering algorithm to provide a reasonable result. It can therefore be assumed that, in the event that such stratified flow exists in industrial application, then an additional instrument may be necessary to account for these flow types. Such an instrument must, of course, satisfy the additional criteria, for which tomography does, in ensuring a non-intrusive and non-invasive nature, therefore being appropriate for oil and gas application.

6.1.6.4 *Churn and transitional flow*

For churn and transitional flows, the issue of instability becomes the biggest factor in accurate metering. The main issue would then be for the CFD model to appropriately model the uncertainties and instabilities which are expected for these flows. Furthermore, a particularly large state space would be required to be sampled from to account for the large forms which the flow could take at any time. It is clear that

this will present a significant challenge to the ability of the FRIMM system, and a measure of its potential can only be gained from further testing.

6.1.7 *Process now-casting*

One of the proposed applicable benefits of a particle filtering based measurement system, is its use as a foundation of process now-casting. As mentioned previously, process now-casting represents the creation of an overriding computational model describing the flow process over long systems of pipelines and equipment, updated in real time, by multiple measurements from the proposed measurement system. In order for such a system to operate, the way in which a specific system interacts with the model must be different, and undoubtedly more complex, than is the case in Section 5.3, with respect to the added requirement of communication between measurement systems. Two proposals will now be presented as a way to accommodate this, with some discussion on the advantages of each.

Single model solution

The most straightforward and obvious solution to this problem is to propose a single computational model which encompasses the entire pipeline along with all points for which measurement systems are deployed. Such a model could be computed at a single location, allowing focussed use of computational resource, as would be required due to the scale of the model, with information to be sent from each measurement system as required. The communication would be relatively simple, involving the raw data being sent from each instrument to the main computing device, pre-processed to provide the relevant measurement, and finally inputted into the particle filtering system and subsequently updating the overriding model. The concept of the single model solution is illustrated in Figure 6.1.

In terms of mesh density, at the measurement system locations, a relatively fine mesh would be required, as used in Section 5.3, in order to provide a suitably informative and accurate model at the locations where data will be extracted and inputted to the particle filter system. In order to reduce the overall computational resources required, locations along the pipeline which connect the measurement system locations, would have a coarser mesh as this would satisfy the accuracy needed at random locations, while also significantly reducing the computational cost.

6.1.7.1 *Multi-model solution*

The alternative to the single model solution is to to use multiple separate models which communicate with each other. Each measurement

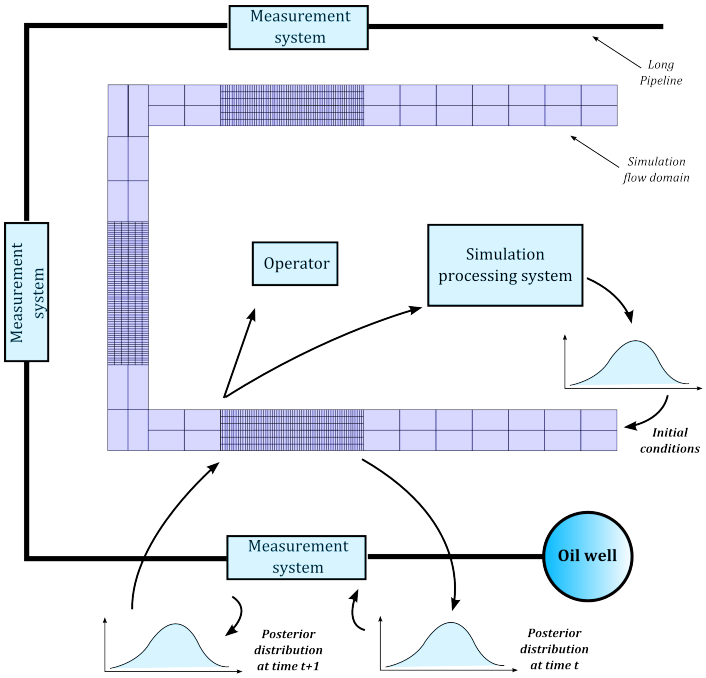

Figure 6.1: Diagram outlining the concept of a single model solution to process now-casting.

system would have its own independent model, similar to that in Section 5.3 in terms of mesh density. Alongside these individual models, there would be a single model covering the entire process flowloop, with a relatively coarse mesh to improve computational efficiency, as with the previous solution. In such a system, the measurement system specific models would require some distribution of initial conditions at their designated inputs. These distributions will be determined by a normal distribution around the value predicted by the large coarse model at that specific point. It would then be possible to use the calculated distributions from each measurement system model (values at the outlet) to update the overall large model; where the final results used would be referenced from the large overriding model. The concept of a multi-model solution is depicted in Figure .

6.1.8 *Informatics*

The final consideration for the proposed FRIMM system is with regards to data output and functionality for the end-user. Though this may seem somewhat trivial in comparison to the operating principles, it has become a significant topic with the introduction of advanced measurement instrumentation, with ultrasonic meters being a prime example, replacing the simple principled systems, such as orifice plates or turbine meters. This importance is raised due to the overall complexity of the data. For turbine meters, the resulting data is clear and fully understandable to the flow operators, and therefore diagnostics and

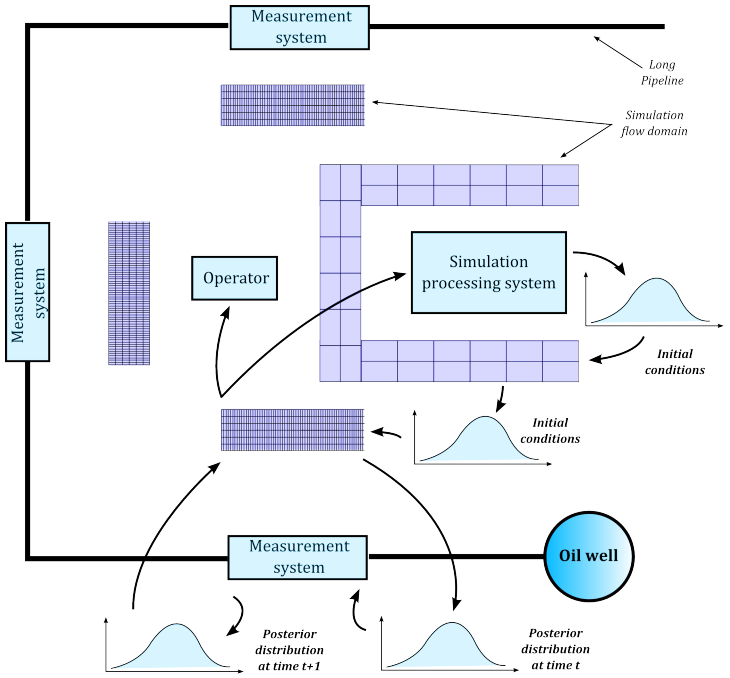

Figure 6.2: Diagram outlining the concept of a multi-model solution to process now-casting.

subsequently adjustments can be made by simply understanding the measurement principle of the instrument. For the modern advanced instruments including ultrasonic and tomographic systems such as the one suggested here, the nature of the data may not be so clear, due mainly to the complex post-processing procedures involved. A potent example of this can be seen with newly deployed ultrasonic based systems for multiphase flow metering in oil and gas pipelines. During normal modes of operation, most notably the restrictive applicable flow regimes, the meters would work as expected and produce data within the accuracy / uncertainty capabilities of the sensor. However, outside of these limitations (in particular at flow regime transitions), not only is the measurement not within the stated capabilities, but the measurement principle is affected to such a degree that the result would be incomprehensible and misleading, with the end-user unable to determine the process which produced it. The main problem being that, the system operated as a black-box sensor in this respect, leaving little that the operator can do to diagnose or understand the process. For this reason, the output and accessibility of the system data should be carefully considered.

The 'top layer' data would inevitably consist of the values of the critical system states of highest likelihood, including the most relevant phase flowrates, but also gauge pressure, temperature and flow regime. After this, the highest likelihood secondary states related to the top layer data would be shown, including phase superficial velocities and phase volume fractions. Along with additional flow variables which

may be, in effect, calculated by the system, such as: phase density, phase viscosity and turbulence intensity. On top of the single highest likelihood value of the discussed states, each of them would also have its own (likely multi-modal) probability distribution, which would provide additional information on the certainty of the initial value given, along with information on other modes which may be possible. Providing this, would allow the end-user to view all relevant values and statistical data in a hierarchy of their relevance.

The next point would be the end-users accessibility to the particle filtering system itself, as a way to provide: 'the pair of pliers of the advanced instrument', with reference to the adjustments which would be made to turbine flow meters by using a pair of pliers on the blades during calibration, a crude yet effective method used with classical metering instruments. With respect to the system proposed, the equivalent would likely be to give control over the system parameters, such as the measurement and model noise, and possibly the re-sampling procedures of the particles. The possible benefit of providing this, is to allow small modifications in how the system operates, in order to account for unforeseen variations or inaccuracies incurred in the pipeline process. For example, excessive build-up of contaminants in the measurement test section could produce higher inaccuracies in the measurement of phase fraction from ECT, which could be accounted for by adjusting the corresponding measurement noise distribution. Alternatively, flows that occur during flow regime transition or have particular attributes such as particularly high viscosity, may require the re-sampling procedure to become more broad and thus explore a larger region of the state space to operate optimally.

The final point of discussion in this topic, is with regard the the probability distributions of the process states. As mentioned previously, such information can give an indication as to how certain a likelihood value is, when analysing the modality and peak of the distribution. During periods of stable and susceptible flows (stable slug flow, for example), it would be expected that the distributions for the phase flowrates would likely be single modal with a relatively small variance, hence the resulting value is likely to be particularly accurate. However, transitional or less susceptible flows are more likely to be multi-modal with flatter distributions. It can be assumed that this information in itself could be used in providing dynamic confidence intervals and uncertainty analysis, thus providing important benefits if the measurement system is used in fiscal metering for example. This, of course, would require significant testing to ensure that the produced values suitably described the measurement uncertainty to a sufficient degree, satisfying the regulatory requirements set out by the industry.

7

CONCLUSION

This chapter concludes the thesis, and includes the following:

- A conclusion section, drawing on the findings of the three studies considered in this work.
- A future work section, describing specific research which can be conducted, following on from the three studies in the previous chapter.
- Answers to the research question posed in the introduction to this thesis, based on the findings throughout this work.
- A summary of the output of this thesis, describing the main achievements and findings.

7.1 CONCLUSION OF WORK

7.1.1 *Self deriving correlations for wave properties in annular flow*

Similarities in wave properties between annular and the film region of slug and flows were used to allow the prediction of gas flowrate for annular flows. Achieved by using slug flow data to self-derive correlation parameters on the basis that slug flows are susceptible to other forms of measurement. It was found that the inter-flow regime waves are comparable in terms of superficial gas/ wave velocity and frequency. The most useful relation was found to be firstly, that between dimensionless wave height and wave velocity, as well as that between the Strouhal number and the modified Froude number. These relationships can be described, to some degree, by a power law approximation. By applying log rules, and assuming that the superficial gas velocity is obtainable for slug flow through other means, the slug flow data alone can be used to determine the parameters for the power law approximation, and hence used to predict the flow characteristics for annular flow data. These self derived parameters can predict the gas superficial velocity for annular flows within $+/-50$. By using this method, the approximation can adapt to changes in the flow range, as well as fluid properties, as was demonstrated particularly with liquid viscosity. This therefore, resolves the biggest downfall in applying correlations to industrial flow measurement.

Even if it is assumed that the achieved accuracy using wave similarities could be improved to a satisfactory level for predicting gas flowrate, by either further developments in refining this method or,

by the application of an additional process, such as machine learning, other issues exist. The most prevalent problem being that the estimation of liquid superficial velocity is not possible with the proposed method, and therefore would rely on linear correlations with the gas superficial velocity, undermining the main benefit gained from applying this technique. Furthermore, any inaccuracy in the prediction of the gas flowrate would be further amplified by the uncertainty present in the linear correlation.

Overall, despite the proposed method, in part, removing the need for correlations which limit the range and applicability in measuring industrial flows, many issues still exist with regard to implementation, but also to the viability of the power law approximation. It is therefore reasonable to assume that this method would be unsuitable in metering annular (or wavy) flows, within a threshold of accuracy suitable for oil and gas applications, like that achievable with intermittent flows. It may be the case that, the integration of a CFD model is required, where the wave behaviour (at the measurement location) is simulated for a range of flowrates, with the results compared to that from tomography to deduce the most likely flowrates. This would require the CFD model itself to be able to describe the wave development accurately and reliably to produce a satisfactory result. This presents further justification for the use of a method such as particle filtering, also used in this work, to provide a flow measurement system for segregated flows such as annular and stratified-wavy.

7.1.2 *Slug front structures and selective cross-correlation flow metering*

ECT measurements were taken for a range of two-phase oil and gas slug flows in a horizontal pipe. Constructed images were used to analyse the slug front structures and determine their individual suitability for measurement of slug translational velocity. It was found that slug front structures can be categorised broadly into three groups (stable rising, gas core and unstable), two of which are susceptible to accurate cross-correlation. As for slug tails, they are more consistent in their shape, with only a single stable type identified throughout the tests conducted. By selecting appropriate zone maps for a given structure, velocity profiles can be obtained along certain symmetrical axis depending on the type of slug structure present, which match that found in other research.

Components of gas core and unstable slug front structures were found to travel at a higher velocity than the actual slug translational velocity, and therefore can be detrimental to cross-correlation type metering. When measured conventionally, unstable and gas core structures show more disparity between front and tail velocities. For unstable type slugs, although a more complex method could be applied to include them within the measurement (disregarding the issue of com-

putational resource), the removal of slugs with these front structures can produce measured velocity results which are more representative of the slug translational velocity, on the basis that such structures are relatively rare. For slugs with gas core front structures, if only the central zones (using an annular based map) are measured, they are more representative of the actual translational velocity, though this may compromise their reliability. A selective cross-correlation measurement technique was proposed where, depending on the structure present, tomography would be used to determine the front structure, and a specific measurement protocol would be applied. By using the selective measurement method proposed, along with differential based cross-correlation and the average velocity of slug front and tail, measurements of mixture superficial velocity can be obtained within $+/-5$, an improvement when compared to similar work. The mixture superficial velocity gained can then be used, along with assumptions detailed in previous sections, to recover the individual phase flowrates, therefore producing an improved method for the cross-correlation metering of slug flows.

7.1.3 *Bayesian approach to tomographic flow measurement*

A particle filtering based system was proposed which integrates tomographic measurement and a CFD model to provide multi-phase flow measurement with the potential to operate over multiple flow regimes, fluid properties and unlimited flow ranges. The results showed that, by using the Euler-Euler CFD model, along with gas phase fraction and cross-correlation measurements from ECT, and the described states, measurement models and algorithm, a highly accurate state tracking of superficial gas velocity for the flow range tested can be achieved within an error margin of $+/-5$. This result specifically refers to tests for gas travelling through a column of oil, and using a simulation database as a simplification. Furthermore, when presented with significant changes in the applied gas flowrate, the system successfully searches the state space and tracks the change in flowrate with a fast response time ($\sim$ 1sec).

The CFD model itself has been validated for the flows tested with a very high accuracy, and has the potential to model any flow types that are encountered in industrial flows, including multiple flow regimes. The measurement models and noise distributions used are suitable for the flows tested, however, they would require further development using more experimental data, in order to provide similar results seen here for two-phase flow covering multiple flow regimes. A simulation and system time resolution of 0.05s is appropriate for allowing a strong comparison between tomographic measurements and the fluid model for the flows tested, whilst minimising computational resource. The bootstrap algorithm used for the particle filtering system

provided suitable results for the simplified system, although, for a real time implementation, a more advanced method would be required to optimise the process and facilitate an efficient system which could meter industrial flows with comparable accuracy.

Overall, the proposed system provided a foundation on which multiphase flow measurement can be conducted, with the tools specified, without the need of limited correlations, and has the potential to cover all flow types encountered in the oil and gas industry. This work has shown that, if the required computational resources become available, a real-time implementation of this system could provide a successful multiphase flowmeter system which satisfies the criteria presented by industry, allowing a significantly reduced complexity in the oil and gas production line.

7.2 FURTHER WORK

Suggestions for further developments for each study conducted are presented below.

7.2.1 *Flow measurement of segregated flows without empirical correlations*

To improve on the thesis work, a larger range of tests can be conducted, specifically during the transition zone between slug and annular flows, allowing a more comprehensive analysis of the inter-flow regime wave behaviour. This would either provide justification for the power law approximation used, or perhaps lead to a better suited approximation which can be included in the proposed method. Also, a more detailed analysis of the different relationships can be undertaken in an attempt to find a more stable relationship between annular and slug waves. This could include different variables, such as more specific attributes of the film height, the wavelength or even additional variables which could be measured by other instruments than ECT is capable of. This could improve the achievable accuracy of the method, or possibly include a relationship which incorporated the liquid superficial velocity.

This method can also be applied to horizontal flows, whereby there may be significant differences in the measurement potential. Additionally, tests could also include replacing annular flow with stratified wavy flow, where the method is also applicable. It may be that, stratified-wavy flows, due to the lower phase velocities, could produce relationship with greater accuracy and therefore the proposed technique may be more applicable.

7.2.2 *Implementation of selective based cross-correlation flow measurement*

Further work for this study could include the following. Firstly, if a greater range of tests are conducted and the occurrence of slug structures are analysed, a greater understanding of the frequency of the defined structures can be achieved. In particular, the slug structures relationship to where the test is conducted with regards to the flow map would be useful, as the transition zones will likely affect the structure occurrence. Furthermore, a larger test range would further validate the method and provide greater clarity on the overall achievable accuracy. By analysing slug flows in vertical test sections, it could be identified whether the phenomena of these structures are limited to horizontal flows only, as it could be assumed that gravitational effects are a considerable factor in their development.

In order to implement the selective based cross-correlation method in a real-time measurement system, slug front structure identification must be achieved automatically. Therefore, developing an algorithm to work alongside the ECT system which automatically detects the slug front structure type would be required. This algorithm can be based on the same principle as ECT-based flow regime detection described earlier in this work. Once identified, the remaining measurement method (dependent on structure) would be calculated automatically and the final phase flowrates for each unit cell recovered.

7.2.3 *Future developments for particle filtering multiphase flow measurement*

For the work on implementing a particle filtering based flow measurement system, further work can include the following. The results could be further justified by conducting blind tests of more data. This would include gathering more experimental data from the same flowloop as done previously, but extending the flow range slightly, or applying intermediate flow points. This would further assure the validity of the model and system as it would include data which has not been specifically validated against the simulation. The next significant advance would be to implement the system for both oil and gas applied flowrates. This would require a new validation and also a new simulation database, although the system itself would remain mostly unchanged except minor modifications to the measurement models. This would give assurances that the system is capable of tracking the two phase flowrate states but also that the measurements from tomography are sufficient in providing enough information to deduce both oil and gas flowrates when compared to the corresponding CFD model results.

The most important step in developing this method is to work towards a real time implementation without the simulation database

simplification. This may require significant improvements in the hardware available and the corresponding cost, but also a substantial improvement in the efficiency of the algorithm and code development in general. This could include model simplification, if possible without compromising accuracy, but would also apply to the particle filtering algorithm itself. If achieved, the real-time system can be tested for a large range of flows including multiple flow regimes, and would give a significant validation to the overall potential of this method. Along with this, the measurement models and noise distributions can also be developed to ensure that they are the most appropriate for applying to all possible flow types. This would include the analysis of larger data sets of ECT measurements. Considering the likelihood that the measurement models themselves may need to change depending on the flow regime present, it is foreseeable that an additional flow regime identification process would need to be integrated to act as a model switcher during operation. This could operate independently with regards to the main system, as outlined in chapter 2, or, alternatively, could be fully integrated, where the flow regime itself becomes part of the state vector. This leads to another point; the expansion of the state vector to include other flow properties, further advancing the complexity of the system. This may require additional measurements, such as temperature, to ensure the additional states improve the systems potential.

7.3 ANSWERS TO RESEARCH QUESTIONS

Q.1 *How capable, in terms of viability and accuracy, is a standalone ECT system of flow measurement when applied to flow regimes that could occur in pipelines in the oil and gas industry?*

A.1 The effectiveness of ECT as a standalone meter is highly dependent on the flow regime present. For intermittent flows, particularly slug flows, ECT as a cross-correlation based flowmeter can achieve a relatively good accuracy of flow measurement, at around $+/-10$ using conventional methods, or approximately $+/-5$ if the proposed selective method is applied. However, this still relies on suitable correlation parameters being set dependent on flow range. For annular / stratified wavy flows, providing suitable wave correlations are applied, a reasonable approximation (though significantly less reliable than slug flows) can be obtained, although this is particularly sensitive and varies significantly to changes in fluid properties / flow ranges, and furthermore is less effective for obtaining the liquid flowrate. Stratified flows cannot be metered with ECT due to their reliance on changes in the phase fractions. Transition based flows are also difficult to meter with ECT, with no clear method presented with stable results.

Q.2 *Can the multiphase flows that tomography is currently capable and suited to measure (specifically slug flows), be improved in terms of its achievable accuracy?*
A.2. For slug flows, the presented method of detecting the slug front structure and basing the measurement method on this structure can improve the measurement potential. Despite more experiments being required to fully validate this method, the results in this work suggest that the selective cross-correlation method can achieve a $+/-5$ accuracy in predicting the mixture superficial velocity, a significant improvement to conventional methods used in other research.

Q.3 *On the basis that currently, a standalone tomographic measurement device is not a viable solution for metering all flows that occur in industry, can the incorporation of a CFD model in the measurement system, using Bayesian Particle filtering, improve their applicability*?
A.3. The results from the implementation of the particle filtering system suggest that the incorporation of CFD in this way is a viable method for tracking the phase flowrates for the intermittent flows tested. It can therefore be said that, assuming CFD is capable of simulating fluctuations of the phase fraction over different flow regimes to a sufficient accuracy, then this method has the potential to extend the applicability of ECT to more problematic flow types such as annular flow.

Q.4 *Can such a system operate without relying on empirical correlations, that are limited in their flow range and applicability to flow regimes?*
A.4. For flows which rely on the measurement of wave properties, the proposed method acts as an example in allowing ECT to conduct flow measurement without the reliance on empirical correlations. However, the results suggest that this method cannot provide accurate enough results. The particle filtering method on the other hand, represents a solution which also satisfies this criteria, but with much more promising results. Though not directly relating to empirical correlations, the assigned noise distributions are based on experiments. However, they are much more flexible and can thus be applied, conceivably, to all flow types and ranges. This therefore represents an achievable solution which is not subject to the limitations imposed by using correlations.

Q.5 *What further research and developments in technology would be required to produce a flow regime independent multiphase flow measurement (FRIMM) system to be used in large oil and gas pipelines in the context of process now-casting, and how could such a system operate?*
A.5. This question is addressed explicitly in Section 6.1, with the main goals described as follows. Significant developments in hardware as well as software implementation are required in order to allow a sufficient number of CFD simulations to be conducted simultaneously for the real non-simplified system. An additional tomography based

measurement system, with a measurement principle based on conductive properties, would need to be incorporated to allow the flow measurement of a water component, along with the development of the multi-modal operation. Conducting tests with multiple measurement systems over long flowloops, and the subsequent development of the system to simulate over the whole flow domain will allow the concept of process now-casting to be further developed.

7.4 THESIS SUMMARY

Through conducting the work presented in this thesis, the following has been achieved. ECT as a standalone instrument has been developed for use as a multiphase flow metering device. This included a proposal to allow ECT measurement of wave properties to recover phase flowrates in a way in which the system derives its own correlation parameters, thus improving generality. Despite the achieved result being limited in its success, this work has highlighted the need for a more sophisticated method for such flow regimes, likely including the integration of CFD modelling. The other significant development of ECT is with regard to its flow measurement capability for slug flows as a cross-correlation flowmeter. By identifying a significant phenomena of varying slug front structures, understanding their effects on the cross-correlation measurement process, and prescribing individual measurement methods accordingly, a higher accuracy in flow measurement of slug flows has been achieved.

Another significant, though indirect, outcome from the work mentioned previously, is the identification of the limitations of ECT as a standalone measurement system for multiphase flows. This included a demonstration of the achievable accuracy of two significant flow regimes, where the accuracy obtained from slug flows was found to be acceptable, as opposed to annular flow, where the accuracy potential is much reduced. This has helped justify the need for a complex interpretation of data from ECT which includes the use of CFD. Furthermore, this work has also defined both the need for separate measurement models for different flow regimes which occur, along with the measurement models themselves. This has contributed overall to the application of the Bayesian based approach taken in the final study.

The final study undertaken was the implementation of a Bayesian particle filtering system, integrating data from ECT and a CFD model, and harnessing knowledge gained from the previous studies. The system itself was simplified due to current hardware limitations, and was tested on a simplified multiphase flow. Despite this, the results have indicated that such a method has the potential to achieve a high accuracy in flow measurement of multiphase flows, regardless of flow range and flow regime. On top of this, the system does not

rely on any fixed empirical correlation which would be detrimental to its applicability. The proposed system, if developed in line with the system proposal defined, could have the potential to provide multiphase flow metering for the oil and gas industry, providing many financial benefits to the overall oil production process.

BIBLIOGRAPHY

[1] *Imaging industrial flows: applications of electrical process tomography*. Institute of Physics Publishing, Bristol, 1995.

[2] M. Abdulkadir, V. Hernandez-Perez, I.S. Lowndes, B.J. Azzopardi, and E. Sam-Mbomah. Experimental study of the hydrodynamic behaviour of slug flow in a horizontal pipe. *Chemical Engineering Science*, 156:147–161, 2016.

[3] Wael H. Ahmed. Experimental investigation of air-oil slug flow using capacitance probes, hot-film anemometer, and image processing. *International Journal of Multiphase Flow*, 37(8):876–887, 2011.

[4] Eissa Al-Safran, Gene Kouba, and James P. Brill. Statistical analysis and hydrodynamic modeling of unsteady gas-liquid slug velocity behavior. *Journal of Petroleum Science and Engineering*, 109:155–163, 2013.

[5] M. B. Alamu and B. J. Azzopardi. Wave and drop periodicity in transient annular flow. *Nuclear Engineering and Design*, 241(12):5079–5092, 2011.

[6] Sergey V. Alekseenko, Andrey V. Cherdantsev, Mikhail V. Cherdantsev, Sergey V. Isaenkov, and Dmitriy M. Markovich. Study of formation and development of disturbance waves in annular gas-liquid flow. *International Journal of Multiphase Flow*, 77:65–75, 2015.

[7] author Lavrent'ev M. M. (Mikhail Mikhailovich). *Computer modelling in tomography and ill-posed problems*. Inverse and ill-posed problems series. 2001.

[8] T. R. Auton. The lift force on a spherical rotational flow. *J . Fluid Mech*, 183(1987):199–218, 1987.

[9] B. J. Azzopardi, L. A. Abdulkareem, D. Zhao, S. Thiele, M. J. da Silva, M. Beyer, and A. Hunt. Comparison between electrical capacitance tomography and wire mesh sensor output for air/silicone oil flow in a vertical pipe. *Industrial & Engineering Chemistry Research*, 49(18):8805–8811, 2010.

[10] M S Beck, A Plaskowski, and R G Green. Imaging for measurement of two-phase flow. *international symposium on flow visualization*, pages 585–588, 1987.

[11] M.S. Beck and A. Pląskowski. *Cross Correlation Flowmeters, Their Design and Application*. Taylor & Francis, 1987.

[12] R J Belt and P R Leinan. Measurement of mean velocity profiles in the slug and liquid film of gas-liquid slug flow. *17th International Conference on Multiphase Production Technology*, (i):233–251, 2015.

[13] Kjell H. Bendiksen. An experimental investigation of the motion of long bubbles in inclined tubes. *International Journal of Multiphase Flow*, 10(4):467 – 483, 1984.

[14] J. U. Brackbill, D. B. Kothe, and C. Zemach. A continuum method for modeling surface tension. *Journal of Computational Physics*, 100(2):335–354, 1992.

[15] N. Brauner and A. Ullmann. Modelling of gas entrainment from taylor bubbles. part a: Slug flow. *International Journal of Multiphase Flow*, 30(3):239 – 272, 2004.

[16] Martin Brühl and Martin Hanke. Numerical implementation of two noniterative methods for locating inclusions by impedance tomography. *Inverse Problems*, 16(4):1029, 2000.

[17] H. Canière, C. T'Joen, A. Willockx, and M. De Paepe. Capacitance signal analysis of horizontal two-phase flow in a small diameter tube. *Experimental Thermal and Fluid Science*, 32(3):892–904, 2008.

[18] Cheng Chang and R Ansari. Kernel particle filter: iterative sampling for efficient visual tracking. *Image Processing, 2003. ICIP 2003. Proceedings. 2003 International Conference on*, 3:III – 977–80 vol.2, 2003.

[19] Cheng Chang and Rashid Ansari. Kernel particle filter for visual tracking. *IEEE Signal Processing Letters*, 12(3):242–245, 2005.

[20] Venkatratnam Chitturi and Farrukh Nagi. Spatial resolution in electrical impedance tomography: A topical review. *Journal of Electrical Bioimpedance*, 8(1):66, 2017.

[21] Claude Cohen-Bacrie. Regularized reconstruction in electrical impedance tomography using a variance uniformization constraint. *IEEE Transactions on Medical Imaging*, 16(5):562–571, 1997.

[22] Shell Company. Manual: gas/liquid separators-type selection and design rules. 2007.

[23] Nextfoam Open Source CFD consulting. Boundary Conditions - OpenFOAM-4.1. (May), 2017.

[24] Marco G. Conte, Govind A. Hegde, Marco J. da Silva, Amadeu K. Sum, and Rigoberto E.M. Morales. Characterization of slug initiation for horizontal air-water two-phase flow. *Experimental Thermal and Fluid Science*, 87:80 – 92, 2017.

[25] G. Costigan and P.B. Whalley. Slug flow regime identification from dynamic void fraction measurements in vertical air-water flows. *International Journal of Multiphase Flow*, 23(2):263–282, 1997.

[26] Ziqiang Cui, Qi Wang, Qian Xue, Wenru Fan, Lingling Zhang, Zhang Cao, Benyuan Sun, Huaxiang Wang, and Wuqiang Yang. A review on image reconstruction algorithms for electrical capacitance/resistance tomography. *Sensor Review*, 36(4):429–445, 2016.

[27] Marco Demori, Vittorio Ferrari, Domenico Strazza, and Pietro Poesio. A capacitive sensor system for the analysis of two-phase flows of oil and conductive water. *Sensors and Actuators, A: Physical*, 163(1):172–179, 2010.

[28] Jonathan Deutscher, Andrew Blake, and Ian Reid. Articulated body motion capture by annealed particle filtering. *Cvpr*, 2:126–133, 2000.

[29] Okto Dinaryanto, Yosephus Ardean Kurnianto Prayitno, Akmal Irfan Majid, Akhmad Zidni Hudaya, Yusnanda Agus Nusirwan, Adhika Widyaparaga, Indarto, and Deendarlianto. Experimental investigation on the initiation and flow development of gas-liquid slug two-phase flow in a horizontal pipe. *Experimental Thermal and Fluid Science*, 81:93–108, 2017.

[30] F. Dong, Y. B. Xu, L. J. Xu, L. Hua, and X. T. Qiao. Application of dual-plane ERT system and cross-correlation technique to measure gas-liquid flows in vertical upward pipe. *Flow Measurement and Instrumentation*, 16(2-3):191–197, 2005.

[31] Xiang Yuan Dong and Shu Qing Guo. Analytical method of generating sensitivity map for electrical capacitance tomography sensor with internal electrode. In *Mechatronics and Control Engineering*, volume 339 of *Applied Mechanics and Materials*, pages 99–103. Trans Tech Publications, 9 2013.

[32] Xiaoxiao Dong, Chao Tan, Ye Yuan, and Feng Dong. Measuring Oil-Water Two-Phase Flow Velocity with Continuous-Wave Ultrasound Doppler Sensor and Drift-Flux Model. *IEEE Transactions on Instrumentation and Measurement*, 65(5):1098–1107, 2016.

[33] Emerson dos Reis and Leonardo Goldstein. A non-intrusive probe for bubble profile and velocity measurement in horizontal

slug flows. *Flow Measurement and Instrumentation*, 16(4):229–239, 2005.

[34] D A Drew. Mathematical modeling of two-phase flow. *Annual Review of Fluid Mechanics*, 15(1):261–291, 1983.

[35] Abraham E. Dukler and Martin G. Hubbard. A Model for Gas-Liquid Slug Flow in Horizontal and Near Horizontal Tubes. *Industrial and Engineering Chemistry Fundamentals*, 14(4):337–347, 1975.

[36] Antoine Dupre, Guillaume Ricciardi, Salah Bourennane, and Saba Mylvaganam. Electrical Capacitance Based Flow Regimes Identification - Multiphase Experiments and Sensor Modelling. *IEEE Sensors Journal*, (c):1–1, 2017.

[37] Emerie Dupuis. Oil and Gas Custody Transfer. *Downstream Focus*, (May), 2014.

[38] J. M. Elmy, L. M A Hanis, A. R. Ruzairi, and M. F M Omar. Real-time velocity profile measurement in two-phase oil/gas flow by twin-plane segmented ECT system. *Conference Record - IEEE Instrumentation and Measurement Technology Conference*, 2015-July:1567–1572, 2015.

[39] M. M F Figueiredo, J. L. Goncalves, A. M V Nakashima, A. M F Fileti, and R. D M Carvalho. The use of an ultrasonic technique and neural networks for identification of the flow pattern and measurement of the gas volume fraction in multiphase flows. *Experimental Thermal and Fluid Science*, 70:29–50, 2016.

[40] Henry G Weller. A new approach to vof-based interface capturing methods for incompressible and compressible flow, 01 2008.

[41] JJM Geraets and JC Borst. A capacitance sensor for two-phase void fraction measurement and flow pattern identification. *International journal of multiphase flow*, 14(3):305–320, 1988.

[42] J.A. Geurst. Virtual mass in two-phase bubbly flow. *Physica A: Statistical Mechanics and its Applications*, 129(2):233 – 261, 1985.

[43] S. Ghosh, D. K. Pratihar, B. Maiti, and P. K. Das. Identification of flow regimes using conductivity probe signals and neural networks for counter-current gas-liquid two-phase flow. *Chemical Engineering Science*, 84:417–436, 2012.

[44] D. Gidaspow. *Multiphase Flow and Fluidization: Continuum and Kinetic Theory Descriptions*. Elsevier Science, 1994.

[45] B. Gokcal, Abdelsalam Al-Sarkhi, Cem Sarica, and Eissa Al-Safran. Prediction of Slug Frequency for High Viscosity Oils in Horizontal Pipes. *SPE Annual Technical Conference and Exhibition*, (September):1–13, 2009.

[46] B Gokcal, Q Wang, H Zhang, and C Sarica. Effects of High Oil Viscosity on Oil / Gas Flow Behavior in Horizontal Pipes. *2006 SPE Annual Technical Conference and Exhibition, San Antonio, Texas*, (June 2006):24–27, 2008.

[47] M Gopal and W P Jepson. Development of Digital Image Analysis Techniques for the Study of Velocity and Void Profiles in Slug Flow. *J. Multiphase Flow*, 23(5):945–965, 1997.

[48] Vinay R. Gopala and Berend G.M. van Wachem. Volume of fluid methods for immiscible-fluid and free-surface flows. *Chemical Engineering Journal*, 141(1-3):204–221, 2008.

[49] N.J. Gordon, D.J. Salmond, and A.F.M Smith. Novel approach to nonlinear/non-Gaussian Bayesian state estimation. In *IEE-Proceedings-F*, number 140, pages 107–113, 1993.

[50] Denis Gueyffier, Jie Li, Ali Nadim, Ruben Scardovelli, and Stéphane Zaleski. Volume-of-fluid interface tracking with smoothed surface stress methods for three-dimensional flows. *Journal of Computational Physics*, 152(2):423 – 456, 1999.

[51] A R W Hall, T S Whitaker, and B C Millington. Multiphase Flow Metering : Current Status and Future Developments. *OTC 8553*, 1997.

[52] Gregory J Hatton. Multiphase Flow Meters and Application Trends. *OTC 8547*, (1):1–8, 1997.

[53] Tatsuya Hazuku, Tomoji Takamasa, and Yoichiro Matsumoto. Experimental study on axial development of liquid film in vertical upward annular two-phase flow. *International Journal of Multiphase Flow*, 34(2):111–127, 2008.

[54] R. He, C. G. Xie, R. C. Waterfall, M. S. Beck, and C. M. Beck. Engine flame imaging using electrical capacitance tomography. *Electronics Letters*, 30(7):559–560, Mar 1994.

[55] E. Hervieu and P. Seleghim. An objective indicator for two-phase flow pattern transition. *Nuclear Engineering and Design*, 184(2):421–435, 1998.

[56] G.F. Hewitt and N.S. Hall-Taylor. *Annular two-phase flow*. Pergamon Press, 1970.

[57] C.W Hirt and B.D Nichols. Volume of fluid (vof) method for the dynamics of free boundaries. *Journal of Computational Physics*, 39(1):201 – 225, 1981.

[58] B S Hoyle, X Jia, F J W Podd, H I Schlaberg, H S Tan, M Wang, R M West, R A Williams, and T A York. Design and application of a multi-modal process tomography system. *Measurement Science and Technology*, 12(8):1157, 2001.

[59] H. L. Hu, J. Dong, J. Zhang, Y. J. Cheng, and T. M. Xu. Identification of gas/solid two-phase flow regimes using electrostatic sensors and neural-network techniques. *Flow Measurement and Instrumentation*, 22(5):482–487, 2011.

[60] H. L. Hu, J. Zhang, J. Dong, Z. Y. Luo, and T. M. Xu. Identification of Gas-Solid Two-Phase Flow Regimes Using Hilbert-Huang Transform and Neural-Network Techniques. *Instrumentation Science & Technology*, 39(2):198–210, 2011.

[61] S M Huang, A B Plaskowski, C G Xie, and M S Beck. Tomographic imaging of two-component flow using capacitance sensors. *Journal of Physics E: Scientific Instruments*, 22(3):173, 1989.

[62] A Hunt, R Foster-Turner, and R Drury. Propellant slosh force and mass measurement. *International Journal of Aerospace Engineering*, 2018(3026872), 2018.

[63] Andrew Hunt. Weighing without touching: Applying electrical capacitance tomography to mass flowrate measurement in multiphase flows. *Measurement and Control (United Kingdom)*, 47(1):19–25, 2014.

[64] Andrew Hunt and David Millington. Multiphase Flow Measurement Through Next-Generation Tomographic Visualisation Technology. *UPM Forum*, (February):24–25, 2016.

[65] Andrew Hunt, J Pendleton, and Y Ladam. Visualisation of Two-Phase Gas-Liquid Pipe Flows Using Electrical Capacitance Tomography. *ASME. Engineering Systems Design and Analysis*, (Volume 1):491–495, 2004.

[66] Michael Isard and A. Blake. Condensation - conditional density propagation for visual tracking. *International journal of computer vision*, 29(1):5–28, 1998.

[67] M. Ishii and T. Hibiki. *Thermo-fluid Dynamics of Two-Phase Flow*. 2nd ed. edition, 2006.

[68] Mamoru Ishii. One-Dimensional Drift Flux Model and Constitutive Equations for Relative Motion Between Phases in Various Two-Phase Flow Regimes. *Anl-77-47*, pages 77–47, 1977.

[69] I. Ismail, J.C. Gamio, S.F.A. Bukhari, and W.Q. Yang. Tomography for multi-phase flow measurement in the oil industry. *Flow Measurement and Instrumentation*, 16(2-3):145–155, 2005.

[70] A. K. Jana, G. Das, and P. K. Das. Flow regime identification of two-phase liquid-liquid upflow through vertical pipe. *Chemical Engineering Science*, 61(5):1500–1515, 2006.

[71] Laurent F.C Jeanmeure, Tomasz Dyakowski, William B.J Zimmerman, and Wayne Clark. Direct flow-pattern identification using electrical capacitance tomography. *Experimental Thermal and Fluid Science*, 26(6-7):763–773, 2002.

[72] U. Kadri, M.L. Zoeteweij, R.F. Mudde, and R.V.A. Oliemans. A growth model for dynamic slugs in gas–liquid horizontal pipes. *International Journal of Multiphase Flow*, 35(5):439 – 449, 2009.

[73] Yiqun Kang, Shi Liu, and Jing Liu. Image reconstruction algorithm for electrical capacitance tomography based on data correlation analysis. *Flow Measurement and Instrumentation*, 62(January):113–122, 2018.

[74] Shanon Keough. Optimising the Parallelisation of OpenFOAM Simulations. *Australian Government, Department of Defence, Defence Science and Technology Organisation*, (June), 2014.

[75] Scott Kirkpatrick, C. D. Gelatt, and Mario P. Vecchi. Optimization by simulated annealing. *Science*, 220 4598:671–80, 1983.

[76] L. Landweber. An iteration formula for fredholm integral equations of the first kind. *American Journal of Mathematics*, 73(3):615–624, 1951.

[77] Jae Young Lee, Mamoru Ishii, and Nam Seok Kim. Instantaneous and objective flow regime identification method for the vertical upward and downward co-current two-phase flow. *International Journal of Heat and Mass Transfer*, 51(13-14):3442–3459, 2008.

[78] Dominique Legendre and Jacques Magnaudet. The lift force on a spherical bubble in a viscous linear shear flow. *Journal of Fluid Mechanics*, 368:81–126, 1998.

[79] Aimin Liao and Qiyou Zhou. Application of ECT and relative change ratio of capacitances in probing anomalous objects in water. *Flow Measurement and Instrumentation*, 45:7–17, 2015.

[80] S. Liu, L. Fu, W. Q. Yang, H. G. Wang, and F. Jiang. Prior-online iteration for image reconstruction with electrical capacitance tomography. *IEE Proceedings - Science, Measurement and Technology*, 151(3):195–200, May 2004.

[81] Process Tomography Ltd. *ELECTRICAL CAPACITANCE TOMOGRAPHY SYSTEM TYPE PTL300E, Issue 1*. Process Tomography Ltd., 2008.

[82] Process Tomography Ltd. *ELECTRICAL CAPACITANCE TOMOGRAPHY SYSTEM TYPE PTL300E, Issue 6*. Process Tomography Ltd., 2008.

[83] G.P. Lucas and I.C. Walton. Flow rate measurement by kinematic wave detection in vertically upward, bubbly two-phase flows. *Flow Measurement and Instrumentation*, 8(3):133 – 143, 1998.

[84] J MacCormick and A Blake. A probabilistic exclusion principle for tracking multiple objects. *Proc. of the Seventh IEEE Inernational Conference on Computer Vision(ICCV99)*, 1:572–578, 1999.

[85] E.W. McAllister. *Pipeline Rules of Thumb Handbook: A Manual of Quick, Accurate Solutions to Everyday Pipeline Engineering Problems*. Elsevier Science, 2015.

[86] Y. Mi, M. Ishii, and L. H. Tsoukalas. Flow regime identification methodology with neural networks and two-phase flow models. *Nuclear Engineering and Design*, 204(1-3):87–100, 2001.

[87] Y. Mi, M. Ishii, and L. H. Tsoukalas. Investigation of vertical slug flow with advanced two-phase flow instrumentation. *Nuclear Engineering and Design*, 204(1-3):69–85, 2001.

[88] Y. Mi, M. Ishii, and L.H. Tsoukalas. Vertical two-phase flow identification using advanced instrumentation and neural networks. *Nuclear Engineering and Design*, 184(2-3):409–420, 1998.

[89] Lamari M.L. An Experimental Investigation of Two-Phase (Air-Water) Flow Regimes in a Horizontal Tube At Near Atmospheric Conditions. *Carleton University, Canada*, 2001.

[90] J.L. Mueller, S. Siltanen, and D. Isaacson. A direct reconstruction algorithm for electrical impedance tomography. *Medical Imaging, IEEE Transactions on*, 21(6):555–559, 2002.

[91] M. K. Nicholson, K. Aziz, and G. A. Gregory. Intermittent two phase flow in horizontal pipes: Predictive models. *The Canadian Journal of Chemical Engineering*, 56(6):653–663, 1978.

[92] D. J. Nicklin, M.A. Wilkes, and J.F. Davidson. Two-Phase Flow in Vertical Tubes. *Transactions of the Institution of Chemical Engineers*, 40:61–67, 1962.

[93] Akiharu Ousaka. Air-Water Annular Disturbance Wave Flow in Horizontal and and Near Horizontal Tubes Characteristics Liquid . 6(1), 1992.

[94] Liang Ming Pan, Hui He, Peng Ju, Takashi Hibiki, and Mamoru Ishii. Experimental study and modeling of disturbance wave height of vertical annular flow. *International Journal of Heat and Mass Transfer*, 89(2015):165–175, 2015.

[95] Simon Pedersen, Petar Durdevic, and Zhenyu Yang. Challenges in slug modeling and control for offshore oil and gas productions: A review study. *International Journal of Multiphase Flow*, 88:270–284, 2017.

[96] Michael K Pitt and Neil Shephard. Filtering Via Simulation: Auxiliary Particle Filters. *Journal of the American Statistical Association*, 94(446):590–599, 1997.

[97] C. Qiu, B. S. Hoyle, and F. J W Podd. Engineering and application of a dual-modality process tomography system. *Flow Measurement and Instrumentation*, 18(5-6):247–254, 2007.

[98] Pravin Sawant, Mamoru Ishii, Tatsuya Hazuku, Tomoji Takamasa, and Michitsugu Mori. Properties of disturbance waves in vertical annular two-phase flow. *Nuclear Engineering and Design*, 238(12):3528–3541, 2008.

[99] L. Schiller and A. Naumann. A drag coefficient correlation. *Z. Ver. Deutsch. Ing*, 77:318–320, 1935. cited By 31.

[100] D. Schubring and T. A. Shedd. Wave behavior in horizontal annular air-water flow. *International Journal of Multiphase Flow*, 34(7):636–646, 2008.

[101] D. Schubring, T. A. Shedd, and E. T. Hurlburt. Studying disturbance waves in vertical annular flow with high-speed video. *International Journal of Multiphase Flow*, 36(5):385–396, 2010.

[102] K. Sekoguchi. New development of experimental study on interfacial structure in gas-liquid two-phase flow. *Proc. 4th World Conference on Experimental Heat Transfer, Fluid Mechanics and Thermodynamics, Brussels*, pages 1177–1188, 1997.

[103] Kotohiko Sekoguchi, Masayuki Takeishi, and Takakazu Ishimatsu. Interfacial structure in vertical upward annular flow. *Journal of the flow visualization society of Japan*, 5(Supplement):61–66, 1985.

[104] Andriyanto Setyawan, Indarto, and Deendarlianto. Experimental investigation on disturbance wave velocity and frequency in air-water horizontal annular flow. *Modern Applied Science*, 8(4):84–96, 2014.

[105] Andriyanto Setyawan, Indarto, and Deendarlianto. The effect of the fluid properties on the wave velocity and wave frequency of

gas-liquid annular two-phase flow in a horizontal pipe. *Experimental Thermal and Fluid Science*, 71:25–41, 2016.

[106] C. Shanthi and N. Pappa. An artificial intelligence based improved classification of two-phase flow patterns with feature extracted from acquired images. *ISA Transactions*, 68:425–432, 2017.

[107] Lev Shemer. Hydrodynamic and statistical parameters of slug flow. *International Journal of Heat and Fluid Flow*, 24(3):334–344, 2003.

[108] Jiangtao Sun and Wuqiang Yang. A dual-modality electrical tomography sensor for measurement of gas-oil-water stratified flows. *Measurement: Journal of the International Measurement Confederation*, 66:150–160, 2015.

[109] Mark Sussman, Peter Smereka, and Stanley Osher. A level set approach for computing solutions to incompressible two-phase flow. *Journal of Computational Physics*, 114(1):146 – 159, 1994.

[110] M. Syamlal and T.J. O'Brien. Computer simulation of bubbles in a fluidized bed. *AIChE Symposium Series*, 85:22–31–, 1989.

[111] N. Hall Taylor, G.F. Hewitt, and P.M.C. Lacey. The motion and frequency of large disturbance waves in annular two-phase flow of air-water mixtures. *Chemical Engineering Science*, 18(8):537 – 552, 1963.

[112] John R Thome. *Encyclopedia of Two-Phase Heat Transfer and Flow I*. World Scientific, 2015.

[113] 1967 Thrun, Sebastian. *Probabilistic robotics*. MIT Press, Cambridge, MA., 2005.

[114] A.N. Tikhonov and V.I.A. Arsenin. *Solutions of ill-posed problems*. Scripta series in mathematics. Winston, 1977.

[115] A. Tomiyama. Struggle with computational bubble dynamics. *Proc. Int. Conf. Multiphase Flow*, 1998.

[116] Priscilla M. Ujang, Christopher J. Lawrence, Colin P. Hale, and Geoffrey F. Hewitt. Slug initiation and evolution in two-phase horizontal flow. *International Journal of Multiphase Flow*, 32(5):527–552, 2006.

[117] R. Van Hout, D. Barnea, and L. Shemer. Translational velocities of elongated bubbles in continuous slug flow. *International Journal of Multiphase Flow*, 28(8):1333–1350, 2002.

[118] A.R. Von Hippel. *Dielectrics and Waves*. Number v. 1 in Artech House microwave library. Artech House, 1995.

[119] Paulo J. Waltrich, Gioia Falcone, and Jader R. Barbosa. Axial development of annular, churn and slug flows in a long vertical tube. *International Journal of Multiphase Flow*, 57:38–48, 2013.

[120] Mi Wang. *Industrial tomography : systems and applications*. Woodhead Publishing Series in Electronic and Optical Materials. 2015.

[121] Kent E. Wardle and Henry G. Weller. Hybrid multiphase CFD solver for coupled dispersed/segregated flows in liquid-liquid extraction. *International Journal of Chemical Engineering*, 2013(1), 2013.

[122] A. Wolf, S. Jayanti, and G. F. Hewitt. On the nature of ephemeral waves in vertical annular flow. *International Journal of Multiphase Flow*, 22(2):325–333, 1996.

[123] A. Wolf, S. Jayanti, and G. F. Hewitt. Flow development in vertical annular flow. *Chemical Engineering Science*, 56(10):3221–3235, 2001.

[124] S H I Xuewei, Dong Xiaoxiao, T A N Chao, and Dong Feng. Flow Velocity Measurement Based on Ultrasonic Cross-correlation Technique in Oil-water Two-phase Flow. pages 4921–4925, 2016.

[125] G. Yadigaroglu and G.F. Hewitt. *Introduction to Multiphase Flow: Basic Concepts, Applications and Modelling*. Zurich Lectures on Multiphase Flow. Springer International Publishing, 2017.

[126] H Yan, Y H Liu, and C T Liu. Identification of flow regimes using back-propagation networks trained on simulated data based on a capacitance tomography sensor. *Measurement Science and Technology*, 15(2):432, 2004.

[127] W Q Yang, M S Beck, and M. Byars. Electrical capacitance tomography - from design to applications. *Measurement and Control*, 28(9):261–266, 1995.

[128] W. Q. Yang, A. L. Stott, M. S. Beck, and C. G. Xie. Development of capacitance tomographic imaging systems for oil pipeline measurements. *Review of Scientific Instruments*, 66(8):4326–4332, 1995.

[129] L. S. Zhai, N. D. Jin, Z. K. Gao, A. Zhao, and L. Zhu. Cross-correlation velocity measurement of horizontal oil-water two-phase flow by using parallel-wire capacitance probe. *Experimental Thermal and Fluid Science*, 53:277–289, 2014.

[130] Lifeng Zhang and Huaxiang Wang. Identification of oil-gas two-phase flow pattern based on SVM and electrical capacitance tomography technique. *Flow Measurement and Instrumentation*, 21(1):20–24, 2010.

[131] M. Zhang, L. Ma, and M. Soleimani. Dual modality ECT-MIT multi-phase flow imaging. *Flow Measurement and Instrumentation*, 46:240–254, 2015.

[132] Y. Zhao, L. Lao, and H. Yeung. Investigation and prediction of slug flow characteristics in highly viscous liquid and gas flows in horizontal pipes. *Chemical Engineering Research and Design*, 102(1990):124–137, 2015.

[133] Yujie Zhao, Christos N. Markides, Omar K. Matar, and Geoffrey F. Hewitt. Disturbance wave development in two-phase gas-liquid upwards vertical annular flow. *International Journal of Multiphase Flow*, 55:111–129, 2013.

[134] Yunlong Zhou, Fei Chen, and Bin Sun. Identification Method of Gas-Liquid Two-phase Flow Regime Based on Image Multi-feature Fusion and Support Vector Machine. *Chinese Journal of Chemical Engineering*, 16(6):832–840, 2008.

[135] N. Zuber and J. A. Findlay. Average volumetric concentration in two-phase flow systems. *Journal of Heat Transfer*, 87(4):453–468, 1965.

Part IV

APPENDIX

A

IDENTIFICATION OF HORIZONTAL SLUG FLOW STRUCTURES FOR APPLICATION IN SELECTIVE CROSS-CORRELATION METERING

[Appendix removed for copyright reasons]

B

MULTIPHASE FLOW: DEVELOPING QUANTITATIVE FLOW VISUALISATION

[Appendix removed for copyright reasons]

C

3-PHASE FLOWLOOP SCHEMATIC

DRAWING No. P3620-039 ISSUE 07

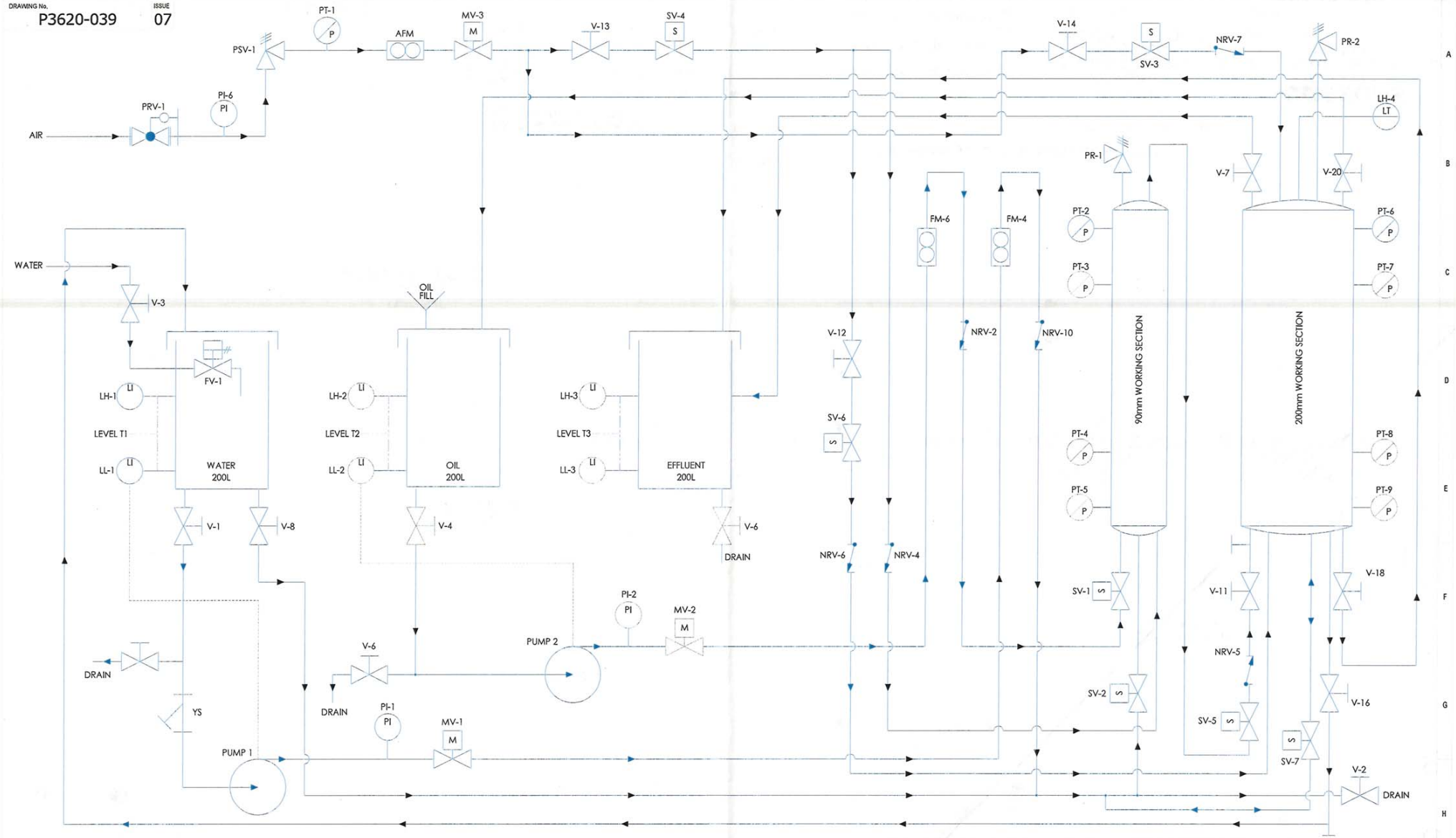

ISSUE	DETAILS OF MODIFICATION	DRAWN	CHKD	APPR/ REL.	DATE
...	...	...	...	...	
...	...	...	...	...	
...	...	...	...	...	
...	...	...	...	...	

MODIFICATION RECORD

FOR GENERAL TOLERANCES SEE DRAWING No. CODP3/1

SURFACE TEXTURE

SYMBOL	MICRO INCH	MICRO METER
M	250 125	6.3 3.2
S	125 63	3.2 1.6
F	63 32	1.6 0.8
SF	32 16	0.8 0.4

PROJECTION: 1st ANGLE 3rd ANGLE

ASSEMBLY

ITEM NUMBER

MATERIAL SPEC.

FINISH -

THE ORIGINAL SIZE OF THIS DRAWING SHEET WAS A1

0 10 20 30 40 50 60 70 80 90 100mm

	INITIAL	DATE	SCALE
DRAWN	NGE	16/12/2015	1:1
CHECKED	CMS	19/04/2016	No. OFF SEE UNITY
APPROVED	CBH	19/04/2016	JOB No.
RELEASED	CMS	19/04/2016	SEE UNITY

DRAWING TITLE: P&ID P3620 MULTIPHASE FLOW TEST RIG

ESTIMATED WEIGHT -

cussons TECHNOLOGY
CUSSONS TECHNOLOGY LTD, 102 GREAT CLOWES STREET, MANCHESTER M7 1RH, ENGLAND.

SHEET 1 of 2

DRAWING No. P3620-039 ISSUE 07

D

ECT CALIBRATION DATA

Calibration for Experiment 1
Calibration file newcal
Absolute Calibration Capacitances (fF)
Plane 1
Low capacitances
63.17 7.45 3.34 3.20 3.90 8.42 55.18
285.00 26.63 9.75 8.86 10.63 26.14
284.84 24.48 11.39 8.72 11.12
203.54 25.83 10.34 8.50
264.52 25.64 10.34
291.38 26.78
269.76
High capacitances
67.81 14.33 8.38 6.93 9.23 15.65 60.53
291.05 45.24 20.62 18.87 22.72 43.69
291.70 41.59 23.74 19.02 22.67
212.05 44.42 22.52 18.29
270.04 42.98 21.11
296.26 44.86
275.33
CH/CL Ratios 2.1660 2.1304 2.1814 2.1510
Mean 2.1572(0.02)
Plane 2
Low capacitances
63.17 7.45 3.34 3.20 3.90 8.42 55.18
285.00 26.63 9.75 8.86 10.63 26.14
284.84 24.48 11.39 8.72 11.12
203.54 25.83 10.34 8.50
264.52 25.64 10.34
291.38 26.78
269.76
High capacitances
67.81 14.33 8.38 6.93 9.23 15.65 60.53
291.05 45.24 20.62 18.87 22.72 43.69
291.70 41.59 23.74 19.02 22.67
212.05 44.42 22.52 18.29
270.04 42.98 21.11
296.26 44.86
275.33
CH/CL Ratios 2.1660 2.1304 2.1814 2.1510
Mean 2.1572(0.02)

Calibration for Experiment 2
Calibration file 2017-01-05_APL140-01_07
Absolute Calibration Capacitances (fF)
Plane 1
Low capacitances
287.18 26.27 10.16 7.66 9.85 23.65 219.58
287.53 26.22 10.20 8.68 10.95 25.96
284.73 23.97 10.77 8.84 11.14
212.97 25.56 10.50 8.41
278.50 25.40 10.76
292.14 26.89
280.80
High capacitances
292.07 42.46 20.71 16.05 20.10 39.57 224.59
294.01 43.22 20.18 17.77 21.66 42.43
289.24 39.18 21.71 18.01 21.44
218.88 42.34 21.62 17.50
280.43 41.61 20.49
296.57 43.46
283.78
CH/CL Ratios 2.0951 2.0482 2.0370 2.0805
Mean 2.0652(0.03)
Plane 2
Low capacitances
276.60 25.60 10.22 7.83 10.13 23.49 203.10
283.04 26.89 10.77 8.94 11.33 25.65
281.04 23.86 10.97 8.72 10.36
206.77 25.14 10.55 8.06
268.12 25.36 10.40
283.77 26.08
277.78
High capacitances
281.52 42.24 20.73 16.27 20.76 39.57 210.60
290.67 43.69 20.89 18.42 22.04 41.72
286.19 39.24 22.11 17.93 21.05
213.85 41.94 21.11 16.89
271.55 41.41 20.26
290.01 42.61
277.07
CH/CL Ratios 2.0775 2.0593 2.0559 2.0953
Mean 2.0720(0.02)

Calibration for Experiment 3
Calibration file combinedcal3
Absolute Calibration Capacitances (fF)
Plane 1
Low capacitances
208.83 20.71 10.98 9.34 11.00 20.29 204.04
199.67 20.56 11.18 9.09 10.71 20.47
196.92 21.19 10.88 8.85 10.78
227.87 20.75 10.66 9.04
206.81 20.58 11.01
192.48 20.41
189.53
High capacitances
310.39 50.30 27.08 23.14 27.17 49.37 300.83
300.39 49.61 27.60 22.75 26.77 49.58
295.43 51.02 27.06 22.34 26.73
316.93 49.92 26.59 22.35
299.56 49.52 26.97
291.51 49.00
285.89
CH/CL Ratios 2.4780 2.5028 2.5238 2.4721
Mean 2.4942(0.02)
Plane 2
Low capacitances
206.13 20.61 10.87 9.29 10.95 20.25 203.55
195.95 20.47 11.17 9.13 10.71 20.53
196.45 21.22 10.86 8.90 10.83
220.30 20.56 10.65 9.03
202.65 20.63 11.08
198.19 20.58
190.06
High capacitances
309.78 50.06 26.91 23.13 27.09 49.17 301.60
298.17 49.30 27.62 22.79 26.71 49.88
295.90 51.26 27.02 22.33 26.82
315.06 49.59 26.52 22.34
298.08 49.90 27.26
296.57 49.42
284.20
CH/CL Ratios 2.4908 2.4966 2.5088 2.4738
Mean 2.4925(0.01)

E

DATASHEET - SERASENSE SF 2 OIL

[Appendix removed for copyright reasons]

F

CODE - PARTICLE FILTERING

F.1 PARTICLE FILTERING SYSTEM SCRIPT

```
import bayesflow as bf
import numpy as np
import matplotlib.pyplot as plt
from matplotlib import colors
from mpl_toolkits.mplot3d import Axes3D
import matplotlib.animation as animation
import scipy.stats as stats
plt.ion()
fig = plt.figure()

final_jgmean=np.array([])
final_W=np.array([])

for testy in range(1,2):

        # Initialisation
        alpha1,alpha2,timey = bf.alphagrabtom('2018-03-16_
            gasflowonly_02.csv')
        #freqtom = bf.getfreqtom(alpha1,timey)
        #freqsim = bf.getfreqsim(80)
        part = bf.createpart()
        result = np.array([])
        U_inlet = np.array([])
        roll_mean = np.array([])
        alpha_stor = np.array([])
        mach_jg= np.array([])
        mach_alpha= np.array([])
        indy=np.ones(609)
        t_sim=1
        W_old=np.ones(609)

        # Set values
        P_meas = 887
        U_cc = 0.909


        # Script

        for t in range(1,151):
        #       Restart sim time

                t_sim+=1
                if t_sim>20:
                        t_sim=1

        #       Change pressure meas

                #if t>100:
                        #P_meas = 931.7
```

```
#       Get measurements and sim data

        alphasim, jgsim = bf.getalphsimt_2(80+(t_sim-1))
        alpha_t1 = np.mean(alpha1[t*67:(t+1)*67])
        jgtom = alpha_t1*U_cc

#       plot

        fig.clf()
        ax1 = fig.add_subplot(221)
        ax1.scatter(alphasim[indy>0],jgsim[indy>0])
#       Create state

        x = np.zeros((609,2))
        x[:,0] = alphasim
        x[:,1] = jgsim

#       Change ucc value

        #if t>0:
                #jgtom = alpha_t1*1.074

#       Weight particles

        W1,maxw = bf.normweight(x[(indy>0),0],alpha_t
            1,0.1)
        #W3,maxw3 = bf.normweight(x[indy>0,1],jgtom,0.05)
        W3,maxw3 = bf.normweight_exp(x[indy>0,1],jgtom
            ,0.3)
        W2,maxw2 = bf.normweight(part[(indy>0),1],P_meas
            ,10)
        #W4,maxw4 = bf.normweight(freqsim[(indy>0)],
            freqtom,4)

        W=np.zeros(609)
        W[indy>0]=W2*W3*W1#*W4
        W=W*W_old
        W=W/sum(W)
        idx = np.argmax(W)

        final_W=np.append(final_W,W[idx])

#       Sample from dicrete distribution

        index = np.random.multinomial(3000,W,1)

#       Re-sample

        if t%1==0:

                        x_new = bf.resample(x,index)
                        x_new =np.array(x_new)
```

```
                            x_new[:,1] = x_new[:,1] + np.
                                random.normal(0,0.01,3000)
                            val_u = bf.getfixedpart(x_new
                                [:,1],x[:,1])
                            mask = np.in1d(x[:,1],val_u)
                            indy = mask*1
                            W_old = np.ones(609)

        #       SIS

                else:

                            indy = np.zeros(609)
                            indy[index[0,:]>0]=1
                            W_old = W

        #       Store result and display data
                #R = sum(W[indy>0]*x[(indy>0),1])
                #result = np.append(result,R)
                result = np.append(result,(x[idx,1]))
                U_inlet = np.append(U_inlet,part[idx,0])
                alpha_stor = np.append(alpha_stor,(x[idx,0]))

                ax = fig.add_subplot(222)
                ax.plot(range(1,t+1),result)
                ax.plot(range(1,t+1),np.ones(t)*0.2675,color='r')
                ax.plot(range(1,t+1),U_inlet,color='black')

        #       Rolling mean

                if t>20:
                        roll_mean = np.append(roll_mean,np.mean(
                            result[20:]))
                        ax.plot(range(21,t+1),roll_mean)
                        print np.mean(result[20:])

        #       Correlation predictor

                        par = np.polyfit(result[20:],alpha_stor
                            [20:],1,full=True)
                        print 'm = '+str(par[0][0])
                        print 'c = '+str(par[0][1])
                        ax4 = fig.add_subplot(224)
                        ax4.scatter(result[20:],alpha_stor[20:])

        #       Print additional data

                #print 'jgsim = '+str(jgsim[idx])
                #print 'jgtom = '+str(jgtom)
                #print 'alphasim = '+str(x[idx,0])
                #print 'alphatom = '+str(alpha_t1)
                #print 'uinlet= ' + str(part[idx,0])
```

```
                #print freqtom
                #print freqsim[idx]

        #       Plot

                ax3 = fig.add_subplot(223, projection = '3d')
                ax3.set_title('Particle weights')
                y=np.arange(0.02 , 0.31, 0.01)
                x=np.arange(850 , 955, 5)
                X,Y = np.meshgrid(x,y)
                Z = W.reshape((29,21))
                ax3.scatter(X,Y,Z)
                plt.draw()

        #

        #np.savetxt('jgmean_1.csv',np.mean(result[20:]),delimiter
            =',')
        np.savetxt('jg_'+str(testy)+'.csv',result,delimiter=',')
        np.savetxt('alpha_'+str(testy)+'.csv',alpha_stor,
            delimiter=',')
        np.savetxt('W_'+str(testy)+'.csv',final_W,delimiter=',')
        np.savetxt('corr'+str(testy)+'.csv',np.array([par[0][0],
            par[0][1]]),delimiter=',')
```

F.2 PARTICLE FILTERING FUNCTION LIBRARY

```
##
import csv
import numpy as np
import numbers
import matplotlib.pyplot as plt
import scipy.stats as scist
import math
#==========================
def alphagrabtom(filename):
        def mapped(x):
                if isinstance(x,numbers.Number):
                        return x
                for tpe in (int, float):
                        try:
                                return tpe(x)
                        except ValueError:
                                continue
                return 0
        b=np.loadtxt(filename,dtype='string',delimiter=',',
            skiprows=3)
        for sub in b:
                sub[:] = map(mapped,sub)
        data = b.astype(np.float)
        nonzeroindex = np.where(data.any(axis=0))[0]
```

```
        with open(filename) as datafile:

                dat = csv.reader(datafile)
                dat.next()
                dat.next()
                header = dat.next()
        time = data[:,0]
        alpha1 = data[:,1]
        alpha2 = data[:,2]
        return alpha1, alpha2, time
#=========================
def getalphsim_mean(t1):

        alpha_res = np.zeros(609)
        u_res = np.zeros(609)

        for i in range(1,610):

                dat=np.loadtxt('/media/ross/Maxtor/simulations
                    2018/'+str(i)+'/'+str(i)+'.csv',delimiter
                    =',',skiprows=1)

        #indexkey:      Uavg = 1 , alphaavg = 17 , alphamin/max =
             19, prghavg = 21
                alpha = dat[:,17]
                u = dat[:,1]

                alpha=alpha**2

                alpha_res[i-1] = np.mean(alpha[t1:(t1+10)])
                u_res[i-1] = np.mean(u[t1:(t1+10)])

        return alpha_res, u_res
#=========================
def getusim_mean(i,t1):

        dat=np.loadtxt('/media/ross/Maxtor/simulations2018/'+str(
            i)+'/'+str(i)+'.csv',delimiter=',',skiprows=1)

        #indexkey:      Uavg = 1 , alphaavg = 17 , alphamin/max =
             19, prghavg = 21
        u = dat[:,1]
        alpha = dat[:,17]
        alpha = alpha**2
        u=u**2
        u_res = (u[t1:(t1+10)])
        alpha_res = (u[t1:(t1+10)])
        jgres = u_res*alpha_res
        return jgres
#=========================
def getalphsim_sd(t1):
```

```
        alpha_res = np.zeros(609)

        for i in range(1,610):

                dat=np.loadtxt('/media/ross/Maxtor/simulations
                    2018/'+str(i)+'/'+str(i)+'.csv',delimiter
                    =',',skiprows=1)

        #indexkey:      Uavg = 1 , alphaavg = 17 , alphamin/max =
             19, prghavg = 21
                alpha = dat[:,17]

                alpha=alpha**2

                alpha_res[i-1] = np.std(alpha[t1:(t1+10)])


        return alpha_res
#=========================
def getalphsim_max(t1):

        alpha_res = np.zeros(609)

        for i in range(1,610):

                dat=np.loadtxt('/media/ross/Maxtor/simulations
                    2018/'+str(i)+'/'+str(i)+'.csv',delimiter
                    =',',skiprows=1)

        #indexkey:      Uavg = 1 , alphaavg = 17 , alphamin/max =
             19, prghavg = 21
                alpha = dat[:,17]

                alpha=alpha**2

                alpha_res[i-1] = np.max(alpha[t1:(t1+10)])


        return alpha_res
#=========================
def createpart():

        part = np.zeros((609,2))

        count=0.02
        part_u=np.array([])
        for i in range(1,30):
                part_temp = np.ones(21)*count
                part_u = np.append(part_u,part_temp)
                count=count+0.01
```

```
        part[:,0] = part_u#np.tile(np.arange(0.02,0.31,0.01)
            ,[21])
        part[:,1] = np.tile(np.arange(850,955,5),[29])
        #part=part.reshape((29,21,2))

        return part
#=========================
def normweight(y,ypred,sig_meas):
    W = (1/(sig_meas*np.sqrt(2*3.1416))) * np.exp(-(((y-ypred)-0)
        **2)/(2*sig_meas**2))
    W=W/sum(W)
    maxw = np.argmax(W)
    return W,maxw
#=========================
def normweight_ucc(y,ypred,sig_meas):
    W = (1/(sig_meas*np.sqrt(2*3.1416))) * np.exp(-(((y-ypred)-0)
        **2)/(2*sig_meas**2))
    W=W/sum(W)
    maxw = np.argmax(W)
    return W,maxw
#=========================
def normweight_exp(y,ypred,lam):
        #W=np.array([])
        #for i in y:
        W = scist.expon.pdf(y,ypred,lam)
                #W_ini = (np.exp(-mu))*((mu^(i-ypred))/(factorial
                    (i-ypred)))
                #W=np.append(W,W_ini)
        #
        W=W/sum(W)
        maxw = np.argmax(W)
        return W,maxw
#=========================
def weight(y,ypred,sig_meas):
    W = (1/(sig_meas*np.sqrt(2*3.1416))) * np.exp(-(((y-ypred)-0)
        **2)/(2*sig_meas**2))

    maxw = np.argmax(W)
    return W,maxw
#=========================
def resample(particles2,index):
    particles1=[]
    for i, count in enumerate(index[0]):
        particles1.extend([particles2[i]]*count)
    return particles1

def getfixedpart(orig_ran,p_array):
#=========================
# function 1 - take particle forest and random generate
        def find_nearest(array, value):
                array = np.asarray(array)
                idx = (np.abs(array - value)).argmin()
```

```
                return array[idx], idx


        answer = np.array([])
        index = np.array([])
        for i in orig_ran:
                ans_new, ind_new = find_nearest(p_array,i)
                answer = np.append(answer,ans_new)
                index = np.append(index,ind_new)

        return answer
#=========================
def getalphsim_mean_thresh(t1):

        alpha_res = np.zeros(609)

        for i in range(1,610):

                dat=np.loadtxt('/media/ross/Maxtor/simulations
                    2018/'+str(i)+'/'+str(i)+'.csv',delimiter
                    =',',skiprows=1)

        #indexkey:      Uavg = 1 , alphaavg = 17 , alphamin/max =
             19, prghavg = 21
                alpha = dat[:,17]

                alpha=alpha**2

                alpha_cut = alpha[t1:(t1+10)]

                thresh = 0.5*(np.max(alpha[52:])+np.min(alpha
                    [52:]))

                alpha_res[i-1] = np.mean(alpha_cut[alpha_cut<
                    thresh])


        return alpha_res
#=========================
def getalphsim(index):

        #alpha_res = np.zeros(609)
        i=index
        #for i in range(1,610):

        dat=np.loadtxt('/media/ross/Maxtor/simulations2018/'+str(
            i)+'/'+str(i)+'.csv',delimiter=',',skiprows=1)

        #indexkey:      Uavg = 1 , alphaavg = 17 , alphamin/max =
             19, prghavg = 21
        alpha = dat[:,17]
        u       = dat[:,1]
```

```
        alpha=alpha**2

                #alpha_res[i-1] = np.mean(alpha[t1:(t1+10)])


        return alpha, u
#=========================
def getalphsimt(t):

        alpha_res = np.zeros(609)
        u_res = np.zeros(609)
        #i=index
        for i in range(1,610):

                dat=np.loadtxt('/media/ross/Maxtor/simulations
                    2018/'+str(i)+'/'+str(i)+'.csv',delimiter
                    =',',skiprows=1)

        #indexkey:      Uavg = 1 , alphaavg = 17 , alphamin/max =
             19, prghavg = 21
                alpha = dat[:,17]
                u = dat[:,1]
                alpha=alpha**2

                alpha_res[i-1] = alpha[t]
                u_res[i-1] = u[t]

        return alpha_res, u_res
#=========================
def getalphsimt_2(t):

        alpha_res = np.zeros(609)
        j_res = np.zeros(609)
        #i=index
        for i in range(1,610):

                dat=np.loadtxt('/media/ross/Maxtor/simulations
                    2018/'+str(i)+'/'+str(i)+'_2.csv',delimiter
                    =',',skiprows=1)

        #indexkey:      Uavg = 1 , alphaavg = 17 , alphamin/max =
             19, prghavg = 21
                alpha = dat[:,18]
                j = dat[:,22]
                alpha=alpha**2

                alpha_res[i-1] = alpha[t]
                j_res[i-1] = j[t]

        return alpha_res, j_res
#=========================
def getalphsimt_2_m(t):
```

```
        alpha_res = np.zeros(609)
        j_res = np.zeros(609)
        #i=index
        for i in range(1,610):

                dat=np.loadtxt('/media/ross/Maxtor/simulations
                    2018/'+str(i)+'/'+str(i)+'_2.csv',delimiter
                    =',',skiprows=1)

        #indexkey:      Uavg = 1 , alphaavg = 17 , alphamin/max =
             19, prghavg = 21
                alpha = dat[:,18]
                j = dat[:,22]
                alpha=alpha**2

                alpha_res[i-1] = np.mean(alpha[t:t+5])
                j_res[i-1] = np.mean(j[t:t+5])

        return alpha_res, j_res
#=========================
def recusens(i,t):

        dat=np.loadtxt('/media/ross/Maxtor/simulations2018/'+str(
            i)+'/'+str(i)+'.csv',delimiter=',',skiprows=1)

        #indexkey:      Uavg = 1 , alphaavg = 17 , alphamin/max =
             19, prghavg = 21
        u = dat[:,1]
        uu = np.mean(u[t:t+10])

        return uu
#=========================
def getfreqtom(alpha1,timey):

        amean = 1*np.mean(alpha1)

        count=0
        indyold = 0

        for i in alpha1:
                #acurr = i

                if i < amean:
                        indynew = 0

                else: indynew = 1

                if indynew != indyold:
                        count+=1

                indyold=indynew
```

```
        return (count)/(np.max(timey)-np.min(timey))
#=========================
def getfreqsim(t1):

        freq_res = np.zeros(609)

        for i in range(1,610):

                dat=np.loadtxt('/media/ross/Maxtor/simulations
                    2018/'+str(i)+'/'+str(i)+'.csv',delimiter
                    =',',skiprows=1)

        #indexkey:      Uavg = 1 , alphaavg = 17 , alphamin/max =
             19, prghavg = 21
                alpha = dat[:,17]

                alpha=alpha**2

                asimmean = 1*np.mean(alpha[t1:(t1+10)])

                alphafreq = alpha[t1:]

                #freq_res[i-1] = np.mean(alpha[t1:(t1+10)])

                count=0
                indyold = 0

                for j in alphafreq:
                        #acurr = i

                        if j < asimmean:
                                indynew = 0

                        else: indynew = 1

                        if indynew != indyold:
                                count+=1

                        indyold=indynew

                freq_res[i-1] = count

        return freq_res*2
```

G

CODE - SIMULATION PROCESSING

G.1 SIMULATION POST-PROCESSING PYTHON SCRIPT

```
# paraview analysis through python

import paraview
from paraview.simple import *

for i in range(0,610):

        print i
        nufile = open("/media/ross/Maxtor/simulations2018/"+str(i
            )+"/"+str(i)+".OpenFOAM","w")
        nufile.close()

        with open('/media/ross/Maxtor/simulations2018/simstate2.
            pvsm', 'r') as file:
                # read a list of lines into data
                data = file.readlines()

        # now change the 2nd line, note that you have to add a
            newline
        data[3199] = '        <Element index="0" value="/media/
            ross/Maxtor/simulations2018/'+str(i)+'/'+str(i)+'.
            OpenFOAM"/>\n'

        # and write everything back
        with open('/media/ross/Maxtor/simulations2018/simstate2.
            pvsm', 'w') as file:
                file.writelines( data )

        servermanager.LoadState("/media/ross/Maxtor/simulations
            2018/simstate2.pvsm")

        quartileChartView1 = FindViewOrCreate('QuartileChartView
            1', viewtype='QuartileChartView')

                # set active view
        SetActiveView(quartileChartView1)

                # export view
        ExportView("/media/ross/Maxtor/simulations2018/"+str(i)
            +"/"+str(i)+"_2.csv", view=quartileChartView1)

        Delete(quartileChartView1)
        #Delete(reader)
```

G.2 SIMULATION RUN SCRIPT

```
#!/bin/bash
```

```
nam=($(seq 1 1 2))

for a in "${nam[@]}"

do

    cd ~/$a/
    cp ~/decomposeParDict ~/$a/system/
    blockMesh
    decomposePar
    mpirun -np 4 -bind-to-socket multiphaseEulerFoam -parallel >
        log
    reconstructPar

done
```

H

CODE - OPENFOAM CFD SIMULATION

H.1 OPENFOAM SIMULATION SETUP - CONSTANTS

```
FoamFile
{
    version     2.0;
    format      ascii;
    class       uniformDimensionedVectorField;
    location    "constant";
    object      g;
}


dimensions      [0 1 -2 0 0 0 0];
value           (0 -9.81 0);


FoamFile
{
    version     2.0;
    format      ascii;
    class       dictionary;
    location    "constant";
    object      transportProperties;
}

phases
(
    air
    {
        rho             1.225;
        nu              1.48e-05;
        kappa           2.6e-2;
        Cp              1007;

        diameterModel   constant;
        constantCoeffs
        {
            d               1e-3;
        }
    }

    water
    {
        rho             870;
        nu              2e-06;
        kappa           1e-6;
        Cp              4195;

        diameterModel constant;
        constantCoeffs
        {
```

```
            d               1e-3;
        }
    }
);


sigmas
(
    (air water)     0.0183
);

interfaceCompression
(
    (air water)     1
);

virtualMass
(
    //(air water)     1
);

drag
(
    (air water)
    {
        type blended;

        air
        {
            type SchillerNaumann;
            residualPhaseFraction 0;
            residualSlip 0;
        }

        water
        {
            type SchillerNaumann;
            residualPhaseFraction 0;
            residualSlip 0;
        }

        residualPhaseFraction 1e-3;
        residualSlip 1e-3;
    }
);


// This is a dummy to support the Smagorinsky model
transportModel  Newtonian;
nu              [0 2 -1 0 0 0 0] 0;
```

```
FoamFile
{
    version     2.0;
    format      ascii;
    class       dictionary;
    location    "constant";
    object      turbulenceProperties;
}


simulationType  laminar;
```

H.2 OPENFOAM SIMULATION SETUP - SYSTEM

```

FoamFile
{
    version     2.0;
    format      ascii;
    class       dictionary;
    object      blockMeshDict;
}

convertToMeters 1;
vertices
(
    (0 0 0)
    (0.08 0 0)
    (0.08 1.32 0)
    (0 1.32 0)
    (0 0 0.1)
    (0.08 0 0.1)
    (0.08 1.32 0.1)
    (0 1.32 0.1)
);

blocks
(
    hex (0 1 2 3 4 5 6 7) (10 100 1) simpleGrading (1 1 1)
);

edges
(
);

patches
(
    patch inlet
    (
        (1 5 4 0)
    )
```

```
    patch outlet
    (
        (3 7 6 2)
    )
    wall walls
    (
        (0 4 7 3)
        (2 6 5 1)
    )
);

mergePatchPairs
(
);


FoamFile
{
    version     2.0;
    format      ascii;
    class       dictionary;
    location    "system";
    object      controlDict;
}


application     multiphaseEulerFoam;

startFrom       startTime;

startTime       0;

stopAt          endTime;

endTime         5;

deltaT          0.0001;

writeControl    runTime;

writeInterval   0.05;

purgeWrite      0;

writeFormat     ascii;

writePrecision  6;

writeCompression uncompressed;

timeFormat      general;
```

```
timePrecision   6;

runTimeModifiable yes;

adjustTimeStep  no;

maxCo           0.5;

maxDeltaT       1;

functions
{
    fieldAverage1
    {
        type            fieldAverage;
        libs ( "libfieldFunctionObjects.so" );
        writeControl    writeTime;
        fields
        (
            U.air
            {
                 mean        on;
                 prime2Mean  off;
                 base        time;
            }

            U.water
            {
                 mean        on;
                 prime2Mean  off;
                 base        time;
            }

            alpha.air
            {
                 mean        on;
                 prime2Mean  off;
                 base        time;
            }

            p
            {
                 mean        on;
                 prime2Mean  off;
                 base        time;
            }
        );
    }
}


FoamFile
```

```
{
    version     2.0;
    format      ascii;
    class       dictionary;
    location    "system";
    object      decomposeParDict;
}

numberOfSubdomains 4;

method          scotch;

simpleCoeffs
{
    n               (1 4 1);
    delta           0.001;
}


FoamFile
{
    version     2.0;
    format      ascii;
    class       dictionary;
    location    "system";
    object      fvSchemes;
}


ddtSchemes
{
    default         Euler;
}

gradSchemes
{
    default         Gauss linear;
}

divSchemes
{
    default         none;

    "div\(phi,alpha.*\)"    Gauss vanLeer;
    "div\(phir,alpha.*,alpha.*\)"   Gauss vanLeer;

    "div\(alphaPhi.*,U.*\)" Gauss limitedLinearV 1;
    div(Rc)                 Gauss linear;
    "div\(phi.*,U.*\)"      Gauss limitedLinearV 1;
}

laplacianSchemes
```

```
{
    default         Gauss linear corrected;
}

interpolationSchemes
{
    default         linear;
}

snGradSchemes
{
    default         corrected;
}


FoamFile
{
    version     2.0;
    format      ascii;
    class       dictionary;
    location    "system";
    object      fvSolution;
}


solvers
{
    "alpha.*"
    {
        nAlphaSubCycles 2;
    }

    p_rgh
    {
        solver          GAMG;
        smoother        DIC;
        tolerance       1e-8;
        relTol          0.01;
    }

    p_rghFinal
    {
        $p_rgh;
        tolerance       1e-9;
        relTol          0;
    }

    pcorr
    {
        $p_rgh;
        tolerance       1e-5;
        relTol          0;
```

```
    }

    "U.*"
    {
        solver          smoothSolver;
        smoother        symGaussSeidel;
        tolerance       1e-05;
        relTol          0;
    }

    "T.*"
    {
        solver          smoothSolver;
        smoother        symGaussSeidel;
        tolerance       1e-8;
        relTol          0;
    }

    "Theta.*"
    {
        solver          smoothSolver;
        smoother        symGaussSeidel;
        tolerance       1e-05;
        relTol          0;
    }

    "k.*"
    {
        solver          smoothSolver;
        smoother        symGaussSeidel;
        tolerance       1e-05;
        relTol          0;
    }

    "epsilon.*"
    {
        solver          smoothSolver;
        smoother        symGaussSeidel;
        tolerance       1e-05;
        relTol          0;
    }
}

PIMPLE
{
    nOuterCorrectors 1;
    nCorrectors     2;
    nNonOrthogonalCorrectors 0;
}

relaxationFactors
{
```

```
    "U.*"           1;
    "T.*"           1;
    "alpha.*"       1;
    "Theta.*"       1;
    "k.*"           1;
    "epsilon.*"     1;
}


FoamFile
{
    version     2.0;
    format      ascii;
    class       dictionary;
    location    "system";
    object      setFieldsDict;
}

defaultFieldValues
(
    volScalarFieldValue alpha.air 1
    volScalarFieldValue alpha.water 0
);

regions
(
    boxToCell
    {
        box (0 0 -0.1) (0.08 1.32 0.1);;
        fieldValues
        (
            volScalarFieldValue alpha.air 0
            volScalarFieldValue alpha.water 1
        );
    }
);
```

H.3 OPENFOAM SIMULATION SETUP - INITIAL CONDITIONS

```

FoamFile
{
    version     2.0;
    format      ascii;
    class       volScalarField;
    object      alphaair;
}


dimensions      [0 0 0 0 0 0 0];

```

```
internalField   uniform 0;

boundaryField
{
    inlet
    {
        type            fixedValue;
        value           uniform 1;
    }
    outlet
    {
        type            zeroGradient;
    }
    walls
    {
        type            zeroGradient;
    }
}


FoamFile
{
    version     2.0;
    format      ascii;
    class       volScalarField;
    object      alpha.water;
}


dimensions      [0 0 0 0 0 0 0];

internalField   uniform 1;

boundaryField
{
    inlet
    {
        type            fixedValue;
        value           uniform 0;
    }
    outlet
    {
        type            zeroGradient;
    }
    walls
    {
        type            zeroGradient;
    }
}


FoamFile
```

```
{
    version     2.0;
    format      ascii;
    class       volScalarField;
    location    "0";
    object      alphas;
}


dimensions      [0 0 0 0 0 0 0];

internalField   uniform 1;

boundaryField
{
    inlet
    {
        type            calculated;
        value           uniform 0;
    }
    outlet
    {
        type            calculated;
        value           uniform 1;
    }
    walls
    {
        type            calculated;
        value           uniform 1;
    }
    defaultFaces
    {
        type            empty;
    }
}


FoamFile
{
    version     2.0;
    format      ascii;
    class       volScalarField;
    object      p_rgh;
}


dimensions          [1 -1 -2 0 0 0 0];

internalField       uniform 0;

boundaryField
{
```

```
    inlet
    {
        type            zeroGradient;
       // value           uniform 0;
    }
    outlet
    {
        type            totalPressure;
        p0              uniform 885;
    }
    walls
    {
        type            zeroGradient;
    }
}


FoamFile
{
    version     2.0;
    format      ascii;
    class       volScalarField;
    object      T.air;
}


dimensions          [0 0 0 1 0 0 0];

internalField       uniform 300;

boundaryField
{
    walls
    {
        type               zeroGradient;
    }
    outlet
    {
        type               inletOutlet;
        phi                phi.air;
        inletValue         $internalField;
        value              $internalField;
    }
    inlet
    {
        type               fixedValue;
        value              $internalField;
    }
    frontAndBackPlanes
    {
        type               empty;
    }
```

```
}


FoamFile
{
    version     2.0;
    format      ascii;
    class       volScalarField;
    object      T.water;
}


dimensions          [0 0 0 1 0 0 0];

internalField       uniform 350;

boundaryField
{
    walls
    {
        type               zeroGradient;
    }
    outlet
    {
        type               inletOutlet;
        phi                phi.water;
        inletValue         uniform 300;
        value              $internalField;
    }
    inlet
    {
        type               fixedValue;
        value              $internalField;
    }
    frontAndBackPlanes
    {
        type               empty;
    }
}


FoamFile
{
    version     2.0;
    format      ascii;
    class       volScalarField;
    object      Theta;
}


dimensions          [0 2 -2 0 0 0 0];
```

```
internalField   uniform 0.0;

boundaryField
{
    inlet
    {
        type            fixedValue;
        value           uniform 1.0e-7;
    }

    outlet
    {
        type            inletOutlet;
        inletValue      uniform 1.0e-7;
        value           uniform 1.0e-7;
    }

    walls
    {
        type            zeroGradient;
    }

    defaultFaces
    {
        type            empty;
    }
}


FoamFile
{
    version     2.0;
    format      binary;
    class       volVectorField;
    object      U.air;
}


dimensions      [0 1 -1 0 0 0 0];

internalField   uniform (0 0 0);

boundaryField
{
    inlet
    {
        type               fixedValue;
        value              uniform (0 0.16 0);
    }
    outlet
    {
        type               zeroGradient;
```

```
    }
    walls
    {
        type               fixedValue;
        value              uniform (0 0 0);
    }
}


FoamFile
{
    version     2.0;
    format      binary;
    class       volVectorField;
    object      U.water;
}


dimensions      [0 1 -1 0 0 0 0];

internalField   uniform (0 0 0);

boundaryField
{
    inlet
    {
        type               fixedValue;
        value              $internalField;
    }
    outlet
    {
        type               zeroGradient;
    }
    walls
    {
        type               fixedValue;
        value              uniform (0 0 0);
    }
}
```